



**DAMPING SUBSYNCHRONOUS RESONANCE
USING HVDC SUPPLEMENTARY CONTROLS**

by

Christophe Basila TAMBWE

BEng.

IN FULFILMENT OF MASTER OF SCIENCE DEGREE IN ENGINEERING
COLLEGE OF AGRICULTURE, ENGINEERING AND SCIENCES
UNIVERSITY OF KWAZULU-NATAL

August 2021

Supervisor: Dr. Rudiren Pillay Carpanen

DECLARATION 1 – PLAGIARISM

I, Christophe Basila Tambwe, declare that:

1. The research reported in this thesis, except where otherwise indicated, is my original research.
2. This thesis has not been submitted for any degree or examination at any other university.
3. This thesis does not contain other persons' data, pictures, graphs, or other information unless specifically acknowledged as being sourced from other persons.
4. This thesis does not contain other persons' writing unless specifically acknowledged as being sourced from other researchers. Where other written sources have been quoted, then:
 - a. Their words have been re-written, but the general information attributed to them has been referenced
 - b. Where their exact words have been used, then their writing has been placed in italics and inside quotation marks and referenced.
5. This thesis does not contain text, graphics or tables copied and pasted from the Internet unless specifically acknowledged, and the source being detailed in the thesis and in the References sections.

Signed Date: 26/08/2021.....

Christophe Basila Tambwe

As the candidate's supervisor, I agree to the submission of this thesis.

Signed:Date:

Dr. Rudiren Pillay Carpanen

DECLARATION 2 – PUBLICATIONS

The following research publications emanated from this research investigation, namely:

Published conference papers

- [1] C.B. Tambwe and R.P. Carpanen. "Investigating the Impact of HVDC on the Damping Subsynchronous Resonance." International SAUPEC/RobMech/PRASA Conference. 2020
- [2] C.B. Tambwe and R.P. Carpanen. "Damping Subsynchronous Oscillations using an HVDC-based Single-Mode Damping Controller." 2021 IEEE PES/IAS Power Africa.

Journal article to appear in the International Journal of Engineering Research in Africa, 2022.

- [3] C.B. Tambwe and R.P. Carpanen, "Damping Subsynchronous Oscillations Using a High Voltage Direct Current based Multimodal Damping Controller,"

Dedicated to my family

ACKNOWLEDGMENTS

I would like to express my gratitude to my supervisor, Dr. Rudiren Pillay Carpanen, for his patient supervision, support, and advice during my time as his student. I have been privileged to have a supervisor concerned about my work. His prompt responses to my queries and concerns and his involvement and guidance made it possible to complete this thesis in a relaxing work atmosphere.

I want to thank all of the academic staff, lecturers, and friends who helped me achieve this research in any manner. Their assistance has been precious to me.

ABSTRACT

In power transmission lines, series capacitors are used to increase power transfer capability. However, series capacitors are the primary source of subsynchronous torsional oscillations of nearby turbogenerator shafts. These electronic components in transmission lines expose the turbogenerator system's torsional dynamics to a resonance phenomenon. Typically, this phenomenon appears in the form of supersynchronous and subsynchronous resonance. Subsynchronous resonance is often the most dangerous for its harmful effects, leading to shaft failure and power system instability. It differs from supersynchronous resonance, which does not adversely affect system stability. A turbogenerator set commonly consists of natural modes with frequencies smaller than the power system rated frequency. When the torsional frequencies resulting from the transmission line's series capacitors affect the turbine-generator shaft's operation by coinciding with one of its natural frequencies, they induce the phenomenon known as subsynchronous resonance. Supersynchronous resonance refers to torsional oscillations whose frequencies exceed the nominal frequency of the electrical network.

Researchers have used many approaches to solve the subsynchronous resonance phenomenon in power systems. This research focuses on exploiting supplementary controls of a parallel HVDC system to address the subsynchronous resonance problem. However, owing mainly to the converter's current regulators and many other parameters, the HVDC system can also potentially induce subsynchronous oscillation on nearby turbine-generator shafts. This work focuses on a power system comprising a modified IEEE First Benchmark Model to incorporate a parallel HVDC link. This power system is subjected to torsional instability from either the resonant line AC line, HVDC controls, or both. Thus, this study contrasts the effectiveness of single-mode and multimodal damping controllers when the turbogenerator shaft's torsional dynamics undergo instability from the parallel AC-DC system.

Furthermore, this thesis utilizes the time domain-based test signal and phase correction methods to design the supplementary subsynchronous damping controllers. These two approaches allow obtaining the optimal parameters of the damping controllers. The controller consists of a Power System Stabilizer to control the inertial mode and Synchronous Damping Controller to control other unstable torsional modes to achieve positive damping. This research uses the FFT analysis to assess the performance of supplementary HVDC damping controllers on the torsional dynamics of the turbogenerator shaft in the parallel AC-DC system.

TABLE OF CONTENTS

DECLARATION 1 – PLAGIARISM	ii
DECLARATION 2 – PUBLICATIONS	iii
ACKNOWLEDGMENTS	v
ABSTRACT.....	vi
TABLE OF CONTENTS.....	vii
NOMENCLATURE.....	xiv
Acronyms.....	xiv
Special symbols.....	xv
LIST OF FIGURES.....	xvii
LIST OF TABLES	xxi
1 CHAPTER ONE: INTRODUCTION.....	1
1.1 Definitions	1
1.1.1 Power System Stability.....	1
1.1.2 Power System Oscillations & Damping System	2
1.1.3 HVDC Links	3
1.2 Research Questions	4
1.3 Problem Statements.....	5
1.4 Aims and objectives	6
1.5 Methodology.....	6
1.6 Thesis Organisation.....	6
2 CHAPTER TWO: LITERATURE REVIEW	8
2.1 Introduction	8
2.2 Mechanism of Subsynchronous Resonance.....	8
2.2.1 Introduction.....	8
2.2.2 Series Capacitor Compensated Networks	9
2.2.3 Type of Subsynchronous Resonance	10

2.2.3.1	Induction Generator Effect.....	10
2.2.3.2	Torsional Interaction.....	10
2.2.3.3	Transient Torque Effect	10
2.2.4	Devices Dependent Subsynchronous Oscillations	11
2.2.4.1	Interaction with excitation controls (PSS and AVR).....	11
2.2.4.2	Interaction with speed governors.....	12
2.2.4.3	Interaction with HVDC controls	12
2.2.5	Subsynchronous Resonance Analysis.....	13
2.2.5.1	Frequency Scanning.....	13
2.2.5.2	Eigenvalue Analysis	14
2.2.5.3	Electromagnetic Transient Programs (EMTP) Analysis	14
2.2.6	SSR Countermeasures	14
2.2.6.1	Reduced Compensation Level and Operating Procedures	14
2.2.6.2	Static Blocking Filters	15
2.2.6.3	Dynamic Filters	16
2.2.6.4	Bypass Damping Filters.....	17
2.2.6.5	Thyristor Controlled Series Compensation (TCSC).....	17
2.2.6.6	Supplementary Excitation Damping Controls (SEDC)	19
2.2.6.7	Static Var Converter-Based Supplementary Damping Controls	21
2.2.6.8	LCC HVDC controls based-countermeasures.....	22
2.2.6.8.1	Introduction	22
2.2.6.8.2	Radial HVDC links.....	22
2.2.6.8.3	Parallel AC-DC System	23
2.3	High Voltage Direct Current Systems.....	25
2.3.1	Introduction.....	25
2.3.2	Advantages of HVDC vs. HVAC.....	25
2.3.3	LCC HVDC	26
2.3.3.1	Mercury arc valves	27

2.3.3.2	Thyristor valves	28
2.3.4	CCC HVDC	29
2.3.4.1	CCC-HVDC Advantages	30
2.3.4.2	Disadvantages of CCC-HVDC compared to LCC-HVDC	30
2.3.5	Components of LCC HVDC	30
2.3.5.1	Converters	31
2.3.5.2	Converter Transformers	31
2.3.5.3	Smoothing Reactors.....	32
2.3.5.4	Harmonic Filters (AC filters)	33
2.3.5.5	Reactive Power Compensation.....	34
2.3.5.6	Electrodes.....	34
2.3.5.7	DC Transmission Lines.....	35
2.3.6	LCC SYSTEM TOPOLOGY.....	35
2.3.6.1	Monopolar HVDC	35
2.3.6.2	Bipolar HVDC-	36
2.3.7	CONVERTER THEORY	37
2.3.7.1	Ideal Diode Bridge.....	37
2.3.7.2	Three-phase thyristor bridge	38
2.3.7.3	Commutation Overlap in Rectification mode	39
2.3.7.4	Commutation Overlap in Inversion Mode	40
2.3.8	LCC HVDC Controls	42
2.3.8.1	Static Characteristics of LCC HVDC	42
2.3.8.2	HVDC Control System Overview	43
2.3.8.3	Implemented HVDC Control System	45
2.3.8.3.1	Gate Control	46
2.3.8.3.2	Control Schemes.....	47
2.3.8.3.3	Phase-Locked Oscillator	48
2.3.8.3.4	Voltage-Dependent Current Limiter (VDCOL)	49

2.3.8.3.5	Tap Changer Control.....	49
2.3.8.3.6	Current Controllers	49
2.3.8.3.7	Extinction Angle Controller	50
2.3.8.3.8	Active Power Controls	50
2.3.8.3.9	Frequency Controls.....	50
2.3.9	Harmonics and Filters.....	51
2.3.9.1	Characteristic Harmonics.....	51
2.3.9.1.1	DC Side Harmonics	52
2.3.9.1.2	AC Side Harmonics	53
2.3.9.1.3	Harmonic Generation in 12-pulse Converters	54
2.3.9.2	Filter Design.....	55
2.3.9.2.1	Single-Tuned Filters.....	56
2.3.9.2.2	Double-Tuned Filter.....	57
2.3.9.2.3	Damped-Type Filters (High-Pass Filters)	59
2.3.10	Interactions Between AC and DC Systems.....	61
2.3.11	Faults Management and HVDC System Protections	63
2.3.11.1	Introduction	63
2.3.11.2	Type of Faults and Nature.....	64
2.3.11.2.1	DC Line Fault	64
2.3.11.2.2	AC Line Fault	64
2.3.11.2.3	Commutation Failure	65
2.4	Conclusion.....	65
3	CHAPTER THREE: POWER SYSTEM MODELLING	67
3.1	Introduction	67
3.2	Synchronous machine	67
3.2.1	Description of the synchronous machine	68
3.2.2	Synchronous Machine Modelling.....	68
3.3	Turbogenerator Mechanical System Modelling.....	72

3.4	Excitation Control System.....	75
3.4.1	Introduction.....	75
3.4.2	Constant Excitation System (Manual Excitation)	75
3.4.3	Static Excitation (IEEE Type ST1A).....	76
3.4.4	Power System Stabilizer	76
3.5	Series compensated transmission line model.....	77
3.5.1	Preliminary Eigenvalue Analysis for the IEEE FBM with Fixed Capacitors	80
3.6	LCC HVDC Modelling	80
3.6.1	12-pulse LCC Modeling	80
3.6.2	DC line modeling	81
3.6.3	Active and Reactive Power	83
3.6.4	Experimental Viewpoint	84
3.6.4.1	Simulation and results.....	85
3.6.4.1.1	Study case 1: Steady-State Operation	86
3.6.4.1.2	Study case 2: DC line fault conditions	87
3.6.4.1.3	Study case 3: Rectifier AC fault Conditions	89
3.6.4.1.4	Study case 4: Inverter AC fault conditions.....	92
3.7	Conclusion.....	94
4	CHAPTER FOUR: INVESTIGATING THE IMPACT OF HVDC ON THE DAMPING SUBSYNCHRONOUS RESONANCE.....	95
4.1	Introduction	95
4.2	Study System	97
4.2.1	Turbogenerator Shaft's Mechanical System	98
4.2.2	Mathematical modeling	99
4.2.3	AC Line Modelling.....	100
4.2.4	DC Line Modelling.....	100
4.3	Simulation and Results.....	102
4.4	Conclusion.....	107

5	CHAPTER FIVE: DAMPING SUBSYNCHRONOUS RESONANCE USING HVDC SUPPLEMENTARY SUBSYNCHRONOUS DAMPING CONTROLLERS.....	108
5.1	Introduction	108
5.2	The study system.....	109
5.3	Torsional oscillation in HVDC-equipped power systems	110
5.3.1	Introduction.....	110
5.3.2	HVDC- based Subsynchronous Damping Controller.....	110
5.3.3	AC / DC Transfer Function.....	111
5.3.4	HVDC-based SSDC Design Block Diagram	113
5.3.4.1	HVDC-based Single-Mode Damping Controller (SMDC).....	115
5.3.4.2	HVDC-based Multimodal Damping Controller (MMDC).....	115
5.3.4.2.1	Introduction	115
5.3.4.2.2	Designing Purpose	117
5.3.4.3	SSDC Design Procedure based on Test Signal and Phase Correction Methods	117
5.3.4.3.1	Single-Mode Damping Controller Design Procedure	118
5.3.4.3.2	Multi-Modal Damping Controller Design Procedure	119
5.4	Simulation and Discussions	120
5.4.1	System Response for the Parallel AC-DC System with $P_{HVDC} = 0.4847$ pu	121
5.4.1.1	HVDC-based Single Mode Damping controller (SMDC)	122
5.4.1.1.1	SMDC and PSS Applied to Case (a).....	122
5.4.1.1.2	SMDC and PSS Applied to Case (b)	126
5.4.1.2	Multimodal Instability with HVDC-based Single Mode Damping Controller Performance.....	127
5.4.1.2.1	Introduction	127
5.4.1.2.2	TG torsional response due to HVDC for case (c)	128
5.4.1.2.3	SMDC and PSS Applied to Case (c).....	129
5.4.1.3	HVDC-based Multi-Modal Damping Controller (MMDC).....	132
5.4.1.3.1	MMDC and PSS Applied to Case (c)	132

5.4.1.3.2	MMDC and PSS Applied to Case (d)	134
5.4.2	System Response for the Parallel AC-DC System with $P_{HVDC} = 0.4154$ pu	136
5.4.2.1	HVDC-based Single-Mode Damping Controller Performance (SMDC) at a different HVDC power	137
5.4.2.1.1	SMDC and PSS Applied to Case (aa)	137
5.4.2.1.2	SMDC and PSS Applied to Case (bb)	140
5.4.2.2	Multimodal Instability HVDC-based Single Mode Damping Controller Performance at a different HVDC power	142
5.4.2.2.1	Introduction	142
5.4.2.2.2	SMDC and PSS Applied to Case (cc)	143
5.4.2.3	Multi-Modal Damping Controller Performance (MMDC) at a different HVDC power 146	
5.4.2.3.1	MMDC and PSS applied to Case (cc)	146
5.4.2.3.2	MMDC and PSS Applied to Case (dd)	148
5.5	Conclusion	150
6	CHAPTER SIX: CONCLUSION AND FUTURE WORK	152
6.1	Summary of the Results	152
6.2	Possible Future Work Suggestions	155
7	REFERENCES	156
8	APPENDIX	164

NOMENCLATURE

Acronyms

AC	Alternating Current
CBM	Cigre Benchmark Model
CC	Constant Current
CCC	Capacitive Commutative Converter
CEA	Constant Extinction Angle
DC	Direct Current
ESCR	Equivalent Short Circuit Ratio
EPC	Equidistant Pulse Control
FACTS	Flexible AC Transmission Systems
FBM	First Benchmark Model
FFT	Fast Fourier Transform
HVAC	High Voltage Alternating Current
HVDC	High Voltage Direct Current
IEEE	Institute of Electrical and Electronic Engineering
IGBT	Insulated Gate Bipolar Transistor
IPC	Individual Pulse Control
LCC	Line-Commutative Converter
MATLAB	Matrix Laboratory
MMDC	Multi-Modal Damping Controller
PI	PI controller
PLL	Phase-Locked Oscillator
PSCAD	Power System Computer-Aided Design
PSS	Power System Stabiliser
RCR	Rectifier Current Regular
SCR	Short Circuit Ratio
SMDC	Single-Mode Damping Controller

SSDC	Supplementary Subsynchronous Damping Controller
SSO	Subsynchronous Oscillation
SSR	Subsynchronous Resonance
TG	Turbogenerator

Special symbols

α	Firing angle
δ	Extinction angle
μ	Commutation overlap angle
β	Ignition advance angle
θ	Generator rotor angle
δ_i	Synchronous generator's rotor angle of the i^{th} rotating mass
ω	Angular velocity
ω_0	Base angular velocity based on the rated power system's frequency
ω_i	Angular velocity of the i^{th} rotating mass
$\lambda_d, \lambda_{1q}, \lambda_{2q}, \lambda_{fd}$	Synchronous machine's rotor circuit's quadratic flux linkages
\varnothing_R	The phase difference between the quadratic rectifier voltage and current
A	State matrix
B	Control matrix
C	Transmission line's series capacitor
L	Transmission line's series inductance
D_i	Internal self-damping coefficient of the i^{th} rotating mass
D_{ij}	External mutual damping between two masses
D_T	Total damping turbogenerator electromechanical system
E_{fd}	Exciter's field voltage
F_1, F_2, F_3, F_3	The fraction of mechanical power of each turbine
H	System's inertial time constant
$i_d, i_q, i_{1q}, i_{1q}, i_{2q}$	Quadratic currents stator and rotor circuits

I_{dc}	The nominal DC line's direct current
I_{Rdc}, I_{Idc}	Rectifier and inverter stations' direct current
i_{qA}^t, i_{dA}^t	Bus A's quadratic AC line currents
i_{fd}	Synchronous machine's field current
I_q, I_d	DC line's current in the quadratic frame
K	Transmission line's compensation level
K_R, K_I	Current controller's gains of the rectifier and inverter
K_{ij}	Shaft sections' spring constant
K_{SSDC}	Damping controller gain
$L_{ffd}, L_{11d}, L_{11q}, L_{22q}$	Self-inductances of rotor circuit and damper windings
L_{ad}, L_{aq}	Rotor circuit's mutual inductances
L_t	Converter Transformer's leakage reactance
L_T	Electrical system's overall inductance
L_{DC}	DC line's reactance (smoothing reactor)
L_d, L_q	Quadratic synchronous inductances
R_a	Synchronous generator's armature resistance
R_{fd}	Rotor circuit winding's resistance
$R_d, R_{1q}, R_{2q},$	Damp windings' resistances
R_{DC}	DC line's resistance
T_e	Synchronous machine's electrical torque
T_i	Electrical torque of the i^{th} mass
T_m	Mechanical torque
T_R, T_I	Current controller's time constants of the rectifier and inverter
$V_{qA}, V_{dA}, V_{qB}, V_{dB}$	quadratic voltages of the parallel ac-dc system's buses
V_{qr}, V_{ql}	AC Voltages of the rectifier and inverter in the rotor d-q reference frame
U	Input vector
X_{CR}, X_{CI}	Converter stations' commutative reactances

LIST OF FIGURES

Figure 2-1: Simplified RLC Circuit [32]	9
Figure 2-2: HVDC and HVAC schemes' cost comparison [104]	26
Figure 2-3: The Nelson River DC System's Mercury-arc valve [106].....	27
Figure 2-4: Twelve-pulse thyristor valves [106]	28
Figure 2-5: Configurations for applying series capacitors at HVDC substations [105]	29
Figure 2-6: LCC HVDC components[20].....	31
Figure 2-7: Large single-phase three winding transformers [111]	32
Figure 2-8: Air core reactor [113]	33
Figure 2-9: High pass filter up to 24 kV [114].....	33
Figure 2-10: Three-phase capacitor bank[114]	34
Figure 2-11: Monopolar HVDC [104].....	36
Figure 2-12: Bipolar HVDC [104]	36
Figure 2-13: Three-phase diode bridge circuit [102].....	38
Figure 2-14: Three-phase full thyristor bridge circuit [102]	38
Figure 2-15: Commutation process from valve T1 to T3 [104]	40
Figure 2-16: Commutation from valve T ₁ to T ₃ [104].....	41
Figure 2-17: Static characteristics of DC voltage and DC current under CC control mode on the rectifier side [40, 99]	42
Figure 2-18: Static characteristics of DC voltage and DC current with positive and negative directions[107]	43
Figure 2-19: Hierarchy of different levels of HVDC controls [4, 51]	44
Figure 2-20: Conventional LCC HVDC Control System [117]	45
Figure 2-21: Rectifier Current Regulator [90, 104].....	46
Figure 2-22: Inverter Voltage Regulator [90, 104].....	46
Figure 2-23: Converter firing configuration [115]	47
Figure 2-24: Three-phase PI-controller phase-locked loop [117]	48
Figure 2-25: Phase Locked based model of PLL [117]	48
Figure 2-26: Static characteristics of VDCOL [115].....	49

Figure 2-27: Converter transformer primary side’s phase currents waveforms [18].....	53
Figure 2-28: AC Filter Configuration [124, 125].....	56
Figure 2-29: Double-tuned filter design [124]	58
Figure 2-30: C-Type Filter Design [125].....	60
Figure 2-31: Converter and AC system [121].....	61
Figure 3-1: IEEE FBM Shaft’s mechanical system [40]	72
Figure 3-2: IEEE Type ST1A’s Simplified Model [3]	76
Figure 3-3: Power System Stabilizer’s Simplified Block [3].....	76
Figure 3-4: SMIB based- RLC Circuit [135]	77
Figure 3-5: The real part of SSR eigenvalues as a function of the series-compensated transmission line’s compensation percentage [44, 135].....	80
Figure 3-6: DC line T-model [40]	81
Figure 3-7: HVDC System Configuration [104]	85
Figure 3-8: Rectifier Response Under Steady-State Operation (Case 1).....	86
Figure 3-9: Inverter Response Under Steady-State Operation (Case 1).....	87
Figure 3-10: Rectifier Response Under DC Fault Condition (Case 2)	88
Figure 3-11: Inverter Response Under DC Fault Condition (Case 2)	89
Figure 3-12: Rectifier Response Under Rectifier Bus AC Fault Condition.....	90
Figure 3-13: Inverter Response Under Rectifier Bus AC Fault Condition	91
Figure 3-14: Inverter Response Under Inverter Bus AC Fault Condition	92
Figure 3-15: Rectifier Response Under Inverter Bus AC Fault Conditions	93
Figure 4-1: Modified IEEE FBM with the Parallel HVDC line [40]	97
Figure 4-2: Rectifier Bus Reference Axis [40]	99
Figure 4-3: System’s time domain response in Case (1)	103
Figure 4-4: System’s time domain response in Case (2)	104
Figure 4-5: System’s time domain response in Case (3)	105
Figure 4-6: System’s time domain response in Case (4)	106
Figure 5-1: Modified IEEE First Benchmark Model with an HVDC line in parallel [40]	109

Figure 5-2: HVDC-Based SSO [139].....	111
Figure 5-3: Transfer functions connecting $\Delta\omega_5$ and ΔT_e in HVDC [93, 142, 144].....	111
Figure 5-4: SSDC path isolation [139, 142]	112
Figure 5-5: Block Diagram of Excitation Control System and Rectifier Current Regulator with two Compensators (PSS and SSDC) [97, 144].....	114
Figure 5-6: Single-Mode Damping Controller Configuration (SMDC) [94, 97, 99]	115
Figure 5-7: Multi-Modal Damping Controller Configuration (MMDC) [93, 95, 143]	116
Figure 5-8: Simplified Transfer Scheme for Phase Correction Analysis [96, 144].....	118
Figure 5-9: Mode 1 (15.99 Hz) Sinusoidal Test Signal.....	122
Figure 5-10: Phase-Frequency Characteristic Curve for Mode 1.....	123
Figure 5-11: Mode 1 Damping Controller's Bode Plot	123
Figure 5-12: System Response in Case (a) following a 75 ms 3-phase short-circuit on the resonant AC line ($K=0.7$, $P_g=0.9$ pu, $P_d=0.4846$ pu, $PF=0.9$).....	124
Figure 5-13: Rotor speed deviation's FFT results in case (a) without compensators.....	125
Figure 5-14: Rotor speed deviation's FFT results in case (a) with SMDC (designed for Mode 1) and PSS	125
Figure 5-15: System Response in Case (b) following a 75 ms 3-phase short-circuit on the resonant AC line ($K=0.61$, $P_g=0.8$ pu, $P_d=0.4846$ pu, $PF=0.9$).....	126
Figure 5-16: FFT analysis of rotor speed deviation for case (b) without Compensators.....	127
Figure 5-17: Rotor speed deviation's FFT results in case (b) with SMDC (designed for Mode 1) and PSS	127
Figure 5-18: Transient response and FFT results of rotor speed deviation in case (c) with HVDC tie on and off.....	128
Figure 5-19: System Response for Various SMDC and PSS applied to Case (c)	130
Figure 5-20: Rotor speed deviation's FFT results in case (c) without compensators.....	130
Figure 5-21: Rotor speed deviation's FFT analysis in case (c) with SMDC and PSS.....	131
Figure 5-22: System Response in Case (c) following a 75 ms 3-phase short-circuit on the resonant AC line ($K=0.41$, $P_g=0.7$ pu, $P_d=0.4846$ pu, $PF=0.9$).....	133
Figure 5-23: Rotor speed deviation's FFT results in case (c) with MMDC and PSS.....	133

Figure 5-24: System Response in Case (d) following a 75 ms 3-phase short-circuit on the resonant AC line ($K=0.23$, $P_g=0.67$ pu, $P_d=0.4846$ pu, $PF=0.9$).....	135
Figure 5-25: Rotor speed deviation's FFT results in case (d) without compensators	135
Figure 5-26: Rotor speed deviation's FFT results in case (d) with MMDC and PSS	136
Figure 5-27: Mode 1's Phase-Frequency Characteristic Curve for Case (aa).....	137
Figure 5-28: Mode 1 Damping Controller's Bode Plot	138
Figure 5-29: System Response in Case (aa) following a 75 ms 3-phase short-circuit on the resonant AC line ($K=0.70$, $P_g=0.9$ pu, $P_d=0.4154$ pu, $PF=0.9$).....	139
Figure 5-30: Rotor speed deviation's FFT results in case (aa) without compensators	139
Figure 5-31: Rotor speed deviation's FFT results in case (aa) with SMDC (designed for Mode 1) and PSS	140
Figure 5-32: System Response in Case (bb) following a 75 ms 3-phase short-circuit on the resonant AC line ($K=0.61$, $P_g=0.8$ pu, $P_d=0.4154$ pu, $PF=0.9$).....	141
Figure 5-33: Rotor speed deviation's FFT results in case (bb) without compensators.....	141
Figure 5-34:FFT analysis of rotor speed deviation for case (bb) with the Multi-Modal Damping Controller and Power System Stabilizer	142
Figure 5-35: Transient response and FFT results of rotor speed deviation in case (cc) with HVDC tie on and off.	143
Figure 5-36: System Response for Various SMDC and PSS applied to Case (cc)	144
Figure 5-37: Rotor speed deviation's FFT results in case (cc) without compensators	144
Figure 5-38: Rotor speed deviation's FFT analysis in case (cc) with SMDC and PSS	145
Figure 5-39: System Response in Case (cc) following a 75 ms 3-phase short-circuit on the resonant AC line ($K=0.41$, $P_g=0.7$ pu, $P_d=0.4154$ pu, $PF=0.9$).....	147
Figure 5-40: Rotor speed deviation's FFT results in case (cc) with MMDC and PSS	148
Figure 5-41: System Response in Case (dd) following a 75 ms 3-phase short-circuit on the resonant AC line ($K=0.23$, $P_g=0.67$ pu, $P_d=0.4154$ pu, $PF=0.9$).....	149
Figure 5-42: Rotor speed deviation's FFT results in case (dd) without compensators.....	150
Figure 5-43:: Rotor speed deviation's FFT results in case (dd) with MMDC and PSS.....	150

LIST OF TABLES

Table 2-1: Classification of SCR and ESCR [131]	63
<i>Table 3-1: Current regulator parameters</i>	84
Table 4-1: Turbogenerator Shaft Torsional Modes	98
Table 4-2: Operating Points (Case Study)	103
Table 5-1: Operating Points (Case Study) with $P_{dc}=0.4846$ pu	121
Table 5-2: Parameters of MMDC designed for case (c)	132
Table 5-3: Parameters of MMDC Designed for Case (d)	134
Table 5-4: Operating Points with $P_{dc}=0.4154$ pu (Case Study).....	136
Table 5-5: Parameters of MMDC Designed for Case (cc).....	146
Table 5-6: Parameters of MMDC used for case (dd)	149

CHAPTER ONE: INTRODUCTION

1.1 Definitions

1.1.1 Power System Stability

The power system's stability is described as its capability to maintain a stable operation when exposed to disturbances [1]. Small fluctuations in power systems usually depend on whether the power grid is directly connected or disconnected from the loads [2]. Thus, depending on the power grid's stability concept, its operation must withstand these disturbances without causing failures. Moreover, relatively large electrical networks have a high probability of being at risk of significant disruptions. In such a case, based on protective devices designed to rid the power grid of the defective component, the electric network must return as fast as possible to its stable operating state and restore energy production to the affected loads [3]. Power system stability has typically been a matter of maintaining synchronous operation. The power system behavior under transient disturbances generally is the primary concern in assessing its stability. In line with [4], a stable power system can effectively provide full load and efficiently work when exposed to disturbances. Power system stability as a whole is an extensive area covering many aspects within its scope. Its key features boil down to rotor angle stability, voltage stability, and Med-term and Long-term stability [3, 5].

- Rotor angle stability is described as a power grid-connected generator's ability to maintain synchronous operation at the same frequency. In general, sustaining the rotor angle stability is a complex process. Achieving rotor angle stability does not exclusively depend on its synchronous machine's electromechanical characteristics. Still, due to their fast regulation-based advantages, damping controllers are used to enhance rotor angle stability [1, 4].
- Voltage stability is the power system's ability to maintain reasonable voltages on all network buses under normal operating conditions and after disturbances. The voltage instability condition often affects the power system operation during a heavy load demand or after disturbances that cause a progressive and uncontrollable decrease in the grid voltage. A power grid's inability to satisfy reactive power needs is an extremely important factor influencing voltage stability [6, 7].
- Medium-term and long-term stability are commonly attributed to the electrical grid's response to significant disturbances and upheavals. These perturbations result in considerable power flow, voltage, and frequency fluctuations. Their occurrence also leads to sluggish systems, controls, and protections usually not modeled in transient stability studies [8, 9].

- Moreover, transient stability is described as the electric network's ability to keep synchronism during extreme transient disruptions, such as power loss, significant load loss, or electrical grid breakdown [10].

This research focuses on a particular case of rotor angle stability known as subsynchronous resonance. SSR effect usually happens in series-compensated transmission lines. The phenomenon usually occurs as subsynchronous oscillations, depending on the type of its origins, which can be power system controls or series capacitors in transmission lines [4].

As per IEEE [11]:

“Subsynchronous resonance is an electric power system condition where the electric network exchanges energy with a turbine generator at one or more of the natural frequencies of the combined system below the synchronous frequency of the system.”

1.1.2 Power System Oscillations & Damping System

The oscillatory phenomenon is one of the core elements of this study. The resonance phenomenon always induces the turbogenerator shaft's torsional oscillations.

Oscillation is described according to [12] as *“The repetitive variation, typically in time, of some measure about a central value (often a point of equilibrium) or between two or more different states. The term vibration is sometimes used more narrowly to refer to mechanical oscillation but is sometimes used synonymously with oscillation..”*

There are many roots of electromechanical oscillations in a power network. As a result, numerous damping studies were performed over several decades to ensure power systems' electromechanical stability. These oscillations typically occur in different modes in power systems, namely torsional modes, control modes, local modes, and inter-area modes [3-5].

- The torsional modes, which typically vary from 5 to 120 Hz, are related to the turbogenerator shaft's rotational modules. The issues associated with the torsional modes are due to the power systems that experience torsional interaction, as their transmission lines include series capacitors [13].
- Power system devices such as AVR, HVDC, FACTS, and generators' high-speed controllers can also generate torsional interaction. The subsequent torsional interaction produces electromechanical oscillations due to power-system control modes varying between 0.1 and 0.5 Hz [1, 13].
- Local modes generally vary between 0.8 to 2.5 Hz. This category of oscillatory modes relates to a one-station unit that oscillates concerning the whole power grid [1, 4].
- Power system oscillations known as inter-area modes (0.1-0.8Hz) include multiple devices swinging in a power grid's specific portion against devices located in other regions. When

linked to weak power systems, the tight couplings of groups of devices and their connections are the fundamental causes of these types of oscillatory modes [1, 13].

The study conducted in this research explores the SSR phenomenon related to torsional oscillation modes in a power grid whose transmission line comprises a series capacitor. Although the primary source of SSR is assumed to be series capacitors, this study also considers interactions between HVDC controls and the turbogenerator set. This consideration then refers to the types of oscillations due to power system controls, taking into account the instability resulting from HVDC controls. This thesis does not consider any instability arising from power system device controls other than HVDC.

As per physics [14]:

“Damping is described as the restriction of vibratory motion, such as mechanical oscillations, noise, and alternating electric currents, by energy dissipation.”

The damping analysis undertaken in this thesis will make it possible to reduce the amplitude of torsional oscillations of the turbogenerator shaft to protect the latter against any resulting failure. The damping of oscillations will also improve the power system's reliability and lead to efficient operation. It will also allow maximum power transfer depending on the operating conditions. Although HVDC Systems controls are considered an alternative to overcome power system instability, in most cases, they are part of the factors inducing subsynchronous oscillations in power systems [15].

1.1.3 HVDC Links

In HVDC systems, AC power received from an AC grid is converted to DC via a converter station, transferred via cables or overhead transmission lines, and reconverted to AC by another converter station [16]. Converter transformers are used at both converter stations to adjust the AC network's power appropriately. The power conversion is typically performed via high-power semiconductor valves. Since only active power is transmitted in HVDC systems, no line power is wasted on the reactive power transmission [17]. As a result, utilizing HVDC systems, it is possible to transfer the same amount of energy through a smaller number of transmission lines. Hence, the need for land to accommodate transmission lines is significantly reduced. In environments where humans live, HVDC systems present a remarkable safety aspect as opposed to HVAC systems. HVDC systems emit reduced magnetic fields, making it easier to install power lines in environments where humans live. When an AC transmission line is upgraded to handle DC, its load capacity increases dramatically. As a result, using a highly controllable DC system can prevent power grids from experiencing power outages [18, 19].

Today, two major HVDC technologies are used: HVDC Classic and HVDC Light. The goal of these technologies mainly focuses on DC power transfer. However, their main difference is the power conversion method within their converter stations, which depends precisely on their respective high-power semiconductor valves. HVDC Classic and HVDC Light use thyristor power semiconductors and

integrated gate bipolar transistors (IGBTs). The HVDC Classic technology is primarily utilized to transmit bulk power over long distances and allow the interconnection of distinct power grids where AC transmission lines are inappropriate. Typical power ratings for these systems range from 100 MW to 8,000 MW. Power transfer in HVDC Classic may be carried out via overhead lines for more than 600 km, submarine cables over 50-100 km, or a combination of cables and overhead lines. Converters used in HVDC Classic are line-commutated because their configuration consists of thyristors whose turn-off signals are usually regulated by the AC line's voltage reversal [19-21].

In 1997, the ABB group developed the HVDC Light, whose converters use IGBT-based technology. This system was designed for electricity transmission, where the power involved is greater than 50 MW. Compared to thyristors as controllable power electronics components, IGBTs give complete power semiconductor switching controllability. HVDC Light is generally used to interconnect different electrical networks, strengthen power grids, offshore links to wind farms, and power oil and gas platforms. One of the critical benefits of HVDC Light is its potential to enhance the AC grid's power transfer capability across its terminals due to its high degree of reactive power controllability [19]

Hence, this work focuses exclusively on a type of HVDC Classic known as Line-Commutated Converter (LCC). This research conducts an in-depth study of LCC HVDC controls to enhance power system operating conditions. This study discusses HVDC supplementary controls to overcome SSR/SSO problems encountered in parallel AC-DC systems equipped with series capacitors.

1.2 Research Questions

Due to the world's growing demand for electrical energy, resorting to methods to improve power transmission capability, such as incorporating series capacitors, whose usage is recognized as one of the most influential and economical, in transmission lines has become necessary. However, the turbine-generator set plays an essential role in power generation processes. The turbogenerator set facilitates renewable energy conversion into mechanical energy and its reconversion into electrical energy. On the other hand, transmission lines are used to carry electrical energy. Thus, using series capacitors helps increase the power system performance by compensating for the transmission line's total reactance [22].

The concept of "series compensation" in power transmission networks consists of a series capacitor bank positioning on each of the transmission line's phase conductors. The transmission line's compensation through a series capacitor reduces its total series impedance. Series impedances are among the primary sources of voltage drop in power grids. They help determine the maximum transmittable power through a transmission system. However, the insertion of series capacitors into power lines exposes them to severe stability issues. Every power grid operates at a predetermined rated frequency, e.g., 50 Hz or 60 Hz. Therefore, due to series capacitors, the turbogenerator shaft experiences torsional frequencies below the power system's rated frequency. This phenomenon is known as

Subsynchronous Resonance (SSR) [23]. The SSR effect has profound consequences on the performance and reliability of power systems. When a turbogenerator undergoes the SSR phenomenon, its shaft failure and electrical network operation disruption are at high risk [24].

Several researchers worldwide have performed multiple SSR damping improvement studies to practically empower series capacitors to be integrated into transmission lines under different operating conditions (i.e., higher compensation levels) and facilitate the power grid's reliable operation. Because of power electronic devices' high controllability, such as HVDC Systems and FACTS, SSR problems have been successfully overcome [3]. However, SSR mitigation studies using LCC HVDC schemes parallel to a resonant AC system have been little exploited.

This work's fundamental problem is how SSR can be mitigated or suppressed by implementing an HVDC system parallel with a resonant AC line. Assuming that the parallel AC-DC system developed by adding an HVDC link parallel with a modified series-compensated AC line is not free of unpredictable SSR conditions, what HVDC controls should be enforced to reduce the SSR effect significantly? The question explored in this research is to find appropriate HVDC controls that need to be established to ensure a much more stable parallel AC-DC system operation than the resonant AC system itself, thereby allowing higher compensation levels.

1.3 Problem Statements

In transmission lines, the series capacitor is essential for its utility in enhancing power transfer capability. Series capacitors are used in a power system to compensate for the transmission line's total inductive reactance [25]. However, the transmission lines' series capacitors induce undesirable turbogenerator shaft oscillations [26]. Due to the series capacitor, the turbogenerator shaft exhibits natural frequency modes lower than the nominal network frequency. Therefore, the power grid and the TG's electromechanical system exchange energy at one or more of the shaft's natural frequencies. The main concern with SSR is that this energy exchange always takes place below the nominal synchronous frequency. However, the series capacitor remains essential in transmission lines even though it adversely affects the turbogenerator shaft's torsional dynamics [27].

Furthermore, HVDC links pose a risk of torsional interaction, although their supplementary controls are generally used to stabilize the turbogenerator shaft's torsional dynamics. Therefore, in a parallel AC-DC system with the AC line equipped with series capacitors, many factors influence the turbogenerator shaft's dynamics, namely the DC converters' control modes, the DC control schemes, the AC system stiffness, the level of compensation, etc... [28]. Theoretically, the parallel AC-DC system would be more susceptible to undesirable oscillations due to the various torsional instability causes it encounters than a simple series compensated transmission line. However, the series capacitor remains an essential factor at the root of this instability in both cases [4, 28].

1.4 Aims and objectives

This research aimed to achieve the following objectives:

- Model and control an HVDC link between two sources and investigate its transient response.
- Model a parallel AC-DC system and investigate the impact of HVDC on the torsional dynamics of the turbine-generator shaft.
- Design subsynchronous damping controllers based on test signal and phase correction methods.
- Evaluate the performance of single-mode and multimodal damping controllers on the parallel AC-DC system.
- Determine the impact of the DC power level and the inverter's AC bus's stiffness on torsional interaction.

In this thesis, PSCAD helped model the parallel AC-DC system consisting of a modified IEEE First Benchmark Model and an HVDC link. The study also used MATLAB extensively tools for the design of damping controllers.

1.5 Methodology

A detailed literature was carried out on:

- The subsynchronous resonance condition in power systems equipped with series compensated transmission lines and HVDC links.
- Device-dependent subsynchronous resonance.
- Modeling of power system components
- LCC HVDC modeling and controls.
- Subsynchronous oscillations due to HVDC controls.
- Impact of LCC HVDC on subsynchronous resonance damping.
- Subsynchronous damping controller design techniques.

1.6 Thesis Organisation

This research work's realization followed the necessary steps from the introduction to the conclusion through a substantial literature review. The thesis contains six chapters: introduction, literature review, power system modeling, HVDC system's impact on subsynchronous resonance damping, damping SSO/SSR using HVDC supplementary controls, and the general thesis's conclusion.

Chapter One offers a summary of the problem statement and the core goals of the study. This chapter emphasizes the problem of series capacitors in power systems, the interaction of HVDC controls with neighboring turbine-generator shafts, and HVDC controls to mitigate torsion oscillation. The chapter

addresses the essential elements of the work quite briefly. The critical goals of the work were also emphasized, along with the methodologies used for them.

Chapter Two sheds light on the SSR phenomenon. It comprehensively overviews the various forms, sources, and mitigation means of subsynchronous resonance in power systems. The chapter deals thoroughly with the HVDC system's specifics, functions, and advantages compared to the AC system. It also deals with components, specifications, various functional requirements, and operating conditions of HVDC schemes. Concerning the subsynchronous oscillation sources in power systems, great importance is given to this problem in radial HVDC and parallel AC-DC systems. Details were also provided on the risk of interaction between AC and DC systems, the generation of harmonics in 6 and 12 pulse converters, and filters' design to remove harmonics.

Chapter Three models the power grid's components, including the synchronous machine, the series compensated transmission line, the excitation system, the PSS, and the HVDC link. It also includes an evaluation of the transient response of the HVDC system between the two sources and discusses the two types of excitation systems: manual excitation and IEEE type ST1A. Both are part of the critical goals of the following two chapters.

Chapter Four studies the impact of adding an HVDC link in parallel with a resonant AC line. This chapter presents quadratic modeling equations governing the parallel AC and DC system, considering their direct relationship within the reference rotor frame. This analysis focused on an inverter station leading to an AC bus with moderate stiffness. The generator was equipped with a constant excitation system.

Chapter Five presents the use of supplementary controls to overcome torsional oscillations. The chapter reviews the test signal method using time-domain simulation to design damping controllers. It also emphasizes the phase correction method for obtaining suitable damping controller parameters and includes the incidence of subsynchronous torsional oscillations in HVDC-equipped power systems. Two damping controller structures were tested on the parallel AC-DC system, considering two different operating points, leading to an inverter station equipped with an AC bus of moderate stiffness. The chapter also mentioned the impact of DC power level and stiffness on the torsional interaction response.

Finally, Chapter Six gives the general conclusion of the work, its contributions, and suggestions for future work.

CHAPTER TWO: LITERATURE REVIEW

2.1 Introduction

Subsynchronous resonance is a significant problem in power systems equipped with series capacitors. Mitigation measures are required to ensure an adequate power system at various operating conditions when exposed to adverse effects of torsional oscillations. In this study, the mitigation method is based on HVDC controls. However, HVDC is often considered a high-risk system for subsynchronous instability. Several HVDC system parameters also contribute to the generation of subsynchronous oscillation.

This chapter describes the TG shaft's torsional oscillations due to series capacitors and HVDC controls. The chapter discusses the type of subsynchronous resonance, its theoretical approaches, its crucial sources in power systems, and a few mitigation techniques. Additionally, the chapter identifies the HVDC system's characteristics, focussing primarily on its components, advantages over the AC System, converter controls, characteristic harmonics, filter designs, interactions with AC systems, and nearby turbocharger shafts.

2.2 Mechanism of Subsynchronous Resonance

2.2.1 Introduction

A power system undergoes subsynchronous resonance when its network is subjected to natural frequencies below its nominal frequency [24]. Several authors underlined this observation showing the existence of two components for the currents flowing in the AC network; a component at the driving voltage's frequency, i.e., 50 Hz or 60 H, and another component wholly dependent on the network elements (the LC combination) [24, 29]. Furthermore, the system condition allows a possible energy exchange at a given subsynchronous frequency from this definition [30]. Therefore, the literature considers two different modes of oscillation concerning the subsynchronous resonance phenomenon [31]. Natural modes of oscillation resulting from power lines influence nearby turbogenerator shafts when fitted with series capacitors. Forced modes of oscillation are caused, in particular, by the interaction between nearby turbogenerator shafts and power system controls [29, 31]. Therefore, these aspects by which subsynchronous resonance occurs, namely "natural modes" of oscillation and "forced modes" of oscillation, are respectively caused by compensated networks in series capacitor and power system components [3, 29].

2.2.2 Series Capacitor Compensated Networks

Based on the simple RLC circuit presented in Figure 2-1, which is similar to a transmission line equipped with a capacitor “C” in series with the RL components, we can analyze the 3-phase current flowing in the branch applying Kirchoff’s voltage and current laws [32].

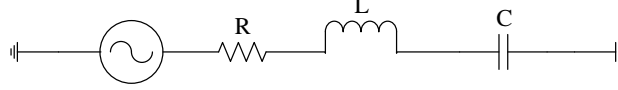


Figure 2-1: Simplified RLC Circuit [32]

However, applying Park’s transformations to the branch’s 3-phase current leads to currents depending on the driving voltage frequency component ω_1 and the network elements ω_2 . Under steady-state conditions, the current’s nominal frequency component appears as DC, as seen from the generator rotor. In contrast, frequency currents like ω_2 , are converted into currents that comprise both the sum ($\omega_1+\omega_2$) and the difference ($\omega_1-\omega_2$) [33, 34]. These are subsynchronous frequencies. The subsynchronous currents in the rotor circuit generally induce torques at sub-synchronous frequencies [35]. Therefore, Eq. (1) summarises the general expression of the current flowing in a series RLC network obtained by applying the inverse Laplace transformation [4, 29].

$$i(t) = K[A \sin(\omega_1 t + \varphi_1) + B e^{-\zeta \omega_2 t} \sin(\omega_2 t + \varphi_2)] \quad 2.1$$

The problem with subsynchronous torques on the rotor needs to be considered substantially. The TG shaft has standard natural modes for every mass-spring device requiring essential monitoring [36]. Generally, the oscillator modes on the TG shaft take place at subsynchronous frequencies. The shaft’s oscillatory modes appear to be at subsynchronous frequencies [37]. The resulting oscillating torques will reach a high amplitude if their frequencies match one of the natural oscillatory modes of the shaft. This condition can cause tremendous damage, including shaft fatigue or failure [29, 32]. Furthermore, concerning the RLC circuit shown in Figure 2.1, the induced subsynchronous resonance due to the series capacitor has a natural resonant frequency, as shown in equation (2.2) [32, 37]:

$$f_{er} = \frac{1}{2\pi\sqrt{LC}} = f_0 \sqrt{\frac{X_C}{X_L}} \quad 2.2$$

Where,

f_0 : Synchronous frequency of the system.

$X_L = 2\pi f_0 L$: line inductive reactance at the synchronous frequency.

$X_C = \frac{1}{2\pi f_0 C}$: Capacitive compensating reactance at the synchronous frequency.

These resulting frequencies occur in the synchronous generator's rotor as modulations of the power system's frequency, known as the base frequency. Only the subsynchronous frequency interacts with one of the TG shaft's torsional frequencies by producing an energy exchange with the risk of causing breakdowns related to shaft fatigue [38]. Usually, the torsional or frequency modes of the turbogenerator shaft are provided by the manufacturer, or they can also be determined by modal analysis. Concerning the network frequency, several factors are determined at a given time, such as the level of transmission line compensation and the network switching arrangement [29].

2.2.3 Type of Subsynchronous Resonance

There are several aspects in which the power grid and the TG shaft can interact with subsynchronous impacts [39]. And most of these interactions have high significance and descriptive names. We list three of which are of specific interest.

2.2.3.1 Induction Generator Effect

Literature defines The Induction Generator Effect (IGE) as the generator rotor's self-excitation behavior resulting from disturbances in the power grid when the armature currents are subjected to subsynchronous frequency components [26]. However, the armature terminals' rotor resistance is negative, while the electric network presents a positive resistance. Thus, the persistence of sub-synchronous currents is inevitable at the same natural frequencies if the magnitude of the network's positive resistance approaches that of the generator rotor's negative. This is referred to as the "induction generator effect" [29, 40, 41].

2.2.3.2 Torsional Interaction

Torsional Interaction (TI) happens when the generated subsynchronous torque inside the generator is adjacent to one of the turbine generator shaft's natural torsional modes [30]. The rotor's oscillations converge as this situation occurs, generating armature voltage elements at both supersynchronous and subsynchronous frequencies. Phasing the developed voltage at subsynchronous frequencies ensures maintaining subsynchronous torques. The system becomes self-excited if this resulting torque is equal to or greater than the rotating system's mechanical damping. This phenomenon is known as "torsional interaction"[29, 40].

2.2.3.3 Transient Torque Effect

The Transient Torque Effect (TTE) usually happens on a power grid consisting of series capacitors when faults and corresponding removal lead to high-power storage in the series capacitor banks [42]. Under a transient torque, series capacitor banks are unloaded via the synchronous generator as a current whose sub-synchronous frequencies coincide with one of the turbogenerator's mechanical system's natural torsional frequencies [40]. Unlike the SSR types, namely the TI and IGE, the torque

amplification growth rate has a generally greater negative impact [43]. The torques of the oscillating shaft can easily attain a detrimental degree in only 0.1 seconds [41]. The common concern regarding the subsynchronous resonance phenomenon remains the shaft fraction at maximum load and rated speed. Danger from such an incident cannot be anticipated correctly; however, substantial equipment exposure can lead to staff safety risks [38]. The most likely and most serious hazard would be cracks on one of the turbogenerator shafts' surfaces, reflecting failure and shaft repair requirements, leading to a 90-day or more unit outage [41, 44]. Therefore, disturbances in the power system are the major causes of the transient torque amplification as they cause sudden changes in the network. Such network changes resulting from disturbances cause current changes, consequently oscillating at a frequency close to the turbogenerator's natural frequencies [40].

2.2.4 Devices Dependent Subsynchronous Oscillations

Several authors have shown that networks compensated in series capacitors are the most exposed to subsynchronous resonance problems. However, subsynchronous resonance is also generated due to interactions between the TG shaft and electrical system components. In the power system, torsional oscillations at sub-synchronous frequencies arise from the turbogenerator's interaction with the excitation system's controls, the high-speed governor, and the HVDC converter. Typically, any device controlling or reacting speedily to power deviations under the subsynchronous frequency range induces SSO [3, 4]

2.2.4.1 Interaction with excitation controls (PSS and AVR)

However, concerning torsional oscillations arising from interactions with the excitation controls, this problem was first seen through the Power System Stabilizer (PSS) operation at the Lambton power plant in 1969 [4, 45]. It was noted that the PSS, with its stabilization signal derived from the deviation in rotor speed measured on the turbogenerator shaft, precisely at the end of the generator, excited the lowest torsional mode. The PSS transfer function design aims at providing a null-phase compensation between the input stabilization signal extracted from the rotor speed deviation and the electromagnetic torque at the system's frequency of 1.67 Hz, Lambton turbogenerator shaft's Mode 0 frequency [4]. This design leads to a purely damping torque element, in which both the speed deviation and the electromechanical torque are in phase. However, it resulted in a phase lag of 135° due to the generator characteristics, making Mode 1 unstable at 16.3 Hz. Also, it generated a negative damping torque factor and thus the 16 Hz component's instability. Therefore, as reference [45] suggested, applying a torsional low pass filter in the PSS control circuit and adjusting or improving its controls may prevent its unpredictable subsynchronous interactions.

Furthermore, in line with [28], the transmission line's power transfer capability, the generator power factor, the generator loading as well as the Automatic Voltage Regulator (AVR) gain are the main

factors causing instability or negative damping in the swing mode as a result of interactions with the excitation system controls. According to Padiyar [18], such instability can be solved by placing a speed transducer close to the unstable mode.

2.2.4.2 Interaction with speed governors

The interaction between the turbogenerator and "speed regulators" was first encountered in 1983 in a nuclear power plant at Ontario Hydro, whose generator produced 635 MVA at a speed-rated 3800 rpm [39]. The study and investigation of this instability in the Ontario Hydro incident identified two primary sources based on modal analysis and computer simulation tools [28, 46]. The first cause was the inaccuracy of the linearization circuit in the valve. The second was because the bandwidth of the electro-hydraulic servo system was wide. The appropriate linearization valve characteristics helped address this issue, steadily keeping the whole load range down by about 4 %. Furthermore, installing filters to remove the speed signal's torsional frequency components was considered a precautionary measure to ensure the system's stability [28, 47].

2.2.4.3 Interaction with HVDC controls

Torsional oscillations due to nearby HVDC converter controls first appeared on the North Dakota DC SQUARE BUTTE system [48]. They were mainly the result of instabilities due to supplementary damping controls and rectifier current regulators [49]. The instability due to auxiliary damping controls was explicitly the result of high gain and significant phase shift in the frequency range below natural torsional frequencies [49, 50]. The observations of this power system instability condition showed that only one of the two units near the rectifier was subjected to a torsional frequency of 11.5 Hz, which was low enough to interact with the HVDC supplementary damping controller. Therefore, this situation was solved using an 11.5 HZ Notch filter in the auxiliary damping controller. Alternatively, the second unit had a high torsional frequency that did not cause instability [28, 49].

Furthermore, the observations made on torsional oscillations due to interactions with HVDC controls showed that the instability due to the rectifier current controller depended on the regulator's bandwidth [49]. These controls typically have bandwidths between 10 to 20 Hz. Only torsional oscillation modes with frequencies below the highest bandwidth range became unstable [4, 28]. In line with [51], torsional interaction due to converter controls can be overcome by simply changing the negative damping's frequency range and magnitude related to the rectifier current controller. However, based on the rectifier current control loop's adjustment, the latter method is applicable only within a relatively small range. Therefore, designing and incorporating a supplementary subsynchronous damping controller may also be required to stabilize the adverse torsional oscillations of all units in the area [39, 51].

The DC converter controls' ability to adversely induce torsional oscillations to adjacent generator units depends on the relative DC system's size compared to the unit and the electrical distance. To minimize

the risks of this type of instability, the ratio, known as the Unit Interaction Factor (UIF), described in equation (2.3), should be less than 0,1 [51, 52].

$$UIF_g = \frac{MW_{dc}}{MVA_g} = \left[1 - \frac{SC_g}{SC_{tot}} \right]^2 \quad 2.3$$

Where

UIF_g : Generator's Unit Interaction Factor,

MW_{dc} : DC system's rated power,

MVA_g : Generator's rated power,

SC_g : DC commutating bus' short circuit capacity, including the generator

SC_{tot} : DC commutating bus' short circuit capacity, excluding the generator.

Furthermore, DC converter controls may negatively interact with turbogenerators depending on the firing angle length [39]. The further a rise in the firing angle, the greater the chance of torsional instability. Hence, operating modes that require low DC voltages are mostly subjected to increased torsional instability. Moreover, beyond the above-described factors affecting torsional interaction due to HVDC controls, it should be mentioned that, in an AC-DC parallel system, the series compensation level should also be considered a potential source of torsional instability [28].

2.2.5 Subsynchronous Resonance Analysis

Many analytical tools have been developed for SSR analysis. The following are the most common methods of SSR analysis [29, 32, 40]:

2.2.5.1 Frequency Scanning

This approach, known as "frequency scanning," has been commonly used as a standard tool for studying SSR problems in North America [37]. This technique's particularity is that it is more appropriate to investigate IGE. This technique calculates the network's equivalent resistance and inductance, obtained depending on frequency from a point behind the generator's stator winding [53]. For cases where the resistance is negative while the inductance value is zero, there is a high likelihood of IGE [37, 54]. This approach also allows the investigation of TI as well as TTE. Typically, These SSR types may occur under the power grid's series resonances. They may also happen when the series reactance induces torsional oscillation, whose frequencies are relatively close to one of the turbogenerator shaft's natural frequencies [29, 32].

2.2.5.2 Eigenvalue Analysis

Eigenvalue analysis is considered the most objective approach as opposed to the frequency scanning approach [55]. This method is obtained by developing complex mathematical models involving linear differential equations of turbogenerator systems electrically connected to the power transmission networks [37]. Using Eigenvalue Analysis, it is possible to determine the oscillatory frequencies, including each torsional mode's dynamics. The downside of this approach is the complexity of mathematical models. This method is limited to reasonably small systems where the research focuses on the fundamental SSR interactions [32].

2.2.5.3 Electromagnetic Transient Programs (EMTP) Analysis

EMTP is power system simulation software first implemented in Bonville and adapted for SSR study around the 1970s [3]. An EMTP and a simple transient stability program (TSP) have different purposes. Typically, a TSP aims to model a power system's positive sequence quantities [56]. In contrast, an EMTP acts as a fully three-phase mechanism designed to model complex power grids, including cables, overhead lines, synchronous generators, etc. Because of its generality and versatility throughout all three SSR kinds, EMTP is commonly used for SSR analyses [3, 40].

2.2.6 SSR Countermeasures

When a power system is subjected to a persistent SSR that can lead to the TG shaft failure and disrupt its operation, it is important to set up mitigation strategies. There are many alternatives to solving the SSR question:

2.2.6.1 Reduced Compensation Level and Operating Procedures

Series capacitor is one of the leading causes of subsynchronous resonance [57]. According to [58], reducing the power line's compensation level close to affected TG' shafts is one method to alleviate the SSR problem. However, power systems use series capacitors for a specific purpose [54]. Usually, they are incorporated into power lines to enhance their transfer capability [59, 60]. The series compensation degree needing implementation in a transmission system is often determined depending on its performance requirements. Therefore, reducing the installed series compensation amount will lead to a limited system functioning or require new transmission. Reducing the implemented compensation amount can be achieved by adjusting the total value of in-service capacitor banks, bypassing their segments [58].

This technique's main objective is to avoid depressing the power system's operation at sub-synchronous torsional frequencies, which would hurt TG shaft reliability. Bypassing series capacitors can also be achieved during the low load stage operation of affected generators. It can also be obtained when the SSR occurrence is at high risk and the inherent mechanical damping is softer. Series capacitors are only

used in some cases when generators operate at maximum power, so specific bypassing of series capacitors won't cause system performance problems [58, 59]. Conducting the series compensation limitation process on transmission lines connected to the affected TG shaft can be obtained through analytical experiments [58]. Usually, these studies focus on measurements of respective TG shafts' torsional oscillation modes. Therefore, this technique can help prevent SSR instability, such as the transient torque effect in capacitive compensated networks [61]. However, it is practically impossible to reduce the amount of series compensation in some cases due to the system's performance requirements [58].

2.2.6.2 Static Blocking Filters

Static filters are generally placed in series with the generator as blocking devices or damping circuits parallel to the series capacitors [4]. In line with [58], blocking filters at the generator is considered an alternative to alleviate the problem of subsynchronous resonance in electrical networks. Based on this SSR mitigation technique, blocking filters are installed to prevent subsynchronous frequency currents from passing through the generator step-up transformer neutral connections to the ground [62]. These devices, mainly used to mitigate SSR, can stabilize the power grid's operation and overcome TTE problems under extensive operating conditions. This approach's introduction minimizes the technique based on transmission lines' compensation limitation in power grids connected to the generators [58, 63].

[64] presented a designed method of blocking filters placed in series with the Koeberg TG in South Africa to limit the troublesome subsynchronous flow components armature current. In order to withstand these oscillations, the literature reveals that the characteristics of the armature current were restricted to values making the mechanical system supply more powerless than the inherent damping. Thus, [64] briefly overviews blocking filters' behavior on SSR mitigation in series-compensated power lines. The conclusions below have been drawn on the Korberg turbine-generators shafts after completion of analyses on the behavior of blocking filters and their sensitivity to impedance changes and variation of compensation percentage [64]:

- The developed blocking filters were able to produce strong transient torque elimination at a high level of compensation.
- The difficulty of adapting a blocking filter to the Koeberg system for very high transmission line impedances. This issue resulted from high transmission line reactance values induced by line-filter combination series resonances toward the filter's parallel resonance frequencies. The instability and poor damping risk could arise for series resonant frequencies closer to parallel resonances.
- The blocking filters were capable of making the lowest torsional oscillation mode unstable at lower levels of compensation.

- System stability could only be achieved when the system frequency varied +/- 2.5% of the nominal system frequency. Usually, when this happens, the blocking filter goes out of tune and ceases to facilitate system stability.
- For the Koeberg system, in particular, a blocking filter with a pre-set configuration and fixed parameters cannot stabilize the SSR over a wide variety of operating conditions (i.e., series compensation levels and power system configuration). It can, therefore, not be regarded as a general alternative. This condition is because of its long transmission line properties (i.e., 1700 km) and the low shaft modal frequency's combined impact. However, blocking filters can suppress SSR in many other systems and provide system stability under various operating conditions (i.e., varying compensation levels, changing the system frequency, and power system configuration) [64, 65].

Furthermore, following [66], many researchers proposed a range of SSR attenuation methods for the Navajo plant due to these concerns' persistence and severity. Besides the previously discussed techniques, supplementary excitation damping controllers and redundant torsional relays were also used. These devices' implementation aimed to eradicate SSR to ensure the power system's efficient operation in a wide range of operating conditions. (i.e., high level of compensation). Without the addition of SSR blocking filters, the Navajo turbogenerators would be susceptible to adverse torsional instability [66].

2.2.6.3 Dynamic Filters

A dynamic filter is an active device usually mounted in series with the generator to counteract subsynchronous voltages due to rotor oscillations and prevent the induction generator effect resulting from the power system's electrical-mechanical interaction from occurring [65]. Typically, the generator stator voltages are exposed to subsynchronous and supersynchronous frequency characteristics when the rotor generates torsional oscillations. Supersynchronous voltages mostly provide the power system with positive damping. In contrast, the turbogenerator system is adversely affected by subsynchronous voltages [67]. With proper control, the static filter provides an out-of-phase voltage and sufficient amplitude to mitigate the resulting subsynchronous voltage in the armature. It also carries an input signal extracted from the rotor motion and fitted with all the TG shaft frequency characteristics [65]. The installation of a dynamic filter with adequate control allows effective prevention against the induction generator effect due, in particular, to torsional interaction [68, 69]. Dynamic filters are typically costly when constructed without saturation to mitigate oscillations arising from transient disturbances [69].

2.2.6.4 Bypass Damping Filters

Another mitigation technique is to install passive blocking filters at the series capacitor bank [67]. Bypass damping filters more efficiently address power system instabilities related to the induction generator effect. Their ability to handle IGE is due to their capacity to inject a large amount of positive resistance into the circuit when the power system is exposed to frequencies up to 90 percent of its nominal frequency. However, bypass damping filters' effectiveness decreases for power system operations above 90 percent of the rated frequency. This SSR damping system design is such that the damping resistor is mounted in series with a parallel reactor-capacitor unit, tuned at the system-rated frequency. This allows for a high filter impedance at nominal system frequency, thereby decreasing the probability of power losses in the resistor under regular power system operating conditions. As a result, the damping resistor becomes much more effective at subsynchronous frequencies, allowing SSR mitigation and power system stability [28, 67]. In the subsynchronous frequency range, it is advised that an SSR blocking filter across a series capacitor bank be designed in such a way that the maximum impedance capacitor and filter are less capacitive and resistive [58].

2.2.6.5 Thyristor Controlled Series Compensation (TCSC)

The TCSC is considered an effective damping device for SSR [23]. In 1986, Vithayathil introduced the basic TCSC scheme, the principle of which was to adjust network impedance [37, 70]. Nowadays, TCSC controls are used to enhance the stability of power systems, emphasizing SSR damping [71]. The TCSC comprises an inductor connected in series with a pair of back-to-back thyristors connected in parallel with a Metal Oxide Varistor (MOV) protected fixed capacitor [72]. The TCSC scheme contains a Thyristor Control Reactor (TCR) located on the branch containing the thyristors, whose role is to allow the control of the variable impedance [73, 74].

Thyristors typically comprise valves for regulating the firing angle. For example, in an LCC HVDC system, the converter firing angle adjustment allows the D.C. current to flow into the transmission line to be regulated [74]. However, in a TCSC, the firing angle regulation controls the current flowing through the series capacitor, thus influencing its (i.e., the series capacitor) dynamic characteristics at sub-synchronous frequencies. Control of the net reactance of the TCSC can be performed in amplitude through the firing angle of the TCR branch, which, consequently, defines its inductive or capacitive property [72]. Therefore, it is necessary to have a properly designed and tuned TCSC control system to facilitate its efficiency to suppress the adverse torsional effect due to the series capacitor and the transmission line inductance and ensure the proper electromechanical system operation [58, 74].

Reference [75] studied the effect of different TCSC control strategies on the SSR phenomenon in a series compensated transmission line (i.e., IEEE FBM). Three control techniques were widely utilized: constant current control, constant power, and constant impedance control. Emphasis was placed on the impact of varying the thyristor firing angle and the influence of ratings. TCSC performance tests were

conducted on IEEE FBM with and without the device using the eigenvalue approach and time domain analysis based on the three control methodologies whose findings are summarized below [75]:

- The device performance under this control method has proven satisfactory after replacing the conventional series capacitor with a TCSC in CC control mode. The results showed greatly improved torsional instability using constant current mode based-TCSC. The same findings were made for different firing angle control methodologies. The various control schemes the study was based on, namely Equidistant Pulse Control (EPC) and Individual Pulse Control (IPC), also led to improved system damping. Both control schemes' impacts resulted in effective damping of all torsional modes, except self-excitation. For this particular oscillatory mode, the performance of the IPC was better than that of the EPC [75].
- Work in [75] has shown the immense need for a significant time constant for a TCSC that works under Conventional Power Control (CPC) to prevent undamped torsional oscillations. However, the Conventional Power Control mode is characterized by a slow response that substantially impacts the device's functioning based on fault recoveries. A much more improved power control structure has been found necessary to improve the system's operation without generating unwanted torsional oscillations. The proposed enhanced power controller then had a faster internal current control loop response and a slower external loop intended for power regulation. The rapid response of the internal current controller had a positive impact on system disturbances. At the same time, the secondary power control slowed down the response of the improved power controller to subsynchronous torsional interactions.
- Contrary to the literature claims, TCSC devices have not been seen to be utterly resistant to SSR problems. Observations have shown that when the TCSC operates in constant impedance control mode with An important firing angle (i.e., beyond a certain critical threshold), its impedance becomes capacitive reactance in the SSR frequency range. Therefore, the operation of a power system equipped with a TCSC device subjected to constant impedance control is known to be stable when the dynamic impedance reflected on the AC grid does not generate instability of any torsional subsynchronous mode of oscillations. Otherwise, setting up a supplementary control system or systematically changing the firing angle to overcome torsional instability would be appropriate [75].

Accordingly, based on studies undertaken by different researchers, reference [58] suggests several restrictions related to the TCSC control system and its ability to influence the power system's operating conditions. The following points refer to the specific shortcomings of the TCSC control system and measures to be followed [76, 77]:

- a. The inability of thyristor valves to intrinsically dampen SSR. Advanced and properly tuned TCSC control algorithms are required to facilitate the desired attenuation of SSR. The change in turning can significantly impact the stability of operating points. This can render a previously

stable operating point unstable, mainly when the need for maintenance of the TCSC control system arises for unrelated SSR reasons.

- b. The control turning sensitivity to the electrical network. A readjustment of the control scheme can be essential to maintain the SSR attenuation level of the TCSC when the electrical grid is subject to potential changes.
- c. The inability of TCSC to stabilize transient torque effect. TCSC can counteract SSR problems but not the transient torque effect. SSR attenuation techniques other than TCSC are generally suggested when a power system is exposed to the transient torque effect.

The TCSC is an efficient SSR damping device, but it requires sophisticated and adapted algorithms to make its damping objective more feasible [72]. It also has certain drawbacks where using a different damping system can prove beneficial. Further information on the use of TCSC for SSR damping can be found in [56, 78, 79].

2.2.6.6 Supplementary Excitation Damping Controls (SEDC)

All the approaches discussed above aim to mitigate electromechanical oscillations to facilitate the power grid to work efficiently under various operating conditions. The excitation device also has an important mechanism that relies on the active possibility of implementing an SSR damping scheme to ensure the stability of electromechanical oscillations [80]. The excitation system's use to solve SSO problems is nothing more than an extension of the PSS concept commonly used for SSO mitigation. The PSS is well known to be an ideal external excitation device tool to suppress low-frequency oscillations. Low-frequency oscillations result from negative damping torque due to the phase shift between the electromagnetic torque and the excitation system's speed input signal. The system is stable when the net phase shift between the electromagnetic torque and the speed input signal is less than 90° ; above this range, the system is unstable [28]. The primary purpose of an SEDC is to modulate the exciter's field voltage to phase the electromagnetic torque with the speed input signal to provide the electromechanical system with positive damping [66, 80].

The SEDC addressed in [69] intended to enhance the inadequate damping provided by the installed static blocking filters at the Navajo power plant. In this approach, the damping of torsional frequency oscillations focuses on the observability concept. This concept involves extracting the speed input signal from the high-pressure turbine's front end and the rotating exciter [81]. Whereas nearly all torsional oscillatory modes are ideally observable at each rotor position, using both speed input signals is strongly recommended. It's also not advisable to use a single dynamic compensator to mitigate all subsynchronous torsional modes [82].

The torsional oscillatory modes are required to be handled individually for the successful results of this SSR damping system. This approach applicability involves processing each torsional mode individually by isolating the latter from the speed input signal using a bandpass filter developed with a significantly

sharp cut-off to reduce interference between adjoining signal channels. Likewise, each oscillatory torsional mode is individually provided with the required gain and phase compensation. Therefore, the SEDC output signal, which is practically obtained by summing all the control signals coming from individual processing in each torsional mode, is sent to a voltage comparator in the excitation device circuit to initiate the field voltage modulation at the torsional frequency whose resulting signal is fed into a high initial response Automatic Voltage Regulator (AVR) [58, 69]

At the end of the study of the first SEDC developed as a damping improvement means provided by the static blocking filters at the Navajo power plant, conclusions were drawn on the conditions under which its effectiveness was based. The efficacy of an SEDC is determined by its rapid response to adverse torsional oscillations. Therefore, its fast response depends on the exciter's power rating, its capacity to cause subsynchronous voltages within the armature circuit, and the exciter mass position on a shaft mass system. This damping system's real drawback is its inadequate response to problems usually associated with severe disturbances that result in severe electromechanical oscillations [69].

Furthermore, [83] discusses the design of an SEDC for mitigating subsynchronous oscillations due mainly to a capacitive region working TCSC within a series compensated transmission line. The research in [83] was based on an optimization technique called Particle Swarm Optimization (PSO) and suggested the optimal phase compensation to resolve the TCSC-related SSO problem. The research in [83] also focused on investigating the TCSC's effect on the power system's operation through the test signal method. The SEDC concept and design used in [28] and [83] are similar.

On the other hand, what makes them distinctive is the speed input signal chosen differently in both cases. Due to its ability to be fitted with all of the torsional oscillatory modes' characteristics, the generator speed deviation was used as the only input signal to SEDC. After proper filtering, the SEDC input signal, which comes as delta mechanical speed, will be normalized to a standard speed signal and then sent to a pre-set bandpass filter to a particular torsional frequency mode. Based on SEDC configuration similarities in both cases, for each torsional mode, the delta mechanical speed input signal was analyzed independently from the other torsional modes, considering the unique characteristics in phase compensations and gains of every oscillatory torsional mode [83].

Moreover, the SEDC architecture in [80] is close to that of a PSS. This configuration is similar to a single-mode damping controller (SMDC), whose primary function is to damp a particular torsional mode of oscillation. Therefore, it should be noted that the SEDCs discussed earlier are similar to a multimodal damping controller (MMDC) whose purpose is to damp all SSR at different modes of torsional oscillation. Usually, an SMDC design involves an input signal that carries the frequency characteristic of the oscillatory torsional mode that needs to get damped, a washout block that fulfills a high pass filter's function, and a phase compensation block [84].

2.2.6.7 Static Var Converter-Based Supplementary Damping Controls

Static var compensator (SVC) is a FACTS device primarily used to address transient stability and SSR. FACTS devices are generally appropriate for handling transient stability because of their fast response to the induced change in power system parameters [82]. The best way to enhance an electric network's transient stability is to set up a device that allows its parameters to change. That's why FACTS devices are used in this perspective [70]. SVC is a device considered a reactive power resource that can be adjusted quickly, thus improving voltage stability and increasing power transfer capability. SVC supplementary controls are often used to address SSR problems in power systems [85].

History has proven that the SVC device has been used for several years for bus voltage controls and low-frequency oscillation damping. The first applications of SVC started with the dynamic stabilizer. However, the dynamic stabilizer's performance was restricted to single-mode damping only owing to the unavailability of the voltage control loop in its circuit [86]. The reactive power controller requiring a torsional monitor designed to obtain the damping of many modes simultaneously was eventually suggested in [87]. Due to the drawbacks of a controller equipped only with a torsional monitor, the voltage control loop equipped-SVC designed to stabilize multimodal instability was proposed in [88]. Therefore, the multimode stability was obtained through a proportional controller using the rotor speed deviation as a feedback signal [86].

Furthermore, an SVC typically has one or more banks of fixed or switched shunt capacitors or reactors, whose thyristors switch at least one bank. Typical components contributing to the SVC design include Thyristor Controlled Reactor (TCR), the Thyristor Switched Capacitor (TSC), Harmonic Filters (HF), and Mechanically Switched Capacitors or Reactors [89]. The thyristors' phase angle modulation facilitates the switching of the reactor through the circuit. This device's operation implies a significantly consumed reactive power in the power circuit. In this configuration, the capacitors mainly provide coarse voltage controls.

In contrast, smooth and regular controls are offered by a TCR. . The TSC can offer smoother control and flexibility [89]. Furthermore, [85] presented an analysis focused on the damping of torsional oscillation due to series capacitors and HVDC using supplementary SVC controls developed depending on the phase compensation method. Following the use of auxiliary SVC controls, the results showed the device's capability to stabilize SSR.

2.2.6.8 LCC HVDC controls based-countermeasures

2.2.6.8.1 Introduction

HVDC systems and TG shafts of nearby turbogenerators can interact in several ways. These interactions, commonly defined as an energy exchange between two systems, occur in the electrical part of the power system and in sections, such as turbines and turbogenerator shafts, where they occur under various torsional frequencies [48]. For the stability of the power network, HVDC controls are of crucial significance[90]. However, as previously highlighted, HVDC controls can potentially cause SSO in a power grid. There is a high risk of SSO due to inappropriate current control parameters in transmission systems equipped with HVDC [91]. This section discusses two aspects of SSO: those encountered in radial HVDC schemes and those in parallel AC-DC systems.

2.2.6.8.2 Radial HVDC links

A radial HVDC is considered in [28] as an HVDC scheme completely isolated from the resonant AC line, i.e., the HVDC link without the parallel AC line. Concerning torsional oscillations due to HVDC, specifics have already been given in section 2.2.4.3. The section reported several factors inducing the torsional interaction between the HVDC and TG's shaft. The most common factors include the UIF to be held within a reasonable threshold, the Rectifier Current Regulator, whose unsuitable parameters usually result in SSO, the firing angle, the DC power level, and the inverter station's control mode. For more details on the factors inducing sub-synchronous torsional interaction due to HVDC, see [92]. The following studies address the issue of torsional oscillation and damping methods in the HVDC network. Wei Li and Sha Tao [93] discussed HVDC's torsional oscillation in power systems. Their work focused on the network connections of the Hulunbier-Liaoning HVDC system in the Northeast power grids. Because of the HVDC controls, the turbogenerators near the rectifier were prone to torsional oscillations in this network. Therefore, to address SSO, they proposed applying a Multimodal Damping Controller (MMDC).

Han Chen and Chunlin Guo [91] investigated SSO sources in an HVDC system whose rectifier bus is connected to several turbogenerators. HVDC Controls were the primary cause of the torsional interaction observed on turbogenerator shafts near the rectifier station. At the end of their work, the authors shed light on using multi-modal and single-mode damping controllers. Both controllers have been claimed to be acceptable, but the design specifications for achieving optimal results differ. According to these authors, the narrowband multi-channel approach must focus on the exact shaft model and the ease of access to the turbogenerator shaft's torsional oscillation frequencies. However, the single-channel broadband approach doesn't have the same requirements as the previous one. It has a more standard and functional benefit and requires optimization techniques to provide the turbogenerator set with effective positive damping. Using a single-channel controller, the authors discovered the

importance of concentrating phase compensation on the most severe oscillatory mode. Therefore, at the end of their research, they adopted the single-channel damping controller designed by the phase compensation method to address the SSO problem due to HVDC. Reference [94] also used a single-channel damping controller designed following the broadband-pass control approach to suppress torsional oscillations due to HVDC. In [94], however, the design of the damping controller utilized eigenvalue analysis.

Qinlei Chen, Chunlin Guo, and Han Chen in [95] also studied torsional oscillations due to HVDC controls. This work is similar to the previously mentioned report, but the configuration of the damping controller differs. The authors adopted the multi-channel bandpass control method for designing the damping controller. The damping controller consisted of an input signal derived from the rotor speed deviation, modal control, phase compensation, gain adjustment, and amplitude limiting process. The proposed multimodal controller has proven effective in damping torsional oscillations.

Furthermore, a study based on test signal and phase compensation methods was conducted in [96]. This work provided a vital literature review on designing multimodal controllers based on test signal and phase correction methods. The goal was to demonstrate the damping controller's effectiveness in suppressing torsional oscillation in a multi-generator network. The multimodal damping controller structure is almost the same as in the previous cases; however, the difference is based on applying each generator's rotor speed deviation as the input signal for each single-mode damping controller.

2.2.6.8.3 Parallel AC-DC System

Many factors affect torsional interaction for an HVDC line in parallel with a series compensated transmission line. In line with [28], current controller's gains, HVDC tie loading, controllers' firing angles, length of transmission lines, generator rated power compared to the HVDC scheme rating, AC system strength, and series compensation are the various factors affecting torsional interaction in a parallel AC-DC system. The literature states that series compensation-based torsional interaction is the most impacting factor [28]. Many authors proposed various SSR countermeasures to enable power grids' stable operations and the TG shafts' reliability due to the resulting torsional oscillations' negative impacts.

Y.Y. Hsu and L. Wang in [97] performed a design analysis of a new control system for a parallel HVDC system linked to a capacitive compensated power line. Their analysis's key objective was to incorporate an SSDC into the control loop of the rectifier's standard current regulator to enhance torsional oscillation damping. They conducted two experiments. The first was based on system response when connecting the AC and DC transmission lines in parallel, taking into account the HVDC tie operation without supplementary control signals. The other was based on the system behavior when the SSDC and PSS were included. Their research showed that the designed SSDC and PSS's commissioning significantly improved the SSR damping.

Y. Jiang, J. Cao, and J. Cheng [98] presented a new genetic algorithm-based approach for designing an SSDC capable of mitigating SSR within the same parallel AC-DC system. The genetic algorithm approach-based optimal parameters were evaluated through eigenvalue analysis—their research aimed at stabilizing SSO resulting from both AC and DC systems.

R.G. Harley and J.C. Balda in [99] investigated SSR damping in a capacitive compensated power line by only regulating a parallel HVDC tie. Their research focused on improving SSR damping by designing an SSDC-based parallel HVDC line. The study started from an initial AC system until it was changed to a parallel AC-DC system. The rectifier controller was set to constant current mode and the inverter to constant voltage mode. The key purpose followed was not only to illustrate the failure of the HVDC system (i.e., in parallel with a resonant AC system) to suppress SSR when it was devoid of ADC, but the research also centered on the design of the ADC. The proposed ADC design consisted of a gain block and a two-stage phase compensation block. The output signal from the ADC was transmitted to the rectifier current regulator (RCR) input and output. The efficiency of ADC applying its output signal to both sides of the RCR is better than when used either at the RCR input or output.

In [100], Hamouda studied the inverter station's impact on the TG shaft's torsional dynamics. It is well known that controlling HVDC converters can adversely affect the stability of electromechanical oscillations within a power system. The controls of inverter stations typically significantly affect the TG torsional dynamic of a parallel AC-DC grid where generators are located on the rectifier side. In such a power system, the generator-inverter coupling and stiffness of the inverter station's bus significantly affect the TG shaft's torsional dynamics. Generally, adverse torsional effects arise as the inverter bus's stiffness reduces. However, in [100], It has been pointed out that a reasonably strong inverter bus within a series-capacitor-equipped parallel AC-DC system can also be susceptible to negative torsional oscillations.

R.M. Hamouda and M.R. Iravani [101] studied an AC-DC parallel system with a series capacitor on the AC line. Their work aimed to analyze the phenomenon of torsional oscillations due to the series capacitor and HVDC controls. Their work showed that supplementary HVDC controls could mitigate SSR, whether the HVDC or the series capacitor causes it. Since SSDC designed based on HVDC controls could not stabilize electromechanical oscillations, the authors proposed a compensator consisting of a coordinated SVC-SSDC to improve system stability.

Therefore, an HVDC link equipped with a rectifier current regulator fitted with an SSDC can resolve SSR issues due to a resonant AC line or DC converter controllers, based on the above authors' work results. According to [99], a supplementary damping controller at the HVDC rectifier could increase the TG system's modal damping and allow a higher compensation percentage on the AC line, improving power transfer capability.

2.3 High Voltage Direct Current Systems

2.3.1 Introduction

Although the alternating current was the main transmission power method during the twentieth century, HVDC technology proved preferable for some of its uses. This technology's use began to grow steadily in 1970. The number of HVDC schemes worldwide has risen significantly; according to [102], it was about 170 in 2015. The largest HVDC networks have a ± 800 kV voltage and can operate at a maximum of 4500 A current. These transmission systems have a wide application area. They are commonly used for overhead lines based-bulk power transmission optimization, subsea or underground power transmission, interconnecting two AC grids of various phases or frequencies, power exchange control between two AC networks, and transmitting power for isolated generation units such as offshore wind farms or oil rigs [102, 103].

In an AC-DC system, the generated AC voltage is converted into DC voltage and reconverted into AC voltage utilizing a rectifier (at the sending end) and an inverter (at the receiving end). The converter comprises valves whose characteristics determine the type of HVDC system. Thus, two HVDC technologies emerged based on the above applications at different periods. In 1954, the point-to-point HVDC installation using mercury-arc valves was made available. During the early years of HVDC, the mercury arc valves-based technology was used but then replaced by power transistors, such as the 1970s thyristors and the 1990s IGBT [102, 104]

2.3.2 Advantages of HVDC vs. HVAC

In the 20th century, transformers' implementation in AC systems gave them considerable importance in energy transmission; alternating current systems were the most widely used and preferred for power transmission. Direct current was used only in specific fields such as electronics or certain chemical industrial processes. Nevertheless, in 1970, HVDC technology's use proved effective in optimizing bulk energy transmission. One of the drawbacks of AC systems is reactive capacitive power, especially when transmitting a large amount of energy via submarine cables. However, HVDC systems do not present or require any reactive power. Since reactive power depends on frequency, the inductive and capacitive effects in an alternating current system result from sinusoidal variations in current and voltage. Since sinusoidal voltage and current changes do not exist in HVDC systems, there is no need for frequency; thus, no need for reactive power. Therefore, DC systems' lack of frequency and reactive power has led to significant benefits. Firstly, the skin effects and proximity do not affect DC systems due to their zero-frequency operation. Secondly, the lack of reactive power in DC systems counteracts the transmission line's inductive and capacitive effects in a steady state, limiting the system to ohmic losses and lowering the transmission system cost. Furthermore, the reactive power absence enhances the power system stability allowing long-distance energy transmissibility through DC systems [102].

Moreover, DC systems need few conductors for power transmission; this is a step forward than AC systems requiring more conductors and entail higher investment costs than DC systems for long-distance energy transmission. Therefore, transmitting power through DC systems has proven to be technologically and economically more advantageous than AC transmissions [5]. Additionally, due to the reduced number of conductors in DC systems, power losses decrease considerably; power losses due to corona effects are lower than those from ac systems. Moreover, another significant benefit of HVDC schemes is their flexibility. Mainly, for bipolar HVDC schemes, the system will work through the line connected to the second pole using the ground for the return current when a line is taken out of service due to a short circuit. Figure 2-2 indicates the cost ratio for HVDC and HVAC power systems. Conversion costs make the original investment significantly higher concerning the HVDC technology. The longer the transmission line's distance, the more HVDC links can compensate for the capital investment. The HVDC system's overall cost at some length is similar to the AC line. Subsea cables have a breakeven distance of 40–70 km, while overhead transmission lines are between 600–800 km [104].

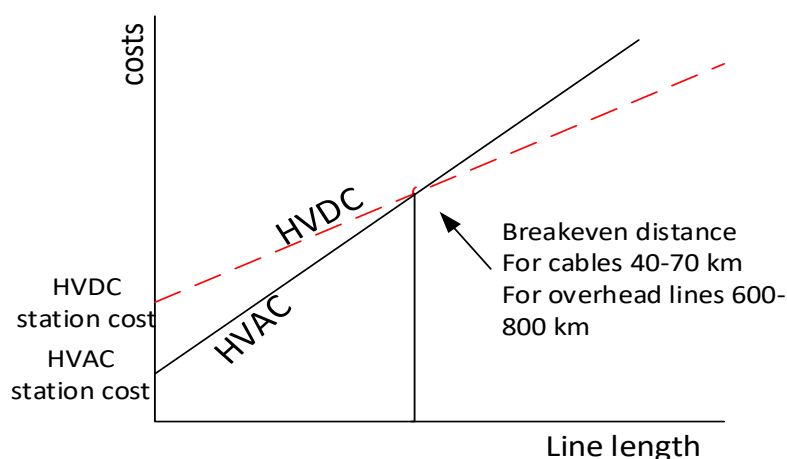


Figure 2-2: HVDC and HVAC schemes' cost comparison [104]

2.3.3 LCC HVDC

Many HVDC links currently in operation are of Line-Commutated Converter type. Considering a converter as a line-commutated device means its power conversion process depends on the AC line voltage to which the converter is electrically connected. One switching device's commutation process to the following is achieved based on the AC line voltage. Line-commutated converters can use uncontrollable switching devices (e.g., diodes) or controllable switching devices (e.g., thyristors), which require a trigger pulse to allow current to flow [105]. However, power converters using diodes (i.e., uncontrollable switches) have the limitation of not working in inversion mode, and their inability to regulate DC voltage remains a considerable drawback. Therefore, all HVDC systems with line-commutated converters use either grid-controlled mercury arc valves (until the 1970s) or thyristors (until today) [106]. What is unique about HVDC LCC is that current flows in one direction only. The

latter goes into a high-value inductance and can thus be regarded as an almost constant current. These systems act as current source converters by inserting network frequency and harmonic currents into the AC network. Changing the DC voltage's polarity at both converter stations may reverse the power flow direction. This choice on the inversion of the direct voltage's polarities is made because of the DC current direction's unchangeability [5, 106].

2.3.3.1 Mercury arc valves

LCC HVDC systems were first developed using mercury-arc valves, with a configuration derived from high-power industrial thyristors. These valves underwent a range of changes to make them fully compliant with HVDC, particularly limiting the chance of arc return at the highly reverse voltages encountered by HVDC by applying a matching technique simply based on electrodes for anode voltage gradation [105]. Due to the enormously long length of anode columns, which were commonly necessary for HVDC applications, most mercury arc valves were equipped with multiple (more often, four) anode columns in parallel per valve, unfortunately, prevented from carrying the current safely. A single mercury arc valve was sufficient to inject six pulses into the bridge, based on the arm configuration of a six-pulse bridge using mercury-arc valves [16, 106]. However, two implemented HVDC projects in the former Soviet Union revealed their peculiarity by using two to three mercury arc valves in series per arm. Despite the ruggedness of the mercury arc valves, regular maintenance was required. The significant need for mercury arc valve maintenance has led HVDC designs based on this technology to be fitted with a bypass gear through each six-pulse bridge to continue operating in six-pulse mode during limited maintenance periods. The nominal voltage and current at which these valves were used were 150 kV and 1,800 A, respectively [106]. Figure 2-3 represents a Canadian HVDC converter's mercury-arc-valves, known as the world's last mercury arc scheme. This transmission system, known as the Nelson River, used six columns of anodes per valve in parallel and was implemented in 1977.



Figure 2-3: The Nelson River DC System's Mercury-arc valve [106]

2.3.3.2 Thyristor valves

In fact, since the advent of the thyristor converter, the HVDC system has become much more attractive. The Eel River project, commissioned in 1972, is recognized as the first HVDC system using thyristor valves. Thyristor valves attracted more attention and became standard DC converter station equipment at the Eel River project implementation. This network, interconnecting New Brunswick and Quebec Canadian provinces, was designed for a rated DC power of 320 MW. Recent developments in thyristor-based conversion equipment have significantly reduced their size and cost and improved their reliability. These developments have advantageously led to the broader use of LCC HVDC-based transmission systems [4].

Indeed, it is vital to understand the origin, design, and working principle of thyristor technology since it plays a massive role in the operation of current source converters-based HVDC systems. The thyristor technology is used in LCC HVDC for the converter's valve commutation process. The thyristor is a silicon semiconductor device with four negative and positive material layers that work as bi-stable switches triggered by a gate pulse. It maintains its state until the following zero current crossings. The two existing thyristor triggering methods are electron injection-based technology known as Electronic Triggered Thyristors (ETT) and light photon injection-based technology known as Light Triggered Thyristor (LTT). However, the circuit converting light signals into an electrical pulse through the ETT consists of many electronic components. The disadvantage of this technique is that it suffers from numerous limitations for generating gate pulses.

In contrast to the shortcomings of ETT, the LTT development drastically lowered the number of electronic components in the conversion circuit by nearly 80 percent, making the thyristor-based conversion system usable and straightforward. The reduced energy consumption and direct light make it useful for black starting capability and, in case of under-voltage or faulty conditions [107]. Figure 2-4 displays a 12-pulse thyristor converter for Pole 2 of the HVDC Inter-Island between New Zealand North and South Islands.



Figure 2-4: Twelve-pulse thyristor valves [106]

2.3.4 CCC HVDC

HVDC systems with capacitive commutated converters (CCC) are also part of CSC-HVDC. The extra series capacitors in the CCC HVDC's converter circuits make them different from LCC-HVDC. The primary purpose of having these capacitors in series with the converter transformer is to facilitate their influence on the thyristor valve's commutation process. Compared to conventional HVDC converters, these capacitors contribute positively to CCC operation by facilitating reactive power consumption minimization [108]. Thus, due to the capacitors' series positioning between the transformer and the thyristor valves, these electronic components are usually known as commutation capacitors. They can also be situated between the converter transformer and AC filters. Figure 2-5 illustrates a typical example of CCC[105].

Indeed, when using a CCC, the switching capacitor provides reactive power relatively proportional to the converter's load current. The voltage polarity induced across the commutation capacitor makes the thyristor valves' voltage higher than the converter's AC side voltage with a specific phase difference. This phase difference is an essential factor making the CCCs more advantageous over an HVDC's typical converter because of its reduced reactive power consumption. Consequently, the reactive power requirement of the CCC is precisely defined depending on switching capacitors. The capacitor size should then be chosen depending on reducing the converter's reactive energy consumption at maximum load. This size's choice should also take into account the induced AC filters' reactive power. Due to the non-dependence of reactive power production and filtering features, the need for switchable shunt capacitor banks' placement is significantly reduced [105, 108].

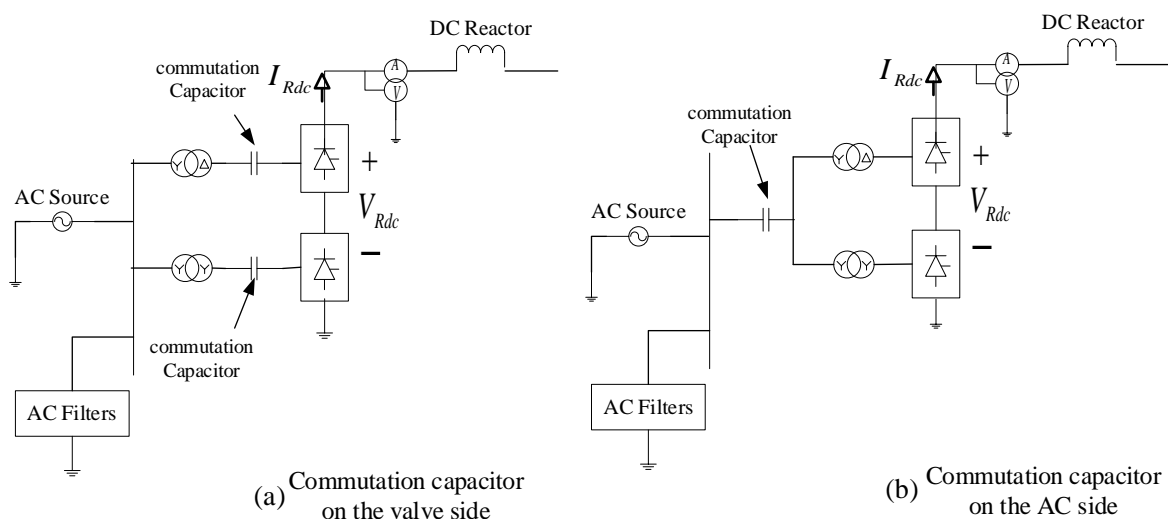


Figure 2-5: Configurations for applying series capacitors at HVDC substations [105]

2.3.4.1 CCC-HVDC Advantages

Any energy conversion device has major reasons justifying its usefulness. The following points describe the importance of choosing a CCC [105, 109]:

- There is no need for switchable shunt filter banks due to using a commutation series capacitor to ensure reactive power compensation.
- The capacitive commutated converter offers more stable operation with weak AC systems
- Valve current reduction when a DC system fault appears results in transformer optimization.
- Probability of keeping the power factor seen from the AC bus close to unity during certain operating ranges.

2.3.4.2 Disadvantages of CCC-HVDC compared to LCC-HVDC

The following points are the disadvantages of CCC-HVDC [105, 109]:

- Compared to conventional HVDC schemes that only have the converter transformer as a risk factor, the commutation series capacitor of CCC-HVDC is an extra component that may influence the adequate availability and reliability of a back-to-back HVDC.
- Risk of series capacitor bank's supplementary pollution due to the DC stresses it is often exposed to, specifically when mounted externally.
- The capacitor bank's extra exposed conductors have increased radio-frequency interference problems especially radiated from the converter station.
- The high cost of civil works following the commutation capacitor's indoor fixing was conducted to shield it from pollution and the rise in RFI production.
- Converter operation at higher delay angles and increase in resulting harmonic currents due to the commutation capacitor.

Furthermore, CCC HVDC's use has decreased significantly due to the complicated structure of capacitive commutative converters' control and protection system. On the other hand, as for LCC HVDC, its commutating process requires a very high synchronous voltage source, limiting its use for a black start operation. Despite all these drawbacks, the LCC still has the highest rated current reaching 6250A and a blocking voltage of 10kV. The LCC-HVDC is the system with the highest voltage and power level of all HVDC schemes [107].

2.3.5 Components of LCC HVDC

A basic LCC HVDC scheme comprises line-commuted converters, converter transformers, smoothing reactors, harmonic filters, reactive power compensation, electrodes, a commutation system, transmission lines, and AC circuit breakers. The basic components of an LCC HVDC are described in Figure 2-6 [20].

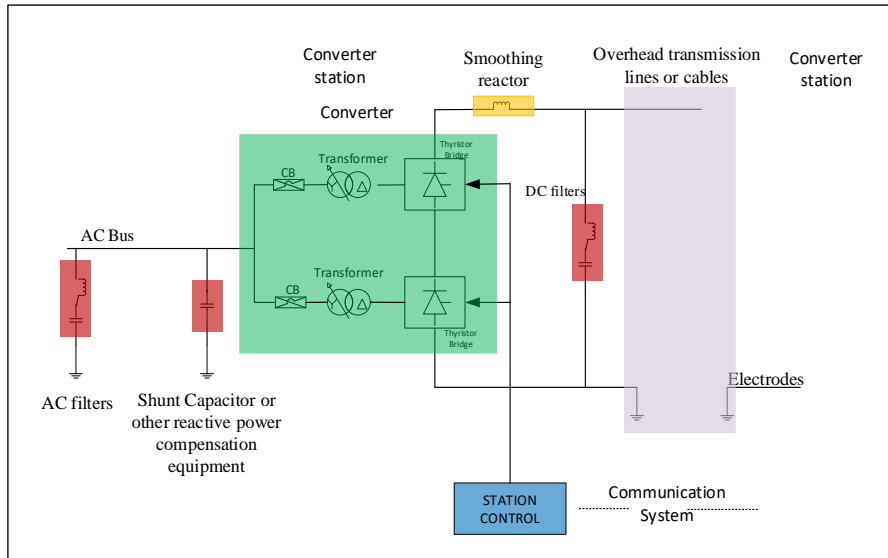


Figure 2-6: LCC HVDC components[20]

2.3.5.1 Converters

The converter is recognized as one of the essential components of HVDC systems due to its powerful conversion function. Practically, an LCC comprises one or more 6-pulse thyristor bridges known as Gratz bridges. An m -pulse converter configuration can be obtained by connecting n 6-pulse bridges in series ($n=m/6$). The advantage of the 6-pulse bridge's series connection is reducing harmonics by taking into account the phase shift [109]. In fact, during the non-conductive phase, the resistance to high Peak Inverse Voltage (PIV) is a quality of suitable converters. Therefore, apart from the fact that suitable converters allow low voltage current through the valves during the conductive phase, the latter must also have significant resistance during the non-conductive phase. Moreover, suitable converters should allow a proper short margin angle of commutation during inverter operation and smooth control during both conducting and non-conducting phases [107].

2.3.5.2 Converter Transformers

The converter transformer links the converter valves with the AC network. Its prominent role is to adjust the AC network's voltage to an appropriate convert AC side voltage [110]. In other words, converter transformers' operation aims to provide the valve bridge with an ungrounded three-phase voltage source of a suitable level. Since the transformer winding on the valve side is not grounded, the DC system can establish its reference to the ground by grounding the converter valve's positive or negative end [109]. Additionally, compared to a standard transformer with the same rating, the converter transformer has been costlier. The key points that differentiate them from typical transformers are converter transformer characteristics such as short-circuit impedance, on-load tap-changers (OLTC), and DC magnetization. It should be noted that the tap-changer transformer provides voltage control on the converter's AC side [102, 107]. Converter transformers are designed to work with high harmonic currents and withstand AC

and DC voltages stress. The internal arrangement of the converter transformer's phases and windings can be described in different ways, such as “three-phase, two windings,” “single-phase, three windings,” and “single-phase, two windings.” To obtain a 30 ° phase shift, the two converter transformers' valve side's windings must be star-connected and delta-connected, respectively. However, the other remaining windings may both be star-connected or delta-connected. However, the remaining windings, i.e., those located on the AC bus side, can be connected in either star or triangle [5, 104, 110]. Figure 2-7 displays a typical example of a large single three-winding transformer.

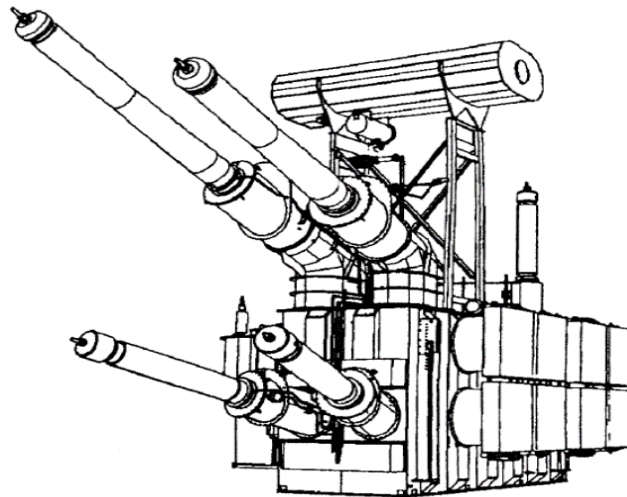


Figure 2-7: Large single-phase three winding transformers [111]

2.3.5.3 Smoothing Reactors

The smoothing reactor is a substantial inductive device of up to 1.0 H with little or no resistance. Smoothing reactors allow DC systems to avoid transient DC currents, resulting in converter damage due to the induced over-voltage. Reactors are also used to prevent the resonance effect from reaching the valve hall due to DC switching yard or DC lines fault and reduce telephone interference [112]. Smoothing reactors are connected in series with each pole in each converter station [28]. Moreover, direct harmonic voltages and currents in the DC line prevent inverter commutation failure, current protection from discontinuity at light load, and limitation of peak current in the rectifier during a DC line short circuit. These are the key roles of smoothing reactors. For HVDC systems, air-insulated dry type with magnetically shielded reactors or braced disk oil type windings is recommended. However, the air-insulated dry type is advantageous for being easier to maintain and providing a cheaper replacement unit. However, it cannot have one single unit with a large inductance. Additionally, the latter is preferred in an earthquake-prone region (seismic region) or a place with restricted space [48, 107]. Figure 2-8 displays an Air core reactor designed by the Beijing Power Equipment Group.



Figure 2-8: Air core reactor [113]

2.3.5.4 Harmonic Filters (AC filters)

Converters' AC and DC sides are often subject to converter-generated harmonic currents and harmonic voltages. The drawback of these generated harmonics is their interference with the communication system, overheating nearby generators. This situation requires incorporating AC filters on both sides of the HVDC converters. Furthermore, adding AC filters provides a low impedance path to the ground, preventing harmonic currents from reaching the AC side. AC filters are used as protection that stops harmonics generated by converters from accessing the AC system. It is essential to provide 11th, 13th, 23th, and 25th filters on the AC side of a typical 12-pulse thyristor converter. They also require a high pass filter.

In some cases, it needs third harmonic filters. Many HVDC systems use DC side filters with overhead cables [104, 110]. Figure 2-9 displays a typical example of a high pass filter that operates up to a nominal voltage of 24 kV.

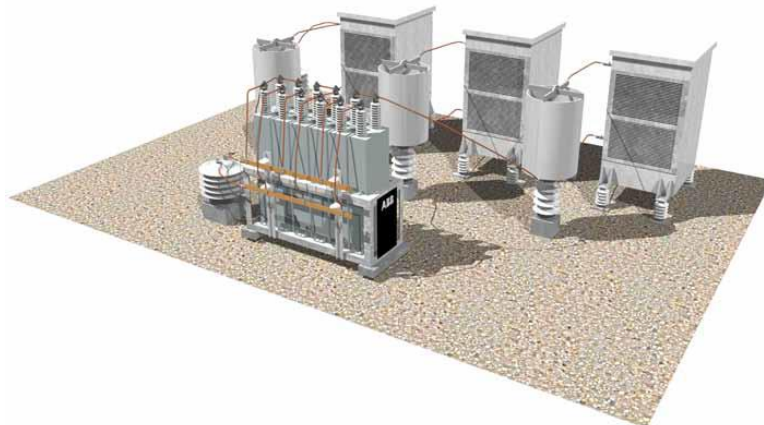


Figure 2-9: High pass filter up to 24 kV [114]

2.3.5.5 Reactive Power Compensation.

The reactive power requirements of HVDC converters return to around 60 percent of their power rating [108]. Most of this reactive power comes from filter banks, and the remaining portion comes from capacitor banks. The demand for reactive power changes concerning DC power level; therefore, the capacitors are arranged in switchable banks. The supplied reactive power near the converter generally is in the form of a shunt capacitor for robust AC systems. However, part of this reactive power can be synchronous condensers or Static Var Compensators (SVC), depending on both DC and AC systems' requirements. Therefore, it should be noted that the capacitor banks compensate for the reactive power in combination with AC filters [48, 105]. Figure 2-10 shows a three-phase capacitor bank designed by ABB for reactive power compensation [114].

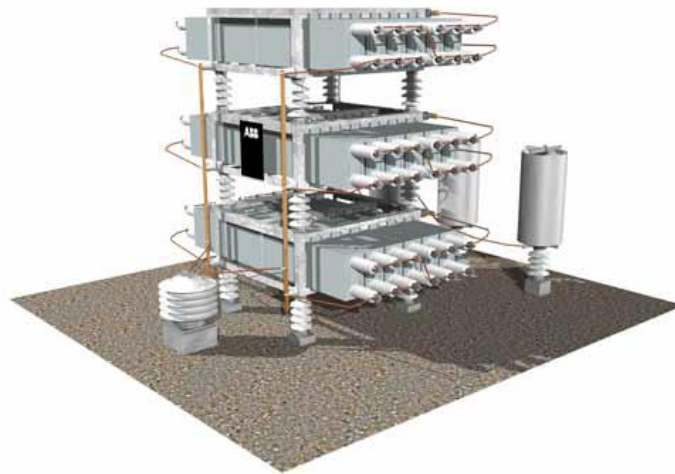


Figure 2-10: Three-phase capacitor bank[114]

2.3.5.6 Electrodes

Many older HVDC systems generally operate with sea/ground return, but network operators no longer permit permanent ground currents for environmental reasons. Therefore, many new DC systems are designed to work with ground return as a neutral conductor at half power for a brief period (10 to 20 minutes) in the event of losing an HVDC pole. The conductor is called an electrode. Thus, an electrode does not carry any current in regular operation, although it is designed for the total current. Furthermore, if necessary, a metallic return conductor may be installed as part of the DC line to counteract current flow through the ground. The ground connection-based electrode requires a wide-area conductor to reduce current densities and gradients of surface voltage, but its maintenance costs are usually very high [4].

2.3.5.7 DC Transmission Lines

LCC HVDC implementation requires using overhead lines and subsea/underground DC cables. In fact, regarding overhead lines, the possibility of using the ground as a conductor is one of the key concerns when designing HVDC systems. Unusually, a ground conductor is permanently used in HVDC systems. However, its use is expected in monopolar HVDC systems where it plays the function of earth return current in the case of a fault. In bipolar HVDC, where the conductors carry equal currents, the temporary use of ground can be exclusively permitted when one of the conductors fails. Power transmission via HVDC lines requires only two electrical conductors to be used, while three are needed in 3-phase AC systems. Accordingly, losses are also minor. The tower structures' dimensions for DC overhead lines are almost similar to those of AC lines. DC lines have a much higher power carrying capacity than AC lines, dramatically reducing land use and visual effect. Before making any decision on the choice of overhead conductors, it is highly recommended that the field and corona effects be considered. Though, in HVDC schemes with voltage up to ± 1200 kV, these unwanted effects are not expected. DC faults occurring as lightning strikes only cause transient disturbances that LCC HVDC schemes using overhead lines can readily manage. The mechanical design is the same for both AC and DC overhead lines. AC and DC overhead lines differ in their conductor structure, electrical field requirement, and insulation design [48, 107, 110].

Furthermore, as far as DC cables are concerned, they are required in transmission systems crossing maritime regions. Unlike overhead line insulators, where cable failure commonly occurs by flashover on the outside, puncturing through the insulation is the leading cause of cable failure in DC systems. This effect is one of the main advantages of the DC system over the AC system. Besides the fact that HVDC has considerably reduced losses due to the lack of significant current in the sheaths and supporting components, its cables are susceptible to less overcurrent. DC cables are preferably used in bipolar HVDC compared to overhead lines, whose length is greater than 50 km. The non-variation of DC current regarding time (i.e., zero frequency) allows the lack of skin effect in the conductors. The conductor's size requirements for DC links are reduced, considering AC systems' same amount of power. Paper-insulated DC cables come in four types: oil-filled, gas-pressurized, mass-impregnated, and XLPE. For more details about the transmission line cables or overhead lines, consult [107].

2.3.6 LCC SYSTEM TOPOLOGY

The most common LCC HVDC topologies are monopolar and bipolar [109, 110].

2.3.6.1 Monopolar HVDC

Figure 2-11 shows the design of a monopolar HVDC system. This configuration is achieved by combining two series 6-pulse converters. The scheme represents a two-terminal HVDC system with converter stations linked by the DC transmission line. Monopolar HVDC schemes are generally used

for small DC lines. These systems comprise one conductor, including ground and/or sea return. A metallic return system is provided in areas prone to the significant issue of harmonic interference or corrosion [110]. Typically, a metallic return cable is used for HVDC Light schemes to fulfill this function. The metallic return conductor's implementation must be done to remain at earth potential with low-level insulation of about 10 kV [104, 109].

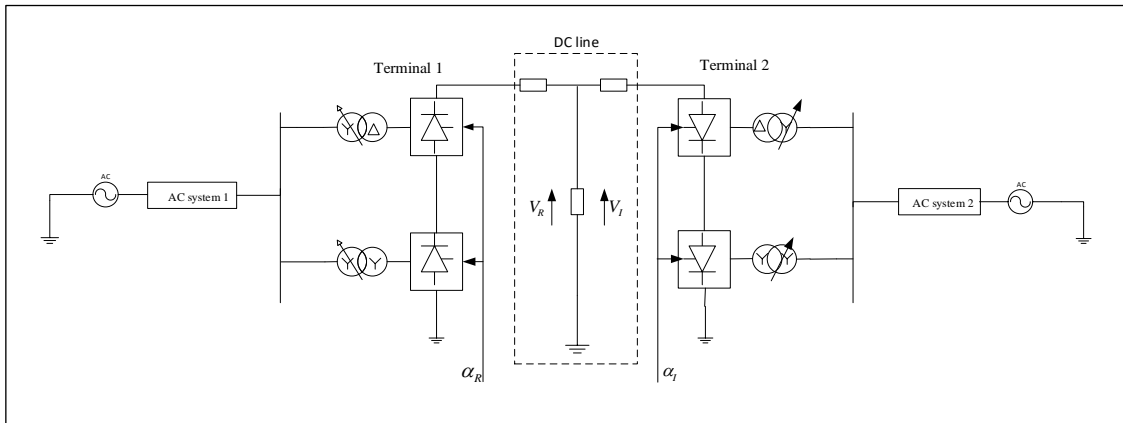


Figure 2-11: Monopolar HVDC [104]

2.3.6.2 Bipolar HVDC-

Figure 2-12 displays the bipolar HVDC. Two distinct poles generally characterize this system. This system's specificity is its ability to operate at half power if a cable or a DC pole is out of service.

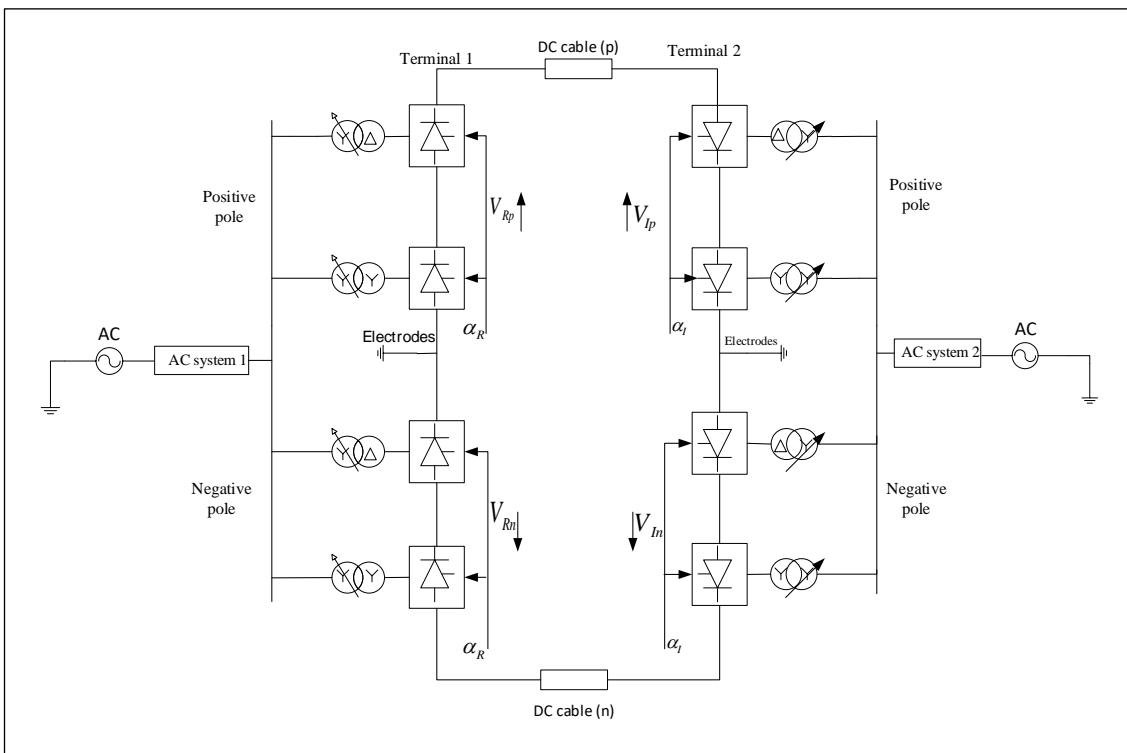


Figure 2-12: Bipolar HVDC [104]

The ground current in regular operation does not exist because both the poles are balanced, but the ground return use only intervenes if one of these poles gets out of service. Due to environmental concerns, ground currents are not recommended based on modern grid codes [109, 110]. However, according to some countries' national standards, ground currents are only allowed in emergencies for concise periods, such as starting a secondary reserve for 10 to 20 minutes [104].

2.3.7 CONVERTER THEORY

As described in the previous section, the converter's function is to convert the DC power to AC and vice versa. A two-terminal HVDC system is fitted with two stations that fulfill the conversion role. These converter stations are known as rectifier and inverter, respectively. To understand the converter working principle, it is necessary first to understand the operation of its two main components: the valve bridge and the transformer. Converter transformers have already been discussed in detail in the previous sections. Converter transformers in HVDC systems are meant to establish a convenient interface between AC and DC systems by adjusting the voltage (AC or DC) to an adequate level [5]. In line with [4], the valve bridge is described as a set of high-voltage switches or valves that ensure a sequential connection of the three-phase AC voltage to the DC terminals to obtain the desired conversion and power. The converter valve is an electronic switch, which can only conduct in the forward direction, from anode to cathode. Only a small voltage drop is observed at the terminals of the converter valve during its conduction. Alternatively, the valve prevents current from flowing in the opposite direction when the voltage applied across the cathode is positive with respect to that at the anode [4, 5].

2.3.7.1 Ideal Diode Bridge

The first step to explain the Line Commutative Converter's working principle based on the AC-DC conversion is through a fundamental 6-pulse diode bridge. The converter has six diodes equally distributed between the positive and negative poles. The valve delay angle is usually zero. The inputs' 3-phase ac voltages are assumed to be balanced and symmetrical with a 120° phase shift. The conduction process occurs through two diodes, one connected to the positive rail and the other to the negative rail. The diode only becomes conductive when forward-biased, i.e., when a positive voltage is applied to the anode terminal. Therefore, the commutation process between valves or phase voltage is directly dependent on the conduction period of diodes. On both rails, the commutation process happens every 120° , but it only lasts 60° for the negative rail [48, 115]. Figure 2-13 shows the 6-pulse ideal three-phase diode bridge known as the Gratz Bridge.

2.3.7.2 Three-phase thyristor bridge

The working principle of a thyristor valve is almost similar to that of the diode valve; however, the turn-on time control can be achieved by sending a pulse to the thyristor gate terminal. Ideally, if the firing pulses were designed to be sent at the beginning of each conductive interval ($\alpha=0$), the thyristor bridge would function just like a diode bridge [102]. The conduction of a thyristor valve is possible only when the voltage applied to the gate is positive, and the anode is positive with respect to the cathode. The thyristor valve must be forward-biased to be able to conduct when it receives a gate pulse. In other words, the current is blocked when the thyristor is forward-biased until it gets triggered. Once the thyristor is triggered through the given gate pulse, conduction starts, and the current flows through the valve until it drops to zero, and a reverse bias voltage appears through the valve. The valve must have the ability to withstand the reverse and forward bias voltage that appears between its terminals when not conducting [4, 102]. Thyristor valves are available in different designs: air-insulated, air-cooled, oil-cooled, oil-insulated, water-cooled, and Freon-cooled; SF6 insulated [107]. The illustration in Figure 2-14 is a three-phase thyristor bridge.

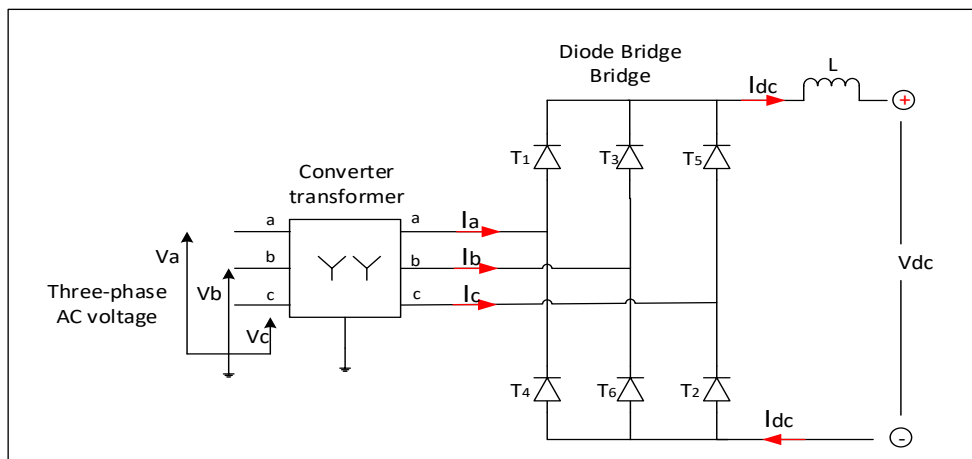


Figure 2-13: Three-phase diode bridge circuit [102]

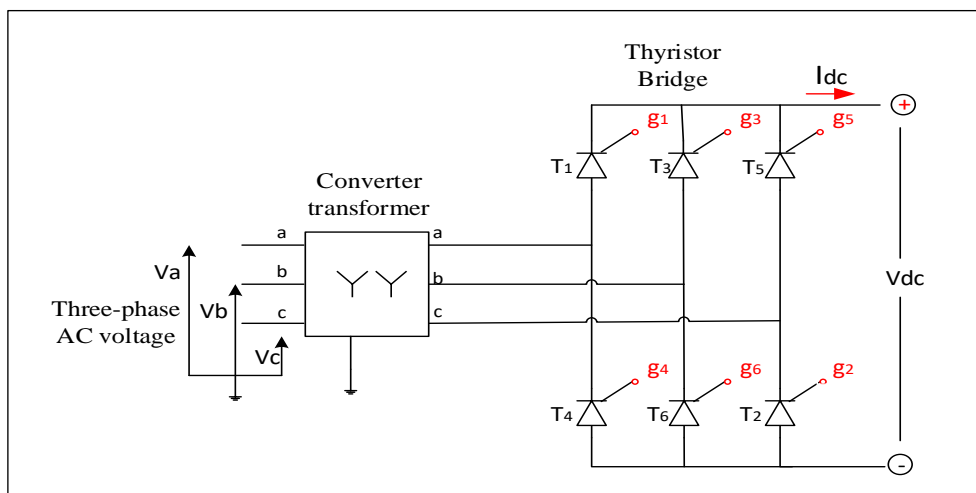


Figure 2-14: Three-phase full thyristor bridge circuit [102]

These valve's converter transformers usually have on-load taps on the AC side voltage control. The transformer's AC side windings are generally star-connected with grounded neutral. The valve side's windings can be star-connected or delta-connected with neutral not connected to the ground [115]. The thyristor delay angle (α) is measured from the positive forward voltage, i.e., from the intersection of two-phase voltages [115]. The DC voltage becomes fully controllable due to the delay angle of the thyristor turn-on and the line-to-line ac voltage. Therefore, neglecting commutation overlap, the average controlled dc voltage resulting from the line-to-line AC voltage, and the thyristor firing angle can be obtained as shown in equation (A) [102].

$$V_{dc} = \frac{3\sqrt{2}}{\pi} V_{LL} \cos \alpha = 1.35V_{LL} \cos \alpha \quad 2.4$$

The factor $1.35V_{LL}$ in equation (2.4) is known as the ideal no-load voltage. Therefore, the above equation defines the DC voltage control's dependence on the influence of both the firing angle and the no-load voltage. In line with [4], the delay angle impact on the average DC voltage regulation reduces its value by the factor $\cos\alpha$.

2.3.7.3 Commutation Overlap in Rectification mode

By considering the commutation overlap induced due to the transformer inductive reactance, the commutation process takes more time than in the previous case; this is referred to as the commutation angle (μ). The typical value of the commutation angle is 10° . This angle is calculated as [104]:

$$\mu = \arccos\left(\cos \alpha - \frac{3\omega L_t}{\sqrt{2}V_{LL}} I_{dc}\right) - \alpha \quad 2.5$$

The converter is subjected to two different effects due to commutation overlap [102, 115]:

- The reduction of the controlled DC voltage V_{dc} by an amount ΔV_{dc} is described by the following equation:

$$\Delta V_{dc} = 3 \frac{\omega L_t}{\pi} I_{dc} \quad 2.6$$

Therefore, due to the commutation overlap, (2.4) becomes:

$$V_{dc} = \frac{3\sqrt{2}}{\pi} V_{LL} \cos \alpha - 3 \frac{\omega L_t}{\pi} I_{dc} \quad 2.7$$

- The commutation overlap sets a practical limit of the delay angle since the commutation process cannot be extended beyond 180° without the risk of commutation failure. The commutation angle directly starts when the delay angle is over.

Figure 2-15 illustrates a three-phase thyristor rectifier's commutation process from phase (a) to phase (b). Figure 2-14 shows six thyristor valves with gate pulses representing a 6-pulse bridge. The bridge consists of a three-phase voltage, with two valves at each phase. Assuming a pulse is given to T_3 while T_1 is conducting when commutation overlap is happening with a duration of $\alpha < \omega t < \delta$, three valves, namely T_1 , T_2 , and T_3 will conduct at the same time (see Figure 2-15). The current flowing in phase (a) through the valve T_1 steadily decreases (I_d to 0), while that of phase (b) flowing through T_3 steadily increases (0 to I_d), assuming the DC current is constant. Phase (b) voltage should be greater than phase (a) voltage ($V_b > V_a$) to allow commutation from T_1 to T_3 (point **H** to point **I**). Hence, it should be mentioned that when the commutation process starts $\omega t = \alpha$, during commutation $\alpha < \omega t < \delta$; and when it ends $\omega t = \delta$ (δ is known as the extinction angle, $\delta = \alpha + \mu$). In rectification mode, as shown in Figure 2-15, commutation happens near point **H** [104].

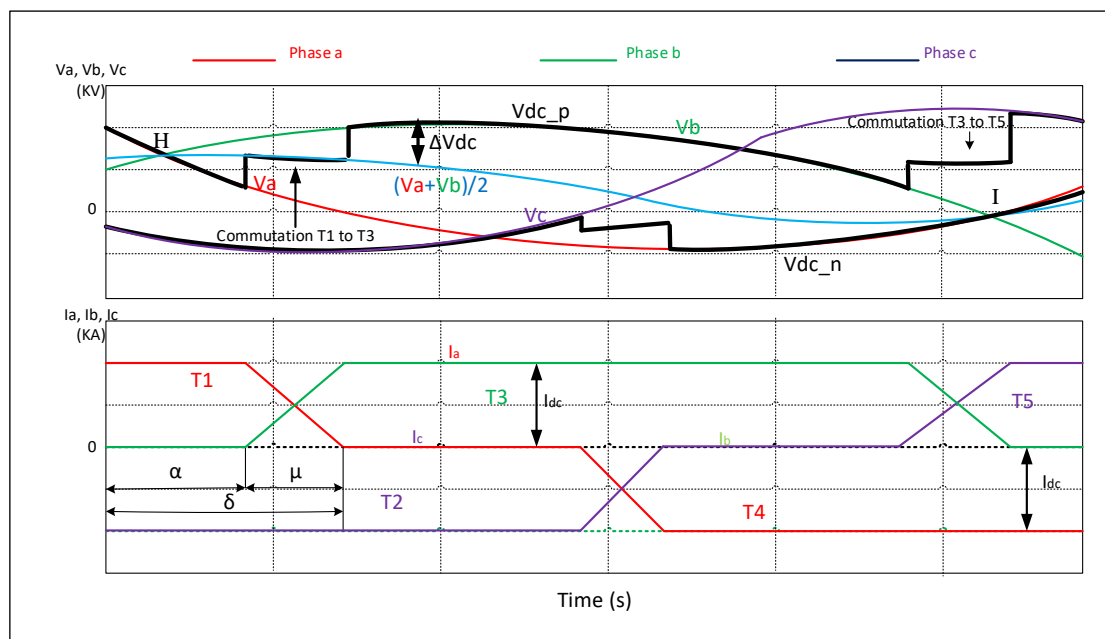


Figure 2-15: Commutation process from valve T1 to T3 [104]

2.3.7.4 Commutation Overlap in Inversion Mode

For convector operations in inversion mode, commutation overlap happens when the firing angle exceeds 90 degrees. At this point, the direct voltage immediately becomes negative. Therefore, the shift of the dc voltage signs from positive to negative induces the reversal of power. The commutation overlap consideration based-inversion mode condition is given by the following equation [102, 104]:

$$\alpha = \frac{\pi - \mu}{2} \quad 2.8$$

$$\sin \alpha + \sin \delta = 0 \quad 2.9$$

The converter's operation in inverter mode considers two distinct angles: the advance ignition angle (β) and the advance extinction angle (γ). These angles have the same meaning as the rectifier firing and extinction angles. However, in inversion mode, these angle values are mostly more significant than 90 degrees. Accordingly, the DC voltage of the inverter side can be determined using “ γ ” and “ β ” as specified in equations (2.10) and (2.11). These two angles are the key elements of different control strategies operating in inversion mode. The DC voltage control directly depends on monitoring one of these angles [102].

$$V_{dc} = \frac{3\sqrt{2}}{\pi} V_{LL} \cos \beta + 3 \frac{\omega L_t}{\pi} I_{dc} \quad 2.10$$

$$V_{dc} = \frac{3\sqrt{2}}{\pi} V_{LL} \cos \gamma - 3 \frac{\omega L_t}{\pi} I_{dc} \quad 2.11$$

Furthermore, Figure 2-16 discusses a brief example of how the commutation process (T_3) is achieved in the inversion mode of operation.

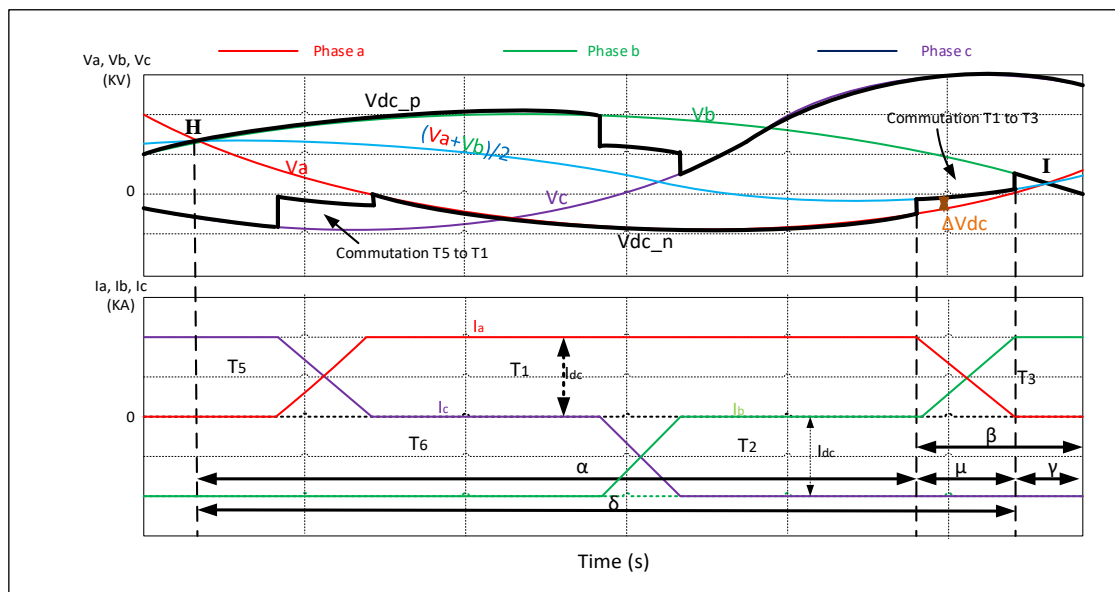


Figure 2-16: Commutation from valve T_1 to T_3 [104]

However, as in Figure 2.6, valve T_1 is allocated to phase (a) and T_3 to phase (b). The commutation process analysis from T_1 to T_3 means, in other words, commutation from phase (a) to phase (b) or H to I . The converter operates with a large firing angle close to the inversion mode point. The extinction angle plays a vital role in facilitating the safety period for the thyristors' reverse recovery. Between H and I , T_1 is turning off. The valve's forward blocking state must be restored immediately after the turn-off for the valve to become biased forward.

Similarly, by the time it is biased forward, valve T_3 firing must also take place. Therefore, valve T_3 must be fired within a short period, as both the commutation overlap and the reverse recovery time must be done before point I. Furthermore, as in the previous case, the commutation overlap on the DC voltage is the same (see ΔV_{dc} in Figure 2-16) [104].

2.3.8 LCC HVDC Controls

2.3.8.1 Static Characteristics of LCC HVDC

The DC current is the fundamental control quantity of HVDC links. The DC current and DC voltage controls must be assigned separately to the two DC link terminals for better HVDC performances. Usually, the rectifier controls the DC current, and the inverter controls dc line voltage. Figure 2-17 shows the V/I characteristics of the High Voltage Direct Current system. Segments AB and EF, respectively, represent the rectifier and inverter constant voltage (firing angles) control modes of operation. The BC and ED vertical segments reflect the Constant Current control (CC) modes of operation. At Point G, which is the power transfer equilibrium point between the two HVDC terminals, the rectifier (ABC) and inverter (DEF) characteristics intercept [40, 116].

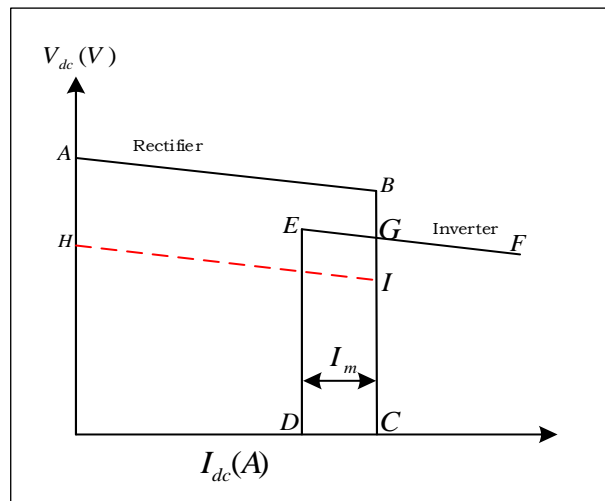


Figure 2-17: Static characteristics of DC voltage and DC current under CC control mode on the rectifier side [40, 99]

Moreover, the purpose of the inverter current regulator (ED) is to prevent the D.C. current from dropping to zero in the event of a significant drop in DC voltage on the rectifier side. That would induce the rectifier side dc voltage (AB) to be lower than that on the inverter side (EF); therefore, there will be no possible equilibrium point. Segment (HI) illustrates this situation. Moreover, the difference between the rectifier side's reference current value and the inverter side is called the current margin; its value ranges from 10% to 15% of the rectifier's reference current. Therefore, it is preferable to operate the rectifier in constant current mode (AB) and the inverter in constant voltage mode (EF) [99, 116].

Furthermore, due to the interchangeability in converters' roles, most two-terminal HVDC systems' control topology remains the same. This operation is known as power reversal. In fact, in power reversal operation, the converter receiving the current margin operates as an inverter. Although the reference DC voltage sign at both terminals is different, the direct voltage across the system remains unchanged. Therefore, due to power reversal, the HVDC control has the properties described in Figure 2-18. The upper part of the I_{dc} axis in Figure 2-18 represents the system operating conditions when the power is transmitted from converter 1 to converter 2.

In contrast, the lower part one reflects the operating conditions due to power reversal (converter 2 to converter 1). To meet the working criteria of two-terminal DC systems where control functions are separately assigned to each converter, G_1 and G_2 reflect the power transfer operating points in the positive and negative directions, respectively. The position of these two operating points on either side of the I_{dc} axis demonstrates the converters' role interchangeability. This operation is also known as the bidirectional power flow. Each converter characteristic consists of CIA (α_{min}) control, CC control, and CEA (γ_{min}) control or CV control [4, 104].

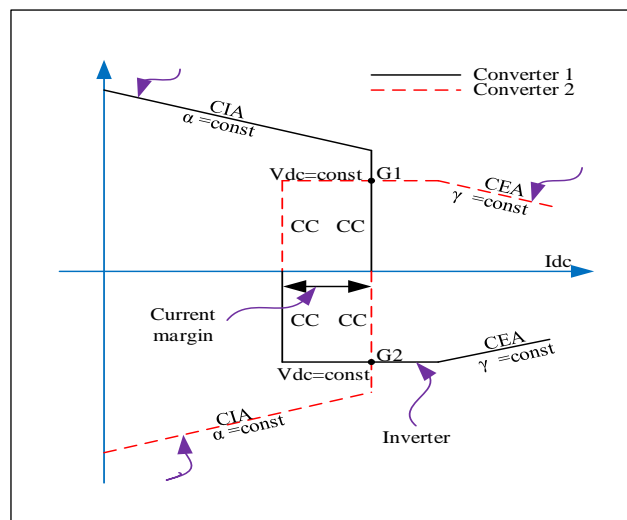


Figure 2-18: Static characteristics of DC voltage and DC current with positive and negative directions[107]

2.3.8.2 HVDC Control System Overview

An HVDC system is highly controllable [109]. The suitable use of HVDC controls plays a major role in their efficiency, facilitating the desired power system performance. The control system architecture of an HVDC system, made up of different levels, is hierarchically structured to ensure the power system's effective and stable operation while optimizing power control efficiency without exposing equipment safety [51]. Because a monopolar HVDC is a subsystem of the bipolar HVDC, the control of a one-pole DC system is included in the overall monitoring of every HVDC tie with two or more poles. Generally, an HVDC pole comprises two or more converter bridges connected in series. A typical two-bridge system with transformers whose windings are connected in Y-Y and ΔY is considered a 12-

pulse unit [48]. Therefore, the smallest unit to control such a system is the 6-pulse unit or the 12-pulse unit. Although the control hierarchy differs depending on the DC system's topology, its concept remains the same. Figure 2-19 displays the control structure of a bipolar HVDC system [4, 51]. It should be remembered that in most implementations, the fundamental control functions of HVDC systems are usually identical. However, the individual systems' specific performance measures make a difference in determining the control functions at a higher level. Each pole should operate as freely as possible for the stable operation of DC systems. The implementation and aggregation of control and protection functions must be effective at the hierarchical minimum available level. The communication mechanism is of paramount importance to achieve a specific operation of HVDC controls. Communication must occur at high speed when the power level encounters rapid changes to maintain consistent current parameters at both terminals.

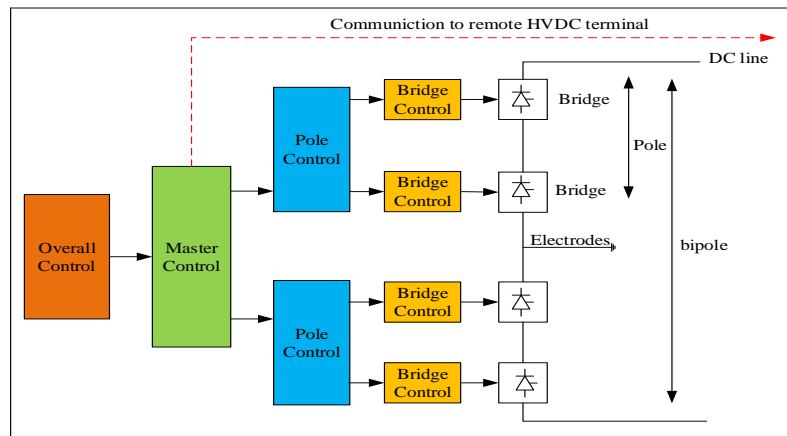


Figure 2-19: Hierarchy of different levels of HVDC controls [4, 51]

The power transfer direction change, known as power reversal, also needs commutation for transferring the current margin parameters between both terminals. The need for commutation between the two HVDC terminals is also significant to protect the system by detecting some faults. The different control parts presented in the block diagram of Figure 2-19 can be described as follows [3, 51]:

- **Thyristor and valve control level:** This is known as the lowest control level of a DC line control hierarchy. This level includes electronic equipment to transmit control pulses to the valve to trigger individual thyristors and track and monitor the valve status.
- **Converter control level:** This substation's primary purpose, known as “bridge controls,” specifies all converter valves' firing instants. The firing control system's operation can be realized in different modes: current control, voltage control, minimum firing angle control (α_{min}), and minimum extinction angle control (γ_0).
- **Pole controls** aim to produce the ordered current with low harmonics, thereby coordinating the pole bridge. The pole controls consist of a current control amplifier. Any series combination of several converter groups within the same pole must carry the same current and be provided with a standard current control amplifier. One of the HVDC controls configurations at the pole

control stage is that the two converter stations, namely the rectifier and the inverter, are equipped with current controllers. Still, only one converter station controller is active. However, a dynamic change of the two controllers' status may happen when disturbances occur.

- **Master control level:** This consists of power control (for current orders determination), transmitting current orders between converter stations, and limiting the current order for overload control. Moreover, the master controller can also perform the power modulation necessary for ac network stability.
- **Overall controls** provide current orders to master controls in response to required functions such as system frequency, power control, system damping, or their combination.

2.3.8.3 Implemented HVDC Control System

Figure 2-20 shows the typical block diagram of a conventional LCC HVDC control system [117]. The converter firing angles are similar to those displayed in Figures 2-11 and 2-12.

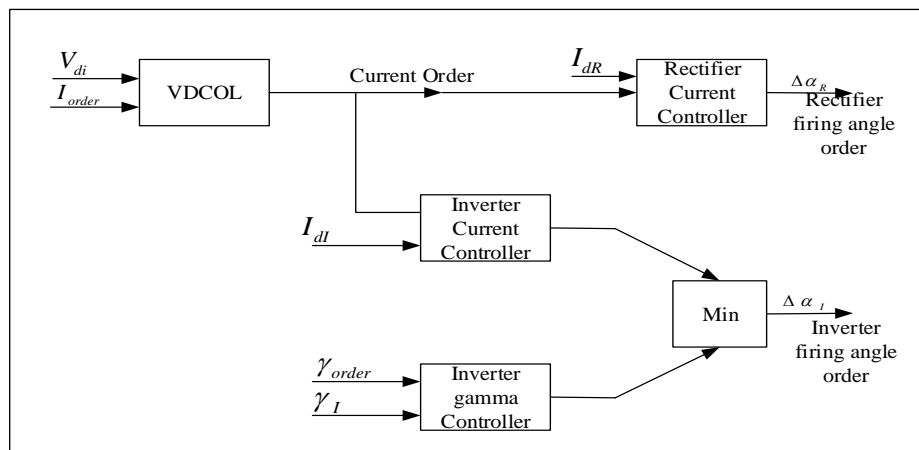


Figure 2-20: Conventional LCC HVDC Control System [117]

Though various control modes can be implemented for a particular HVDC operation, this study considers a rectifier in CC mode of operation. Simultaneously, the inverter operates under the CEA mode of operation (i.e., constant voltage mode) during the DC system's regular operation. PI controllers govern the control systems of both converter stations. Figures 2-21 and 2-22 represent the detailed configuration of converter controllers as described in Figure 2-20. These figures illustrate the rectifier current controller and the inverter voltage controller, respectively, according to PSCAD [90, 104].

Note that current controls can be achieved either on the rectifier or inverter [4]. Converters can operate in two modes, namely Current Control or Voltage Control, using a controlled firing. In a two-terminal HVDC link, the converters work in different control modes to each other [104]. The converter operation aims to adjust the firing angle in the current control mode. However, the voltage control mode of operation seeks to maintain the DC voltage close to the rated value [40]. Therefore, current and voltage controls are assigned to the rectifier and inverter in many HVDC schemes due to optimal design results [118].

angle is denoted by (α); it corresponds to the time delay α/ω seconds where ω is the AC system angular frequency [115]. This angle is measured from positive thyristor forward voltage from the intersection of two-phase voltages. The converter is also subjected to a commutation overlap (μ) resulting from the transformer inductance. For the firing pulse generation to be processed, two input signals, namely the firing angle signal (α) and the ramp signal (θ), providing information about the three-phase bus voltage, are essential [104, 115].

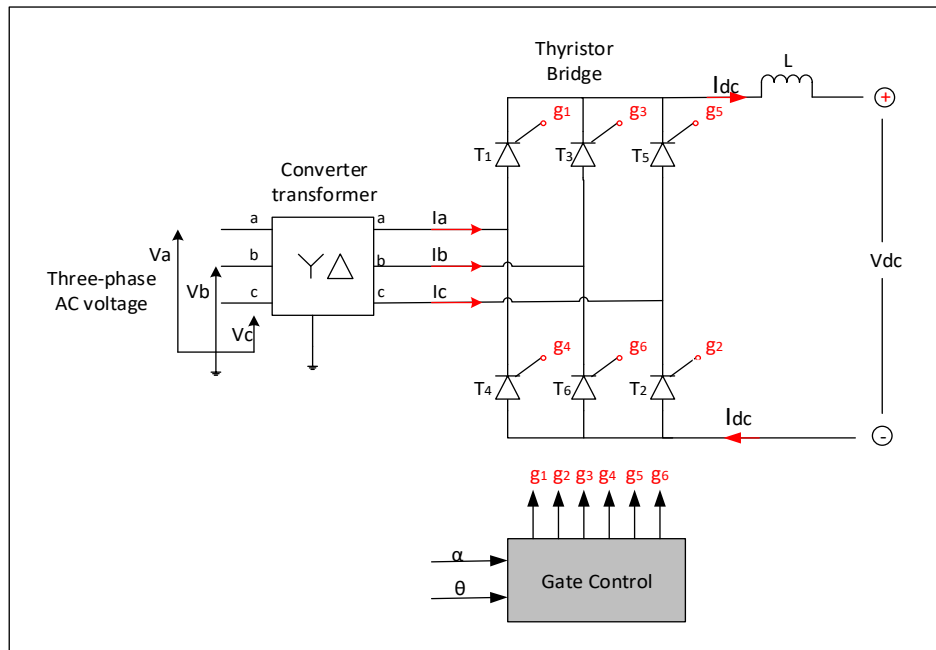


Figure 2-23: Converter firing configuration [115]

2.3.8.3.2 Control Schemes

Usually, HVDC control schemes are designed to get the converter circuits firing correctly. If sent to the gate pulse generation in turns, the output of the constant current controller or constant extinction angle controller defines each valve's firing instant. Thus, regarding the operation and control of an HVDC link, Individual Pulse Control (IPC) and Equidistant Pulse Control (EPC) are the primary control schemes for pulse generation [20].

- Individual Pulse Control: In fact, when each valve produces its firing pulse independently, and the generated pulse is synchronized rigidly with the commutation voltage, this type of control scheme is called IPC.
- Equidistant Pulse Control: By considering p as the number of pulses and f as the fundamental frequency; when the firing pulses are generated in a steady state at equal intervals of $1/pf$, this type of control scheme is known as EPC

2.3.8.3.3 Phase-Locked Oscillator

The thyristor firing control requires information about the position of alternating voltages. This requirement is because the alternating voltages' zero-crossings move as the operating conditions of the ac system change. A forward-biased voltage at the thyristor terminals is essential to allow its firing process, whether the converter operates in rectification or inversion mode. However, the thyristor firing process should sufficiently start early for a given alternating voltage magnitude to allow reverse recovery. Therefore, the Phase Locked Loop (PLL) creates an interface between the ac system voltages and the converter controller by providing the AC bus phase angle information. For a converter controller, generating a reference signal that is synchronized with the alternating commutation voltage is the primary function of a PLL. The PSCAD-based-PLL model used in this thesis is shown in Figure 2-24 [117].

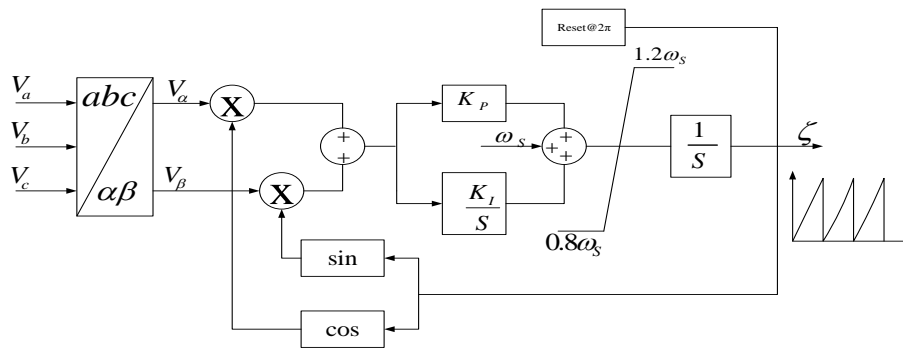


Figure 2-24: Three-phase PI-controller phase-locked loop [117]

The generated output of the PLL is a ramp train between $[0, 2\pi]$ whose frequency and phase are closed to that of the alternating voltage. The integrator's limits illustrated in Figure 2-24 show the fundamental frequency range ($\pm 20\%$) in which the PLL tracks the corresponding AC voltage. From the standpoint of the fundamental AC component, the control system of the PLL can, however, be represented as displayed in Figure 2-25. It should be noted that system disturbances or system setpoint variations may cause changes in the voltage phase angle at the PLL point. The PLL output is exposed to a transient period in such scenarios until the latter can detect and lock the phase angle. Figure 2-25. describes the PLL control system, specifically used to monitor the transient period dynamics [117].

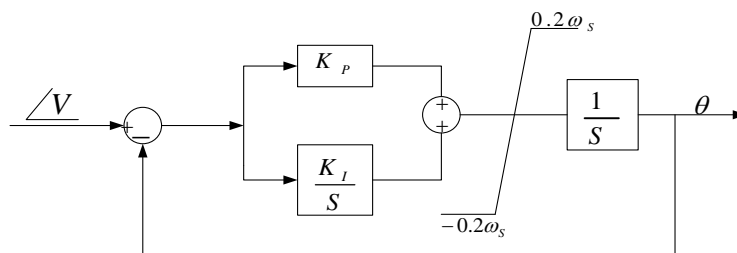


Figure 2-25: Phase Locked based model of PLL [117]

2.3.8.3.4 Voltage-Dependent Current Limiter (VDCOL)

The static characteristics of the VDCOL function are displayed in Figure 2-26 [115]. In general, the DC voltage is more often affected in the event of DC fault, short-circuit commutation failure, or generator disturbances. Mostly, when any of these situations happen, the DC voltage collapses. Therefore, the VDCOL reduces the current order to ensure DC voltage recovery.

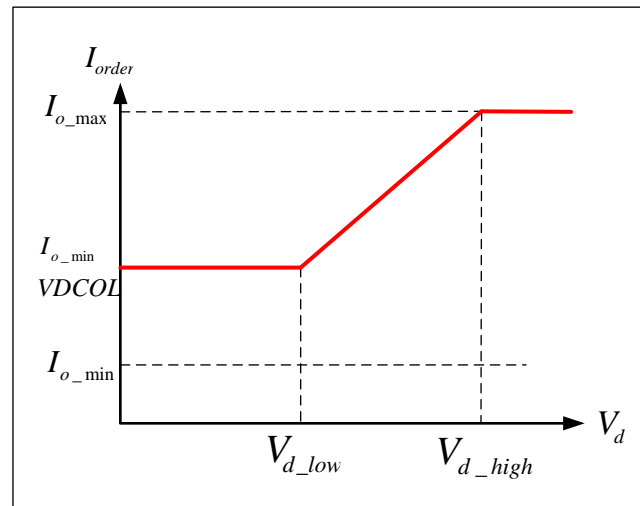


Figure 2-26: Static characteristics of VDCOL [115]

Protection against high reactive power consumption is the critical advantage provided by a VDCOL. VDCOL also ensures converter recovery after disturbance and reduces voltage stresses [90, 107] for a long time in the event of a commutation failure [48]. Additionally, it maintains the DC power flow when the rectifier's AC voltage collapses due to perturbations [109]. In power control, the VDCOL stops the individual thyristor from carrying maximum current

2.3.8.3.5 Tap Changer Control

Converter transformers are provided with tap changers to optimize the valve-side alternating voltage, thus influencing DC quantities. The tap-changer keeps the steady-state DC voltage close to its nominal value when the inverter is in constant extinction angle control. A current control rectifier is typically used to control the firing angle around the rated value. A tap changer's primary function is to increase or decrease the AC voltage on the convertor transformer's valve side through the transformation turns ratio [51, 90].

2.3.8.3.6 Current Controllers

Both the rectifier and inverter have current controllers. However, the two converters cannot operate simultaneously in the current control mode, and the inverter current controller's setting value is generally lower. The practical technical experience of HVDC schemes states that the current margin should be fixed at 10% of the rated DC. The HVDC control system must keep the current margin within

this range under all operating conditions. Otherwise, the DC system will collapse. The rectifier station naturally regulates the DC Current, and the inverter controls aim to maintain the DC line voltage close to the rated value. The rectifier side current controller plays a significant role as it makes it easy to adjust unpredictable DC current fluctuations rapidly and efficiently [17]. Improved damping of electromechanical oscillations can be obtained in power grids by modulating the rectifier current order [4]. In this analysis, all work involving adding auxiliary stabilizing signals to the HVDC control system (i.e., SSDC) relies on the rectifier current regulator. Thus, every improvement of the HVDC control mechanism will focus on the rectifier current controls.

2.3.8.3.7 Extinction Angle Controller

The inverter station generally handles the extinction angle control. This control mode on the inverter station side is usually held in the same way as constant current control on the rectifier station side. However, the gamma (γ) measurement often complicates this control method. Measuring valve voltage would be a straightforward method to measure the gamma angle. Following this procedure, the value of the “gamma” angle would correspond to the instant at which the valve voltage would be negative. As the direct valve voltage measurement technique for gamma computation is hardly usable, most authors prefer using indirect methods for calculating or predicting gamma. Literature recommends using the minimum gamma value for both valves due to the 6-pulse or 12-pulse configurations of line commutative converters [109]. The gamma estimation or prediction methods can be found in the references [119, 120].

2.3.8.3.8 Active Power Controls

Active power controls should be given priority among the primary purposes of controlling an HVDC system. However, previous HVDC control systems used the current control loop for simplification purposes. Regarding the power controls, each HVDC link’s converter station contains a dividing circuit comprising a power calculation device and a high gain working amplifier. In most cases, a single master controller installed at just one converter station is meant to handle the transfer on both sides of the two converter stations of the current order to the pole controls. The mechanism of multiplying voltage and current from both poles ensures power monitoring. Right after the completion of this process, the power returns to the controller. During startup, limits are generally built-in to avoid exceeding current orders [110].

2.3.8.3.9 Frequency Controls

A transmission grid's frequency control interconnected with another larger one via an HVDC link is carried out utilizing an intermediate-circuit frequency feedback loop to allow the more extensive network's necessary power change to influence the smaller one. The Gotland link’s control system provides a typical example of frequency controls. This power system provides a specific example of

frequency controls as its original configuration contains a synchronous compensator. The structure of this network was only used with the DC link. Likewise, the DC line's terminals were exploited in frequency control when its rated power was equal to or higher than the AC grids' operating generators to which the DC line was connected [110].

2.3.9 Harmonics and Filters

Usually, a conventional two-terminal LCC HVDC unit is composed of 12-pulse converters. Each converter comprises two coupled series 6-pulse bridges whose transformer windings are connected in Y-Y and Δ - Δ with a 30-degree phase difference. The addition of DC voltages is done to neutralize much of the ripple. On the AC side of the converter, the current from AC sources is non-sinusoidal. Its waveform is generally rectangular, especially for valve side windings connected in Y. The AC current's rectangular signal includes harmonics, of which only the fundamental takes the sinusoidal shape [121]. Converters can therefore be considered as another instability source in HVDC links. DC and AC harmonics, due to Line-Commutated Converters, are often injected into the DC and AC systems, respectively. Usually, injecting harmonics into the power system presents several problems [48, 110]. These are listed below [48]:

- Telephone interference
- Excessive power losses and resulting heat in system-related devices and capacitors
- Overvoltage due to resonances
- Instability of converter controls specifically with IPC scheme based-firing pulse generation
- Ripple control mechanism interference

Due to the drawback of converters often generating current and voltage harmonics, AC and DC filters' implementation is necessary to filter them out. The most commonly used are bandpass (turned) and high pass filters as they also provide reactive power compensation [48].

2.3.9.1 Characteristic Harmonics

The induced harmonics have an order depending on the pulse number describing the corresponding HVDC converter [122]. In general, this number of pulses is referred to as the number of non-simultaneous commutations per fundamental frequency cycle. Ideally, a pulse number p converter induces pk order voltage's characteristic harmonics on its DC side and $pk \pm 1$ order current harmonics on its AC side (e.g., k is an integer) [18]. 12-pulse converters' AC side harmonics typically are 11th, 13th, 23th, 25th, etc. However, the DC side harmonics usually are 12th and 24th on the DC side [121]. For the derivation of harmonic characteristics, the following assumptions should be taken into consideration [18, 110]:

- The Supply voltages comprise the fundamental frequency
- The direct current time response is constant, i.e., with zero frequency elements

- The valve conduction begins at equivalent time intervals.
- The similarity of commutation reactance per phase

2.3.9.1.1 DC Side Harmonics

Typically, a 6-pulse three-phase bridge configuration's harmonics' order is $N=6k$. Consider the waveforms displayed in Figure 2-14, reflecting a 6-pulse converter's voltage and current with α and μ representing the delay and commutation overlap angles. By considering the time reference's value at the crossing of the voltage waveforms, the output of the DC voltage can be expressed as follows [18, 110]:

- For $0 < \omega t < \alpha$

$$V_D = \sqrt{2}V_C \cos\left(\omega t + \frac{\pi}{6}\right) \quad 2.12$$

- For $\alpha < \omega t < \alpha + \mu$

$$V_D = \sqrt{2}V_C \cos\left(\omega t + \frac{\pi}{6}\right) + \frac{\sqrt{2}}{2}V_C \sin(\omega t) - \frac{\sqrt{6}}{2}V_C \cos(\omega t) \quad 2.13$$

- For $\alpha + \mu < \omega t < \pi/3$

$$V_D = \sqrt{2}V_C \cos\left(\omega t - \frac{\pi}{6}\right) \quad 2.14$$

Equation (2-15), elaborated from Fourier Analysis, helps calculate harmonic voltages' RMS magnitudes.

$$V_N = \frac{V_{C0}}{\sqrt{2}(N^2-1)} \left\{ \begin{array}{l} \left((N^2-1) \cos^2 \left[(N-1) \frac{\mu}{2} \right] + (N+1) \cos^2 \left[(N-1) \frac{\mu}{2} \right] \right)^{\frac{1}{2}} \\ -2(N-1)(N+1) \cos \left[(N+1) \frac{\mu}{2} \right] \cos \left[(N-1) \frac{\mu}{2} \right] \cos(2\alpha + \mu) \end{array} \right\} \quad 2.15$$

Considering $\alpha = 0$ and $\mu = 0$, equation (2.16) represents the nth harmonic's relative value deduced from equation (2.15).

$$\frac{V_{N0}}{V_{C0}} = \frac{\sqrt{2}}{(N^2-1)} \square \frac{\sqrt{2}}{N^2} \quad 2.16$$

Usually, as the firing angle (α) increase induces harmonics' growth, and for $\alpha = \pi/2$ and $\mu = 0$. Therefore, the nth harmonic's value becomes:

$$\frac{V_{N0}}{V_{C0}} = \frac{\sqrt{2}N}{(N^2 - 1)} \square \frac{\sqrt{2}}{N^2} \quad 2.17$$

2.3.9.1.2 AC Side Harmonics

Figure 2-27 displays the converter transformer's primary current when connected in star-star and star-delta modes. For the star-star connected converter transformer with zero commutation reactance (See Figure 2-27 (a)), the ideal current waveform is illustrated as follows [110]:

- For $-\pi/3 < \omega t < \pi/3$

$$i = I_D \quad 2.18$$

- For $-2\pi/3 < \omega t < -\pi/3$ and $\pi/3 < \omega t < 2\pi/3$

$$i = 0 \quad 2.19$$

- $\pi < \omega t < -2\pi/3$ and $2\pi/3 < \omega t < \pi$

$$i = -I_D \quad 2.20$$

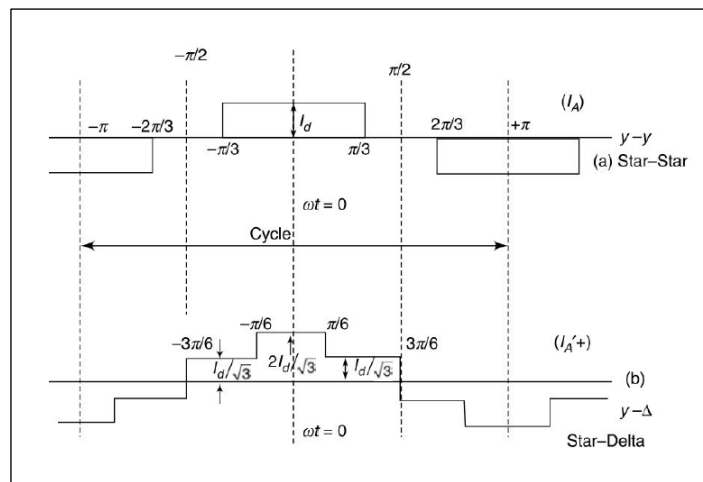


Figure 2-27: Converter transformer primary side's phase currents waveforms [18]

The Fourier series for this current waveform is described in equation (2.21), which shows that the harmonics of orders $(6k-1)$ rotate in the positive sequence. In contrast, those of orders $(6k+1)$ rotate in the negative sequence [18, 110].

$$i = \frac{2\sqrt{3}}{\pi} I_D \left[\cos(\omega t) - \frac{1}{5} \cos(5\omega t) + \frac{1}{7} \cos(7\omega t) - \frac{1}{11} \cos(11\omega t) + \dots \right] \quad 2.21$$

Therefore, the order of the above equation's characteristic harmonic is $N=6k \pm 1$ or $6k \pm 1$, and the magnitude of the N th harmonic is given by:

$$i_N = \frac{\sqrt{6}}{N\pi} I_D \quad 2.22$$

And that of the fundamental is:

$$i_1 = \frac{\sqrt{6}}{\pi} I_D \quad 2.23$$

The Fourier analysis results conducted on the above equation culminated in the following equation:

$$i = \frac{2\sqrt{3}}{\pi} I_D \left[\cos(\omega t) + \frac{1}{5} \cos(5\omega t) - \frac{1}{7} \cos(7\omega t) - \frac{1}{11} \cos(11\omega t) + \dots \right] \quad 2.24$$

Except for negative θ for specific harmonics, the equations (2.21) and (2.24) are similar.

2.3.9.1.3 Harmonic Generation in 12-pulse Converters

Suppose two 6-pulse converters whose transformer windings are YY and Y Δ connected, respectively, are placed in series to form a 12-pulse converter as displayed in Figure 2-11 on the rectifier side. In that case, the AC system will only be subject to harmonics linked to $N=12k \pm 1$ [121]. The converter AC bus's net current, reflecting its two series-connected 6-pulse bridges' transformer windings' primary side, is given by the sum of both converter transformers' primary windings' line currents (this is, $I_{YA}+I_{Y\Delta}$). The following expression describes the Fourier component of this current is provided by [18]:

$$i_a = \frac{4\sqrt{3}I_d}{\pi} \left[\cos \omega t - \frac{1}{11} \cos(11\omega t) + \frac{1}{13} \cos(13\omega t) - \frac{1}{23} \cos(23\omega t) + \frac{1}{25} \cos(25\omega t) \dots \infty \right] \quad 2.25$$

Suppose the direct voltage at each 6-pulse bridge equals one-half the maximum 12-pulse converter's direct voltage, and the transformer's line current on the primary side is half that of the net AC current. In that case, the line current of the 12-pulse bridge will therefore be expressed as follows:

$$i_a = \frac{2\sqrt{3}I_d}{\pi} \left[\cos \omega t - \frac{\cos(11\omega t)}{11} + \frac{\cos(13\omega t)}{13} - \frac{\cos(23\omega t)}{23} + \frac{\cos(25\omega t)}{25} \dots \infty \right] \quad 2.26$$

Taking into account the AC line voltage and the no-load direct voltage, equation (2.26) can be expressed in the following way:

$$i_a = \frac{I_d V_{D0}}{\sqrt{3}V_{SL}} \left[\cos \theta - \frac{\cos(11\theta)}{11} + \frac{\cos(13\theta)}{13} - \frac{\cos(23\theta)}{23} + \frac{\cos(25\theta)}{25} \dots \infty \right] \quad 2.27$$

The exact value of the fundamental and harmonic currents will be from the above:

$$i_{10} = 2\sqrt{3}I_d \left(\frac{\sqrt{6}I_d}{\pi} RMS \right) \quad 2.28$$

$$I_{ho} = \frac{I_{10}}{h} \quad 2.29$$

The N shows the harmonic order in the equations, and 0 indicates that the commutation overlap angle is neglected ($\mu=0$).

2.3.9.2 Filter Design

The literature recommends two approaches in order to remove harmonics: increasing the converter's pulse number or completely using filters. From the converter operation's investigation, the literature reports that it is possible to significantly reduce the harmonics accessing the AC system by simply augmenting its number of phases. This consideration sufficiently proves that a six-pulse converter is more sensitive than a 12-pulse converter to the risk of harmonics. A converter can potentially have up to 108 pulses. With this pulse number, the converter design typically involves costly transformers. Thus, the configuration of a 12-pulse converter is commonly most preferred [18].

Furthermore, installing AC harmonic filters on the HVDC link's terminals meets two objectives: compensating for the total or limited reactive power absorbed by the HVDC converter and minimizing current distortion due to HVDC-converter harmonics. Their generally low impedance, including inductive and capacitive characteristics, makes them resonate at specific frequencies, giving them great significance in specifying the converter AC busbar's transient overvoltage properties. Delays in the ignition angle and commutation process in HVDC converters are usually the cause of harmonics' occurrence in the form of non-sinusoidal currents [121, 123]. Moreover, telephone interference is one of the critical factors involving filter design. It is typically presented as the current harmonic distortion aforementioned, telephone influence factor (TIF), telephone harmonic form factor (THFF), and IT product [18]. References [18, 121] provide more details on telephone interference. The selection of

filter types for removing AC harmonics in power systems depends primarily on specifications for harmonics' order to be suppressed. A filter designed to remove harmonics to a particular target resonant frequency will eliminate all harmonics of frequencies above the threshold [123]. Figure 2-28 illustrates the types of AC filters the power system commonly uses for harmonic suppression:

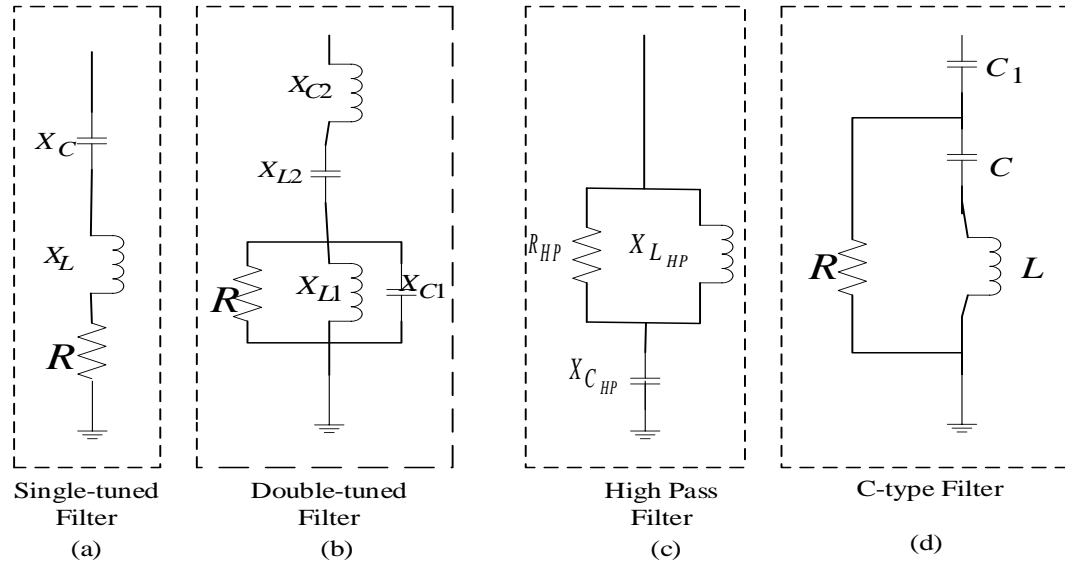


Figure 2-28: AC Filter Configuration [124, 125]

2.3.9.2.1 Single-Tuned Filters

Figure 2-28 (a) displays the equivalent circuit of a single-tuned filter. This filter's configuration represents an LC circuit in series with the inductor's parasitic resistance [104]. Its low investment costs and commonly low power losses at the fundamental frequency make it one of the most widely used harmonic filtering devices. It has a satisfactory impact on the tuning frequency due to its typically zero impedance. Its downside is its tendency to generate resonance frequencies lower than its specific frequency [126]. Their essential purpose is to suppress low-order harmonics, i.e., the 11th and the 13th harmonics in a 12-pulse converter [104]. To hold the cost down, engineers prefer using a double-tuned filter to suppress the 11th and 13th harmonics as its structure contains two single-tuned filters. A high-pass filter for removing 23rd harmonics order and higher is generally provided to resolve problems associated with telephone interference [104, 126]. Parameters such as the order of the harmonic current requiring filtering, the filter's nominal reactive power, and quality factor are needed to build a single-tuned filter. The designer should also know the phase-to-phase voltage and the system's rated frequency at the PCC. The equations below offer the procedure for obtaining parameters of a single-tuned filter [123, 125].

Considering the filter-rated reactive power, Q_{MVAR} , and the line-to-line voltage V_{LL} , equation (2.30) illustrates the filter capacitance.

$$C_{sf} = \frac{Q_{MVAR}}{2\pi f_0 V_{LL}^2} \quad 2.30$$

Given f_0 as the system's nominal frequency and h_p the harmonic order of the filter, equation (2.31) establishes the relationship between these two parameters and the filter's inductance and capacitance.

$$L_{sf} = \left(\frac{1}{2\pi f_0 h_p C_{sf}} \right)^2 \times C_{sf} \quad 2.31$$

The following relation illustrates the filter's resistance calculation knowing the quality factor and its inductance obtained from the preceding equation [125]:

$$R_{sf} = \frac{2\pi f_0 L_{sf}}{Q_F} = \frac{X_{L_{sf}}}{Q_F} \quad 2.32$$

Where,

$$X_{C_{sf}} = \frac{1}{2\pi f_0 C_{sf}}$$

$$X_{L_{sf}} = 2\pi f_0 L_{sf}$$

f_0 : The system rated frequency

Q_F represents the quality factor. It describes the series filter's bandwidth. In this case, it's determined by the ratio between the filter's reactance and resistance. Its conventional values concerning single-tuned filters range from 30 to 60 [125].

2.3.9.2.2 Double-Tuned Filter

Typically, a single-tuning filter removes harmonic distortion at a specific resonant frequency. In a 12-pulse configuration, multiple single-tuned filters can be used to reduce the harmonics of various orders. One of the major downsides of using single-tuned filters is the significant loss of power that usually results. A double-tuned filter allows reducing the harmonics of two distinct resonant frequencies. It is better to use a double-tuned filter because it drastically reduces power losses and minimizes the cost compared to two equivalent single-tuned filters. Figure 2-29 shows the configuration of an equivalent circuit of two single-tuned filters (see Figure 2-29 (a)) and the resulting double-tuned filter (see Figure 2-29 (b)) [124]. There are several configurations of double-tuned filters. However, the conventional double-tuned filter has the elements shown in Figure 28 (b) except resistance. The filter is considered of the damped type by taking into account the resistance component [127]. Several methods exist for

designing double-tuned filters or determining their parameters [127, 128]. It is possible to obtain the double-tuned filter parameters from the equivalent circuit of two single-tuned filters.

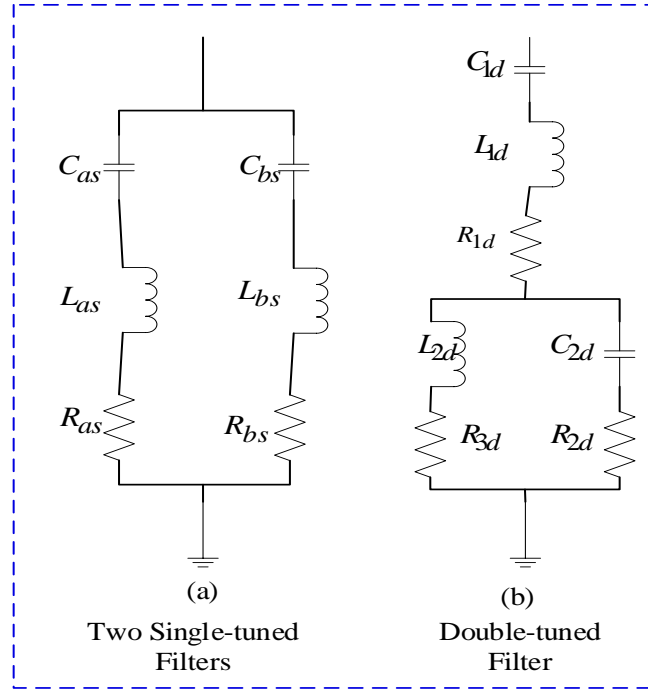


Figure 2-29: Double-tuned filter design [124]

Equations (2.33) to (2.37) represent approximate relationships allowing the connection between the double-tuned filter's parameters and those of an equivalent circuit of two single-tuned filters (see Figure 2.29) [124].

$$C_{1d} = C_{as} + C_{bs} \quad 2.33$$

$$C_{2d} = \frac{C_{as} C_{bs} (C_{as} + C_{bs})(L_{as} + L_{bs})^2}{(L_{as} C_{as} - L_{bs} C_{bs})} \quad 2.34$$

$$L_{1d} = \frac{(L_{as} \times L_{bs})}{(L_{as} + L_{bs})} \quad 2.35$$

$$L_{2d} = \frac{(L_{as} C_{as} - L_{bs} C_{bs})^2}{(L_{as} + L_{bs})(C_{as} + C_{bs})^2} \quad 2.36$$

$$R_{2d} = R_{as} \left[\frac{m^2 (1 - y^2)}{(1 + my^2)(1 + y^2)} \right] + R_{bs} \left[\frac{1 - y^2}{(1 + my^2)(1 + y^2)} \right] + R_{1d} \left[\frac{(1 - y^2)(1 - my^2)}{(1 + y^2)(1 + my^2)} \right] \quad 2.37$$

These different approximations are conducted considering the omission of R_{ld} , obtained from the inductor's (i.e., L_{ld}) minimum resistances. High voltages are one of the essential applications of double-tuned filters.

Where,

$$m = \frac{C_{as}}{C_{bs}}$$

$$y = \sqrt{\frac{C_{bs} L_{bs}}{C_{as} L_{as}}}$$

2.3.9.2.3 Damped-Type Filters (High-Pass Filters)

The high-pass filters, namely second-order filters and type-C filters, are commonly used in power systems. Figures 2-28 (c) and (d) indicate the equivalent circuits of High-pass filters. Second-order high-pass filters' (see Figure 2-28 (c)) primary purpose is to remove characteristic and non-characteristic harmonics. The filters' implementation in power systems primarily focuses on high-order harmonics [121]. i.e., those beyond the single-tuned filter's order threshold [104, 129]. This implies that if a 12-pulse converter has tuned filters set up to remove the 11th and 13th harmonics, a second-order high-pass damped filter designed for the 24th order can eventually be provided, eliminating the 23rd and 25th harmonics [104]. C and L's series arrangement in the C-type filters produces a relatively low impedance at the fundamental frequency, making the device remarkably advantageous due to its considerably reduced power losses. Therefore, this advantage makes it a filter designed for eliminating low-order and high-frequency harmonics [121]. This is also because of the complete reduction of the fundamental current that passes through the parallel damping resistor [125].

- **Second-Order High-Pass Filter Design**

Figure 28 (c) illustrates the second-order high pass filter design. This filter configuration has a flat impedance feature for high-frequency applications. Its parameters are determined using the same procedure as that of a single-tuned filter. However, they have different impedance characteristics [125]. This high-pass filter's quality factor's standards vary from 1 to 10 for sufficient damping over a broad range of frequencies [104]. Compared to the single-tuned filter, the quality factor designed for this particular high-pass filter establishes a relationship between the three parameters of the filter's characteristic impedance. Equation (2.38) describes it.

$$R_{HP} = Q_F \sqrt{\frac{L_{HP}}{C_{HP}}} \tag{2.38}$$

▪ **C-type High-Pass Filter Design [125]**

Figure 2-28 (d) shows the equivalent circuit of the C-type Filter. The C-type filter's parameters derive from a series filter [125]. Figure 2.30 illustrates the configuration of the C-type filter and its corresponding series filter from which its parameters derive. The figure shows that the C-type filter has four parameters (i.e., R, L, C, and C₁) deduced from the single-tuned filter's equivalent circuit (i.e., C_S, L_S, and R_S). As in the previous cases, the necessary factors requiring the C-type filter's design are the filter's rated reactive power (Q_C), the quality factor (Q_F), the order of the harmonic current to be filtered (h_p), and the line-to-line voltage of the converter AC bus (V_{LL}).

The following steps should be taken into account for the design of the C-Type filter:

- Determine the parameters of the single-tuned filter, namely L_S and C_S
- Consider L=L_S
- Consider that C and C₁ are in a series connection and equivalent to C_S.

Equations (2.39) to (3.43) allow obtaining the C-type filter parameters based on the above assumptions.

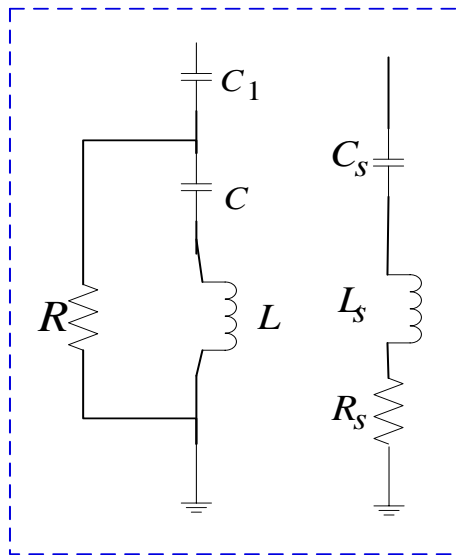


Figure 2-30: C-Type Filter Design [125]

Equation (3.39) gives the filter's inductance.

$$L_S = L = \frac{V_{LL}^2}{2\pi f_0 Q_{MVAR} (h_p - 1)} \quad 2.39$$

Equations (2.40) and (2.41) make it possible to determine C_S and C₁ from which C is obtained.

$$C_S = \frac{(h_p^2 - 1) Q_{MVAR}}{2\pi f_0 h_p^2 V_{LL}^2} \quad 2.40$$

$$C = \frac{Q_{MVAR}(h_{tp}^2 - 1)}{2\pi f_0 V_{LL}^2} \quad 2.41$$

Considering the third assumption, C can be determined as follows.

$$\frac{1}{C_s} = \frac{1}{C_1} + \frac{1}{C} \quad 2.42$$

Finally, equation (2.43) makes it possible to determine the filter's resistance.

$$R = \frac{Q_F V_{LL}^2}{h_{tp} Q_{MVAR}} \quad 2.43$$

2.3.10 Interactions Between AC and DC Systems

AC and DC systems' interactions are relatively complex and diverse [130]. Section 2.2.4.3 addressed this while discussing the UIF, one of the criteria for determining the risk of interaction between HVDC and turbogenerators. Also, the SCR-based approach and its derivatives are considered better ways of addressing this question [48, 121]. Figure 2-31 shows the generator-converter electrical coupling via an AC bus. SCR, in other words, determines the AC system's strength. As per [82], it is also described as the ratio between the AC bus's short-circuit level (SCL) and the DC link's nominal power. As the AC system is electrically coupled to the HVDC converter bus's AC side, the SCR can be determined utilizing the resulting Thevenin equivalent impedance.

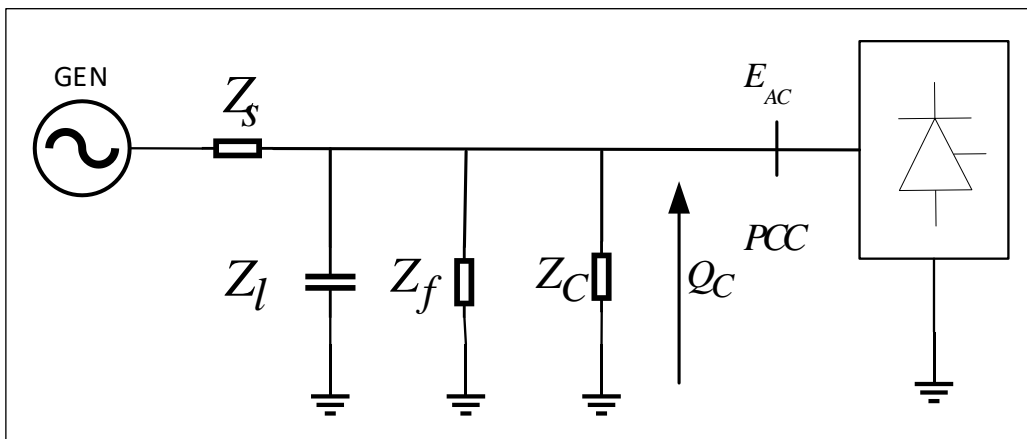


Figure 2-31: Converter and AC system [121]

The following equation represents the SCR:

$$SCR = \frac{SCL}{P_d} \quad 2.44$$

Where,

SCL: Short Circuit Level [MW]

P_d : Converter Rated Power [MW]

Based on the system displayed in Figure 2-31, the short-circuit level is described as the power generated when the converter terminals are shorted. The following equation can determine this:

$$SCL = \frac{E_{ac}^2}{Z_{ac}} \quad 2.45$$

By putting (2.30) into (2.31), the short-circuit ratio becomes:

$$SCR = \frac{E_{ac}^2}{P_d \cdot Z_{ac}} \quad 2.46$$

$$SCR = \frac{1}{Z_{ac}} Z_{base} \left(\frac{1}{Z_s} + \frac{1}{Z_l} \right) Z_{base} \quad 2.47$$

A high Thevenin impedance can lead to problems including harmonic resonances, voltage stability, dynamic overvoltage, and frequent commutation failure. The explanation is that high impedance limits the strength of the AC system. The higher the Thevenin impedance, the lower the stiffness of the AC bus. Furthermore, the capacitor bank and AC filters also generate reactive power to the converter AC bus. Because of these factors' impact, Equivalent Short-Circuit Ratio (ESCR) is preferably used to express the AC bus strength based on the reactive power effect induced by the shunt and capacitor filters on the converter AC bus. Therefore, equation (2.48) illustrates the resulting reactive power generated due to AC filters and the capacitor bank [121]:

$$Q_C = \frac{E_{ac}^2}{\frac{1}{Z_f} + \frac{1}{Z_C}} \quad 2.48$$

The induced ESCR is given by:

$$ESCR = \frac{SCL - Q_C}{P_d} \quad 2.49$$

Taking into account the Thevenin equivalent impedance in Figure 2-31 and the base impedance, the ESCR can be calculated as follows:

$$ESCR = \frac{1}{Z_e} Z_{base} = \left(\frac{1}{Z_s} + \frac{1}{Z_l} + \frac{1}{Z_f} + \frac{1}{Z_c} \right) Z_{base} \quad 2.50$$

Table 2-1 depicts the converter AC bus's classification concerning the SCR and ESCR levels.

Table 2-1: Classification of SCR and ESCR [131]

Stiffness	SCR	ESCR
Very low	$SCR \leq 2$	$ESCR \leq 1.5$
Low	$SCR \leq 3$	$ESCR \leq 2.5$
Moderate	$3 < SCR < 5$	$3 < ESCR < 4.5$
High	$SCR \geq 5$	$ESCR \geq 4.5$

HVDC controls have a meaningful influence when interacting with the AC system. HVDC links face severe performance issues for low and very low (E)SCR, which typically require the implementation of FACTS such as SVC or STATCOM to facilitate system operation[131]. In line with [104], very few HVDC systems operate with an SCR lower than 2.

2.3.11 Faults Management and HVDC System Protections

2.3.11.1 Introduction

Despite their control actions, it should be remembered that HVDC ties are not excluded from faults that might occur on AC busbars, the DC overhead line (or cables), or conversion transformers. The faults occurring in an HVDC system have adverse effects on its performance. Under this condition, the power system's shutdown may happen if appropriate control measures are not implemented within the time frame [107]. The controls of thyristor-based HVDC systems are usually able to address transient faults in a minimal period. Different automatic circuit breakers typically respond if the fault lasts for a long time in an HVDC system. These automatic circuit breakers provided within the HVDC link's control system usually act as a final protective measure, i.e., they offer complete system isolation when HVDC controls cannot maintain the occurrence of significant disturbances[104]. Most faults in an HVDC link are self-cleared or cleared by an appropriate converter control action. Therefore, the HVDC tie's fault-clearance aspect based on its controls and circuit breakers or relays when necessary is a massive advantage over AC systems. During significant disturbances, an immediate network's isolating response is required from circuit-breakers until the fault's effect is cleared [109].

2.3.11.2 Type of Faults and Nature

2.3.11.2.1 DC Line Fault

DC faults generally occur on the HVDC transmission line (cable) as a single line-to-ground fault [16]. In either positive or negative regions, thyristor-based HVDC systems (LCC HVDC) can quickly regulate the direct voltage and thus respond to the DC line's fault per fault monitoring strategies. These fault monitoring strategies intend to lower the direct current's amplitude and modify its related direct voltage's polarity [104]. Moreover, when a DC fault occurs, the rectifier controls the DC current that eventually feeds the fault condition to its reference value (i.e., 1 pu). This condition involves a significant decrease in the rectifier station's direct voltage and, therefore, an increase in its corresponding firing angle while remaining below 90° [105].

Furthermore, on the inverter station's side, the reference direct current's amount decreases by a level equivalent to the rectifier's reference current, from which the current margin is subtracted [16]. This condition makes the inverter enter the CC mode of operation by lowering its ignition angle. Nevertheless, to maintain the same direct current's polarity, the inverter station's direct voltage's polarity varies, and its corresponding ignition angle takes a value of less than 90° [103, 104].

2.3.11.2.2 AC Line Fault

AC faults generally occur on the rectifier or inverter end. During a fault's occurrence at either HVDC tie's terminal, an alternating voltage's depression induces direct current reduction. When the HVDC system encounters an AC fault, the three-phase alternating voltage drops to a minimum value that depends on the AC fault's impedance [132].

Indeed, when a fault occurs on the rectifier end, its controller's central role is to avoid small drops in AC voltage. HVDC controls act in such a way as to drop the rectifier station's firing angle up to a degree compatible with working conditions, avoiding AC voltage drop in the incident of AC fault [110]. If the rectifier AC voltage is depressed further, it will cause both DC current and DC voltage reduction, ultimately switching the inverter to CC control mode. Therefore, the HVDC system will operate with an inverter reference DC current equivalent to 85-95% of the rated DC current. Due to the high demand for reactive power and the large firing angle required when the rectifier's AC (or DC) voltage is exclusively low, operating at 90 percent of DC current would be inappropriate. Therefore, a special VDCOL is essential to minimize the direct current for smaller direct voltages [103, 104].

2.3.11.2.3 Commutation Failure

This fault, commonly encountered on inverter stations, results from the incoming valves' failures due, in particular, to insufficient extinction time to induce the DC line current's regulation before the commutating voltage polarity reversal [110]. The commutation failure is not directly related to the converter valves' malfunction but rather to the external AC and DC conditions. It is mainly caused by a converter station's short circuit occurrence resulting in either a late ignition process, an increased DC current, or low AC voltage [16]. For minimal voltage disturbances, inverter stations under fault conditions usually result in commutation failure [104].

In line with [109], a commutation failure is a DC short circuit that principally happens on the inverter side and temporally induces HVDC power transfer losses. However, commutation failure doesn't generate short-circuit on the converters' AC sides. An immediate increase in gamma on the inverter side and a progressive increase in power to normal operating conditions are often initiated after HVDC controls (i.e., VDCOL) detect commutation failure. After a successful recovery, the inverter gamma gradually (slowly) returns to the nominal values [133].

2.4 Conclusion

Chapter Two focused on developing a substantial literature review. The main elements of the chapter focused on subsynchronous resonance and HVDC links. The chapter has discussed the type of SSR, its different analysis methods, and its causes in power systems. The transmission line series capacitor is practically the primary source of the SSR occurrence. Regarding the types of SSR, we have seen three: induction generator effect, torsional interaction, and transient torque amplification. Depending on their features, the three kinds of SSR often affect the power system operation and reliability. However, only the transient torque amplification was investigated in this thesis, mainly because the phenomenon results from significant disturbances.

This chapter indicated that the controls of the power system's components, such as FACTS, HVDC, PSS, AVR, and governor, typically interact with the TG's shaft in a frequency range regarding SSR sources beyond the series capacitors coinciding with its natural frequencies. For SSR analysis methods, the chapter pointed out that the most used are the Eigenvalue method, the frequency scanning method, and EMTP. Discussions on SSR ended with a series of cases illustrating SSR mitigation techniques. Special mention was made of points of instability in power systems equipped with HVDC links. The chapter reported SSR cases found in HVDC systems under radial and parallel AC-DC systems and discussed SSR suppression techniques in both cases.

The other important part of this chapter focused on the general design of the HVDC system. The chapter presented a solid overview of the HVDC theory, i.e., its entire architecture, its advantages compared

with the AC system, its different topologies, its various components, the principle of its converters, including the current commutation process, its controls, AC harmonics, including the mitigation means and, finally, its interactions with the TG shaft. The research undertaken in this chapter's development has contributed significantly to understanding how the HVDC system works in PSCAD and the design of its parts necessary for proper operation. The HVDC control system is among the most relevant points described in this chapter. The system consists of a rectifier operating in constant current mode and an inverter in constant voltage mode. The chapter provided detailed discussions of these controllers to set up supplementary controls further to stabilize the turbine-generator shaft's torsional oscillations. The chapter has also provided essential tools for calculating the inverter AC bus's stiffness. The bus stiffness significantly impacts the response in torsional oscillations of a parallel AC-DC system comprising series capacitors. As a result, this chapter has contributed substantially to this research methodology and provided a complete understanding of SSR and HVDC systems. It allowed us to uncover the origins of SSR/SSO in parallel AC-DC systems and mitigation strategies. This was of paramount importance in the methodology to achieve the objectives of this research.

CHAPTER THREE: POWER SYSTEM MODELLING

3.1 Introduction

The under-investigation power grid's mathematical equations must be properly understood for an in-depth analysis of the adverse torsional oscillations to which the power system is subjected. The study system initially consists of a series-compensated transmission line adopted from IEEE FBM [11] for SSR analysis with the parameters given in Appendix A. The second system consists of an LCC HVDC with the parameters given in [97] and is built by modifying the Cigre Benchmark Model in PSCAD. This chapter aims to model the different elements making up the power system. These are practically synchronous machines, turbogenerator shaft systems, the series compensated AC line, the excitation system, and HVDC system. The nonlinear modeling equations are developed depending on the two-axis synchronous machine model known as d-q axis reference frame.

Using differential equations previously described in earlier studies has helped achieve this chapter's goals. The objective of this chapter and our major contribution is to model the HVDC and AC systems separately and determine the critical points of compensation inducing the instability of the torsional dynamics of the TG shaft of the First Benchmark Model. This chapter also modeled the excitation system, describing the IEEE constant excitation and the IEEE ST1A systems. It's worth noting that the fundamental IEEE FBM generator and multi-mass parameters that led to critical operating points were extracted from [11] using its constant excitation system. Constant excitation was also used in Chapter 4 with the parameters given in [134]. However, in Chapter 5, we extended Chapter 4 using an IEEE ST1A to study the impact of HVDC controllers and PSS on TG torsional dynamics. After this separate modeling of the two systems, the next chapter will look at torsional oscillations in a parallel AC-DC system connected to an inverter bus of moderate stiffness.

3.2 Synchronous machine

A synchronous machine is typically used as a synchronous motor or generator. As a generator, its role consists of converting mechanical power into electrical. However, it acts as a motor in reverse operation. The two devices operate according to the electromagnetic induction principle, which consists of a change in the magnetic field depending on the induced voltage [22]. A turbine usually drives a synchronous machine as an AC generator to enable energy conversion. The synchronous machine is the world's foremost electric power generator. The windings form a group of inductively coupled electrical circuits in a polyphase synchronous machine. Some of them rotate compared to each other such that the mutual inductances vary. Typically, the general equations developed for the various windings' flux linkages apply to steady-state and transient analysis [3, 22].

3.2.1 Description of the synchronous machine

Beyond the variety of components inside a synchronous machine, two main parts are considered ferromagnetic structures. The fixed part called the stator or armature as a hollow cylinder contains longitudinal slots wherein the armature windings' coils are connected. In the synchronous generator mode of operation, the current intended for the electric load is ordinarily carried by the stator windings. In contrast, they receive current from a power source while operating as a synchronous motor. On the other hand, the rotor is a shaft-mounted dynamic component rotating relative to the stator, which is relatively hollow. Typically referred to as field winding, the rotor winding is provided with a direct current from an exciter mounted practically along the same shaft or another direct current source whose connection to the windings is made via brush bearings on the slip ring [3, 22].

3.2.2 Synchronous Machine Modelling

The synchronous machine model used here conforms to that of the IEEE FBM. The internal circuit of the IEEE FBM's generator has three stator windings and one rotor winding. According to the quadratic representation of this synchronous generator's internal circuit, two stator windings refer to the d-axis while only one refers to the q-axis. The rotor winding is generally known as field winding, as mentioned earlier. In this case, the per-unit equations governing the synchronous generator's stator windings' working principle are, as in most cases, represented in the rotor reference frame, that is to say, using the quadratic d-q axes [22]. Expressing time "t" in "seconds," the rated angular frequency " ω_0 " of the synchronous machine as "376,9912 radian/second", and d-q axis quantities in per-unit, the machine's stator voltages can be expressed as [40]:

$$v_d = \frac{1}{\omega_0} \frac{d\lambda_d}{dt} + \lambda_q \frac{\omega}{\omega_0} - R_a i_q \quad 3.1$$

$$v_q = \frac{1}{\omega_0} \frac{d\lambda_q}{dt} + \lambda_d \frac{\omega}{\omega_0} - R_a i_d \quad 3.2$$

Where i_d and i_q represent the quadratic stator currents, R_a describes the stator's per-phase resistance, ω defines the angular frequency variable. λ_d and λ_q . Illustrate the quadratic flux linkages. Moreover, the main synchronous generator's rotor per-unit quantities are given in equations (3-1) and (3-2) [3, 40] as:

$$0 = \frac{1}{\omega_0} \frac{d\lambda_{1q}}{dt} + R_{1q} i_{1q} \quad 3.3$$

$$0 = \frac{1}{\omega_0} \frac{d\lambda_{2q}}{dt} + R_{2q} i_{2q} \quad 3.4$$

$$0 = \frac{1}{\omega_0} \frac{d\lambda_{1d}}{dt} + R_{1d} i_{1d} \quad 3.5$$

$$v_{fd} = \frac{1}{\omega_0} \frac{d\lambda_{fd}}{dt} + R_{fd} i_{fd} \quad 3.6$$

In the above equations, i_{1d} , i_{1q} , i_{2q} define the rotor reference frame's quadratic currents and the flux linkage by λ_{1d} , λ_{1q} , and λ_{2q} . The rotor circuit's resistances are illustrated as R_{1q} , R_{2q} . Regarding the quadratic field quantities, v_{fd} , λ_{fd} , i_{fd} , R_{fd} , are field voltage, field flux, field current, and field resistance. Furthermore, the generator stator's flux linkage equations depending on the rotor reference frame, respectively, are [44, 135]:

$$\lambda_d = -L_d i_d + L_{ad} i_{fd} + L_{ad} i_{1d} \quad 3.7$$

$$\lambda_q = -L_q i_q + L_{aq} i_{1d} + L_{aq} i_{1q} \quad 3.8$$

The quadratic flux linkages' formulas of the rotor can be seen from (3.9) to (3.12) [44, 135]:

$$\lambda_{fd} = L_{ff} i_{fd} + L_{ad} i_{1d} - L_{ad} i_{1d} \quad 3.9$$

$$\lambda_{1d} = L_{ad} i_{fd} + L_{11} i_{1d} - L_{ad} i_{1d} \quad 3.10$$

$$\lambda_{1q} = L_{11} i_{1q} + L_{aq} i_{2d} - L_{ad} i_{1q} \quad 3.11$$

$$\lambda_{2q} = L_{aq} i_{1q} + L_{22} i_{2q} - L_{aq} i_{1q} \quad 3.12$$

The per-unit electrical torque is given by [40]:

$$T_e = \lambda_d i_d - \lambda_q i_q \quad 3.13$$

(3.14) and (3.15) represent the generator's swing equation [3]:

$$\frac{d\omega}{dt} = \frac{1}{2H} (T_m - T_e - K_D (\omega - 1)) \quad 3.14$$

$$\frac{d\delta}{dt} = \omega_0 (\omega - 1) \quad 3.15$$

In the above formulas, the mechanical torque is denoted by T_m , the damping torque by K_D , the system's inertial constant by H , and the rotor angle by δ . The overall differential equations that describe the synchronous machine performance under transient conditions are expressed by the following matrix [44]:

$$\left[\frac{dX_{syn}}{dt} \right] = [At_{syn}] [X_{syn}] + [Bt_{syn}] \begin{bmatrix} V_{td} \\ V_{tq} \\ v_{fd} \end{bmatrix} \quad 3.16$$

$$[X_{syn}] = [i_d \quad i_q \quad i_{fd} \quad i_{1q} \quad i_{1d} \quad i_{2q}] \quad 3.17$$

Where,

$$[At_{syn}] = [L]^{-1} [Q_t] \quad 3.18$$

$$[Bt_{syn}] = [L]^{-1} [R_t] \quad 3.19$$

$$[L] = \begin{bmatrix} -L_d & 0 & L_{ad} & 0 & L_{ad} & 0 \\ 0 & -L_q & 0 & L_{aq} & 0 & L_{aq} \\ -L_{ad} & 0 & L_{ffd} & 0 & L_{ad} & 0 \\ 0 & -L_{aq} & 0 & L_{11q} & 0 & L_{aq} \\ -L_{aq} & 0 & L_{ad} & 0 & L_{11d} & 0 \\ 0 & -L_{aq} & 0 & L_{aq} & 0 & L_{22q} \end{bmatrix} \quad 3.20$$

$$[Q_t] = \begin{bmatrix} \omega_0 R_a & -\omega L_q & 0 & -\omega L_{aq} & 0 & \omega L_{aq} \\ \omega L_d & \omega_0 R_a & -\omega L_{ad} & 0 & -\omega L_{ad} & 0 \\ 0 & 0 & -\omega_0 R_{fd} & 0 & 0 & 0 \\ 0 & 0 & 0 & -\omega_0 R_{1q} & 0 & 0 \\ 0 & 0 & 0 & 0 & -\omega_0 R_{1d} & 0 \\ 0 & 0 & 0 & 0 & 0 & -\omega_0 R_{2q} \end{bmatrix} \quad 3.21$$

$$[R_t] = \begin{bmatrix} \omega_0 & 0 & 0 \\ 0 & \omega_0 & 0 \\ 0 & 0 & \omega_0 \\ 0 & 0 & 0 \\ 0 & 0 & 0 \\ 0 & 0 & 0 \end{bmatrix} \quad 3.22$$

The subscript (^T) denotes the matrix's transpose in these above equations, and (⁻¹) indicates the inverse matrix. Therefore, the linearization and arrangement of (3-16) lead to the following equation [44]:

$$\left[\frac{d\Delta X_{syn}}{dt} \right] = [A_{syn}] [\Delta X_{syn}] + [B_{syn}] [\Delta U_{syn}] \quad 3.23$$

Where,

$$[\Delta X_{syn}] = [\Delta i_d \quad \Delta i_q \quad \Delta i_{fd} \quad \Delta i_{1q} \quad \Delta i_{1d} \quad \Delta i_{2q}] \quad 3.24$$

$$[\Delta U_{syn}] = [\Delta V_{1d} \quad \Delta V_{1q} \quad \Delta V_{e_{fd}} \quad \Delta \omega]^T \quad 3.25$$

$$[A_{syn}] = [L]^{-1} [Q] \quad 3.26$$

$$[B_{syn}] = [L]^{-1} [R] \quad 3.27$$

$$[Q] = \omega_0 \begin{bmatrix} R_a & -L_q & 0 & L_{aq} & 0 & L_{aq} \\ L_d & R_a & -L_{ad} & 0 & -L_{ad} & 0 \\ 0 & 0 & -R_{fd} & 0 & 0 & 0 \\ 0 & 0 & 0 & -R_{1q} & 0 & 0 \\ 0 & 0 & 0 & 0 & -R_{1d} & 0 \\ 0 & 0 & 0 & 0 & 0 & -R_{2q} \end{bmatrix} \quad 3.28$$

$$[R] = \begin{bmatrix} \omega_0 & 0 & 0 & \lambda_{q0} \\ 0 & \omega_0 & 0 & -\lambda_{d0} \\ 0 & 0 & \omega_0 & 0 \\ 0 & 0 & 0 & 0 \\ 0 & 0 & 0 & 0 \\ 0 & 0 & 0 & 0 \end{bmatrix} \quad 3.29$$

3.3 Turbogenerator Mechanical System Modelling

Figure 3-1 displays the shaft sections of the IEEE FBM. Six lumped masses reflecting the turbines' different phases constitute the IEEE FBM turbogenerator shaft's mechanical architecture. Therefore, the shaft's whole structure consists of an exciter (EX), a generator (GEN), two low-pressure turbines, namely LPA and LPB, and a high-pressure turbine (IP). The PSCAD software contains the prototype of IEEE FBM, mainly used to analyze the time domain response of different case studies. The natural frequencies calculated using the model below are usually lower than the grid's nominal frequency. Low-frequency modes, resulting from short-circuit, typically induce shaft stresses. Hence, the model below makes it possible to determine the shaft sections' behavior [11, 136].

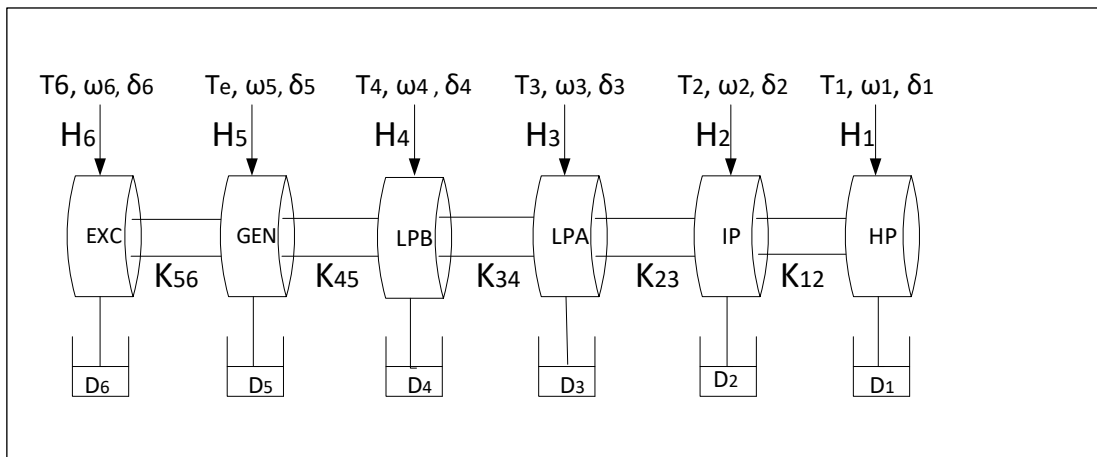


Figure 3-1: IEEE FBM Shaft's mechanical system [40]

Consider $i \geq 0$ and $j \geq 0$. D_i represents the internal self-damping of a mass (i), D_{ij} represents the external mutual damping between two masses (i, j) and is expressed in sec^{-1} or rad/sec , $K_{i,j}$ illustrates the spring constant of shaft sections measured in pu or $pu \cdot torque/rad$, δ_i describes the rotor angle of mass (i) measured in electrical radians, T_i are the electrical torque of masse (i), and ω_i the angular velocity of mass (i) (i.e., the angular speed of i^{th} shaft section). The mechanism can be considered as a mass-spring-damper system. The torque developed in each turbine's shaft section can

be described via differential equations. Therefore, the formulas of the i^{th} mass linked by the flexible shaft's sections to mass $(i-1)$ and mass $(i+1)$ are expressed in equations (3.30) to (3.35) [3] :

$$\begin{aligned} \frac{2H}{\omega_0} \frac{d^2 \delta_i}{dt^2} + D_i \frac{d\delta_i}{dt} + D_{i,i-1} \left(\frac{d\delta_i}{dt} - \frac{d\delta_{i-1}}{dt} \right) + D_{i,i+1} \left(\frac{d\delta_i}{dt} - \frac{d\delta_{i+1}}{dt} \right) \\ + K_{i,i-1} (\delta_i - \delta_{i-1}) + K_{i,i+1} (\delta_i - \delta_{i+1}) = T_{mi} - T_{ei} = T_a \end{aligned} \quad 3.30$$

The differential equation representing the generator's motion is given by:

$$\begin{aligned} \frac{2H}{\omega_0} \frac{d^2 \delta_5}{dt^2} + D_5 \frac{d\delta_5}{dt} + D_{5,4} \left(\frac{d\delta_5}{dt} - \frac{d\delta_4}{dt} \right) + D_{5,6} \left(\frac{d\delta_5}{dt} - \frac{d\delta_6}{dt} \right) \\ + K_{5,4} (\delta_5 - \delta_4) + K_{5,6} (\delta_5 - \delta_6) = T_{m5} - T_{e5} = T_5 \end{aligned} \quad 3.31$$

The differential equation representing the LPB's motion is given by:

$$\begin{aligned} \frac{2H}{\omega_0} \frac{d^2 \delta_4}{dt^2} + D_4 \frac{d\delta_4}{dt} + D_{4,3} \left(\frac{d\delta_4}{dt} - \frac{d\delta_3}{dt} \right) + D_{4,5} \left(\frac{d\delta_4}{dt} - \frac{d\delta_5}{dt} \right) \\ + K_{4,3} (\delta_4 - \delta_3) + K_{4,5} (\delta_4 - \delta_5) = T_{m4} - T_{e4} = T_4 \end{aligned} \quad 3.32$$

The differential equation representing the LPA's motion is given by

$$\begin{aligned} \frac{2H}{\omega_0} \frac{d^2 \delta_3}{dt^2} + D_3 \frac{d\delta_3}{dt} + D_{3,2} \left(\frac{d\delta_3}{dt} - \frac{d\delta_2}{dt} \right) + D_{3,4} \left(\frac{d\delta_3}{dt} - \frac{d\delta_4}{dt} \right) \\ + K_{3,2} (\delta_3 - \delta_2) + K_{3,4} (\delta_3 - \delta_4) = T_{m3} - T_{e3} = T_3 \end{aligned} \quad 3.33$$

The differential equation representing the IP's motion is given by:

$$\begin{aligned} \frac{2H}{\omega_0} \frac{d^2 \delta_2}{dt^2} + D_2 \frac{d\delta_2}{dt} + D_{2,1} \left(\frac{d\delta_2}{dt} - \frac{d\delta_1}{dt} \right) + D_{2,3} \left(\frac{d\delta_2}{dt} - \frac{d\delta_3}{dt} \right) \\ + K_{2,1} (\delta_2 - \delta_1) + K_{2,3} (\delta_2 - \delta_3) = T_{m2} - T_{e2} = T_2 \end{aligned} \quad 3.34$$

The differential equation representing HP's motion is given by:

$$\frac{2H}{\omega_0} \frac{d^2 \delta_1}{dt^2} + D_1 \frac{d\delta_1}{dt} + D_{1,2} \left(\frac{d\delta_1}{dt} - \frac{d\delta_2}{dt} \right) + K_{1,2} (\delta_1 - \delta_2) = T_{m1} - T_{e1} = T_1 \quad 3.35$$

The formula that expresses the relationship linking the mechanical power and the mechanical torque of the i^{th} masse is given by:

$$\Delta P_{mi} = T_{mi} \frac{\omega_i}{\omega_0} \quad 3.36$$

After initialization, (3.36) can be rewritten as:

$$\Delta P_{mi} = T_{m0} \frac{\Delta \omega_i}{\omega_0} + T_{mi} \quad 3.37$$

Where T_{m0} is the initial torque developed.

The turbogenerator mechanical system's state equation can be summarized as follows:

$$\dot{X}_m = [A_m][X_m] + [B_{m1}]\Delta P_m + [B_{me}]\Delta T_e \quad 3.38$$

Where,

$$X_m = [\delta_6 \quad \delta_5 \quad \delta_4 \quad \delta_3 \quad \delta_2 \quad \delta_1 \quad \Delta \omega_6 \quad \Delta \omega_5 \quad \Delta \omega_4 \quad \Delta \omega_3 \quad \Delta \omega_2 \quad \Delta \omega_1] \quad 3.39$$

$$[A_m] = \begin{bmatrix} 0_{6 \times 6} & I_{6 \times 6} \\ A_{21} & A_{22} \end{bmatrix} \quad 3.40$$

$$[A_{m21}] = \begin{bmatrix} -\frac{K_{6,5}}{2H_6} & \frac{K_{6,5}}{2H_6} & 0 & 0 & 0 & 0 \\ \frac{K_{6,5}}{2H_5} & -\frac{K_{6,5} - K_{5,4}}{2H_5} & \frac{K_{5,4}}{2H_5} & 0 & 0 & 0 \\ 0 & \frac{K_{5,4}}{2H_4} & -\frac{K_{5,4} - K_{4,3}}{2H_4} & \frac{K_{4,3}}{2H_4} & 0 & 0 \\ 0 & 0 & \frac{K_{4,3}}{2H_3} & -\frac{K_{4,3} - K_{3,2}}{2H_3} & \frac{K_{3,2}}{2H_3} & 0 \\ 0 & 0 & 0 & \frac{K_{3,2}}{2H_2} & -\frac{K_{3,2} - K_{2,1}}{2H_2} & \frac{K_{2,1}}{2H_2} \\ 0 & 0 & 0 & 0 & \frac{K_{2,1}}{2H_1} & -\frac{K_{2,1}}{2H_1} \end{bmatrix} \quad 3.41$$

$$[A_{m22}] = \begin{bmatrix} \frac{D_6 + D_{6,5}}{2H_6} & \frac{D_{6,5}}{2H_6} & 0 & 0 & 0 & 0 \\ \frac{D_{6,5}}{2H_5} & \frac{D_5 + D_{6,5} + D_{5,4}}{2H_5} & \frac{D_{5,4}}{2H_5} & 0 & 0 & 0 \\ 0 & \frac{D_{5,4}}{2H_4} & \frac{D_4 + T_{m0}F_4 + D_{5,4} + D_{4,3}}{2H_4} & \frac{D_{4,3}}{2H_4} & 0 & 0 \\ 0 & 0 & \frac{D_{4,3}}{2H_3} & \frac{D_3 + T_{m0}F_3 + D_{4,3} + D_{3,2}}{2H_3} & \frac{D_{3,2}}{2H_3} & 0 \\ 0 & 0 & 0 & \frac{D_{3,2}}{2H_2} & \frac{D_2 + T_{m0}F_2 + D_{3,2} + D_{2,1}}{2H_2} & 0 \\ 0 & 0 & 0 & 0 & \frac{D_{2,1}}{2H_1} & \frac{D_1 + T_{m0}F_1 + D_{2,1}}{2H_1} \end{bmatrix} \quad 3.42$$

Where,

F_1, F_2, F_3, F_4 indicate the fraction of each turbine's mechanical power. A single turbine's section's torque depends on the dynamics and the control mechanism governing the whole steam turbine. Literature has reported standards of F_1, F_2, F_3, F_4 depending on various cases of SSR study methods. Some of them can be found in references [3, 28, 137].

3.4 Excitation Control System

3.4.1 Introduction

The excitation mechanism's primary purpose is to supply the direct current to the generator's field winding. Power system stability is maintained due to the excitation system's regulation of the field voltage "Efd," thereby operating on the field current. The field voltage regulation is achieved via an automatic voltage regulator to see the voltage reference's setpoint (Et) across the generator stator terminals reached, thereby achieving the swing mode's stability. Usually, to maintain the successful stability of "mode 0," also known as "swing mode," excitation systems are provided with the possibility to enhance the power grid's operation and stability by adding a Power System Stabilizer (PSS) that acts as a supplementary excitation control device [5, 134].

3.4.2 Constant Excitation System (Manual Excitation)

The PSCAD model of the IEEE FBM comprises a constant excitation device, also known as a manual excitation system. This excitation mechanism's primary purpose is to hold the field voltage (E_{fd}) at a constant value defined during the initialization of the generator parameters. What makes this excitation system different is its non-use of AVR and the generator voltage's reliance on variations of the system's operating conditions [3, 5].

3.4.3 Static Excitation (IEEE Type ST1A)

There are several types of excitation systems. However, given the parameters, the static excitation system known as IEEE Type ST1A provided in Figures 3-2 will be used in this work [134]. The IEEE type ST1A excitation control system regulation is obtained via a controlled rectifier. This excitation system allows its maximum voltage to be linked to the generator terminal's voltage. Moreover, based on the selection of gain (K_A), the excitation system's input-output relationship is assumed to be linear; however, it is generally influenced by the firing angle on the rectifier side [134]. In line with [3, 5], the simplified configuration of the type IEEE ST1A mechanism displayed in Figure 3.2 comprises a transient gain reduction (TGR), an exciter, and a voltage transducer delay.

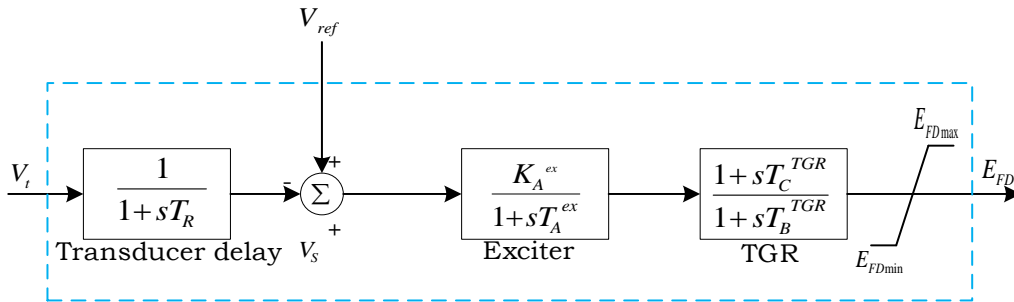


Figure 3-2: IEEE Type ST1A's Simplified Model [3]

3.4.4 Power System Stabilizer

Figure 3-3 displays the simplified PSS configuration used in this work. The PSS operates with the typical lead-lag structure. Its working principle is such that it uses the rotor speed deviation based-input signal ($\Delta\omega$), thereby inducing a component in phase with the electromagnetic torque (ΔT_e) and supplying the supplementary stabilizing signal (V_S) to the excitation control device [134]. The typical lead-lag structure comprises three main sections: a gain section (K_{PSS}), a signal washout section, and the phase compensation section made up of two stages ($m=2$). The phase compensation section's primary purpose is to offset the phase difference for both input and output signals by providing suitable phase-lead characteristics. The signal washout section acts as a high pass filter using a time constant varying from 1 sec to 10 sec. However, this time constant should be set to a high enough value within its typical range to allow unchanged passage of the input signals produced based on oscillations [138].

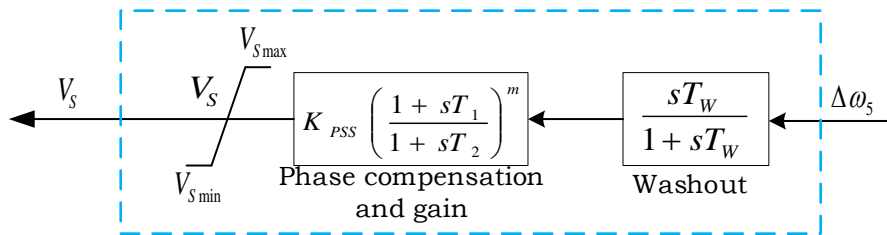


Figure 3-3: Power System Stabilizer's Simplified Block [3]

3.5 Series compensated transmission line model

Figure 3-4 represents the simplified SMIB representation of IEEE FBM. The differential equations governing the system are taken from [11]. The system is represented by an RLC branch where X_L illustrates the transmission line's total inductive reactance; X_C defines the capacitive reactance. R represents the transmission line's series resistance.[135].

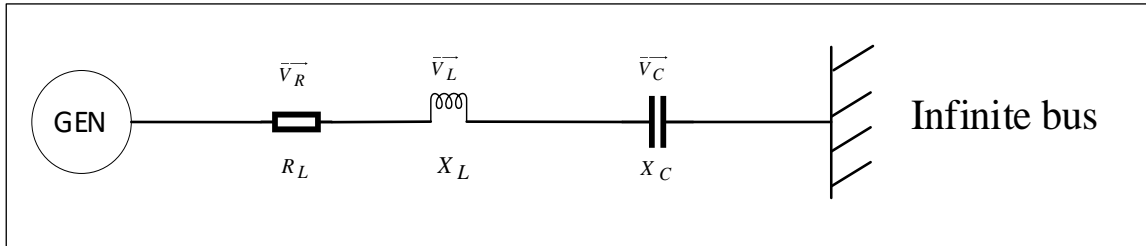


Figure 3-4: SMIB based- RLC Circuit [135]

Equation (3.43) defines the transmission line's series resistance voltage:

$$\begin{bmatrix} v_{Rd} \\ v_{Rq} \end{bmatrix} = \begin{bmatrix} R_L & 0 \\ 0 & R_L \end{bmatrix} \begin{bmatrix} i_d \\ i_q \end{bmatrix} \quad 3.43$$

The voltage across the inductance is given by:

$$\begin{bmatrix} v_{Ld} \\ v_{Lq} \end{bmatrix} = \begin{bmatrix} 0 & -\frac{\omega}{\omega_0} X \\ \frac{\omega}{\omega_0} X_L & 0 \end{bmatrix} \begin{bmatrix} i_d \\ i_q \end{bmatrix} + \begin{bmatrix} \frac{X_L}{\omega_0} & 0 \\ 0 & \frac{X_L}{\omega_0} \end{bmatrix} \begin{bmatrix} \frac{di_d}{dt} \\ \frac{di_q}{dt} \end{bmatrix} \quad 3.44$$

The voltage across the capacitor:

$$\begin{bmatrix} \frac{dv_{Cd}}{dt} \\ \frac{dv_{Cq}}{dt} \end{bmatrix} = \begin{bmatrix} \omega_0 & 0 \\ 0 & \omega_0 X_C \end{bmatrix} \begin{bmatrix} i_d \\ i_q \end{bmatrix} + \begin{bmatrix} 0 & \omega \\ -\omega & 0 \end{bmatrix} \begin{bmatrix} v_{Cd} \\ v_{Cq} \end{bmatrix} \quad 3.45$$

Equation (3.46) represents the overall transmission line's differential equation.

$$\begin{bmatrix} \frac{dv_{Cd}}{dt} \\ \frac{dv_{Cq}}{dt} \\ v_{id} \\ v_{iq} \end{bmatrix} = [Att] \begin{bmatrix} v_{Cd} \\ v_{Cq} \end{bmatrix} + [Rt_1] \begin{bmatrix} \frac{di_d}{dt} \\ \frac{di_q}{dt} \end{bmatrix} + [Rt_2] \begin{bmatrix} i_d \\ i_q \end{bmatrix} + [Btt] [v_b] \quad 3.46$$

Where,

$$[Btt] = \begin{bmatrix} 0 \\ 0 \\ \sin \delta \\ \cos \delta \end{bmatrix} \quad 3.47$$

$$[Rt_2] = \begin{bmatrix} \omega_0 X_C & 0 \\ 0 & \omega_0 X_C \\ R_L & -\frac{\omega X_L}{\omega_0} \\ \frac{\omega X_L}{\omega_0} & 0 \end{bmatrix} \quad 3.48$$

$$[Att] = \begin{bmatrix} 0 & \omega \\ -\omega & 0 \\ 1 & 0 \\ 0 & 1 \end{bmatrix} \quad 3.49$$

$$[Rt_1] = \begin{bmatrix} 0 & 0 \\ 0 & 0 \\ \frac{X_L}{\omega_0} & 0 \\ 0 & \frac{X_L}{\omega_0} \end{bmatrix} \quad 3.50$$

Equation (3.51) describes the transmission line's linearized form of equation (3.46) gives:

$$\begin{bmatrix} \frac{d\Delta v_{Cd}}{dt} \\ \frac{d\Delta v_{Cq}}{dt} \\ \Delta v_{id} \\ \Delta v_{iq} \end{bmatrix} = [At] \begin{bmatrix} \Delta v_{Cd} \\ \Delta v_{Cq} \end{bmatrix} + [R_1] \begin{bmatrix} \frac{d\Delta i_d}{dt} \\ \frac{d\Delta i_q}{dt} \end{bmatrix} + [R_2] \begin{bmatrix} \Delta i_d \\ \Delta i_q \end{bmatrix} + [Bt] \begin{bmatrix} \Delta \omega \\ \Delta \delta \end{bmatrix} \quad 3.51$$

Where,

$$[At] = \begin{bmatrix} 0 & \omega_0 \\ -\omega_0 & 0 \\ 1 & 1 \\ 0 & 1 \end{bmatrix} \quad 3.52$$

$$[R_1] = \begin{bmatrix} 0 & 0 \\ 0 & 0 \\ \frac{X_L}{\omega_0} & 0 \\ 0 & \frac{X_L}{\omega_0} \end{bmatrix} \quad 3.53$$

$$[R_2] = \begin{bmatrix} \omega_0 X_C & 0 \\ 0 & \omega_0 X_C \\ R_L & -X_L \\ X_L & 0 \end{bmatrix} \quad 3.54$$

$$[Bt] = \begin{bmatrix} v_{Cq0} & 0 \\ -v_{Cd0} & 0 \\ -\frac{\omega}{\omega_0} i_{q0} & v_{bq0} \\ \frac{\omega}{\omega_0} i_{d0} & v_{bq0} \end{bmatrix} \quad 3.55$$

3.5.1 Preliminary Eigenvalue Analysis for the IEEE FBM with Fixed Capacitors

The major problem in a transmission line equipped with a series capacitor is the compensation's critical operating points. The TG shaft's dynamics react negatively when the transmission line's compensation degree is critical [80]. Therefore, significant negative damping resulting from AC line compensation's necessary level will be observed in the TG shaft's torsional dynamic response [5]. Several authors have investigated IEEE FBM's critical operating points [18, 19]. Figure 3-5 displays the IEEE transmission line's compensation percentage, the reactances of which result in subsynchronous resonance [23, 40].

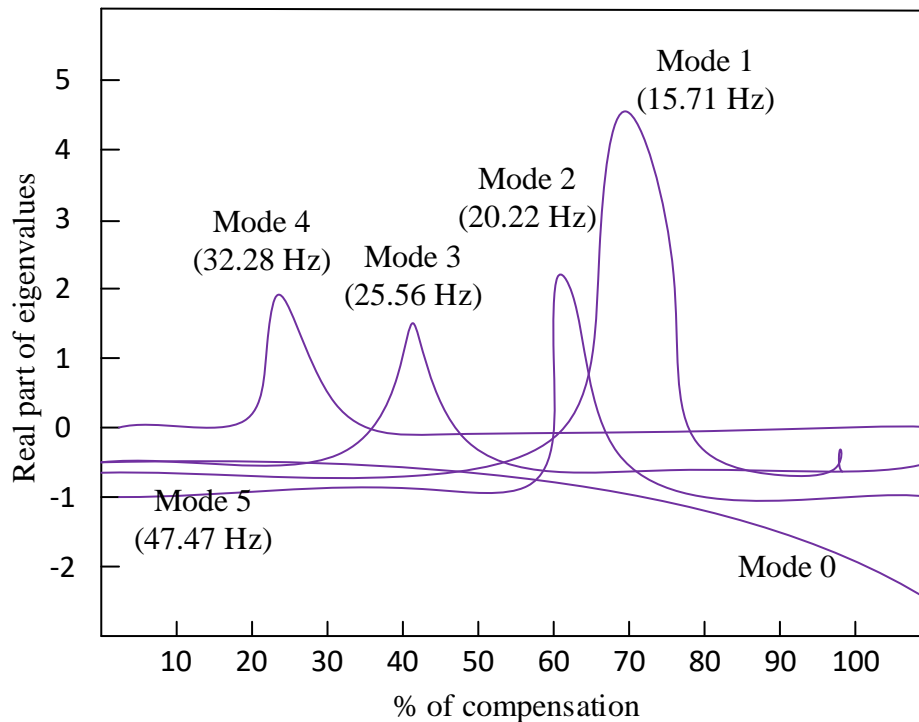


Figure 3-5: The real part of SSR eigenvalues as a function of the series-compensated transmission line's compensation percentage [44, 135].

3.6 LCC HVDC Modelling

3.6.1 12-pulse LCC Modeling

The HVDC system modeling equations were briefly introduced in Section 2.3.7 when discussing the converter commutation process. However, the discussion was more focused on a 6-pulse line commutated converter. Since the HVDC link of this research works with 12-pulse converters, the equations reported in section 2.7.3 will consider factor B, indicating the number of 6-pulse series converters. Therefore, equations (3.56) and (3.57) represent the modeling equations governing the rectifier and inverter stations, taking into account B [104]. The different factors describing these equations are specified in the same manner as in Chapter Two, i.e., the ideal no-load voltage, line-to-line converter's voltages, the rectifier's firing angle, and inverter's ignition angle.

$$V_{Rdc} = B \frac{3\sqrt{2}}{\pi} V_{LL_R} \cos \alpha_R - B \frac{3}{\pi} \omega L_{t_R} I_{dc} \quad 3.56$$

$$V_{Rdc} = B \frac{3\sqrt{2}}{\pi} V_{LL_I} \cos \alpha_I + B \frac{3}{\pi} \omega L_{t_I} I_{dc} \quad 3.57$$

Where [116],

V_{LL_R} : RMS line-to-line rectifier station's voltage.

V_{LL_I} : RMS line-to-line inverter station's voltage.

α_R : The rectifier station's firing angle.

α_I : The inverter station's advanced ignition angle.

L_{t_R} : The rectifier station's commutative inductance.

L_{t_I} : The inverter station's commutative inductance.

3.6.2 DC line modeling

The HVDC system's transmission line is represented by a T-model, as shown in Figure 3-6. The DC line has two series impedances on both sides and a lumped charging capacitance at its midpoint. The inductive reactance of the transmission line typically plays the role of a smoothing reactor. The inductive reactance of the transmission line typically plays the role of a smoothing reactor. Formula (3,58), (3,59), and (3,60) illustrate the DC line's modeling equations resulting from the system's T-model representation [40, 107].

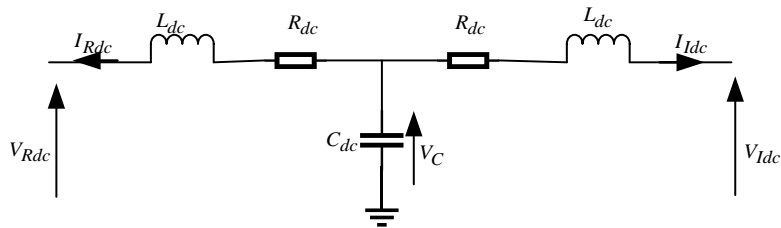


Figure 3-6: DC line T-model [40]

$$V_{Rdc} = R_{dc} I_{Rdc} + L_{dc} \frac{dI_{Rdc}}{dt} + V_C \quad 3.58$$

$$V_{Idc} = R_{dc} I_{Idc} + L_{dc} \frac{dI_{Idc}}{dt} - V_C \quad 3.59$$

$$\frac{dV_C}{dt} = \frac{1}{C_{dc}} (I_{Rdc} - I_{Idc}) \quad 3.60$$

The equivalent DC current's expression in the line is shown in (3.61):

$$I_{dc} = \frac{V_{Rdc} - V_{Idc}}{R_{dc}} \quad 3.61$$

V_{Rdc} and V_{Idc} were given in (3.56) and (3.57), respectively.

Equations (3.62) to (3.66) represent the small-signal mathematical model of the HVDC link's equivalent circuit displayed in Figure 3-6. Equations (3.56) to (3.60) helped deduce them [102, 116]

$$L_{Rdc} \frac{d\Delta I_{Rdc}}{dt} = \Delta V_{Rdc} - (R_{Rdc} + K_1 X_{CR}) \Delta I_{Rdc} - \Delta V_{Cdc} \quad 3.62$$

$$L_{Idc} \frac{d\Delta I_{Idc}}{dt} = \Delta V_{Idc} - (R_{Idc} + K_1 X_{CI}) \Delta I_{Idc} + \Delta V_{Cdc} \quad 3.63$$

$$\frac{d\Delta V_{Cdc}}{dt} = \frac{1}{C_{dc}} \left(\frac{dI_{Rdc}}{dt} - \frac{dI_{Idc}}{dt} \right) \quad 3.64$$

$$\frac{dV_{Rdc}}{dt} = (K_1 \cos \alpha_{R0}) \frac{dV_{LLR}}{dt} - (K_1 V_{LLR0} \sin \alpha_{R0}) \frac{d\alpha_R}{dt} \quad 3.65$$

$$\frac{dV_{Idc}}{dt} = (K_1 \cos \alpha_{I0}) \frac{dV_{LLI}}{dt} - (K_1 V_{LLI0} \sin \alpha_{I0}) \frac{d\alpha_I}{dt} \quad 3.66$$

Where,

$$\left\{ \begin{array}{l} X_{CR} = \omega L_{t_R} \\ X_{CI} = \omega L_{t_I} \\ K_1 = \frac{3\sqrt{6}}{\pi} \\ K_2 = \frac{3}{\pi} \end{array} \right. \quad 3.67$$

With,

X_{CR} is the rectifier station's commutative reactance

X_{CI} is the inverter station's commutative reactance

3.6.3 Active and Reactive Power

Since the two converters' power losses are primarily insignificant, the AC power is typically considered equal to the DC power. Formula (3.68) represents this equality between the powers on the converter's AC and DC sides.

$$3V_{LN_x} I_{LN_x} \cos \phi_x = V_{dc_x} I_{dc_x} \quad 3.68$$

Where

x : The quantity on either the rectifier side or the inverter side.

ϕ_i : The lagging angle of the line-to-neutral current relative to the voltage.

Considering the influence of both the firing angle and extinction angle on the AC commutation process from one thyristor to another, the DC voltage can be expressed as follows:

$$V_{dc_x} = \frac{3\sqrt{6}}{2\pi} V_{LN_x} (\cos \alpha + \cos \gamma) \quad 3.69$$

Where,

$$\gamma = \alpha + \mu$$

Let's assume AC harmonics are infinitely reduced. This assumption makes it possible to take into account only the fundamental of the current. Therefore, the expression (3.70) represents the resulting RMS phase current, depending on the DC current.

$$I_{LN_x} = \frac{\sqrt{6}}{\pi} I_{dc_x} \quad 3.70$$

By putting equations (3.70) and (3.69) into (3.68), the power factor can be expressed as follows:

$$\cos \phi_x = \frac{(\cos \alpha + \cos \gamma)}{2} \quad 3.71$$

Therefore, expression (3.72) represents reactive power

$$Q_x = V_{dc_x} I_{dc_x} \tan \phi \quad 3.72$$

From equation (3.68), the deduced active power is given by:

$$P_x = V_{dc_x} I_{dc_x} \quad 3.73$$

More details about differential modeling equations of the HVDC tie can be found in the literature [116]

3.6.4 Experimental Viewpoint

Since the LCC HVDC system must be added in parallel with a resonant AC line subject to severe transient conditions, it is essential to assess its controls-based efficiency under different operating conditions. This work's HVDC scheme has the parameters listed in [97]. The 12-pulse monopolar HVDC design in Figure 3-7 aims to be incorporated in parallel with the modified IEEE FBM [11] with the parameters provided in Appendix A. The rectifier is under CC control mode, and the inverter is in CEA. The system uses equidistant pulse control (EPC) for the firing of thyristors and does not consider tap changer controls. Two three-phase voltage sources with the same characteristics as [97] were placed on either side of the rectifier and the inverter to test the HVDC performance. The transmission line's length is 276 miles (444 km), and the rated voltage is 500 kV (0.01Ω/Km). The three-phase rated power is fixed at 892.4 MVA, and the line-to-line AC voltages of the rectifier and inverter power sources are 539 kV and 477.8 kV, respectively. PSCAD Cigre Benchmark Model provides the current regulator parameters for the rectifier and inverter. We've considered the current regulators' gains equal to 5 ($K_{PIDR}=5$ and $K_{PIDI}=5$) [97]. Table 3.2 illustrates the current regulators' parameters.

Table 3-1: Current regulator parameters

Rectifier				Inverter			
K_R	T_R	U_{Rmax}	U_{Rmin}	K_I	T_I	U_{Imax}	U_{Imin}
5	0.0109	0.1	-0.1	5	0.0109	1.92	0.52

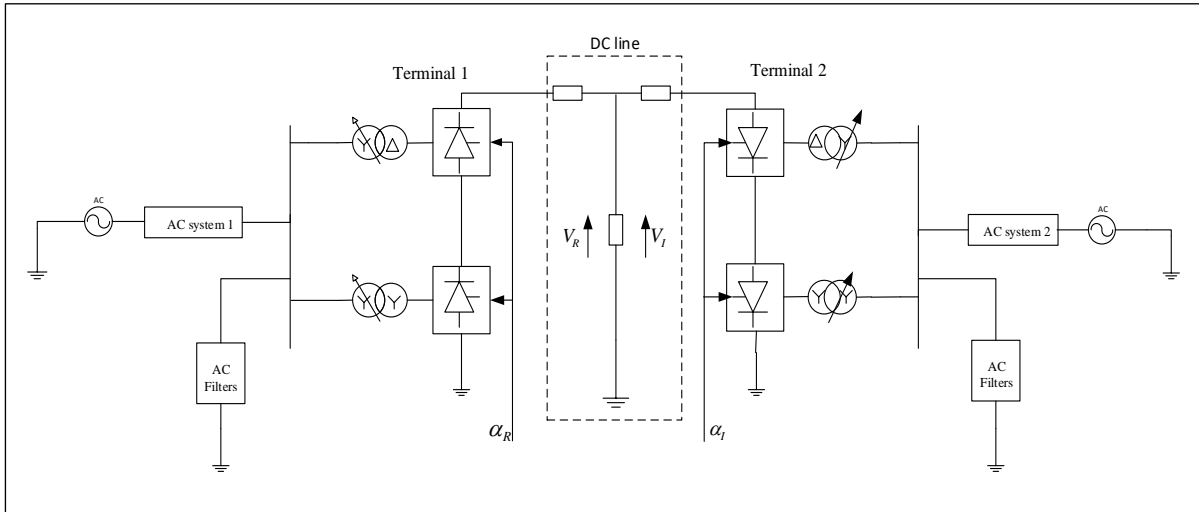


Figure 3-7: HVDC System Configuration [104]

As stated in the previous chapter, the converter is considered one of the most important HVDC link components. It can provide commutation voltage, suppress fault currents and overvoltage, reduce harmonic pollution produced by converters and ensure the electrical isolation between AC and DC systems [17]. The HVDC system uses 12-pulse converters (i.e., two 6-pulse converters connected in series) with two three-phase double winding transformers connected in Y / D and Y / Y, respectively. Additionally, the reactive power compensation system's configuration consists of capacitors and different parallel passive filters on the converters' AC side. Besides removing harmonics, the reactive power compensation devices on the converter's AC side typically provide reactive power since all AC filters' impedances are capacitive at power frequency [17]. Figure 3-7 shows that the reactive power compensation device consists of a capacitor bank, a low pass filter, and a high pass filter on both sides of the rectifier and inverter stations. Moreover, to avoid overvoltage damage and smooth the ripple of DC current on both sides of the rectifier and the inverter, smoothing reactors by which the converter outputs and the DC line are connected are used to perform this function. In this study, the value of 0.528 H is used as the transmission line's smoothing reactor.

3.6.4.1 Simulation and results

We used PSCAD software for the HVDC system's nonlinear modeling obtained by modifying the Cigre Benchmark Model test system based on the new system's parameters. We undertook four scenarios to assess the system response to major disturbances and the performance of converter controls. The first scenario observed the system's response under steady-state conditions. The second scenario was a 0.001 DC fault that lasted 75 ms and applied at 350 ms in the middle of the DC line. In the third scenario, We applied an AC fault of 1 Ω for 100ms at 500ms on the rectifier AC busbar. And the fourth scenario consisted of an AC fault of 0.001 Ω lasting 150 ms and applied at 600 ms on the inverter's AC busbar.

3.6.4.1.1 Study case 1: Steady-State Operation

For the steady-state system response, the simulation lasted 0.4 s and was captured from 0.2 to 0.6 s. Figures 3-8 and 3-9 illustrate the system response under steady-state conditions on the rectifier and inverter sides. Due to initial transients in the modified PSCAD model used, the system enters a steady state at approximately 0.3s on the rectifier side and 0.5s on the inverter side. The steady-state response is more sensitive on the inverter side since the modified CBM with its parameters was initially exposed to a three-phase AC fault on the inverter's AC bus. It can be seen that the findings meet the standards and proper HVDC performance under steady-state operation as discussed in [104, 107].

▪ Rectifier Side's Steady-State Response

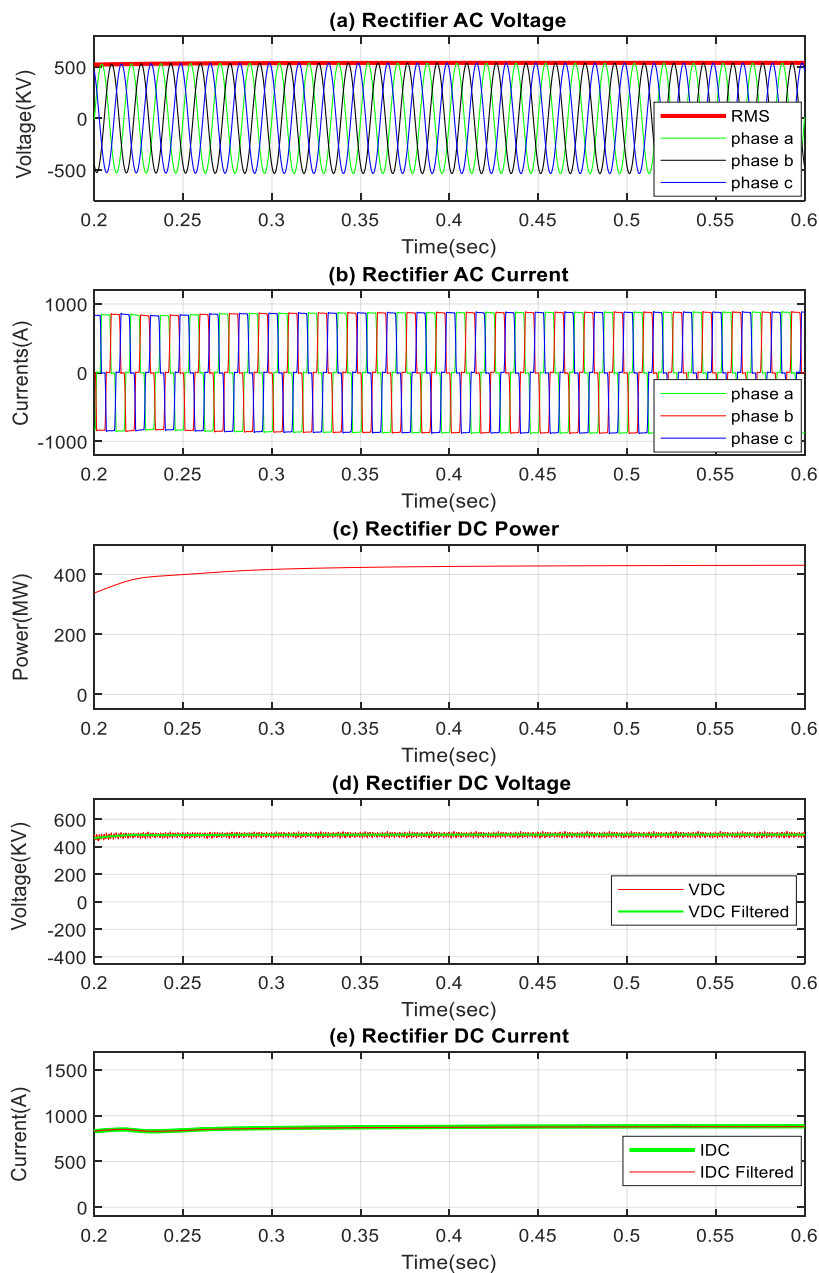


Figure 3-8: Rectifier Response Under Steady-State Operation (Case 1)

▪ **Inverter Side's Steady-State Response**

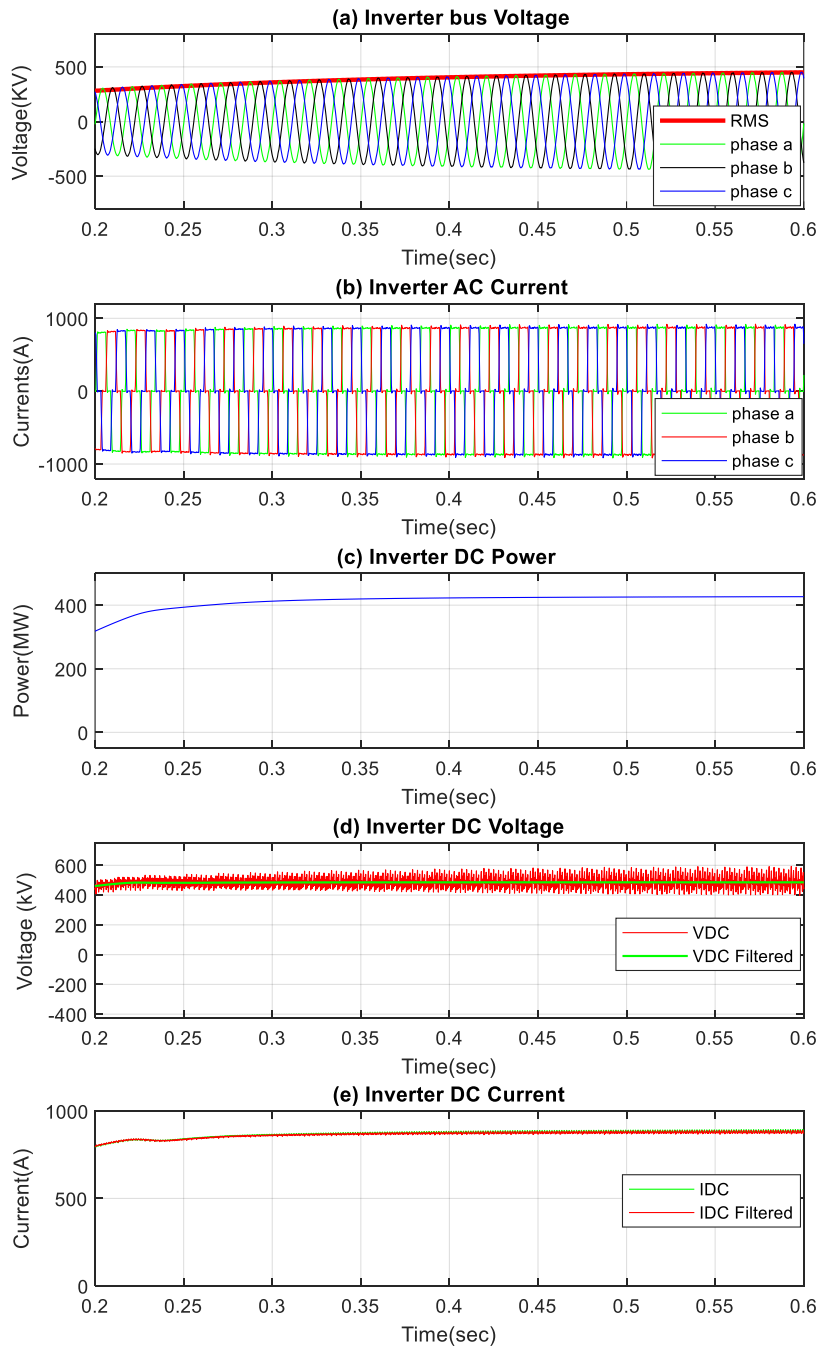


Figure 3-9: Inverter Response Under Steady-State Operation (Case 1)

3.6.4.1.2 Study case 2: DC line fault conditions

Figures 3-10 and 3-11 display the transient responses of the rectifier and inverter for a 0.001Ω DC fault applied on the middle of the DC line at 350 ms and lasting 75 ms. It can be observed via both figures that the Converter's AC voltages are not affected by DC fault. The DC fault impact is more effective on the inverter side than on the rectifier side; this is why the inverter should be equipped with a robust control strategy to sustain severe transient conditions. It can be observed that the inverter DC current

and DC voltage drop to zero when the DC fault occurs. An immediate DC voltage ramp is initiated after the fault clearance due to HVDC Controls. A regular operation is reached after 300 ms, the typical post-fault recovery time as per [104] for a DC system under transient conditions. It can be seen that the findings meet the standards and proper HVDC performance under DC line fault conditions as discussed in [104, 107].

▪ **Rectifier DC Fault Response**

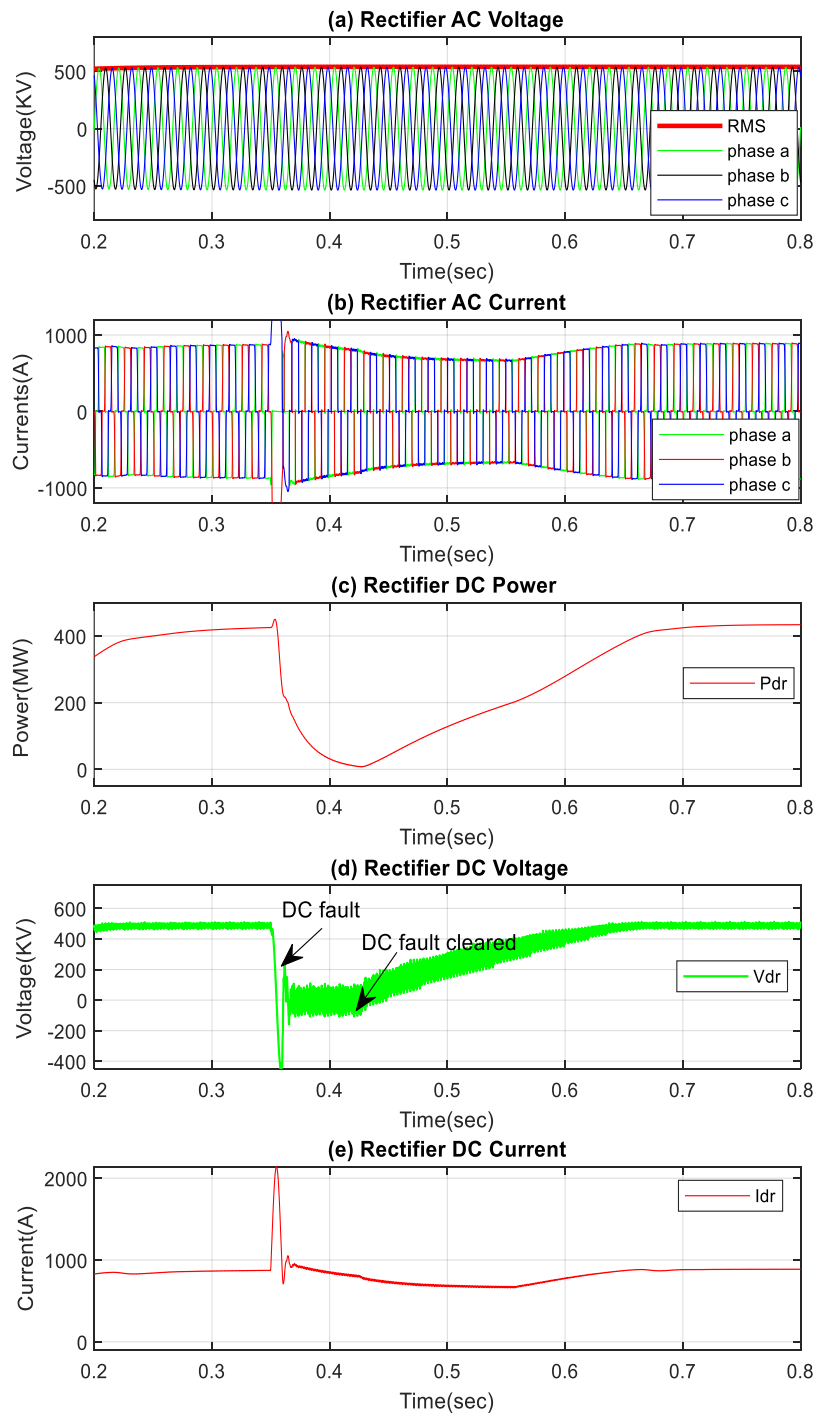


Figure 3-10: Rectifier Response Under DC Fault Condition (Case 2)

▪ **Inverter DC Fault Response**

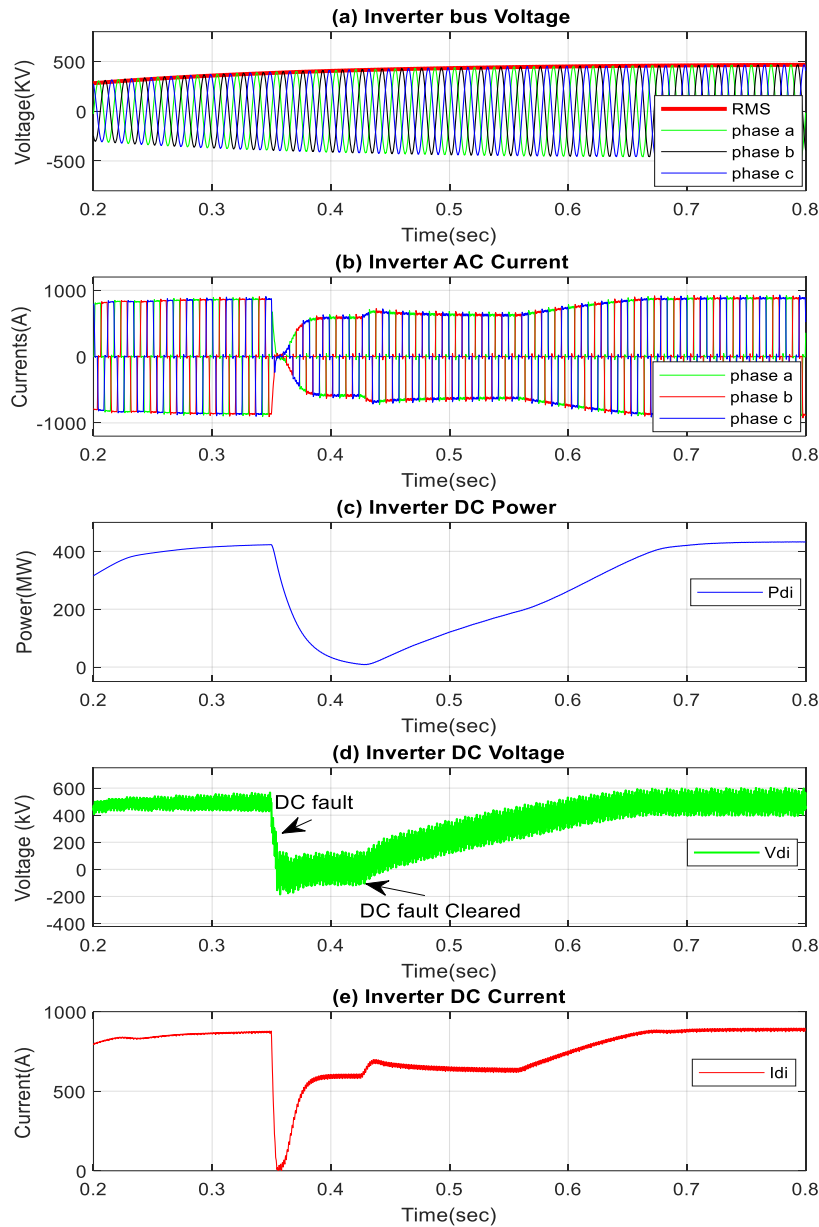


Figure 3-11: Inverter Response Under DC Fault Condition (Case 2)

3.6.4.1.3 **Study case 3: Rectifier AC fault Conditions**

Figures 3-12 and 3-13 show the system response when an AC fault of 1Ω lasting 100ms has been applied at 500ms to the AC rectifier busbar. Figure 4-12 (a) indicates that a voltage drop of around 50 percent on the rectifier busbar's AC voltage is detected at 500 ms and returns to its rated value at 600 ms. The RMS voltage also confirms this. The voltage decreases significantly by the same amount as the instantaneous voltages until it rises within the same period to its pre-fault value. It was also observed from Figure 3-12 (b) that when the HVDC controls detected the fault, there was an instantaneous AC current drop up to zero amps on the rectifier side. The A.C. current then increased and was kept below the DC current's rated value until it increased significantly (i.e., due to the firing angle increase) after

the fault clearing to maintain the system's steady-state value. This is also observed in the DC current Figure 3-12 (e), which fell to zero when the fault appeared and took a value lower than its nominal value until it increased significantly after the fault had been cleared to maintain its pre-fault value in a steady state. Figure 3-12 (c) shows that the DC power is gradually restored after the fault has been cleared.

▪ **Rectifier AC fault Conditions (Rectifier response)**

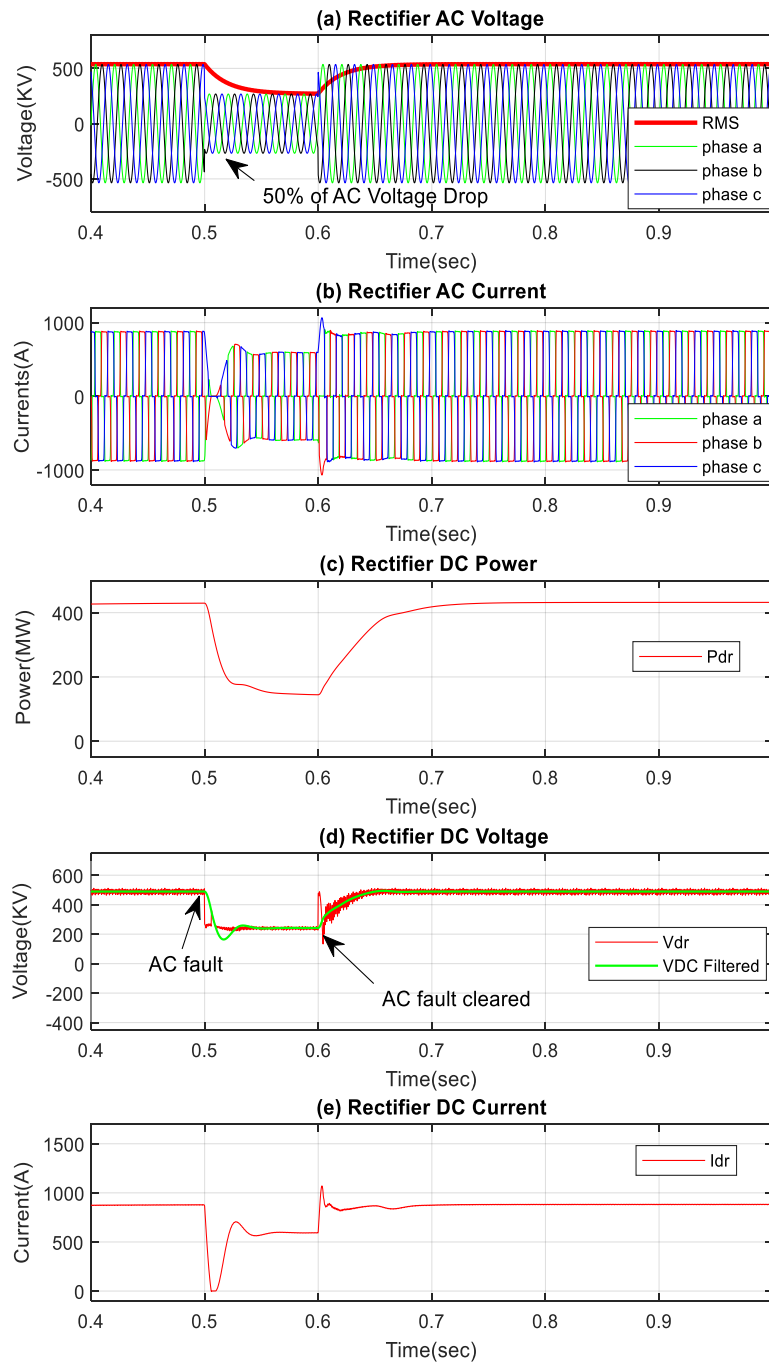


Figure 3-12: Rectifier Response Under Rectifier Bus AC Fault Condition

Furthermore, On the inverter side (Figure 3-13), the busbar AC voltage (Figure 3-13 (a)), was not affected at all compared to that on the rectifier side. The insensitivity of the inverter AC voltage is because the AC fault was applied to the rectifier. The AC current's response on the inverter side also confirms the reduced impact of the rectifier AC fault on the inverter operation. It can also be seen that it can be seen that the system reactions on the inverter side are the same as those on the rectifier side, but with a much lower impact for an AC fault appearing on the rectifier side [107]. It can be seen that the findings meet the standards and proper HVDC performance under rectifier AC fault Conditions, as discussed in [104, 107].

- **Rectifier AC fault Conditions (Inverter response)**

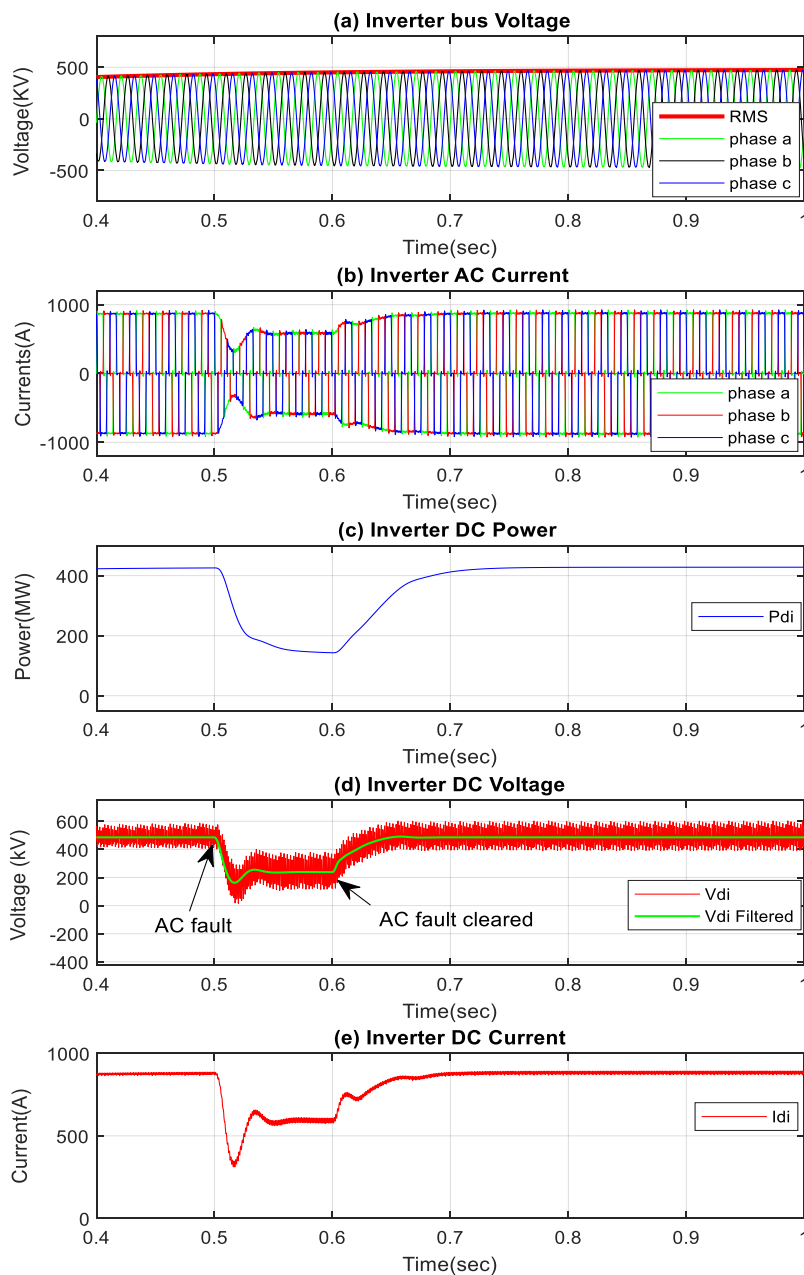


Figure 3-13: Inverter Response Under Rectifier Bus AC Fault Condition

3.6.4.1.4 Study case 4: Inverter AC fault conditions

Figures 3-14 and 3-15 display the system response when an AC fault of 0.001Ω lasting 150 ms is applied at 600 ms on the AC busbar at the inverter. The voltage drop caused by an AC fault generally depends on the fault's impedance [132]. Usually, AC fault on the inverter side results in commutation failure [104, 107]. In this case, where the AC fault is applied to the inverter side, it can be observed (Figures 3-14 (a)) that the AC voltage drop is much more significant (almost 100% voltage drop) compared to the previous case (rectifier AC fault). This is because the AC fault impedance on the inverter side is much lower than that of the last scenario. AC Fault Inverter Side (Inverter Response)

- **Inverter AC fault conditions (Inverter Response)**

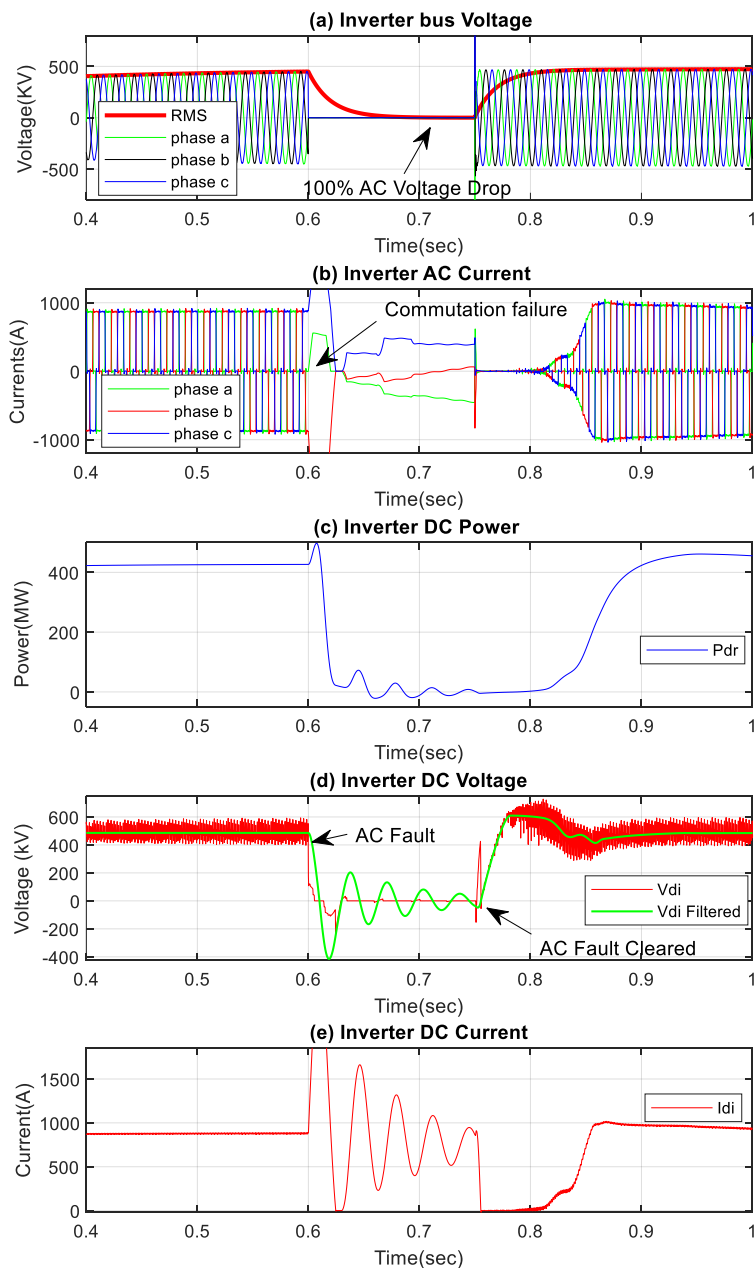


Figure 3-14: Inverter Response Under Inverter Bus AC Fault Condition

Therefore, in Figures 3-14 (a), it can be seen that the voltage drops to zero at 600 ms and returns to its pre-fault steady-state value after 150 ms. Moreover, in Figures 3-14 (b) showing the inverter AC current's response, it can be observed that the AC fault on the inverter side results in commutation failure. It was found that there was no current transfer during this time of the fault duration. This hinders the commutation process at the inverter end, resulting in power loss or zero transfer along the line before the fault clearance.

- **Inverter AC fault conditions (Rectifier Response)**

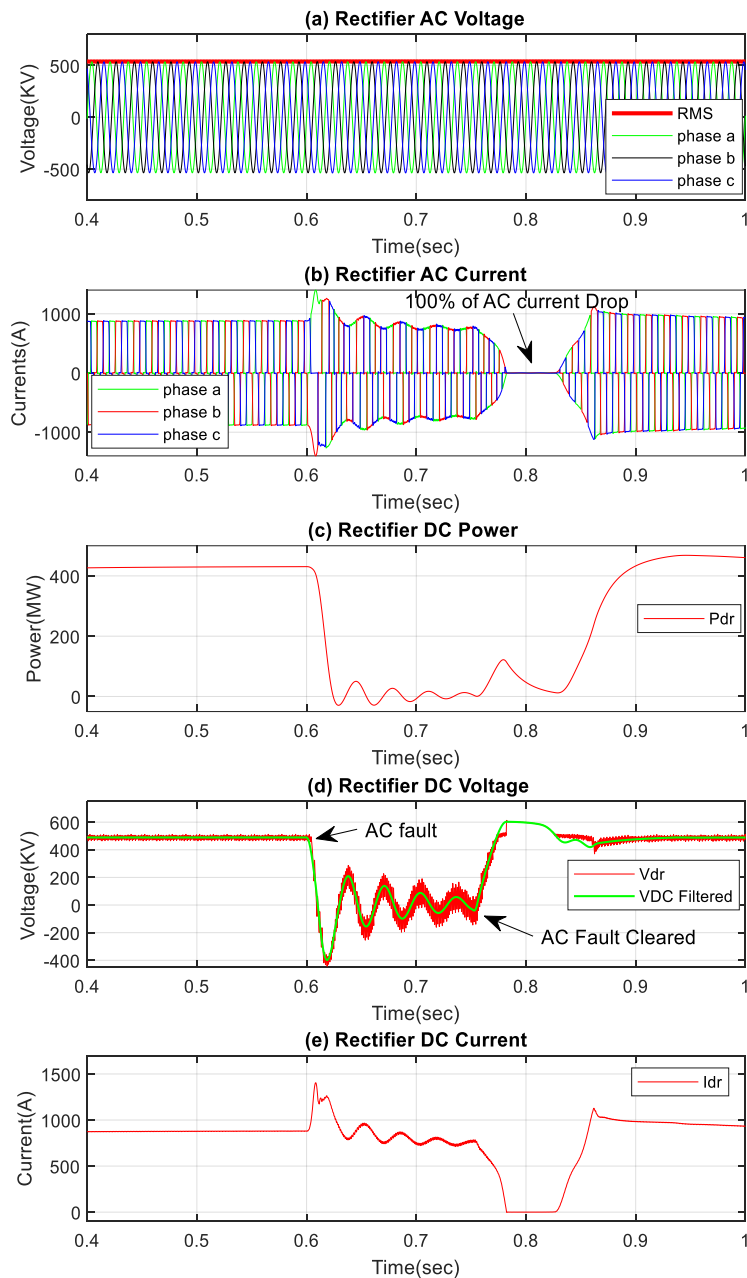


Figure 3-15: Rectifier Response Under Inverter Bus AC Fault Conditions

Therefore, due to the inverter side commutation failure caused by the AC fault, the inverter station needs adequate control measures for good system reliability. Figure 3-15, however, illustrates the rectifier response to an inverter bus AC fault. The findings are almost identical to the inverter response, except that commutation failure does not significantly affect the rectifier side. It can be seen that the results meet the standards and proper HVDC performance under Inverter AC fault conditions as discussed in [104, 107].

3.7 Conclusion

Chapter Three focussed on modeling the power system components, namely the synchronous machine, the AC transmission line, the excitation system, and the HVDC link. This modeling considered the type of synchronous machine used for IEEE FBM, a device whose circuit's internal representation of the rotor and the stator includes four windings, namely a field winding, two windings on the q-axis, and one winding on the d-axis.

We've also developed The series-compensated transmission line's modeling equations. After establishing the resonant AC line equations, we discussed the critical compensation points inducing negative responses in the TG shaft torsional dynamics. These critical operating points are addressed in the thesis, in particular in chapters Four and Five.

The equations governing the excitation system took into consideration the manual excitation and the IEEE type ST1A. PSCAD software initially contains IEEE FBM equipped with a manual excitation called the constant excitation system. Particular attention has been paid to the operating principles of these two types of excitation systems.

The power system's modeling equations after excitation components focused on the HVDC scheme. The HVDC link's modeling equations were obtained based on T-model representation with two impedances in series and a lumped charging capacitor. Following the DC link's modeling equations, the chapter studied the HVDC system's transient response between two sources with the same characteristics as the FBM IEEE sources, considering a constant excitation system.

In this chapter, we have studied the performance of the HVDC system under various operating conditions. The results proved the effectiveness of the HVDC scheme in restoring its normal operation after major disturbances. Despite commutation failure in some cases studied, the HVDC operation was efficient. Therefore, the following chapter analyzed an HVDC link's impact on the TG shaft's torsional dynamics when added in parallel with a resonant AC line. This analysis is limited to a power grid with a turbogenerator system equipped with a constant excitation system.

CHAPTER FOUR: INVESTIGATING THE IMPACT OF HVDC ON THE DAMPING SUBSYNCHRONOUS RESONANCE

4.1 Introduction

Turbine generators have natural torsional frequencies due to the physical properties of their long multi-element shafts. Series capacitor compensation in transmission networks tends to reduce the damping of torsional vibrations of neighboring turbogenerators. This phenomenon is called subsynchronous resonance (SSR). It affects the turbogenerator's shaft at subsynchronous frequencies equivalent to its torsional oscillatory modes. Series capacitors also amplify the shaft stress when significant transient events occur on the grid [40]. Because of DC links' high controllability, several research works have shown the possibility of stabilizing the power system operation based on HVDC converters' additional controls [4].

Moreover, based on the studies conducted in [97, 139], the HVDC system was a potential source of torsional interaction, although they offer a means of power system stabilization. Typically, a parallel AC-DC system containing a series capacitor on the AC line has many risks of subsynchronous oscillation instability from both AC and DC systems [48, 140]. In such a power system, torsional oscillation generally results from the transmission line's series capacitor or interaction between DC converter controls and neighboring turbogenerator shafts. The literature claims that assessing interactions between the AC and DC systems can be done based on the unit interaction factor (UIF). No critical interaction risk can be observed only when the UIF is less than 0.1 [52].

This chapter first seeks to implement an additional HVDC link in parallel with a modified resonant AC line before considering the DC link's advantages based on its high controllability and designed for the power system's stabilization. It is devoted only to observing the impact of HVDC on the torsional dynamics of the turbogenerator set. Adding the parallel HVDC link will be limited to watching its effects on SSR damping. Further studies regarding the exploration of HVDC controllers are presented in the next chapter. The HVDC system's implementation does not replace the resonant AC line but supplements it [99, 116]. Therefore, the DC link's parallel addition will make it possible to design supplementary damping controllers to address the SSR/SSO issue from the AC line's series capacitor and the HVDC tie. The torsional oscillation's stability resulting from the DC link's supplementary damping controllers will allow the power grid to safely transfer the maximum power possible at each compensation level, countering SSO occurrence.

The use of auxiliary HVDC controls can enhance the operation and performance of a power grid. However, in most cases, HVDC controls act as a potential source of SSR [4]. An HVDC system in radial operation, i.e., with no parallel AC line, is also most exposed to torsional interactions (TI) due to its converter controllers [48].

As a reminder, for an HVDC system in parallel with a series compensated transmission line, torsional oscillation sources are numerous (i.e., series capacitors, DC converters controls, AC bus strength, transmission line length, HVDC control schemes, etc....) [28]. The controls of HVDC links can adversely influence the stability of torsional electromechanical oscillations. The rectifier and inverter controllers can affect the torsional dynamics of the turbogenerator set. The inverter station-based torsional oscillation's risk can be assessed depending on the generator-inverter electrical coupling (i.e., the series compensation level), the inverter station's control mode, and the stiffness of its bus [100]. Consequently, without adequate supplementary controls (i.e., SSC), the effect of adding an HVDC link in parallel with a resonant AC system is entirely reliant on all the aspects mentioned above.

The experiment conducted in [99, 116] on a 400 kV series compensated transmission line demonstrated the inability of HVDC without an auxiliary damping controller to mitigate SSR. The series of tests performed in [99, 116], varying the compensation level from 14% to 104%, showed that adding HVDC with only its standard current regulator could not stabilize an SSR condition. However, only the damping of torsional oscillations for operating points with a compensation level lower than 56% improved. In contrast, that of torsional oscillations for operating points with more than 56 percent compensation decreased. Above 56 percent, some torsional frequency modes had also been excited due to HVDC controls. Therefore, as per BALDA [99, 116]: "an HVDC link without ADC marginally raises the allowable degree of series compensation at which the torsional oscillation is unstable, thus incorporating the HVDC system does not stabilize an unstable SSR state. Nonetheless, incorporating the HVDC link would improve the total power transmission capability".

The experiments in reference [40] proved to be similar to [99], although, in both studies, the torsional interactions between HVDC controls and the turbogenerator shaft's mechanical system were neglected. The time-domain results in [40] demonstrated an HVDC link's ability to improve damping operating points without fully stabilizing the SSR condition. The study was conducted considering a stiff inverter bus ($X_s=0.1$). The inverter station's AC bus stiffness usually substantially affects the stability of electro-mechanical torsional oscillations in parallel AC-DC systems when the generator is situated on the inverter side [51, 100]. Compared to [40], this chapter only deals with an HVDC link whose inverter station is connected to an AC bus with moderate stiffness, $X_s=0.5$ pu. Calculations of ESCR are provided in Appendix C.

Several experiments confirm the assumption of the inverter station's non-significant adverse impact on the dynamic of the TG's shaft. However, this assumption is valid when the HVDC link is in a radial

operation, i.e., disconnected from the parallel resonant AC line or forming with the AC line a parallel AC-DC system whose inverter station's AC bus is stiff. Therefore, in this chapter, the investigation of the parallel DC-link addition's impact on torsional oscillation damping is limited to a synchronous generator with a constant excitation system, a DC link's rectifier station fitted with its standard current controller only, and an inverter station connected to a moderate AC bus. However, analyzing the effect of inverter controls on SSR damping is beyond the scope of this work. The particularity of this work is the study of IEEE FBM parallel to an HVDC link connected to a moderate bus on the inverter side. This chapter is divided as follows: an introduction section describing the chapter's topic as well as its objectives, a second section presenting the parallel AC-DC system as well as the modeling equations governing its quadratic representation, a third section designed for the power system simulation using PSCAD and the results' discussions, and finally a fourth section concluding the chapter.

4.2 Study System

The study system illustrated in Figure 5-1 consists of two parallel transmission lines: the modified resonant AC line adopted from the IEEE First Benchmark Model (FBM) for SSR analysis and a parallel HVDC system. The AC system consists of a single 892.4 MVA generator connected synchronously to an infinite bus via 276 miles of 500-kV AC transmission lines and asynchronously by 276 miles of 500 kV DC transmission line. The nominal power of the HVDC is chosen as equal to 0.485 pu [97]. The AC filters and capacitor banks provide the total reactive power at both the rectifier and inverter AC buses.

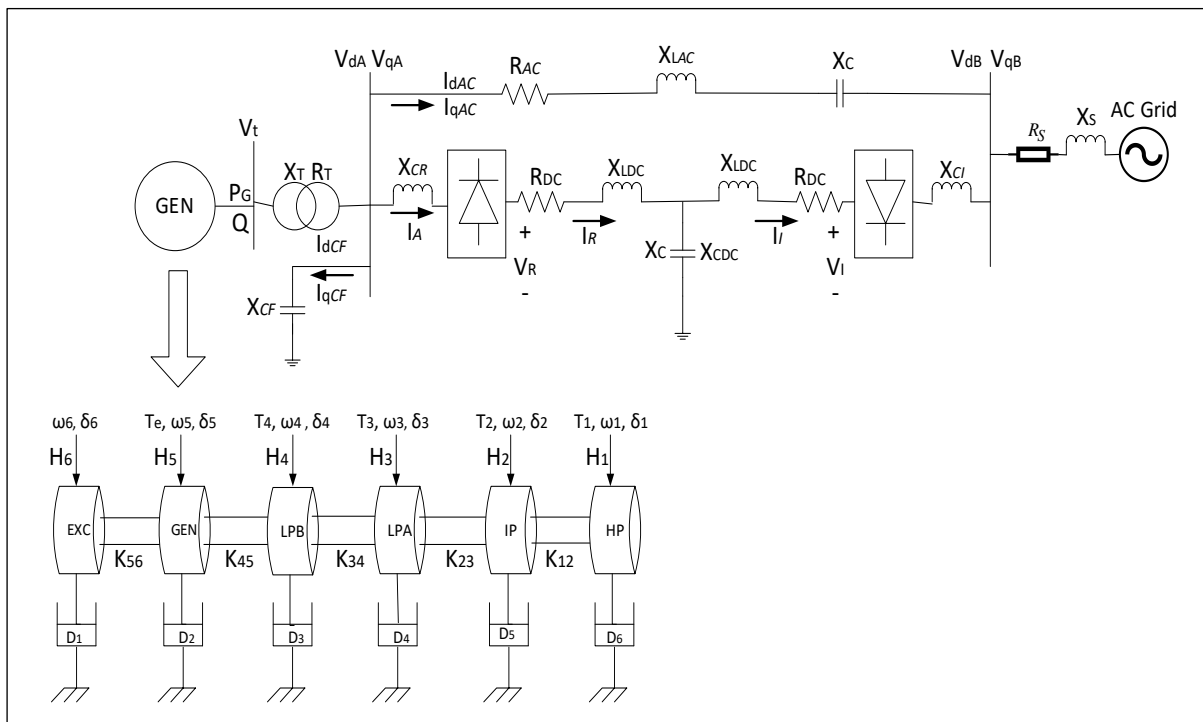


Figure 4-1: Modified IEEE FBM with the Parallel HVDC line [40]

4.2.1 Turbogenerator Shaft's Mechanical System

The IEEE FBM rotor shaft system comprises six lumped masses representing the turbine's different levels. The entire system includes a high-pressure turbine (HP), an intermediate pressure turbine (IP), two low-pressure turbines (LPA & LPB), a generator (G), and an exciter (Ex). The shaft system has five torsional modes, with mode 0 referred to as the inertial (or swing) mode of oscillation. Table 4-1 shows the mechanical resonance frequencies of the IEEE FBM with a nominal frequency of 60 Hz.

Table 4-1: Turbogenerator Shaft Torsional Modes

Torsional Modes	Frequency (Hz)
Mode 0	1.6
Mode 1	15.71
Mode 2	20.21
Mode 3	25.25
Mode 4	32.285
Mode 5	47.46

As a reminder, the phenomenon of SSR occurs when the generator rotor, oscillating at a frequency f_n , generates induced voltages comprising subsynchronous ($f_0 - f_n$) and supersynchronous ($f_0 + f_n$) components in the generator armature. This situation usually occurs when the electric network connected to the generator armature is in resonance around the frequency of ($f_0 - f_n$) [28]. However, series compensated transmission lines have a resonant frequency given by equation (4.1). Equation (4.1) represents the compensation level, K [135].

$$f_{er} = f_0 \sqrt{\frac{X_{CAC}}{X_{LAC} + X_T + X_S + X_{ad}''}} \quad 4.1$$

$$K = \frac{X_{CAC}}{X_{L_{tot}}} = \frac{X_{CAC}}{X_{LAC} + X_T + X_S + X_{ad}''} \quad 4.2$$

Where,

X_{ad}'' = Generator sub transient reactance

X_{LAC} = Transmission line inductive reactance

X_T = Transformer reactance

X_S = Infinite bus equivalent series inductive reactance

X_{CAC} = Transmission line series compensated reactance

f_0 = Operating system frequency

f_n = Natural frequencies

The capacitive reactance is usually less than the transmission line inductive reactance. Such a case makes f_{er} to be less than f_0 . Thus, for particular levels of series compensation, it is possible to have a situation such that f_{er} is equivalent to $f_0 - f_n$. The actual frequency generates similar frequency torques on the generator's rotor. Consequently, SSR problems are frequently due to fatigue created by parasitic torque pulsations $f_0 - f_{er}$ that coincide in frequency with a natural frequency shaft section, f_n [40].

4.2.2 Mathematical modeling

Unlike the modeling equations presented in the previous chapter, the parallel AC-DC system modeling is explained in this section. The modeling equations presented in Chapter Three referred to the AC power system comprising all IEEE FBM elements, including the transmission line. In the previous chapter, another full-fledged model was carried out on a radial operating HVDC system mounted between two voltage sources with the same properties as the IEEE FBM sources. Since this HVDC is to be installed parallel to the resonant AC line, the purpose of modeling the parallel AC-DC system provided in this section is to demonstrate the fundamental equations governing the operation of the parallel system (see Figure 4-1).

The mathematical equations concerning the synchronous machine and the AC system will not be repeated, mainly because the previous chapter has already addressed them. They're only briefly covered in this section. Modeling the parallel AC-DC system is what matters most. Chapter 3 also reported the equations of the turbogenerator mechanical system for inertia, damping, and spring constants.

Figure 4.2 shows the well-known two-axis machine model considered for AC-DC system modeling. The parallel AC-DC system was modeled in line with its quadratic representation suggested in [141].

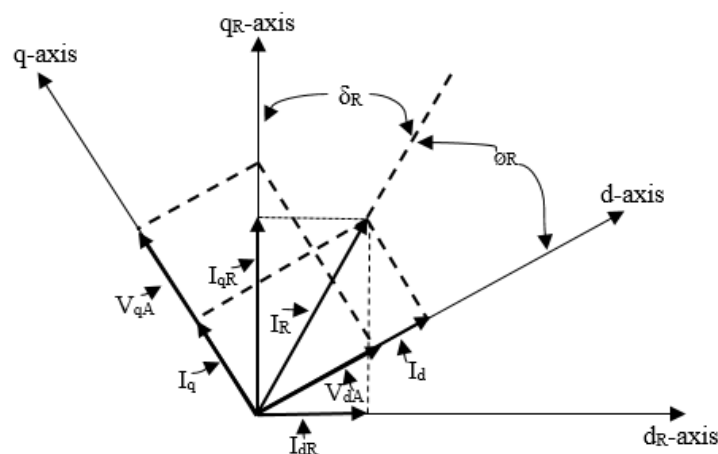


Figure 4-2: Rectifier Bus Reference Axis [40]

The quadratic representation makes it possible to establish the exact relationship between the power system quantities (e.g., current, voltage, and power) depending on the rotor reference frame. The synchronous machine rotor has a fixed reference frame based on the d-q axis, which rotates at frequency

“ ω ” concerning the rectifier AC bus. In contrast, the d_R - q_R axis is a reference frame that rotates at the synchronous speed “ ω_s ” of the infinite bus [22, 141]. Figure 4-2 is mainly used to determine the quasi-steady-state model of the parallel ac/dc system. The quasi-steady-state model is also valid under transient conditions.

4.2.3 AC Line Modelling

The equations depicting the AC line's behavior as a function of the synchronous rotating frame (i.e., d-q axis) are thoroughly described in [141]. A and B are used to identify variables related to the rectifier bus and the infinite bus. Therefore, the AC line's quadrature voltages concerning the synchronous rotating frame are given by [40, 141]:

$$v_{qA} = Ri_{qA} + \frac{x_l}{\omega_0} \frac{di_{qA}}{dt} + \frac{x_l}{\omega_0} i_{dA} \frac{d\theta}{dt} + v_{qc} \quad 4.3$$

$$v_{dA} = Ri_{dA} + \frac{x_l}{\omega_0} \frac{di_{dA}}{dt} + \frac{x_l}{\omega_0} i_{qA} \frac{d\theta}{dt} + v_{dc} \quad 4.4$$

Where superscript “t” s used to identify the currents that flow through the AC line, “ $d\theta/dt$ ” is the synchronous rotating frame's electrical angular velocity, “ v_{dc} ” and “ v_{qc} ” are the d-axis and q-axis capacitor voltages. The infinite bus equations related to the d-q axis synchronous rotating frame are established in the same manner as bus A. [141]. These equations provide further specifics, including those for capacitor voltages as a function of the synchronous rotating frame.

4.2.4 DC Line Modelling

HVDC Modelling is based on its T-model representation. Section 3.8.1 has already outlined T-model representation-based HVDC modeling equations. However, this section specifies the HVDC system's modeling equations for the fixed synchronous reference frame. Therefore, the average rectifier voltage is given by [141]:

$$V_{Rdc} = \frac{3\sqrt{6}}{\pi} V_{qR} \cos \alpha_R - \frac{3}{\pi} X_{CR} I_{Rdc} \quad 4.5$$

V_{qR} is the voltage applied to the rectifier bus in the d_R - q_R reference frame. The q_R -axis coincides continuously with the right triangle's hypotenuse formed by voltages v_{dA} and v_{qA} .

$$V_{qR} = v_{qA} \cos \delta_R + v_{dA} \sin \delta_R \quad 4.6$$

$$V_{dR} = 0 \quad 4.7$$

Where δ_R is the angle between the quadrature axes of the machine and the infinite bus. The power factor at the AC side of the rectifier is given by [40]:

$$\cos \phi_R = \frac{\pi}{3\sqrt{6}} \frac{V_{Rdc}}{V_{qR}} \quad 4.8$$

Rectifier AC current d_R-q_R axis components as a function of rectifier DC current and infeed power factor are obtained by neglecting rectifier losses and equalizing the active power expressions on both sides of the rectifier.

$$I_{qR} = \frac{\sqrt{6}}{\pi} I_{Rdc} \cos \phi_R \quad 4.9$$

$$I_{dR} = \frac{\sqrt{6}}{\pi} I_{Rdc} \sin \phi_R \quad 4.10$$

The following equations are used to refer I_{qR} and I_{dR} to the d-q axis:

$$I_q = I_{qR} \cos \delta_R - I_{dR} \sin \delta_R \quad 4.11$$

$$I_d = I_{qR} \sin \delta_R + I_{dR} \cos \delta_R \quad 4.12$$

Where,

$$\cos \delta_R = \frac{V_{qA}}{V_{qR}} \quad 4.13$$

$$\sin \delta_R = \frac{V_{dA}}{V_{qR}} \quad 4.14$$

The inverter station is connected to the infinite bus “B”. The equation governing its controls is described below:

$$V_{Idc} = \frac{3\sqrt{3}}{\pi} V_{qI} \cos \alpha_I - \frac{3}{\pi} X_{CI} I_{Idc} \quad 4.15$$

The d-q axis voltages of the infinite bus are expressed as:

$$v_{dB} = V_B \sin \delta \quad 4.16$$

$$v_{qB} = V_B \cos \delta \quad 4.17$$

Where V_B is the per-unit line-to-neutral voltage of the infinite bus.

4.3 Simulation and Results

To investigate the impact of adding an HVDC link in parallel to a conventional series compensated AC line, the study system's time-domain response is analysed in PSCAD following a three-phase to ground fault lasting 75 ms and applied at 1.5 sec at the infinite bus. The generator is enabled at 1.1 s while the multi-mass system at 1.4 sec. Table 4-2 describes the scenarios undertaken to study the effect of HVDC on SSR damping. Four distinct operating points characterize the case studies.

The operating points were obtained considering the generator output voltages at critical compensation levels where the TG shaft torsional modes get excited. In all cases, the generator power factor is 0.9 p.u. The magnitudes and phases of the equivalent AC voltages at converters buses are also given. The percentage of compensation K was computed using Equation (4.2). The simulation results were captured over 6 secs.

Compared to the study in [40], this research considers torsional interaction due to HVDC controls. Literature indicated that HVDC controls should also be considered as a potential SSO source. In previous chapters, we have stated that several factors influence SSO HVDC-based power grids. However, mismatched current regulator settings are one of the main sources of SSO in these systems. To investigate the impact of the HVDC system on SSO damping, we used the current regulator parameters stated in Chapter Three for scenarios (1) and (2) (see Table 3.1). These parameters proved effective as incorporating the parallel HVDC system met our expectations.

We conducted several tests on the parallel AC-DC system, varying the gains of the current regulators since keeping $K_{PID}=5$ did not meet our expectations aiming at observing positive damping of the TG shaft. Therefore, we chose $K_{PID}=10$ as both converters' current regulators' gains for scenarios (3) and (4). Appendix A and Appendix B provide the entire AC-DC power system. Chapter Five applies the same scenarios as Chapter 4, considering the same current regulators' parameters. In all the cases, $X_S=0.5$ p.u. We chose this X_S value because it results in a moderate inverter AC bus and adverse torsional oscillations, distinct from a stiff bus that effectively resists significant oscillations. (e.g., $X_S=0.1$ p.u.). A moderate AC bus as its stiffness, $3 < ESCR < 4.5$.

Table 4-2: Operating Points (Case Study)

Pdc=0.4846pu								
N°	K (%)	P _g (pu)	PF	V _g (pu)	V _{a, Mag} (pu)	V _{a, Ph} (deg)	V _{b, Mag} (pu)	V _{b, Ph} (deg)
1	23	0.67	0.900	1.007	0.968	27.64°	0.914	19.72°
2	41	0.70	0.900	1.007	0.968	21.90°	0.923	20.18°
3	61	0.80	0.900	1.007	0.964	24.09°	0.943	23.64°
4	70	0.90	0.900	1.007	0.968	23.55°	0.957	26.9°

Figure 4-3 shows the system response regarding Case (1). However, without HVDC in operation, the system experiences electromechanical oscillations of increasing amplitude, leading to severe electrical torque degradation and machine current. Torsional instability due to the series capacitor increases dramatically in amplitude in the AC system. Following the parallel DC line's addition, the results show that the turbogenerator shaft's torsional dynamics received substantial positive damping. With the current regulator's parameters in [55], adding the HVDC system effectively improved the electromechanical system damping at this operating point. Although the SSR damping has been substantially enhanced with the HVDC system's insertion, the torsional oscillation remains erratic and requires additional damping investigation.

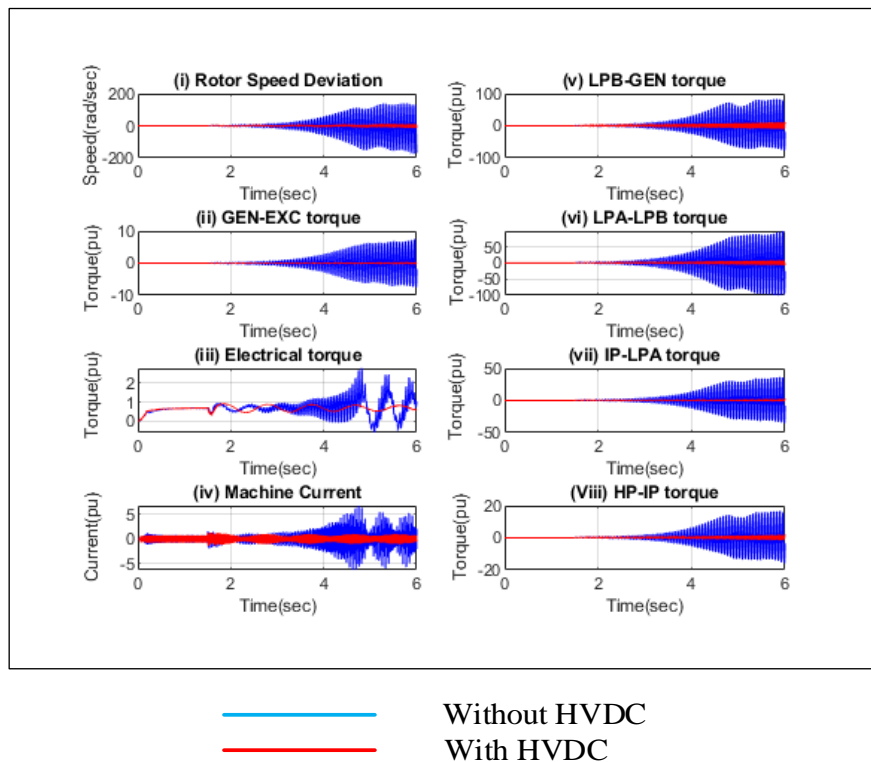


Figure 4-3: System's time domain response in Case (1)

The system response for case (b) is illustrated in Figure 4-4. Torsional oscillation due to the series capacitor generally depends on the system operating conditions [101]. The results displayed in Figure 4-4 show a significant increase in oscillatory amplitude across various turbine generator shaft sections when the HVDC system is out of service. For instance, this is the case of the rotor speed deviation in which the torsional oscillation moves from a low amplitude at the instant 1.5 seconds, when the fault occurs, to an oscillatory variation of almost ± 100 rad/seconds at instant 6.0 seconds. This substantial oscillatory growth threatens the stability of the power system's operation. Due to the series capacitor, this torsional instability strongly affects the turbogenerator's electrical torque. Under these operating conditions, the torsional oscillation's significant adverse effect to which the power system is subjected when HVDC is out of operation can cause rapid failure of the turbine generator shaft. However, a substantial improvement in the SSR damping was observed through the shaft sections due to the parallel incorporation of the DC line at this particular compensation level. The addition of HVDC, when fitted only with its standard current regulator given in [97], was efficient in improving the SSR damping. However, the parallel AC-DC system remains unstable and requires further SSR mitigation analysis.

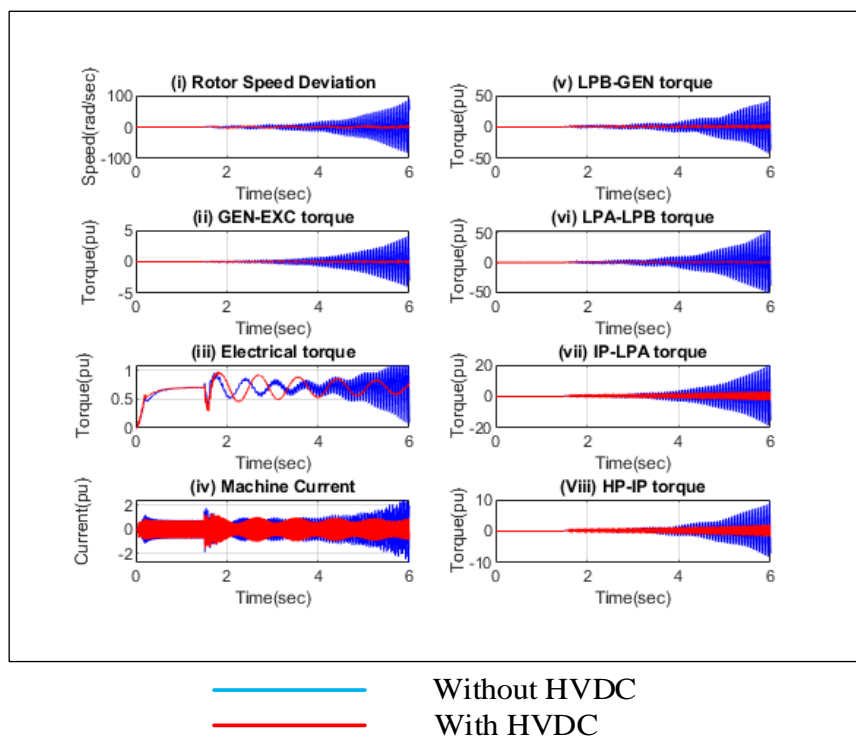
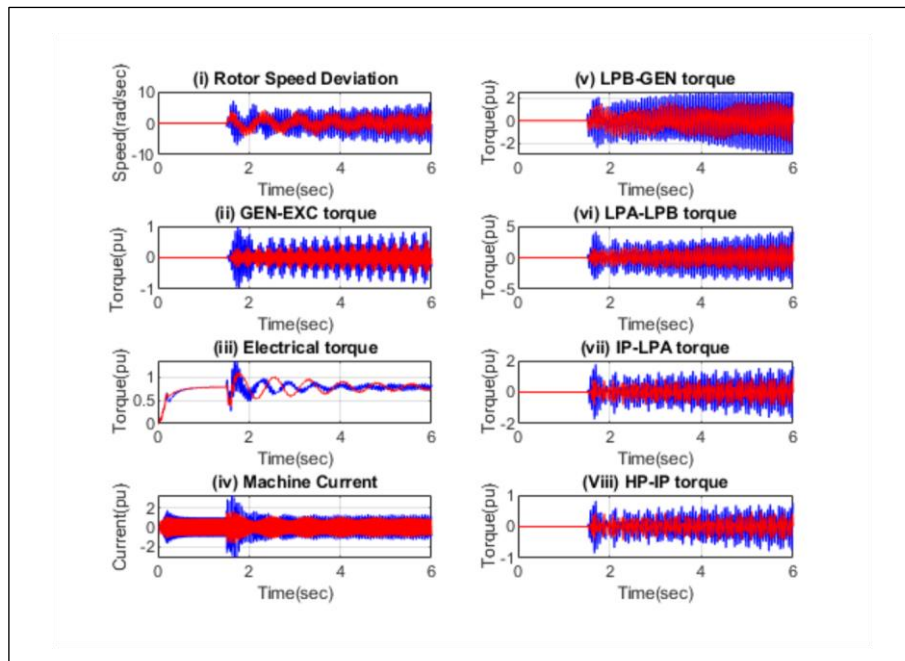


Figure 4-4: System's time domain response in Case (2)

The system response for case (3) is displayed in Figure 4-5. In line with [28], the DC converters' controls can induce torsional oscillations and provide the means to suppress them. SSO can come from converter controllers, series capacitors, or both [4, 28]. In [60], Hamada stated that the adverse torsional effect of converter controls depends on the operating condition. Usually, in a parallel AC-DC configuration where the generator is located on the rectifier side, the adverse torsional effect due to converter controls

(i.e., inverter station) increases as the coupling between the inverter's AC bus and the generator increases (i.e., the series compensation level). The worst case is when the powers of the AC and DC lines are comparable [100]. In this chapter's scenarios, the DC line power is higher than the AC line's. In fact, under these operating conditions relating to 61% compensation, the rectifier-inverter electrical coupling has increased compared to the previous cases. The rectifier's current regulator parameters provided in [55] have proved ineffective for this operating point. The inability of HVDC to provide positive damping in the system also occurred in the Koeberg turbogenerator set at around 56% compensation [99, 116]. Thus, new rectifier current regulator parameters (i.e., $T_r=0.01$ sec, $K_r=10$) led to positive damping of the turbogenerator shaft's dynamics. The results also show that the HVDC system's contribution when fitted only with its standard current controller does not guarantee adequate damping at this specific operating point. Compared to the previous scenarios, the positive damping contribution is not significant. Although the HVDC link contributed to the positive damping of the electromechanical system, it should be noted that the parallel AC-DC system itself remains exposed to the risk of torsional oscillation from various sources. The added HVDC system's failure to provide adequate positive damping can be seen via all the shaft sections of the turbogenerator, the electrical torque, the machine current, and the generator speed deviation. Therefore, this demonstrates the significance of implementing supplementary HVDC controls to mitigate all torsional oscillations and get a more stable operating system, which is frequently exposed to multiple sources of torsional oscillations.



— Without HVDC
 — With HVDC

Figure 4-5: System's time domain response in Case (3)

Figure 4-6 describes the system's response under case (4) operating conditions. Case (4) is associated with high compensation percentage. $T_r=0.01$ sec, $K_r=10$, as in the previous scenario, are the current regulator parameters that counteract the rectifier control loop's adverse effect on the torsional dynamic of the turbogenerator set. It should be mentioned that the reduction of the AC system's net series resistance between the generator and the inverter station generally results in two effects, namely the strengthening of the generator-inverter electrical coupling and also an increase in the inverter station AC bus stiffness. The strong electrical coupling between the generator and the inverter usually raises the inverter controls' negative torsional effect, whereas the high short-circuit ratio decreases that effect. The electromechanical system remains unstable despite using new parameters of the rectifier current regulator, which made it possible to observe the enhancement of the SSR damping. Therefore, further studies are needed to mitigate SSR. Thus, the results show the necessity of implementing supplementary HVDC controls to improve the stability of electromechanical oscillations.

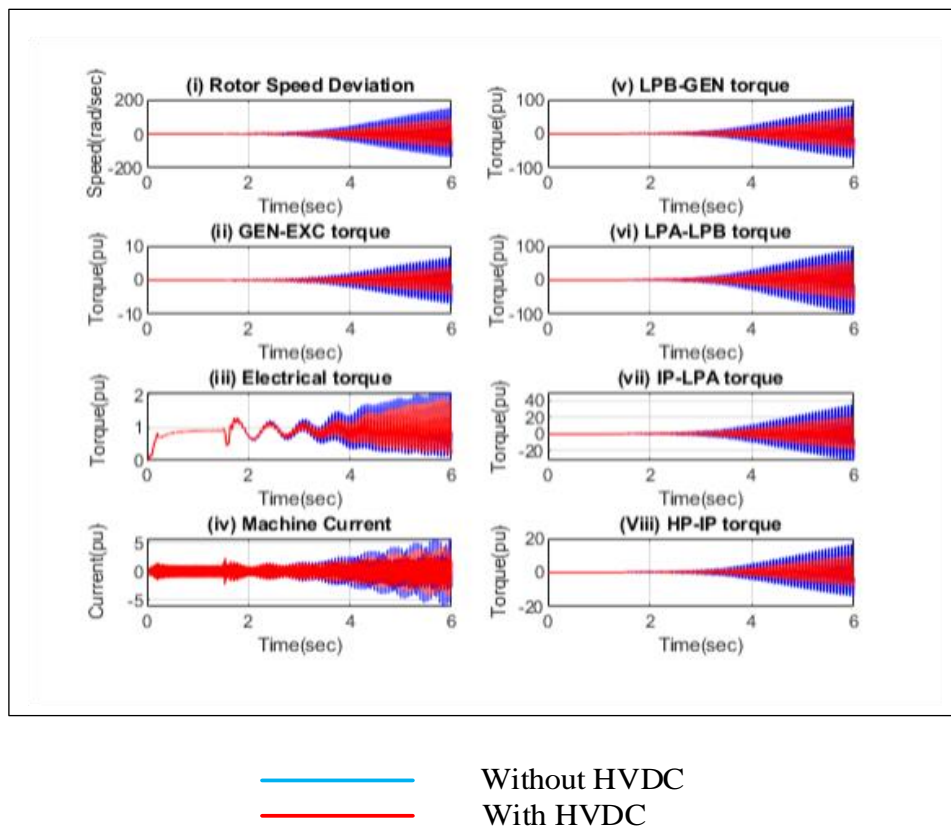


Figure 4-6: System's time domain response in Case (4)

4.4 Conclusion

Subsynchronous resonance is a significant problem experienced in series compensated transmission systems. This problem is considered SSR when the turbine-generator shaft oscillates frequencies below the grid's rated frequency. Subsynchronous torsional oscillations generally affect power grid stability and cause turbogenerator shaft failure. Today, several approaches have been suggested for overcoming this issue. However, auxiliary HVDC controls are the fundamental alternative for addressing this problem in this thesis.

Initially, this chapter centered on investigating the impact of adding an HVDC link in parallel with a resonant AC line on the turbogenerator torsional dynamics. This study was limited to an HVDC link whose inverter station was connected to an AC bus of moderate stiffness. The objective pursued focused on the effect of an HVDC link on subsynchronous resonance damping when it lacks adequate and appropriate controls, i.e., when the rectifier operates only with its standard current regulator.

However, numerous experiments have demonstrated the ability of HVDC to induce and mitigate SSO based on its DC converter controls, whether in radial operation or parallel with AC lines. Moreover, studies have shown that HVDC converter controls and series capacitors are the significant SSO source in parallel AC-DC grids. According to the literature, operating points resulting in a strong generator-inverter electrical coupling (i.e., high compensation level) are usually exposed to undesirable torsional oscillations, especially in a parallel AC-DC grid where the generator is located on the rectifier side,

The findings of this investigation have shown that the addition of the parallel DC link, the rectifier of which is only fitted with a standard current regulator, could improve the damping without totally stabilizing the torsional oscillation. Using the current regulator parameters given in [97], the HVDC is efficient in enhancing the SSR damping of the operating points with a compensation percentage of less than 61 percent. However, beyond this percentage, adding the parallel HVDC had a somewhat negative impact on SSR due to several parameters, particularly the stiffness of the inverter bus, the converter control mode, standard current regulator, control schemes, etc. New current regulator's parameters leading to positive SSR damping were used for operating points with a compensation level more significant than 61 percent. Despite improving the rectifier current controller's gain, the damping provided was meaningless, and the torsional dynamic of the turbogenerator shaft was always unstable. As a result, it is necessary to exploit the supplementary controls of HVDC to suppress SSR further. Therefore, essential auxiliary HVDC controls to stabilize the SSR should be provided to the current regulator.

CHAPTER FIVE: DAMPING SUBSYNCHRONOUS RESONANCE USING HVDC SUPPLEMENTARY SUBSYNCHRONOUS DAMPING CONTROLLERS

5.1 Introduction

The Series capacitor in transmission lines is of paramount importance for its contribution to enhancing power transfer capability. However, the major drawback of the series capacitor in a transmission line is its negative impact on the turbogenerator's torsional dynamics. This adverse effect usually manifests at subsynchronous frequencies (SSR) and affects nearby turbogenerator shafts. However, power systems' operation is usually disturbed when nearby turbogenerators experience subsynchronous oscillations [42]. In this analysis, HVDC controls are used to solve subsynchronous resonance (i.e., SSR or SSO) in a parallel AC-DC scheme where the AC line is equipped with a series capacitor.

In the previous chapter, the addition of the parallel HVDC without proper controls influenced the TG's torsional dynamics in two ways, namely, positive damping contribution for operating points below 61% compensation and risk of system destabilization and failure to produce adequate positive damping for operating points with a compensation percentage more significant than 61%. The previous chapter reveals that the impact of the incorporation of a parallel HVDC system fitted only with a standard current regulator was dependent on the operating point characteristics. Implementing the parallel HVDC link improved the torsional oscillation but could not stabilize it at all compensation levels.

This chapter aims to set up adequate HVDC controls to stabilize the SSR. The block diagram configuration intended to suppress SSR comprises a Power System Stabilizer (PSS) and a Supplementary Subsynchronous Damping Controller (SSDC). The PSS aims at controlling the inertial electromechanical mode zero (Mode 0), while the SSDC at damping out unstable torsional modes.

Several SSDC design approaches based on HVDC controls have been proposed in different studies to overcome the SSR problem in the parallel AC-DC system [97, 99, 101, 142]. However, this research primarily focuses on the phase correction methodology conducted through the test signal method for designing SSDC. Besides using an inverter station equipped with an AC bus of moderate stiffness, the test signal methodology-based-phase correction approach is the main specificity of this research compared to the works addressed in [97]. The work in [97] purely focused on the modal control theory for designing subsynchronous damping controllers. However, the approach conducted in this thesis focuses on obtaining the difference in phase between the rectifier's reference current deviation and the induced electromagnetic torque. The test signal method is performed through PSCAD-based time-

domain simulation to compensate for the required phase angle. This research uses Fast Fourier Transforms (FFT) analysis to demonstrate the impact of the proposed supplementary controllers.

Furthermore, this work compares two types of controllers: single-mode damping controllers and multimodal damping controllers within the parallel AC-DC system typically subject to several torsional oscillatory instability sources, namely the resonant AC line and HVDC controls. This study also attempts to demonstrate the possibility of torsional interaction during the multimodal instability condition due, in particular, to single-mode damping controller parameters.

This chapter has five sections organized as follows: The introductory part describes the general overview of this chapter's objective, the second part gives a brief explanation of the study system, the third section focuses on the causes of torsional oscillation in power systems with HVDC links, and the use of supplementary HVDC controls in parallel AC-DC systems to mitigate torsional oscillations, the fourth section presents the simulation results for the case studies considered, and the final part giving the chapter conclusion.

5.2 The study system

The system studied shown in Figure 5-1 is made up of two parallel transmission lines. The network consists of a single 892.4 MVA generator synchronously connected to an infinite bus through 276 miles of AC 500 kV line and asynchronous through 276 miles of 500 kV DC line.

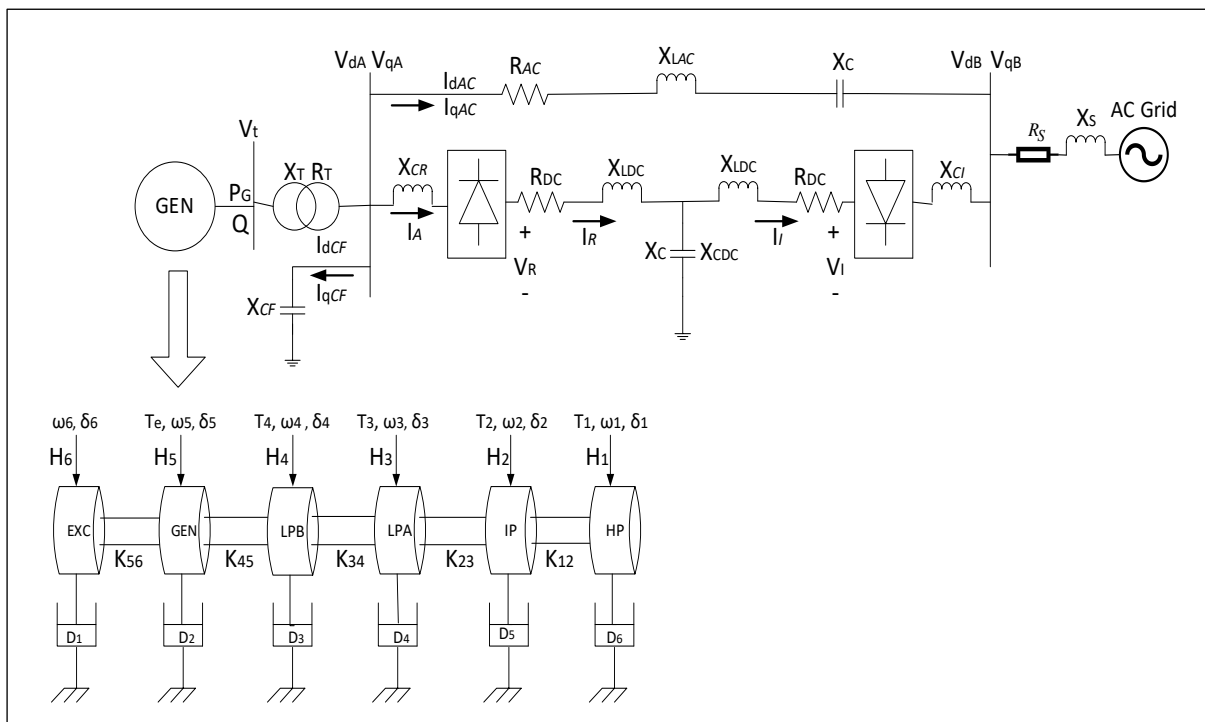


Figure 5-1: Modified IEEE First Benchmark Model with an HVDC line in parallel [40]

The single generator was adopted from the IEEE First Benchmark Model for SSR analysis. Two different nominal DC line powers: 0.485 pu [97] and 0.4154 pu are considered for evaluating the supplementary controllers' performance in this chapter. AC filters and capacitor banks provide the total reactive power in both HVDC ties to the rectifier and inverter busbars. The parameters of both HVDC operating points and AC filters are presented in Appendix [B].

5.3 Torsional oscillation in HVDC-equipped power systems

5.3.1 Introduction

In a parallel AC-DC system where the AC line is fitted with conventional series capacitors, torsional oscillation can result from HVDC controls or series capacitors [28]. The SSR phenomenon was first seen on long transmission lines equipped with series capacitors. However, the concept of torsional interaction due to inappropriate HVDC controls emerged later [143]. Unlike SSR, which comes from series capacitors, the torsional interaction phenomenon due to HVDC and power system controllers is frequently referred to as subsynchronous oscillation (SSO) [142]. Several damping controller design approaches have been proposed in the literature to solve torsional oscillation in a power system equipped with an HVDC link. Most of those methods are based on the system's eigenvalue analysis and robust controls, but the phase-compensation approach was little employed. Therefore, as in [96, 143], this chapter broadly uses a method based on phase correction to stabilize torsional oscillations encountered in the power system shown in Figure 5-1. In this study, regardless of the torsional instability source in the parallel AC-DC system, the high controllability of HVDC is intensely explored to solve the SSR problem.

5.3.2 HVDC- based Subsynchronous Damping Controller

Since DC converter controls are one of the leading causes of SSO in power grids equipped with HVDC, this aspect needs to be addressed to suggest a mitigating strategy focused on appropriate HVDC controls. This analysis is worth investigating as the SSDC studies focus on HVDC controls only. In fact, in power grids where turbogenerators are electrically close to the rectifier, the leading cause of torsional frequency oscillations is the closed-loop direct current control system [96, 143].

Typically, when the turbogenerator shaft experiences specific disturbances, there is an occurrence of sinusoidal fluctuations in the speed and angle (i.e., $\Delta\omega$, $\Delta\theta$) of the natural torsional modes (see Figure 5-2 (b)). This condition causes voltage and corresponding phase angle fluctuations (i.e., ΔU , $\Delta\theta_U$). Furthermore, this situation also adversely impacts the converter bus voltage by inducing phase and amplitude fluctuations. The essential point to note is that perturbations influence many power system parameters, including the firing angle ($\Delta\alpha$), DC line voltage (ΔU_{dc}), DC power (ΔP_{dc}), and DC current (ΔI_{DC}) [96]. Regarding power systems fitted with HVDC, the best alternative to the torsional oscillation

problem is establishing an appropriate phase compensator in the DC current control loop. When this step is done, the torsional dynamics of nearby turbogenerator shafts will experience positive damping following the DC converters' rapid response [142].

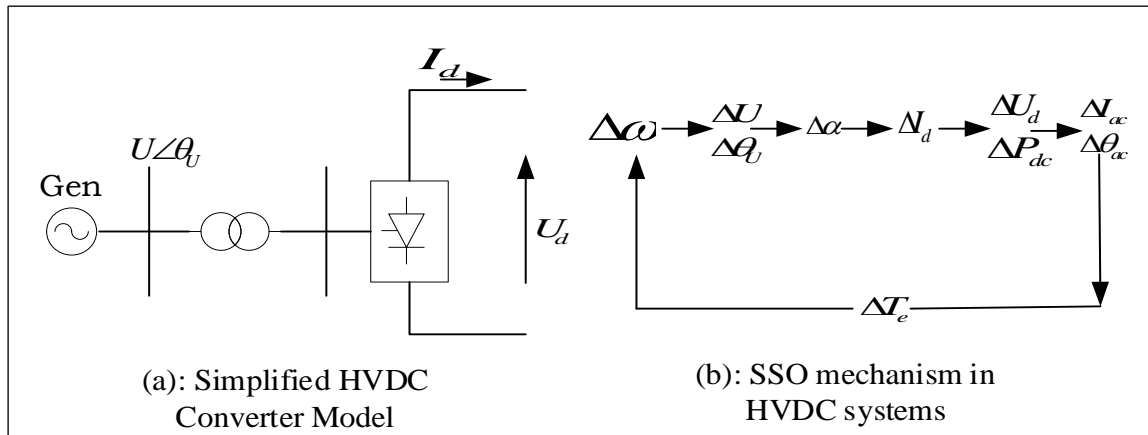


Figure 5-2: HVDC-Based SSO [139]

5.3.3 AC / DC Transfer Function.

To properly set up auxiliary compensation signals in the DC converter current control closed-loop, it is essential to establish the transfer functions that govern the DC current controls and connect the rotor speed deviation and the electromagnetic torque. Thus, the transfer function describing the link between rotor speed deviation and electromagnetic torque, including SSDC of an AC-DC system, is shown in Figure 5-3 [93, 142]. This transfer function applies to every HVDC-equipped power grid, including parallel AC-DC systems [142]. Figure 5-3 shows that the SSDC provides a supplementary link in the closed-loop DC current control within the converter circuit.

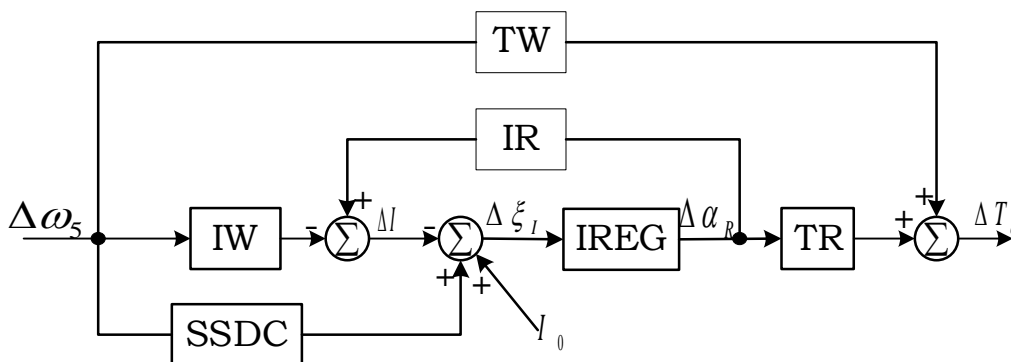


Figure 5-3: Transfer functions connecting $\Delta\omega_5$ and ΔT_e in HVDC [93, 142, 144]

This extra control system (i.e., SSDC) aims to adjust the difference in phase angle (i.e., due to the ac / dc system) between the generator speed deviation and the electromagnetic torque. The new control structure gives no transfer path between SSDC and generator speed deviation. Therefore, this control structure's benefit is that the SSDC does not produce any new internal current [142]. Equations (5.1) are the expressions of the transfer functions illustrated in Figure 5-3.

$$IW = \left. \frac{\Delta I_{dc}}{\Delta \omega_5} \right|_{\Delta \alpha_R=0} \quad IR = \left. \frac{\Delta I_{dc}}{\Delta \alpha_R} \right|_{\Delta \omega_5=0} \quad TW = \left. \frac{\Delta T_e}{\Delta \omega_5} \right|_{\Delta \alpha_R=0} \quad TR = \left. \frac{\Delta T_e}{\Delta \alpha_R} \right|_{\Delta \omega_5=0} \quad IREG = \left. \frac{\Delta \alpha_R}{\Delta \xi_R} \right|_{\Delta \omega_5=0} \quad 5.1$$

Where,

IREG: the DC current regulator's transfer function

TW: transfer function due to AC transmission system

$\Delta \alpha_R$: Rectifier's firing angle variation

$\Delta \omega_5$: generator angular velocity (speed deviation)

ΔI_{dc} : DC current deviation

SSDC: SSDC transfer function

The design of an SSDC requires consideration of several transfer functions in the DC current control circuit. IR represents the transfer function, which establishes the link between the converter's DC current and its firing angle. Additionally, this transfer function controls everything related to the AC strength and inverter controls. The simplified block diagram of the transfer functions taken from the general diagram in Figure 5-3 can be represented, as shown in Figure 5-4.

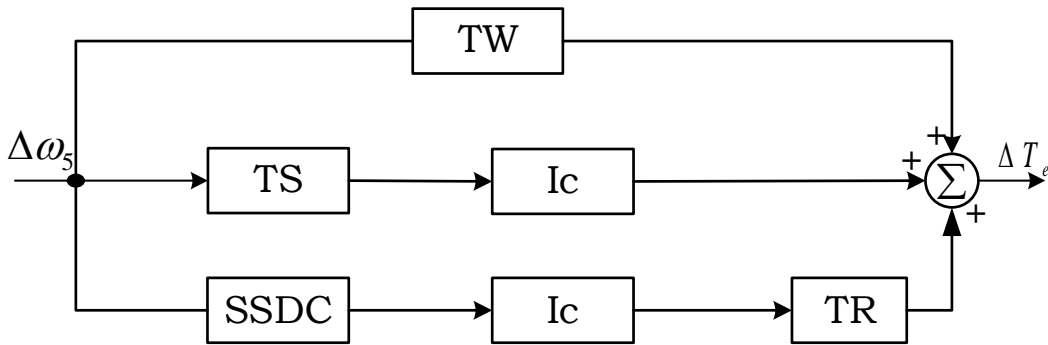


Figure 5-4: SSDC path isolation [139, 142]

Transfer functions in Figure 5-4 can be written as follows:

$$TS = -(IW)(IR) \quad 5.2$$

$$I_c = \frac{(IREG)(IR)}{1 + (IREG)(IR)} \quad 5.3$$

Where,

TS: transfer function of the HVDC system characteristics

I_c : Current control loop transfer function

The simplified circuit diagram's unique aspect in Figure 5-4 is that the SSDC is separated from the other transfer paths. The mechanism of Figure 5-4 contains three transfer paths, all contributing to electrical damping within the system. In this control scheme, the current control paths known as IC are found in two transfer paths while one (i.e., TW) is not provided with IC. Due to their reliance on HVDC controls, the two lower transfer paths typically generate negative damping within the parallel AC / DC system. On the other hand, the upper path, TW, takes into consideration the electric damping torque resulting from the AC transmission system (i.e., series capacitors) and inherent load characteristic, which usually does not rely on HVDC controls. The control path in the middle is directly linked with the firing angle change due to the AC network's fluctuations induced by the generator's angular velocity variation. The generator's angular velocity variation usually causes torsional interaction between the turbogenerator set and HVDC controls [28, 142]. The following equation describes the basic idea of an SSDC, which consists of providing an electromagnetic torque in phase with the rotor speed deviation by generating compensation for the phase lag due to IC and TR transfer functions.

$$\frac{\Delta T_e}{\Delta \omega_s} = D_e = (SSDC)(I_c)(TR) \quad 5.4$$

$$SSDC = \frac{D_e}{(I_c)(TR)} \quad 5.5$$

5.3.4 HVDC-based SSDC Design Block Diagram

Figure 5-5 displays the configuration of the SSR damping system used in this work. This block diagram was taken from [97]. This mitigation technique is made up of two compensators, namely PSS and SSDC. It should be recalled that the use of PSS aims to control the electromechanical Mode 0, and the SSDC seeks to stabilize the other unstable oscillatory modes. The research typically uses two fundamental approaches of damping controller design: the broad bandwidth approach and the narrow bandwidth approach. A wide-bandwidth damping controller typically contains a single-mode channel whose target frequency is often that of the most unstable torsional mode. The narrow bandwidth damping controller typically requires correct and accurate knowledge of the turbogenerator shaft's torsional frequencies and model. Usually, the narrow bandwidth damping controller consists of a multimodal structure controlling each torsional mode individually.

Furthermore, SSR damping devices can use input signals that can be selected as a local system variable (e.g., line power, node voltage, or frequency). The input signals can also be chosen as a remote system variable (e.g., generator speed deviation) or as both. Selecting these parameters depends on various factors, such as efficiency, cost, and accessibility. Local variables tend to be the most preferred since they are available at low prices, but sometimes they are devoid of specific torsional mode

characteristics, leading to controller inefficiency. Several researchers prefer using the rotor speed deviation because of its features based on the turbine-generator shaft's torsional oscillatory modes [135]. Rotor speed deviation also has drawbacks. However, because of its primary advantage based on its dynamic characteristic equipped with all torsional oscillatory modes' features, the rotor speed deviation was chosen as a feedback signal for both SSDC and PSS. Compared to the work conducted in chapter 4, an ST1A type excitation system and PSS are incorporated in the SSR mitigation block diagram. The parameters of ST1A are the same as in [134]. The PSS-designed parameters have been proposed in [97].

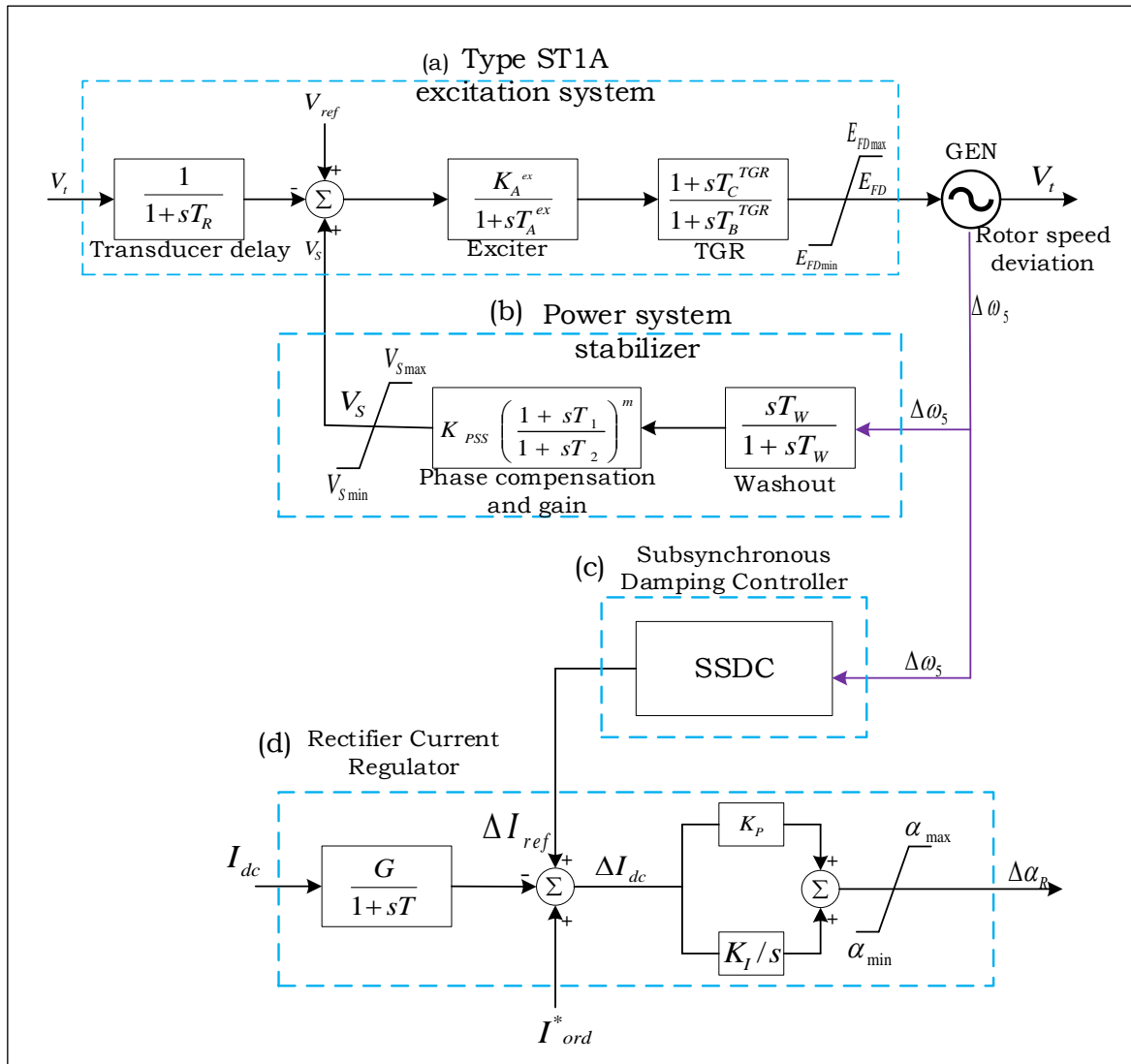


Figure 5-5: Block Diagram of Excitation Control System and Rectifier Current Regulator with two Compensators (PSS and SSDC) [97, 144]

5.3.4.1 HVDC-based Single-Mode Damping Controller (SMDC).

A single-mode damping controller (SMDC) works much like a PSS. These two devices have identical interfaces, although they are slightly different in function. Unlike PSS used for low-frequency oscillation damping, the object of the SMDC used in this thesis is to mitigate the natural torsional frequencies of the turbogenerator shaft. Figure 5-6 displays the SMDC configuration adopted in the study. The lead-lag design is selected to generate the phase compensation as it provides ease of online tuning and ensures system stability. The washout signal is the damping controller's first element, acting as a high pass filter with a time constant T_w . Typical values of T_w range between 1s-20s [135, 145]. The lead-lag block plays a crucial role in compensating for the phase difference between the generator speed deviation and the electromagnetic torque at the interest frequency.

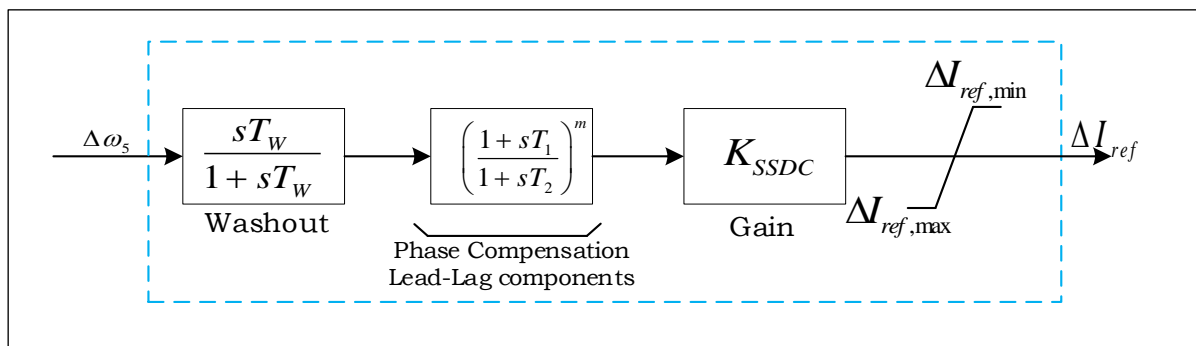


Figure 5-6: Single-Mode Damping Controller Configuration (SMDC) [94, 97, 99]

5.3.4.2 HVDC-based Multimodal Damping Controller (MMDC).

5.3.4.2.1 Introduction

Due to single-mode damping controllers' limitations to effectively mitigate torsional oscillations from various sources, such as power grids equipped with series compensated transmission lines and HVDC or FACTS devices, it is generally advised to use multimodal damping controllers. In [28], Padiyar proposed two solutions to the SSO problem in a parallel AC-DC system. He first suggested that the problem can be solved by modifying the current control loop (the firing angle control loop) or setting up a supplementary controller if instability persists. However, he suggested two configurations for the supplementary controller: the single-mode broad bandwidth damping controller discussed in the previous section and the multimodal narrow bandwidth s damping controller [28].

The MMDC consists of several modal controller channels allowing the monitoring of each mode. Each control channel acts as a single-mode controller to stabilize its corresponding torsional frequency in the TG shaft. Therefore, the multimodal controller requires precision on the torsional frequencies of each mode of the TG shaft. Previous research has shown that adding proper auxiliary controls to an HVDC unit parallel to a resonant AC line would be enough to solve the SSO question in the resulting parallel AC-DC system, regardless of the source of instability. (i.e., series capacitor or HVDC controls) [99,

100]. Huang [146] and Iravani [100, 101] proposed using the narrow bandpass multimodal damping controller to stabilize torsional oscillations in power networks subjected to multiple SSO sources. Huang applied a static synchronous series capacitor (SSSC)-based supplementary damping controllers to mitigate SSR in a power grid equipped with the conventional series capacitor and an SSSC. However, Iravani applied multimodal damping controllers to suppress SSR in parallel AC-DC systems. According to [28, 97, 100], both the HVDC tie and the series-compensated transmission line can contribute to SSO in a parallel AC-DC system. In 1989 and 1993, The MMDC structure was designed to receive feedback signals from the shaft's modal speed [100, 101]. Since measuring the shaft's modal speed was impossible, these two authors used linear approximations of the shaft speed deviations to produce signals with modal characteristics comparable to the corresponding shaft's modal speed.

In the same vein, proper HVDC controls are sufficient to stabilize SSO/SSR [99]. More recent research on HVDC control-based damping controllers has used the multimodal structure using the rotor speed deviation as a feedback signal, especially since it has all the TG shaft's modal characteristics [93, 95, 139, 143]. In this thesis, due to the rotor speed deviation modal characteristics, we opted for the HVDC controller shown in Figure 5-7, mainly due to its effective performance. Nowadays, PSCAD also provides enough components, such as bandpass filters and a washout block, to process the rotor speed deviation feedback signal. Thus, To extract the TG shaft's modal characteristics, the structure includes a washout signal acting as a high pass filter only to allow subsynchronous frequency signals to pass through it. Also, the device comprises a well-tuned bandpass filter in each modal channel to enable the processing of each TG shaft modal frequency component, which is most important in determining the modal characteristics from the rotor speed deviation. The controller also has a phase compensation block to correct the phase difference between the rotor speed deviation and the electromagnetic torque. It also contains proportional gains to provide oscillation damping [93, 95].

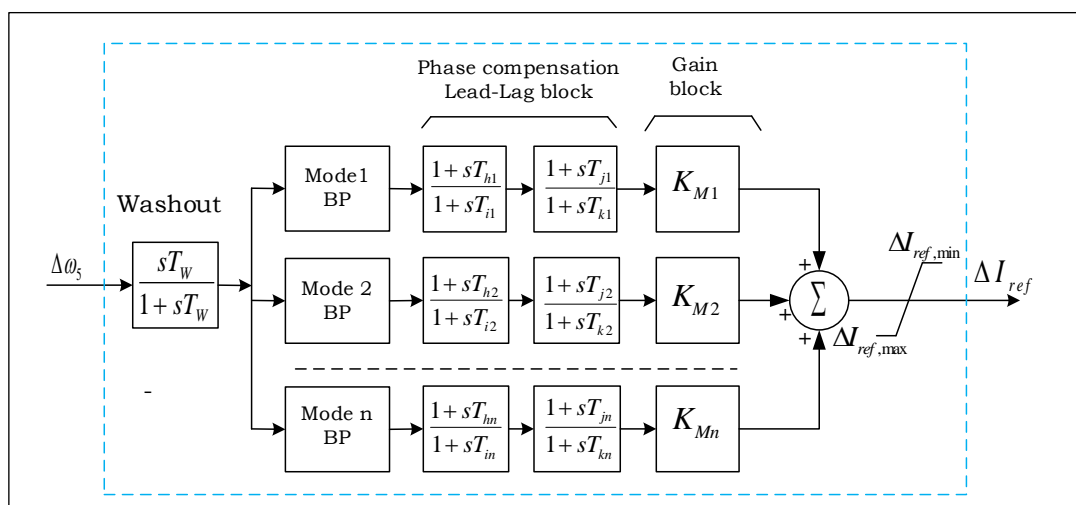


Figure 5-7: Multi-Modal Damping Controller Configuration (MMDC) [93, 95, 143]

5.3.4.2.2 Designing Purpose

The single-mode damping controller (SMDC) is known for its efficiency in damping unstable torsional modes resulting from a particular source, e.g., the series capacitor in a series-compensated transmission line. Using an MMDC to control every oscillatory torsional mode is typically highly recommended when a power system, fitted with series capacitors and HVDC controls or FACTS devices, is subjected to various SSO sources [146]. In [146], the single-mode damping controller was ineffective in damping torsional oscillations resulting from both the static synchronous series capacitor and the series capacitor. However, the single-mode damping controller has also been extensively used to stabilize torsional oscillation in parallel AC-DC grids [97, 99] and radial HVDC links, i.e., HVDC operating without a parallel series-compensated AC line [91, 94]. As previously reported, the use of multimodal controllers on parallel HVDC-AC systems whose AC line comprises series capacitors was indicated in [100, 101].

Figure 5-7 shows that a multimodal controller has multiple single-channel controllers depending on the torsional modes for which they are designed. Interactions between its modal sub-controllers with the TG shaft are significant drawbacks of an MMDC. Thus, this section analyzes the performance of SMDC applicable to the study framework in [97] on operating points exposed to instability from AC and DC systems based on the theory reported in [146] involving power systems subjected to several sources of torsional oscillation. The adverse impact of HVDC ties on subsynchronous torsional oscillation has been extensively discussed in the previous sections. Usually, in a parallel AC-DC system, the cause of the subsynchronous torsional oscillation source is a bit difficult to know right out of the gate, mainly as many parameters, both on the series compensated transmission line side and on the HVDC control side, contribute to this instability. However, several studies have shown that the most influencing factor would be the AC line's series capacitor without ignoring that HVDC controls can also be seen as a potential SSO source [28]. Torsional interactions between an HVDC tie and the nearby turbogenerator shafts, among all the parameters described in the previous sections, are mainly due to the inappropriate current regulator parameters or their configuration, typically on the rectifier side. More details on torsional oscillation resulting from HVDC systems can be found in [28, 92]. The primary objective of multimodal damping control is to suppress SSO from various sources adequately.

5.3.4.3 SSDC Design Procedure based on Test Signal and Phase Correction Methods

As reported in the previous sections, the TG shaft at a particular subsynchronous frequency oscillates when the difference in phase between the induced electromagnetic torque and rotor speed deviation is above the range $\pm 90^\circ$. However, the phase correction method makes it possible to compensate for this phase difference by providing the angle required for this electromechanical stability condition to be fulfilled. This phase angle difference is determined using the test signal method realized by the time-domain simulation proposed in [96, 147]. The test signal method also allows the transfer function of

the SSDC described in equation (5-10) to be established. The transfer path in Figure 5-4, leading to the SSDC transfer function expressed in equation (5-10), can be summarized as follows (see Figure 5-8).

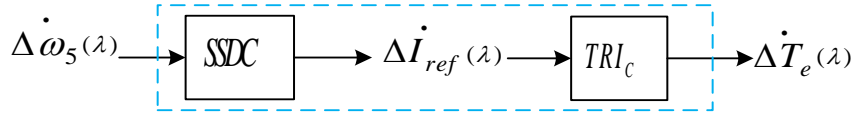


Figure 5-8: Simplified Transfer Scheme for Phase Correction Analysis [96, 144]

In Figure 5-8, the generator speed deviation ($\Delta\omega_5$) is used as a feedback signal to SSDC, whose output is the DC converter's reference current deviation (ΔI_{ref}). Thus, TRI_c receives the resulting current deviation from the damping controller as a feedback signal to generate an extra electromagnetic torque in phase with the rotor speed deviation ($\Delta\omega_5$). Considering (f_n) as the nominal frequency of the power grid and Ψ as a constant varying within $0 < \Psi < 1$, for each torsional frequency mode Ψf_n , the primary objective of SSDC is to generate an extra electromagnetic torque ($\Delta T_e(\Psi)$) having a difference in phase within $\pm 90^\circ$ with the rotor speed deviation ($\Delta\omega_5(\Psi)$). As soon as this condition is met, positive damping will be observed in the TG shaft's torsional dynamics [96, 144].

Figure 5-8 shows that two key parameters, namely SSDC and TRI, require careful attention as they play a critical role in SSO stability. The phase difference between $\Delta\omega_5(\Psi)$ and $\Delta T_e(\Psi)$ comprises two parts: the part between $\Delta T_e(\Psi)$ and $\Delta I_{ref}(\Psi)$ denoted as $\angle TRI_c(\Psi)$ and that between $\Delta I_{ref}(\Psi)$ and $\Delta\omega_5(\Psi)$ denoted as $\angle SSDC(\Psi)$. Note that the primary objective sought in this schematization is to have $\angle SSDC(\Psi) + \angle TRI_c(\Psi)$ in the range $\pm 90^\circ$ for any subsynchronous oscillatory mode Ψf_n , [96, 144]. The transfer function $\angle SSDC(\Psi)$ provides the required angle to compensated for $\angle TRI_c(\Psi)$. These techniques have been used in many recent studies to obtain the optimal parameters of HVDC-based damping controllers [96, 139, 143].

5.3.4.3.1 Single-Mode Damping Controller Design Procedure

The design procedure of the HVDC-based damping controller was established following the syntheses made from [94, 96, 144, 146]. The following steps were undertaken to design the single-mode damping controller :

- **Step 1:** First, we identified the phase difference $\angle TRI_c(\Psi)$ between $\Delta I_{ref}(\Psi)$ and $\Delta T_e(\Psi)$ using the time-domain simulation-based test signal method. This step was obtained by injecting a small amplitude sinusoidal test signal into the converter's DC current control loop (e.g., 0.05 pu) at a torsional frequency of interest. After injecting the sinusoidal test signal, we ran the simulation using PSCAD and measured $\angle TRI_c(\Psi)$ using Fourier resolutions. We temporarily set the generator inertia constant to a very high value to prevent the steady-state simulation from harming generator speed.

- **Step 2:** After determining the phase difference $\angle TRI_C(\Psi)$ between the induced electrical torque and the converter's reference DC current, we used the phase correction method to evaluate the characteristic angle (i.e., $\angle SMDC(\Psi)$) of the SMDC utilizing the lead-lag components. This step made it possible to develop a compensator with the appropriate phase (lead or lag) to correct the phase difference. Note that If $\Delta \dot{T}_e(\Psi)$ leads $\Delta \dot{I}_{ref}(\Psi)$, a lag compensator is required, and if $\Delta \dot{T}_e(\Psi)$ lags $\Delta \dot{I}_{ref}(\Psi)$, then a lead compensator is needed.
- **Step 3:** We appropriately adjusted each torsional oscillatory mode's proportional gain after the system met the subsynchronous frequency stability requirement. This step adequately induced a positive damping contribution from the damping controller to the turbogenerator shaft's torsional dynamics.
- **Step 4:** We finally built the controller with all its necessary components (see Figure 5-6)

5.3.4.3.2 Multi-Modal Damping Controller Design Procedure

The configuration shown in Figure 5-7 is the basis for designing the multimodal damping controller in this study [93]. Usually, using a single-mode damping controller does not fulfill the absolute need for stability in a multimodal instability system. The single-mode damping controller can provide its corresponding frequency component and other modes with positive damping without completely stabilizing the system. It can also interact negatively with these oscillatory modes. Therefore, the design of the multimodal damping controller shall follow the specifications set out below [96, 146]:

- The controller must be designed to damp out more than one mode; it must be a multi-modal controller.
- Each single-channel controller must be designed to add damping to its mode while minimizing its adverse impact on the other torsional modes.

Referring to the multimodal controller's configuration shown in Figure 5-7, the controller consists of a set of single-mode controllers designed to control each particular torsional mode. However, every single-mode damping controller is equipped with a bandpass filter for each specific frequency component's extraction. The rotor speed deviation signal filtered via the washout block also passes through the bandpass filter. These bandpass filters allow the frequency of interest to pass through the single-mode channel [96, 146]. Signals reflecting the output modulations of single-mode damping controllers are added to create the supplementary subsynchronous damping controller signal (ΔI_{ref}) to the rectifier current regulator to correct the phase difference between the electromagnetic torque and rotor speed deviation.

This work focuses on the system suggested in [40, 97] but uses two different HVDC operating points with an X_S set at 0.5 pu, resulting in an inverter station with moderate stiffness. As in [97], despite the

variety of operating points used in varying the compensation level from 20% to 80%, three torsional modes were found to be unstable, namely Mode 1 (15.99 Hz), Mode 3 (25.25 HZ), and Mode 4 (32.28Hz). Thus, this study extends on [56] to investigate the MMDC design aimed at stabilizing the three unstable modes while avoiding destabilizing the condition of Mode 2 (20.25 Hz). The procedure for obtaining the controllers' optimal design parameters was established according to the multimodal structures' design process proposed in [96, 139, 143, 146].

The following steps were undertaken for the multimodal damping controller design:

- **Step 1:** The multimodal damping controller design started from the design of each single-mode damping controller's bandpass filters. In this study, each SMDC has a band-pass filter based on the mode's torsional frequency to be damped. This step allowed every single-mode controller to focus on its target torsional frequency component. The bandpass filters' parameters were obtained under open-loop conditions by adjusting their gains and damping ratios to get the best damping results.
- **Step 2:** We measured the phase angle difference $\angle TRI_C(\Psi)$ between $\dot{\Delta}I_{ref}(\Psi)$ and $\Delta\dot{T}_e(\Psi)$ using the test signal method described in the previous section and determined the time constants ($T_1, T_2, \dots T_N$) of the single-mode controllers using the phase correction method to compensate for phase angle $\angle TRI_C(\Psi)$.
- **Step 3:** We determined the gain (K_{M1}) of the first single-mode damping controller by experimentally closing its control loop while leaving those of the other two. We took several K_{Mi} values into consideration and chose only the one that offered significant positive damping without affecting the stability of the other dominant torsional modes, i.e., Mode 3 and Mode 4 (again based on inspection of time-domain and FFT results).
- **Step 4:** The other controller gains, K_{M3} , and K_{M4} were also determined similarly; in turn

5.4 Simulation and Discussions

In the study system displayed in Figure 5-1, PSCAD software was used to conduct the time domain simulation to analyze damping controllers' ability to solve the problem associated with torsional oscillations. The system was subjected to a three-phase-to-ground fault applied at 1.5 s for a period of 75 ms. The generator was activated at 1.1 sec while the multi-mass system at 1.4 sec. As a reminder, the rectifier station and the inverter station are respectively in CC control mode and CEA control mode. Equidistant pulse control was selected for the firing of thyristors. In all cases, the shaft's mechanical damping is neglected to represent the worst situation, and the governor dynamics are not included in the analysis.

The ST1A Type excitation system replaces the original constant excitation system with the parameters listed in Appendix F [134]. The PSS parameters were taken from [97]. The damping controllers' performance was evaluated considering two HVDC operating points. The value X_S is kept at 0.5 pu with R_S equals 6% of X_S leading to an inverter station with moderate stiffness. As we explained in Chapter 4, this X_S value was chosen due to the adverse torsional oscillations it induces in the parallel AC-DC system. Also, this choice was made to investigate the controller's performance under the resulting system response. Thus, this research only deals with moderate stiffness inverter AC buses. Appendix A and Appendix B provide the parameters for the TG set and transmission lines. AC filters and capacitor banks provide reactive power compensation at the rectifier and inverter stations.

The following remarks should be kept in mind before investigating the torsional oscillation response in the parallel AC-DC system [13]: (a) The TG shaft's torsional dynamics respond differently at each operation point (i.e., percentage of compensation). The adverse impact of torsional oscillation depends on the operating point's characteristics. (b) The inverter station generally has no significant effect on the TG shaft's torsional dynamics. However, this assumption holds when the power system isn't a parallel AC-DC scheme or a parallel AC-DC scheme whose inverter station is connected to a stiff bus. (c) Adverse torsional oscillations considerably affect the parallel AC-DC system when the electrical coupling between the inverter station and the generator is strong (i.e., a higher compensation level). The generator-inverter electrical coupling becomes strong when the AC line's power becomes comparable to the DC line's.

5.4.1 System Response for the Parallel AC-DC System with $P_{HVDC} = 0.4847$ pu

Based on the stiffness equation in Chapter 2, equation 4.49, the DC power has an impact on the ESCR. We set DC power to 0.4846 p.u leading to an ESCR=3.20. ESCR calculations are given in Appendix C. The operating points discussed in this chapter are the same as those in Chapter 4. however, due to the torsional oscillation distinct responses in each scenario, we rearranged them as shown in Table 5-1. The current regulators' parameters are provided in Table 3.1, except gains (K_{PID}). We considered $K_{PID}=10$ for cases (a) and (b) and $K_{PID}= 5$ for cases (c) and (d). We incorporated the Power System Stabilizer [97] in all cases through the IEEE ST1A [134]. Per-unit base is 892.4 MVA, 539 kV.

Table 5-1: Operating Points (Case Study) with $P_{dc}=0.4846$ pu

Case study	Pdc=0.4846pu							
	N°	K (%)	P_g (pu)	PF	V_g (pu)	$V_{a, Mag}$ (pu)	$V_{a, Ph}$ (deg)	$V_{b, Mag}$ (pu)
A	70	0.90	0.900	1.007	0.968	23.55°	0.956	26.9°
B	61	0.80	0.900	1.007	0.964	24.90°	0.943	23.64°
C	41	0.70	0.900	1.007	0.968	21.90°	0.923	20.18°
D	23	0.67	0.900	1.007	0.968	27.64	0.914	19.72

5.4.1.1 HVDC-based Single Mode Damping controller (SMDC)

The single-mode damping controller is known for its efficiency in stabilizing torsional modes that generally have only one source, e.g., the transmission line series capacitor [146]. However, it has also been routinely used in parallel AC-DC links, as in [97, 99], where torsional oscillation originated from both series capacitor and HVDC controls. The single-mode damping controller and the Power System Stabilizer are intended to be incorporated into the block diagram displayed in Figure 5-5 to form a complete SSR damping system capable of controlling the inertial mode (Mode 0) and the unstable torsional modes.

5.4.1.1.1 SMDC and PSS Applied to Case (a)

As illustrated in Figure 5-6, the single-mode damping controller configuration is made up of a signal washout, a gain block, and a phase compensation block. The phase compensation block, also called lead-lag block, is designed to compensate for the phase difference $\angle TRI_C$ related to a subsynchronous frequency mode of interest. At this operating point, the AC line's compensation level is set at 70%, and the generator delivers a power of 0.9 pu distributed over the two parallel lines with a DC power fixed at 0.4847 pu. The power factor is set at 0.9. The operating point indeed is categorized by a dominant Mode 1 instability. Therefore, the design of the Mode 1 (15.99 Hz) damping controller was carried out as follows, in compliance with the procedure outlined in section 5.3.4:

In the converter's direct current control loop, a sinusoidal test signal of 15.99 Hz and an amplitude of 0.05 pu (i.e. $\Delta I_{ref} = 0.05 \sin 15.71t$) was applied, and the induced electrical torque was measured by time-domain simulation. The applied sinusoidal test signal is displayed in Figure 5-9.

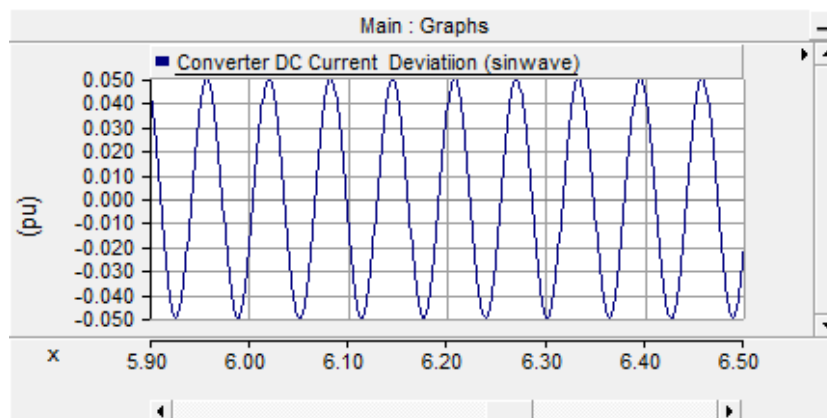


Figure 5-9: Mode 1 (15.99 Hz) Sinusoidal Test Signal

Therefore, the measured phase difference $\angle TRI_C(\Psi)$ between the electromagnetic torque increment phasor variable $\Delta \dot{T}_e(\Psi)$ and the converter's reference direct current increment phasor variable $\Delta \dot{I}_{ref}(\Psi)$ resulting from Fourier resolution of ΔT_e and ΔI_{ref} is displayed in Figure 5-10. Figure 5-10 shows that

the phase difference between ΔI_{ref} and ΔT_e at 15.99 Hz (Mode 1) is 130° . Therefore, the lead compensator requires 130° to correct this lagging. Following the lead-lag correction principle stated in Appendix G, the resulting optimal lead-lag compensator parameters of the SMDC designed for Mode 1 (15.71 HZ) are shown in equation (5.11). The washout signal's time constant is 10 sec in all the cases.

$$SMDC(s)_{M1} = 4 \left(\frac{1 + 0.044896908s}{1 + 0.002206617s} \right) \times \left(\frac{1 + 0.044896908s}{1 + 0.002206617s} \right) \quad 5.6$$

The bode diagram of the SSDC is displayed in Figure 5-11. From Figure 5-11, it can be seen that the single-mode damping controller provides the required phase compensation.

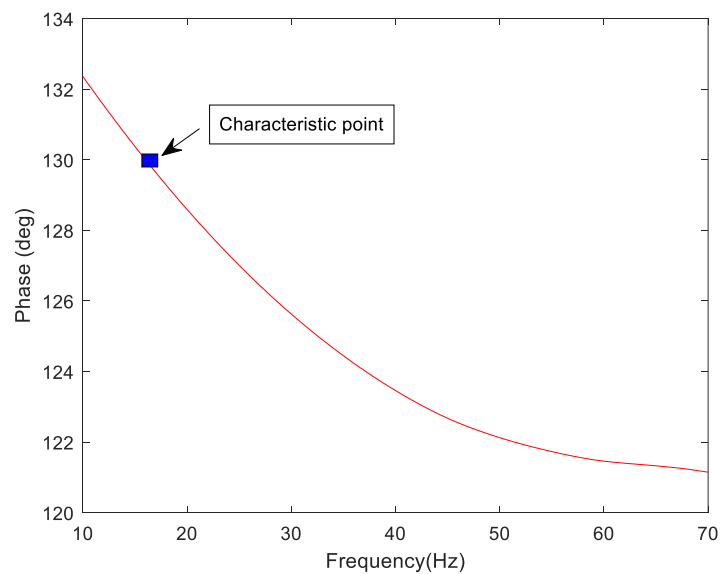


Figure 5-10: Phase-Frequency Characteristic Curve for Mode 1

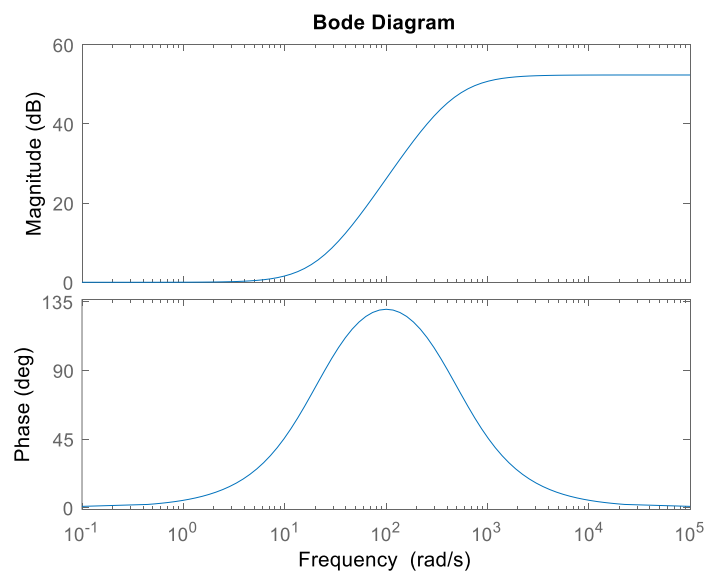


Figure 5-11: Mode 1 Damping Controller's Bode Plot

Figure 5-12 shows the power system's time domain response corresponding to case (a). The time-domain response graph includes the power system's signals before and after the damping compensators' addition. It can be seen that the dynamic system is prone to torsional oscillations that worsen in amplitude while the compensators are out of operation, that is, without PSS and SMDC. By observing the rotor speed that is generally fitted with all the TG shaft's modal characteristics, it can be seen that its deviation ranges from about -100 rad/sec to almost 100 rad/sec. This torsional instability is also felt in all the sections of the TG shaft. There is an extreme degradation of power transfer when compensators are out of service. However, following the application of PSS [97] for the inertial swing Mode 0 and SSDC for Mode 1 (15.99 Hz), a considerable improvement in the torsional dynamics of the TG shaft can be observed. The oscillations observed in the AC and DC lines are also considerably reduced.

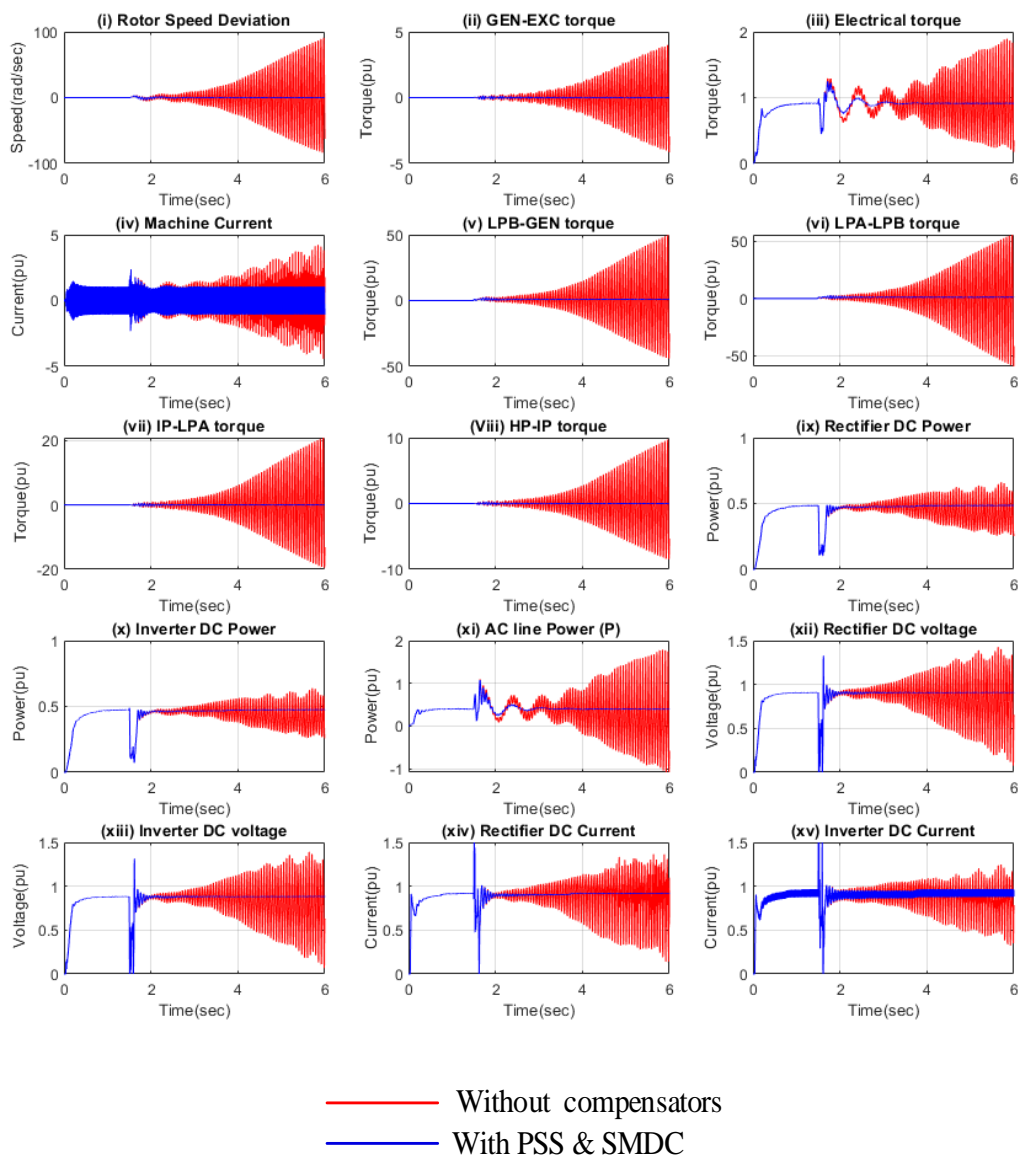


Figure 5-12: System Response in Case (a) following a 75 ms 3-phase short-circuit on the resonant AC line ($K=0.7$, $P_g=0.9$ pu, $P_d=0.4846$ pu, $PF=0.9$)

Therefore, the time domain signals shown in Figure 5-12 reflect the single-mode damping controller's efficiency to stabilize SSR at this particular operating point. Due to the substantial reduction in torsional oscillation, compensators have a relatively positive impact at this point of operation.

Figure 5-13 displays the FFT results of rotor speed deviation illustrating the torsional behavior of the operating point, the characteristics of which relate to case (a) with the compensators out of service. The FFT capture was made over three-time intervals: 1.5 sec to 3 sec, 3.0 sec to 4.5 sec, and 4.5 sec to 6.0 sec. These results indicate a sharp rise in the Mode 1 (15.71 Hz) amplitude obtained over three intervals. Mode 1 torsional amplitude growth started from a value of 5,152 pu in the 1.5 s to 3.0 s interval and reached 1,139,000 pu between 4.5 s to 6.0 s. This torsional instability poses a significant risk to the power system operation and, even more, to the turbogenerator shaft's reliability.

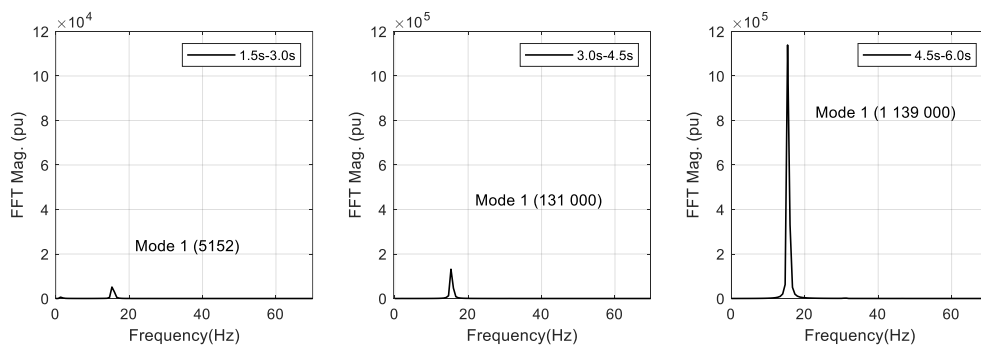


Figure 5-13: Rotor speed deviation's FFT results in case (a) without compensators

The FFT results of rotor speed deviation shown in Figure 5-14 demonstrate the impact on damping torsional oscillation of the commissioning PSS and single-mode damping controller. Note that the oscillatory amplitude trend decreases from 1.5 s to 6.0 s. For this operating point's stability, the damping compensators' commissioning has proven efficient. Single-mode damping controller performance is confirmed by reducing the Mode 1 oscillatory amplitude (15.99 Hz) in the FFT results' time intervals. Therefore, the FFT outcomes of Figure 5-14 validate the time-domain results of Figure 5-12 after applying the damping compensators (SMDC and PSS).

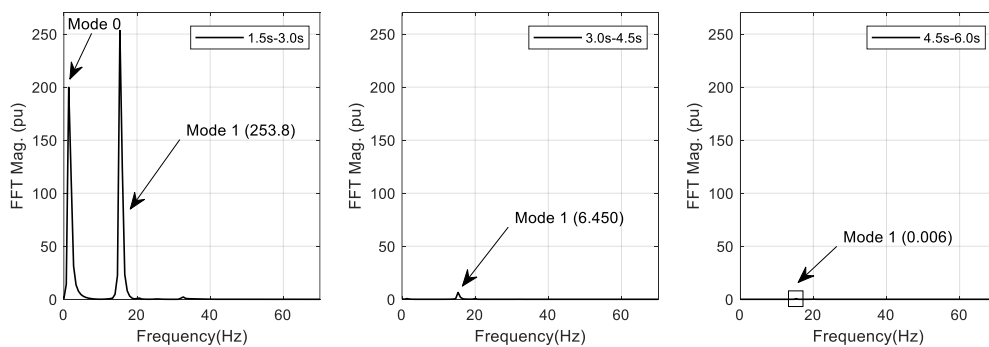


Figure 5-14: Rotor speed deviation's FFT results in case (a) with SMDC (designed for Mode 1) and PSS

5.4.1.1.2 SMDC and PSS Applied to Case (b)

The generator provides a power of 0.80 pu at this operating point, corresponding to 61 percent compensation. The turbogenerator system's torsional behavior is characterized by extreme Mode 1 instability. Therefore, Mode 1 (15.71Hz) damping controller is required. Following the methodology outlined in subsection 5.3.4, the resulting SMDC parameters are shown in equation (5.12).

$$SMDC(s)_{M1} = 3.5 \left(\frac{1 + 0.004641349s}{1 + 0.021345146s} \right) \quad 5.7$$

Figure 5-15 depicts the system's time domain response under case (b) operating conditions. It can be seen that the torsional dynamics of the turbogenerator set were prone to torsional oscillations of rising amplitude before applying the PSS and SMDC.

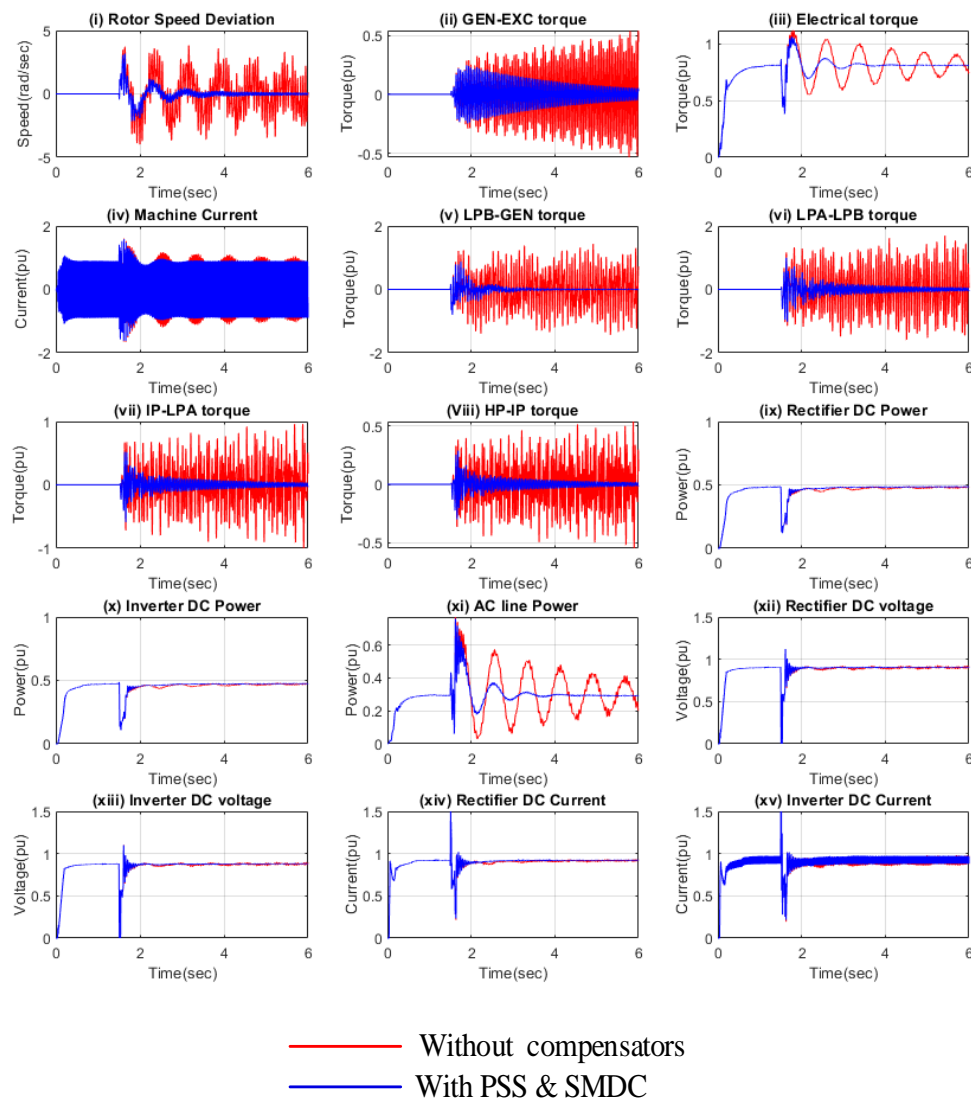


Figure 5-15: System Response in Case (b) following a 75 ms 3-phase short-circuit on the resonant AC line ($K=0.61$, $P_g=0.8$ pu, $P_d=0.4846$ pu, $PF=0.9$)

There are also large fluctuations in the synchronous machine's electric torque and the AC line's power. Figure 5-15 shows that following the PSS and SMDC, the torsional oscillations became stable. The compensators have improved the damping of the power transfer oscillations and the torsional oscillations' damping.

Figure 5-16 displays the power system's behavior through the FFT results of rotor speed deviation corresponding to case (b) without considering the compensators. A strict Mode 1 instability characterizes this operating point. Results show that the turbogenerator shaft is subjected to increasing torsional oscillations around 15.99 Hz. Figure 5.17 illustrates the positive impact of SMDC and PSS on the damping of torsional oscillations. The application of SMDC and PSS compensators has proved to be successful in mitigating, under these operating conditions, the torsional oscillations the turbogenerator shaft undergoes and the AC line's power fluctuations. Therefore, these FFT results confirm the time-domain results shown in Figure 5-15.

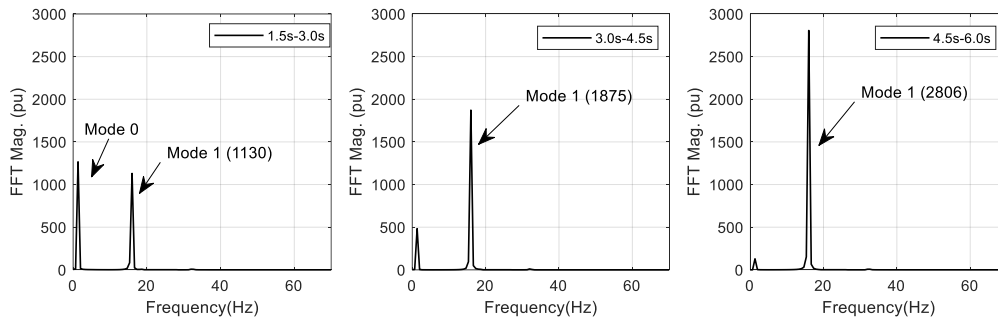


Figure 5-16: FFT analysis of rotor speed deviation for case (b) without Compensators

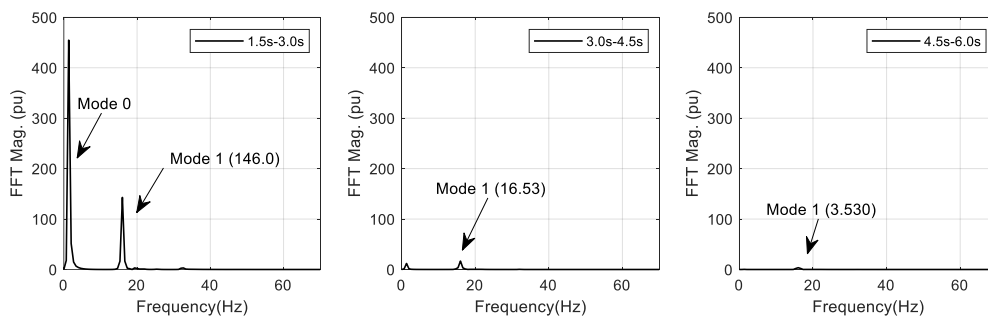


Figure 5-17: Rotor speed deviation's FFT results in case (b) with SMDC (designed for Mode 1) and PSS

5.4.1.2 Multimodal Instability with HVDC-based Single Mode Damping Controller Performance

5.4.1.2.1 Introduction

The multimodal damping controller has advantages centered on stabilizing oscillations of diverse sources. In [146], the MMDC was used to mitigate subsynchronous instability in a dual compensation system. In Ref [28], Padiyar demonstrated the risk of an HVDC link to induce SSO in radial operation

and when connected parallel to a resonant AC line. He listed various parameters that cause torsional interaction in such power systems. He observed that the AC-DC parallel system is usually subjected to torsional instability, either from the series capacitor or HVDC controls [28]. According to Padiyar and many other authors [92], HVDC controls can interact differently with nearby turbine-generator shafts. HVDC control schemes, inverter bus stiffness, current regulator settings, etc., are the main factors influencing the torsional interaction due to the HVDC system. However, only the rectifier's current regulator's parameters' influence is considered in this study.

In this chapter, single-mode controllers' performance is evaluated on the parallel AC-DC system in the same perspective as the research conducted in [146], especially since the AC-DC parallel system is subjected to multiple torsional oscillation sources [28]. Some authors have used single-mode damping controllers built based on the broad bandpass method [97, 99], and some have also used the multimodal approach built based on the narrow bandpass method [100, 101]. This section discusses the impact of single-mode controllers designed for each unstable torsional oscillation mode.

5.4.1.2.2 TG torsional response due to HVDC for case (c)

At this operating point corresponding to 41% compensation, the generator delivers 0.70 pu, of which 0.4847 pu goes to the DC line and the remaining power to the AC line. The power factor is 0.9. The rectifier's current regulator parameters are: $T_R=0.0109$, $K_R=5$, $U_{Rmax}=0.1$, and $U_{Rmin}=-0.1$.

After the fault has been applied at 1.5 s, the turbogenerator system, under these operating conditions, experiences three instability modes: Mode 1 (15.71 Hz), Mode 3 (25.25 Hz), and Mode 4 (32.285 Hz). Figure 5-18 illustrates the time-domain results for case (c) with and without the addition of the HVDC link. This investigation showed that adding the parallel HVDC link under these operating conditions excited Mode 1 (15.71 Hz) and Mode 4 (32.285 Hz), including Mode 0 (1.67 Hz). Therefore, these results show that the AC-DC parallel system undergoes unstable torsional oscillations from both the AC and DC systems.

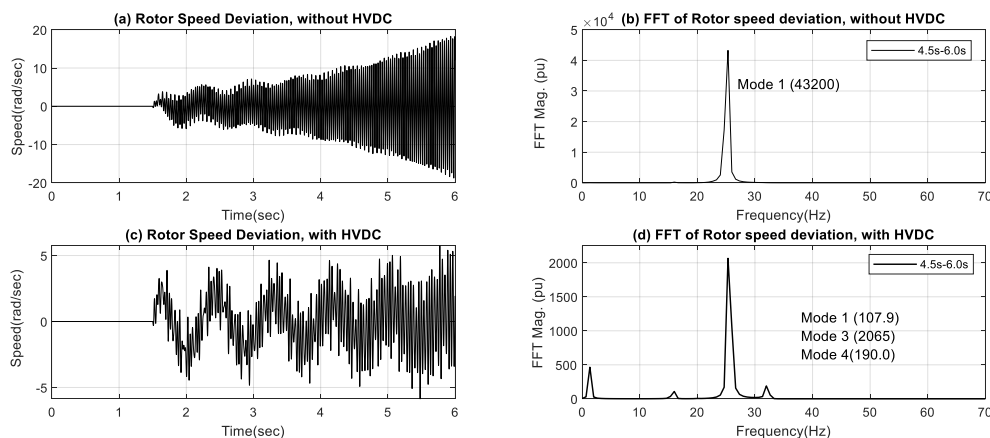


Figure 5-18: Transient response and FFT results of rotor speed deviation in case (c) with HVDC tie on and off.

5.4.1.2.3 SMDC and PSS Applied to Case (c)

This section is intended to evaluate the impact of a single-mode damping controller designed for a specific torsional mode on the damping of subsynchronous oscillation (or resonance) in the parallel AC-DC system. The parallel AC-DC system is exposed to torsional instability from various sources. Similar experiments have been performed in [146] on a system with multiple subsynchronous oscillation instability sources, namely the AC line's series capacitor, and the SSSC. In [146], the need to use suitable controllers in systems exposed to several subsynchronous oscillation instability sources has been stressed. The previous section revealed that the HVDC system's addition not only provided positive damping to the TG set's torsional dynamics, but Mode 1 (15.99 z) was slightly excited due to the inappropriate parameters of the rectifier current regulator. This operating point is, therefore, subject to three unstable modes, namely, Mode 1 (15.99 Hz), Mode 3 (25.25 Hz), and Mode 4 (32.28 Hz). However, Mode 3 (25.25 Hz) is the most extreme torsional oscillation. Therefore, equations (5.13) to (5.15) represent each SMDC's resulting parameters, following the design process explained in section 5.3.4 for these particular operating conditions.

Figure 5-19 illustrates the system's time domain response before and after applying a damping compensator set consisting of an SMDC and PSS. It can be shown that the application of each set of damping compensators affects torsional oscillations, either positively or negatively.

$$SMDC_{M1}(s) = 3.5 \left(\frac{1 + 0.004021437s}{1 + 0.024635541s} \right) \times \left(\frac{1 + 0.004021437s}{1 + 0.024635541s} \right) \times \left(\frac{1 + 0.004431541s}{1 + 0.001770553s} \right) \quad 5.8$$

$$SMDC(s)_{M3} = 4.5 \left(\frac{1 + 0.023523736s}{1 + 0.001688928s} \right) \times \left(\frac{1 + 0.023523736s}{1 + 0.001688928s} \right) \times \left(\frac{1 + 0.022439261s}{1 + 0.001770553s} \right) \quad 5.9$$

$$SMDC(s)_{M4} = 2.5 \left(\frac{1 + 0.025633583s}{1 + 0.00094834s} \right) \quad 5.10$$

Note that Mode 1 (15.99 Hz) and Mode 4 (32.28 Hz) damping controllers, including the PSS, provided positive damping to the system without stabilizing the subsynchronous oscillation. However, the Mode 4 (32.28 Hz) damping controller, including PSS, offered more effective damping than the previous damping compensator sets, but the system still seems unstable.

Feng-Wei [146] also observed that a damping controller designed for a specific torsional oscillatory mode could not provide effective damping to the power system when subjected to multiple sources of instability. Controlling designed for the less influential torsional modes is often the least effective. However, using single-mode damping controllers based on the most unpredictable torsional oscillatory mode, most HVDC-equipped power systems have resulted in better system stability [99]. It should be noted that the time domain results are generally devoid of the system's torsional modal aspects. The

influence of controllers on the oscillatory modes is complex to describe without conducting in-depth studies focused on either the system's eigenvalue analysis or signal processing. In this research, the FFT analysis was found to be successful in investigating the efficiency of damping controllers on subsynchronous oscillation damping.

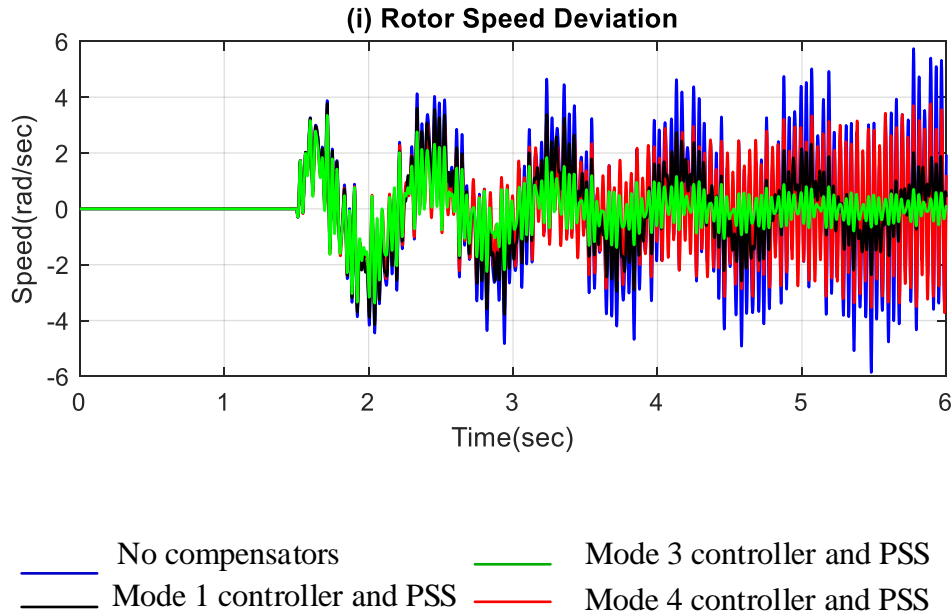


Figure 5-19: System Response for Various SMDC and PSS applied to Case (c)

Therefore, Figure 5-20 illustrates the FFT analysis of rotor speed deviation for case (c) without compensators. Increasing instability of the three oscillatory modes is observed, with a more prominent Mode 3 (25.25 Hz) peak.

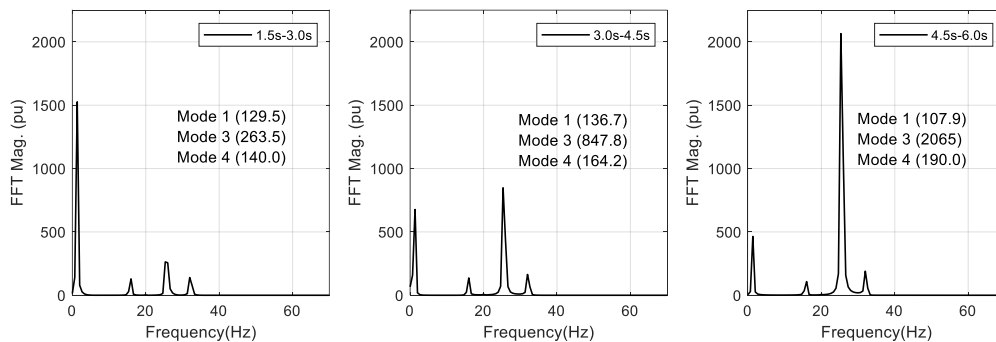


Figure 5-20: Rotor speed deviation's FFT results in case (c) without compensators

The impact of each SMDC, including the PSS, on the subsynchronous oscillation damping, is shown in Figure 5-21. Figure 5-21 (a) shows the impact of Mode 1 damping controller and PSS on the damping torsional oscillation. It has been observed that implementing the Mode 1 (15.99 Hz) damping controller, including the PSS, improved the TG shaft's oscillatory condition but did not stabilize it. The figure reveals that all the unpredictable oscillatory modes received positive damping at the end of these compensators' commissioning even though they were not stabilized.

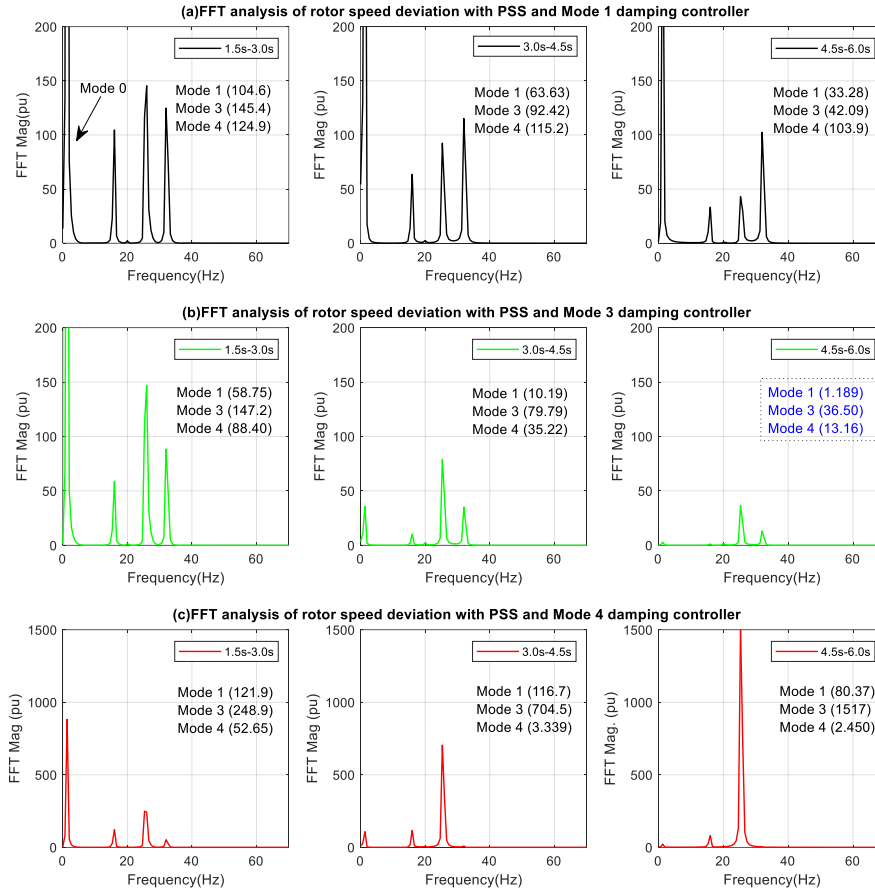


Figure 5-21: Rotor speed deviation's FFT analysis in case (c) with SMDC and PSS

The result of the Mode 3 (15.99 Hz) damping controller, including PSS, is shown in Figure 5-21(b). The Mode 3 damping controller provides more improved stability than the previous case. It can be seen in the time interval from 4.5 s to 6 s that the system's modal behavior has improved considerably. The stability of electromechanical mode 0 is also significant.

The FFT analysis of the rotor speed deviation following the application of the SMDC designed for Mode 4, including PSS, is displayed in Figure 5-21(c). The Mode 4 controller fully damped its frequency component (32.28 Hz) and provided positive damping to the system but did not stabilize its torsional dynamics. Modes 1 (15.71 Hz) and Mode 3 (25.25 Hz) were also impacted by positive damping generated by Mode 4 (32.28 Hz) damping controller. The positive damping in Mode 0 has also been significant.

These FFT results of the rotor speed deviation signals displayed in Figure 5-21 validate their corresponding time domain response in Figure 5-19. The Mode 3 damping controller, targeting damping of its corresponding modal frequency, deemed the most extreme, is the most effective and produces more effective damping relative to Mode 1 and Mode 4 controllers. However, the torsional dynamics of the system have not been fully stabilized. Therefore, the next section is devoted to MMDC performance in this case.

5.4.1.3 HVDC-based Multi-Modal Damping Controller (MMDC)

5.4.1.3.1 MMDC and PSS Applied to Case (c)

Based on the MMDC design procedure described in section 5.3.4, the parameters of single-mode controllers used in the previous section were modified slightly. The adjustment of the preceding single-mode controllers' parameters was based, in particular, on the third stage of the MMDC design since the compensation phases provided met requirements. Table 5-3 provides the optimal gains and parameters of the MMDC following step 3, which was conducted through experimental isolation of each single-channel's control loop while leaving open the remaining two. The essential precaution during this process was to avoid exciting Mode 2 (20.25 Hz). The realization of this step took into account the parameters preventing the interactions between single-channel controllers. Bandpass filters have also been incorporated into each control channel to facilitate tracking each specific torsional frequency.

The time-domain response after applying both the MMDC and PSS is shown in Figure 5-22. Figures 5-22 (i) indicate that the MMDC and the PSS have stabilized the system following the disturbance. Following these devices' applications, the rotor speed deviation's time domain response became better than that of the single-mode damping controllers shown in Figure 5-19. We notice the torsional dynamic's stability in both the AC and DC systems. The AC line's power fluctuations were also totally reduced. These findings demonstrate the MMDC and PSS's efficiency on SSO damping in the AC-DC parallel system for operating points at risk of instability of different origins.

After applying the coordinated MMDC-PSS, the FFT analysis of the rotor speed deviation shown in Figure 5-23 proves these compensators' effectiveness. In this case, the MMDC, with its benefits centered on each torsional frequency mode's specific control through the band-pass filters, provides considerable torsional stability. They have also made it possible to minimize the transient torque amplification's impact when the AC fault appears.

Table 5-2: Parameters of MMDC designed for case (c)

Controller	Lead-Lag compensators	Gains
Mode 1 Channel	$\left(\frac{1 + 0.004021437s}{1 + 0.024635541s}\right) \times \left(\frac{1 + 0.004021437s}{1 + 0.024635541s}\right) \times \left(\frac{1 + 0.004431541s}{1 + 0.001770553s}\right)$	5
Mode 3 Channel	$\left(\frac{1 + 0.023523736s}{1 + 0.001688928s}\right) \times \left(\frac{1 + 0.023523736s}{1 + 0.001688928s}\right) \times \left(\frac{1 + 0.022439261s}{1 + 0.001770553s}\right)$	7.5
Mode 4 Channel	$\left(\frac{1 + 0.025633583s}{1 + 0.00094834s}\right)$	5

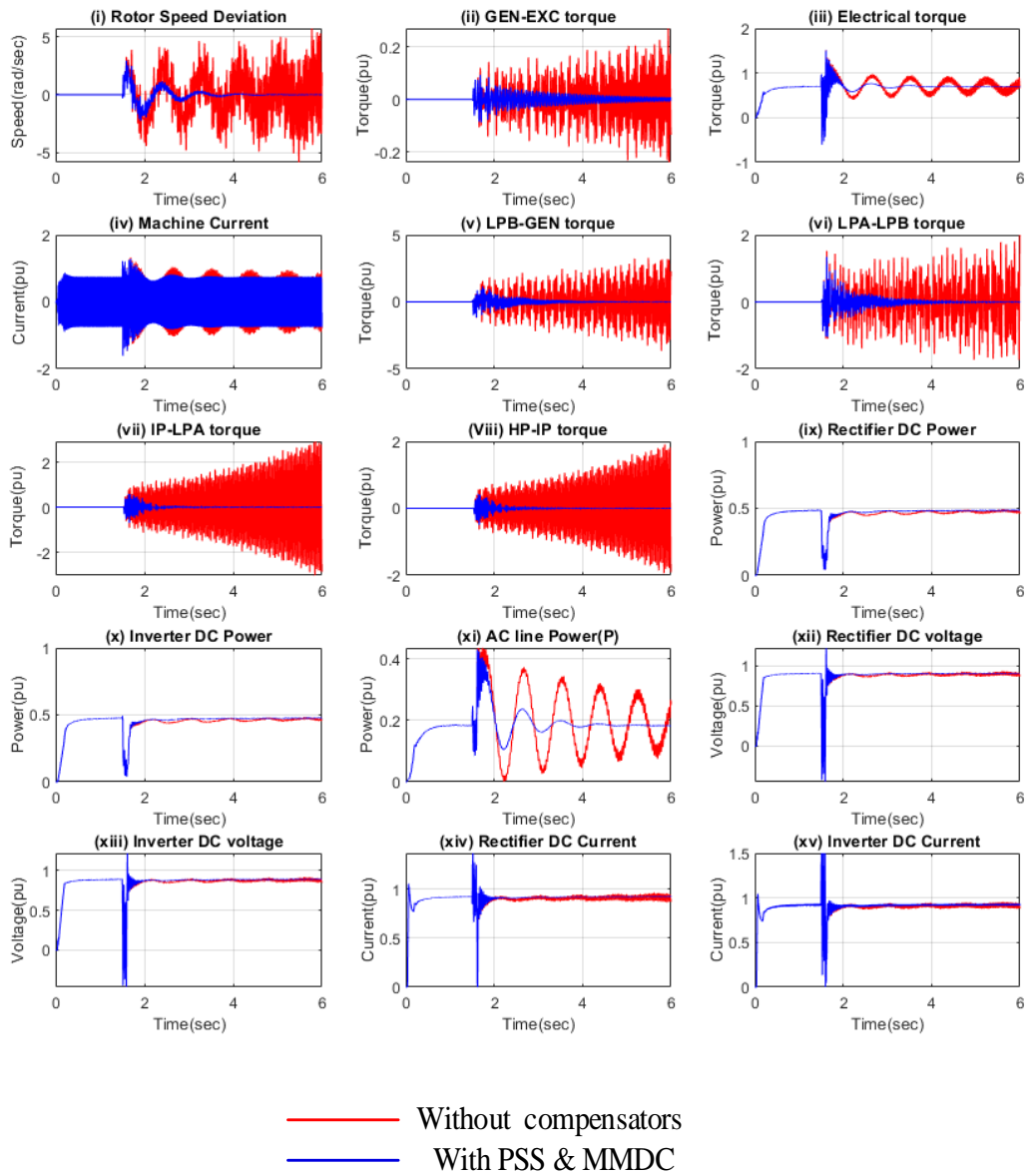


Figure 5-22: System Response in Case (c) following a 75 ms 3-phase short-circuit on the resonant AC line ($K=0.41$, $P_g=0.7$ pu, $P_d=0.4846$ pu, $PF=0.9$)

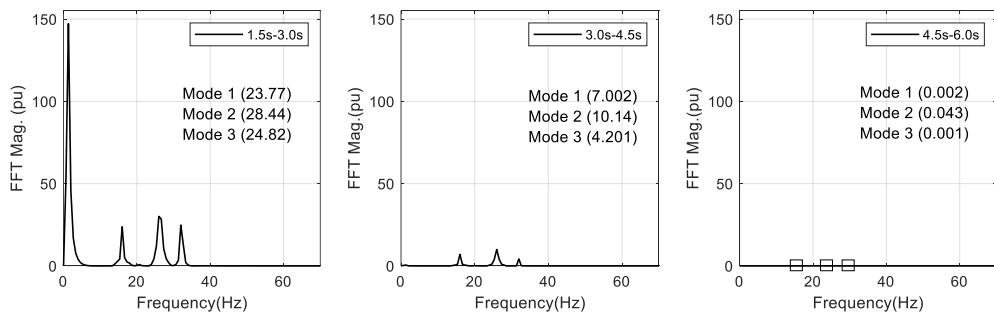


Figure 5-23: Rotor speed deviation's FFT results in case (c) with MMDC and PSS

5.4.1.3.2 MMDC and PSS Applied to Case (d)

As in the past example, this operating point's assessment led to a multimodal damping controller requirement to ensure the TG set's torsional dynamics' better stability. At this operating point, the generator produces a power of 0.67 pu with a power factor of 0.9. The AC line's compensation was set to 23 percent. The rectifier current regulator parameters at this operating point are the same as the previous case. Following the MMDC design procedure in section 5.3.4, the optimal controller parameters designed to stabilize the power system under these operating conditions are described in Table 5-4. The washout signal's time constant is 10sec.

Table 5-3: Parameters of MMDC Designed for Case (d)

Modes	Lead-Lag compensators	gains
Mode 1 channel	$\left(\frac{1 + 0.005980609s}{1 + 0.016565247s} \right)$	1.5
Mode 3 channel	$\left(\frac{1 + 0.011655031s}{1 + 0.003408820s} \right)$	4
Mode 4 channel	$\left(\frac{1 + 0.013411406s}{1 + 0.001812587s} \right)$	3.5

Figure 5-24 indicates the system's time-domain response before applying the MMDC's combination with the PSS and after. It can be seen that the system is susceptible to significant instability in the absence of compensators. The rotor speed deviation practically varies in the system's range of +/- 10 rad / s without compensators. The adverse impact is also felt in the DC and AC system variables and the TG set's torsional dynamics when the compensators are out of service. However, Figure 5-24 also demonstrates, through the time domain signals reflecting the insertion of MMDC and PSS, the positive contributions of these compensators on the SSO stability improvement. These results prove the efficiency of these controllers to damp out subsynchronous oscillation. One of the visible effects of applying these offsetting devices is the stability of the AC line. Figures 2-24 (xi) show huge power transfer fluctuations through the AC line. However, the power transfer capability was significantly stabilized following the compensators' application of MMDC and PSS.

The power system's torsional behavior at this point of operation is shown in Figure 5-25. As in [97], the power system is distinguished by three unstable torsional oscillatory modes, namely Mode 1 (15.99 Hz), Mode 3 (Mode 25.25 Hz), and Mode 4 (32.28 Hz). However, Mode 4 is the most unstable. It can be observed that the oscillations have an erratic trend over time in the absence of the MMDC and the PSS. It has been found that over time, the fluctuations have an irregular tendency with faster growth of Mode 4 (32.28 Hz) than the other two modes when the MMDC and PSS are out of service

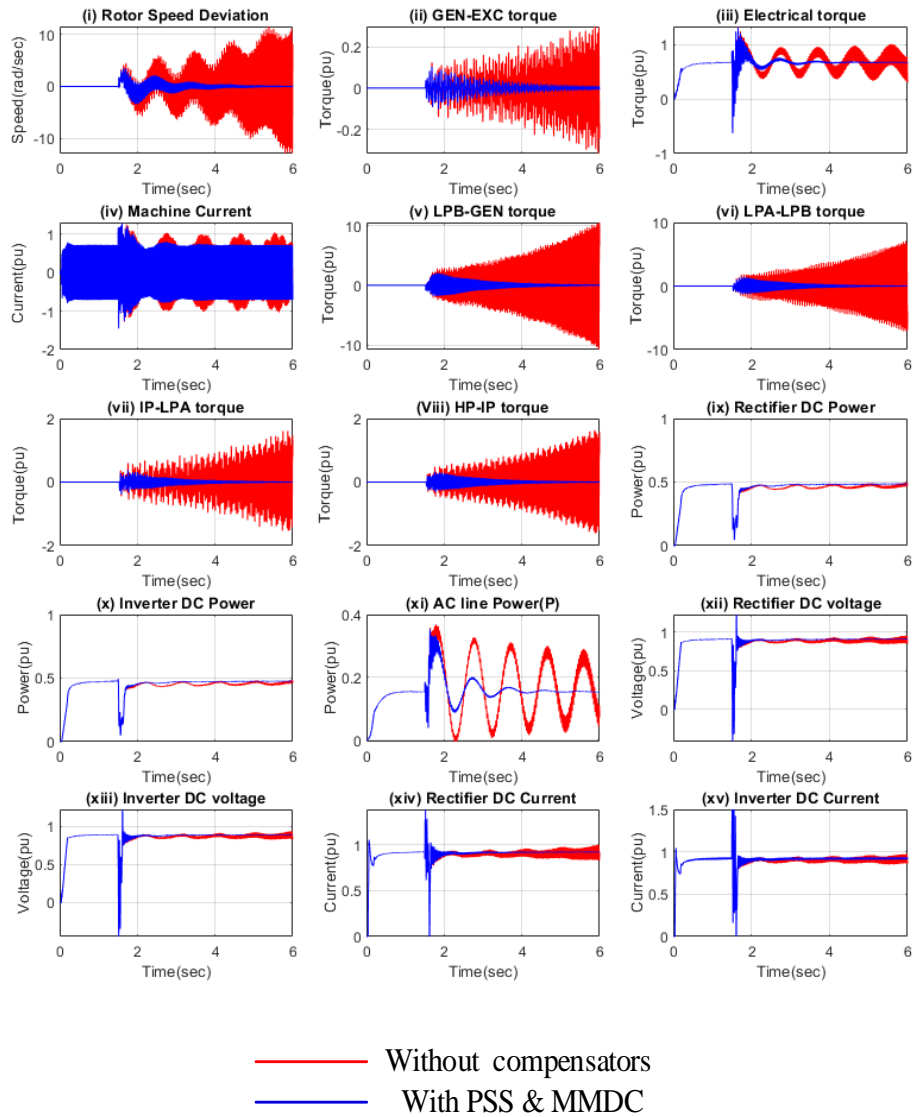


Figure 5-24: System Response in Case (d) following a 75 ms 3-phase short-circuit on the resonant AC line ($K=0.23$, $P_g=0.67$ pu, $P_d=0.4846$ pu, $PF=0.9$)

This increasing trend of torsional oscillatory modes indicating the system's stability state's worsening demonstrates the torsional instability observed through the time domain signals shown in Figure 5-24 without considering the damping compensators.

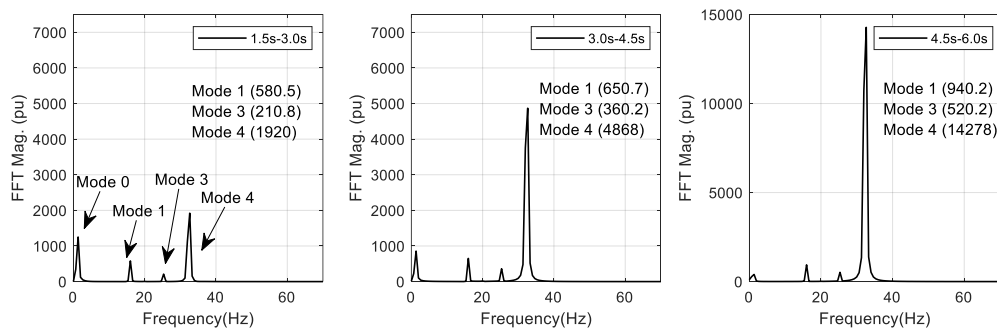


Figure 5-25: Rotor speed deviation's FFT results in case (d) without compensators

Furthermore, Figure 5-26 shows the impact of both the MMDC and PSS on SSO damping for this operating point. A significant improvement in the SSO state can be seen following the application of compensators. The three unstable oscillatory modes have been stabilized following the application of this set of compensators. Therefore, these modes' stability justifies the MMDC and the PSS efficiency shown in the system's time domain response in Figure 5-24.

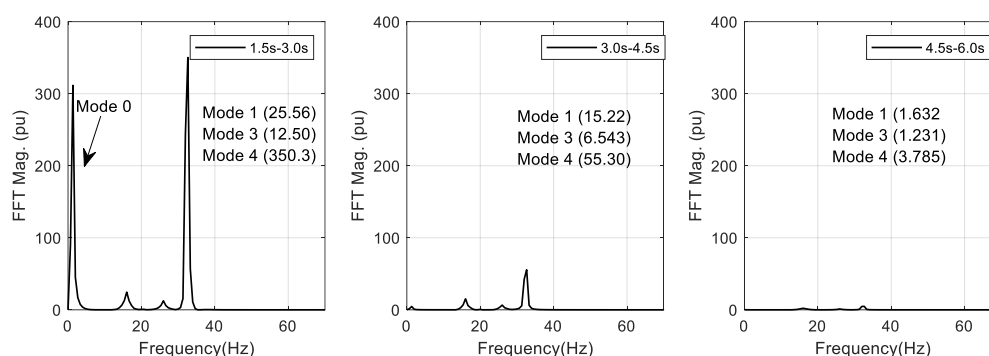


Figure 5-26: Rotor speed deviation's FFT results in case (d) with MMDC and PSS

5.4.2 System Response for the Parallel AC-DC System with $P_{HVDC} = 0.4154$ pu

The previous scenarios are also conducted in this section, taking the new HVDC operating point into account. At this HVDC operating point, the DC power has been reduced to 0.4154 pu, improving the stiffness of the inverter AC bus ($X_S=0.5$ pu, $R_S=0.06$ pu, $ESCR=3.73$). The parameters of this HVDC operating point, including AC filters, are shown in Appendix B. The variation of the AC transmission line compensation level over a wide range results in three unstable torsional modes, namely Mode 1 (15.71 Hz), Mode 3 (25.25 Hz), and Mode 4 (32.28 Hz), including Mode 0 (1.67 Hz). Table 5-5 shows the different case studies. This section considers all the parameters of the current regulators given in Table 3.1 except the gains (K_{PID}). The current regulators' gains leading to the system's positive damping contribution after adding the HVDC link in parallel with the resonance AC line were obtained, as described in Chapter 4. $K_{PID}=8.5$ for cases (aa) and (bb) and $K_{PID}= 5$ for cases (cc) and (dd).

Table 5-4: Operating Points with $P_{dc}=0.4154$ pu (Case Study)

Pdc=0.4154pu								
N°	K (%)	P_g (pu)	PF	Vg(pu)	$V_{a, Mag}$ (pu)	$V_{a, Ph}$ (deg)	$V_{b, Mag}$ (pu)	$V_{b, Ph}$ (deg)
Aa	70	0.90	0.900	1.007	0.968	23.55°	0.957	26.9°
Bb	61	0.80	0.900	1.007	0.968	24.47°	0.942	23.73°
Cc	41	0.70	0.900	1.007	0.967	26.97°	0.919	20.51°
Dd	23	0.67	0.900	1.007	0.967	29.85°	0.906	19.65°

5.4.2.1 HVDC-based Single-Mode Damping Controller Performance (SMDC) at a different HVDC power

5.4.2.1.1 SMDC and PSS Applied to Case (aa)

The level of compensation in Case (aa) is 70%, with a generator delivering a 0.9 pu output power at PF=0.9. The parameters of the rectifier current regulator are: $T_R=0.0109$, $K_R=8.5$, $U_R=0.1$ and $U_{Rmin}=-0.1$. Following the design methodology for SMDC outlined in section 5.4.3.3 and used in previous cases, Figure 5-27 displays the phase-frequency graph from the test signal method that was established to determine the phase angle difference between the electromagnetic torque and the converter DC current deviation. It can be observed that the phase difference between ΔI_{ref} and ΔT_e (i.e., $\angle TRI_c(\Psi)$) at 15.99 Hz (Mode 1) is -105° . Therefore, the lag compensator $\angle SMDC(\Psi)$ needs -105° to correct this leading. Equation (5-16) describes the transfer function showing the parameters of the SMDC designed to damp out the 15.99 Hz frequency component at this operating point. Figure 5-28 shows the bode plot of the supplementary damping controller designed for Mode 1 (15.71 Hz). It can be seen the controller provided the angle required to correct the phase lag of ΔT_e with respect to ΔI_{ref} .

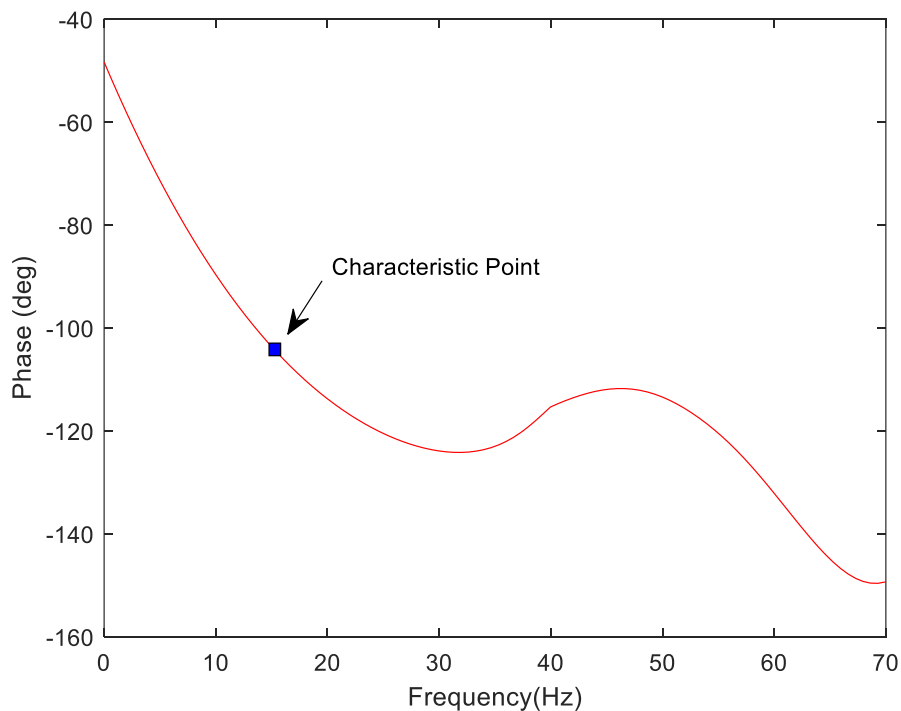


Figure 5-27: Mode 1's Phase-Frequency Characteristic Curve for Case (aa)

$$SMDC(s)_{M1} = 3.5 \left(\frac{1 + 0.001310391s}{1 + 0.005746601s} \right) \times \left(\frac{1 + 0.075603616s}{1 + 0.017239803s} \right) \quad 5.11$$

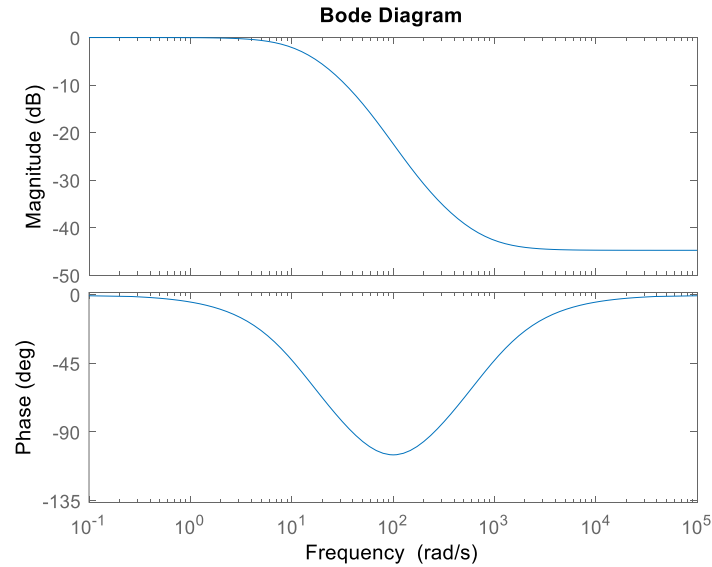


Figure 5-28: Mode 1 Damping Controller's Bode Plot

Figure 5-29 illustrates the power system's response to the operating conditions described in Case (aa). Growing amplitude oscillations can be observed in the system without damping compensators. The rotor speed deviation varies from -50 rad/s to 50 rad/s and in the power system's other magnitudes. This operating point generates extreme Mode 1 (15.71 Hz) instability. Applying the SMDC designed for Mode 1 (15.71 Hz), the PSS has effectively damped SSO/SSR. It can be observed from the time domain results of the power system that the (-105°) angle given by the phase compensation block significantly stabilized the turbogenerator shaft's torsional dynamics. Before applying the subsynchronous damping compensators, the AC and DC lines also have significant power fluctuations. These fluctuations generally reduce the power transfer capability. As a result, thanks to the SMDC and PSS application, this operating point's stability provides ample evidence of the damping compensators' usefulness in stabilizing torsional oscillations and fostering higher compensation levels in the power system.

The FFT results for case (aa) are displayed in Figures 5-30 and 5-31. These results illustrate the power system's torsional behavior. A significant Mode 1 instability degrades in oscillatory amplitude after fault occurrence at 1.5 sec. The results also reveal that the oscillatory amplitude increases dramatically from 1.5 s to 6.0 s, disrupting the power system's operation and can pose risks to the TG shaft reliability. Figure 5-31 highlights the impact of both the SMDC and the PSS on the power system's subsynchronous oscillations. Torsional mode 1 (15.71 Hertz) and electromechanical mode zero (Mode 0) have also been effectively mitigated. The oscillatory amplitude of 15.71 Hz, significantly reduced due to the SMDC's performance with the parameters mentioned in equation (5-16), begins at 115 pu between 1.5 s and 3.0 s and hits 2.5 pu between 4.5 s and 6.0 s. These torsional oscillation amplitudes' reduction of Mode 1 (15.99 Hz) and Mode 0 (0-2Hz) indicate the effectiveness of controllers, thus confirming the time domain results seen in Figure 5-29.

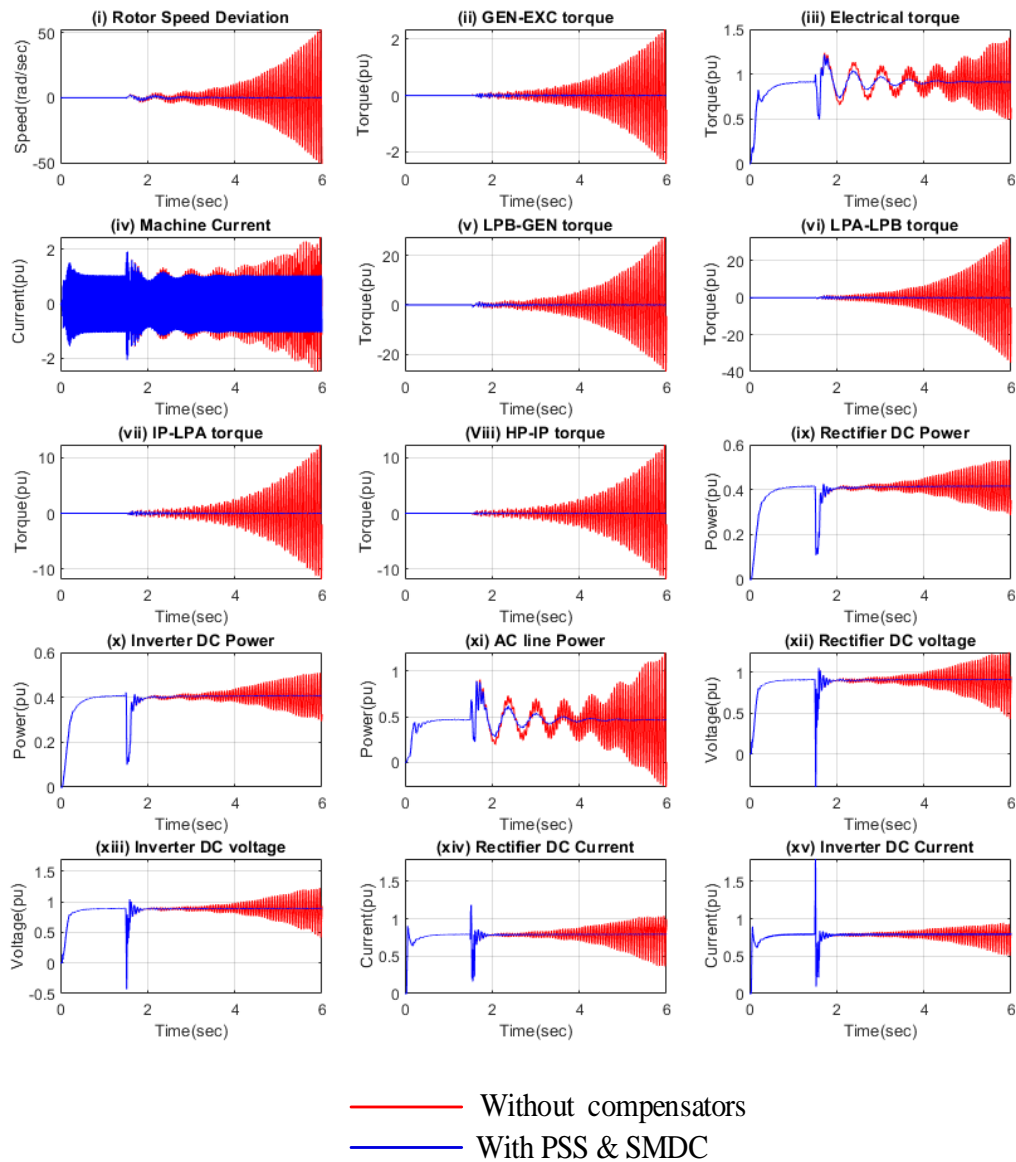


Figure 5-29: System Response in Case (aa) following a 75 ms 3-phase short-circuit on the resonant AC line ($K=0.70$, $P_g=0.9$ pu, $P_d=0.4154$ pu, $PF=0.9$)

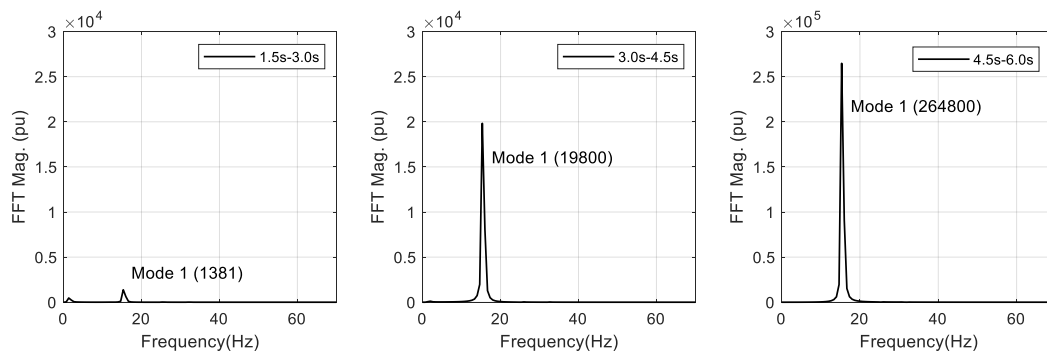


Figure 5-30: Rotor speed deviation's FFT results in case (aa) without compensators

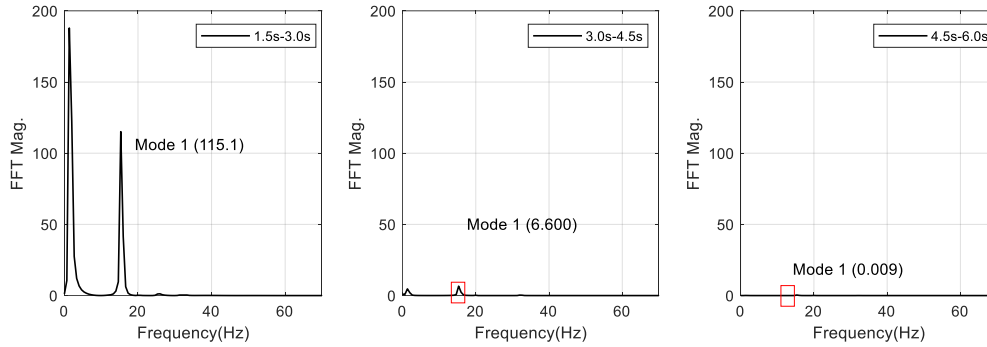


Figure 5-31: Rotor speed deviation's FFT results in case (aa) with SMDC (designed for Mode 1) and PSS

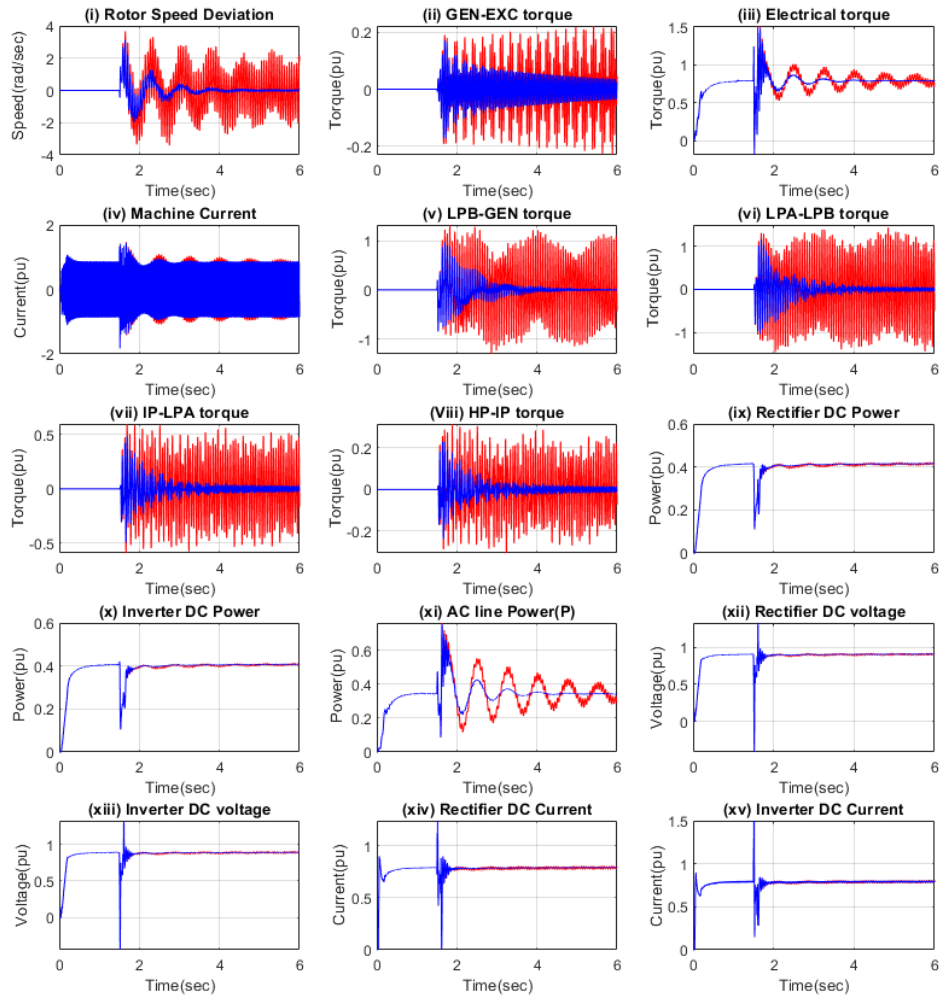
5.4.2.1.2 SMDC and PSS Applied to Case (bb)

This operating point is characterized by compensation of 61 percent, with the generator power set at 0.80 pu, and a PF=0.9. The torsional oscillation study of this operating point also revealed extreme Mode 1 (15.71 Hz) instability. As in the previous case, the application of an SMDC designed for Mode 1 was required. Following the procedure described in section 5.3.4, equation (5-17) describes the transfer function of the SMDC designed for this specific case with its resulting optimal parameters.

$$SMDC(s)_{M1} = \left(\frac{1 + 0.191199249s}{1 + 0.000518152s} \right) \quad 5.12$$

Figure 5-32 indicates the time domain behavior of the AC-DC parallel system's signals before applying appropriate HVDC auxiliary controls with PSS and after. The figure shows a rapid deterioration in AC-DC component oscillatory amplitude and TG's torsional dynamics when the damping compensators are out of service. This oscillatory torsional instability has also adversely influenced the AC line's power and synchronous machine's electrical torque response. AC line power undergoes huge fluctuations restricting its good transfer quality. However, these oscillations do not affect the DC system's operation significantly.

Furthermore, Figure 5-32 also shows the improvement of torsional oscillations' stability and the transmission lines' fluctuations in voltages and powers. The application of SMDC and PSS is effective in stabilizing the condition of this critical operating point. The line's AC power and electrical torque damping have been drastically improved. The Fourier analysis of the rotor speed deviation for case (bb) is seen in Figure 5-33. The Mode 1 (15.71 Hz) oscillatory amplitude increase seen via its peak, ranging from 949 pu between 1.5 sec to 3.0 sec up to 1299 pu between 4.5 sec to 6.0 sec, shows the instability demonstrated in Figure 5-32 before connecting the damping controller and PSS.



— Without compensators
— With PSS & SMDC

Figure 5-32: System Response in Case (bb) following a 75 ms 3-phase short-circuit on the resonant AC line ($K=0.61$, $P_g=0.8$ pu, $P_d=0.4154$ pu, $PF=0.9$)

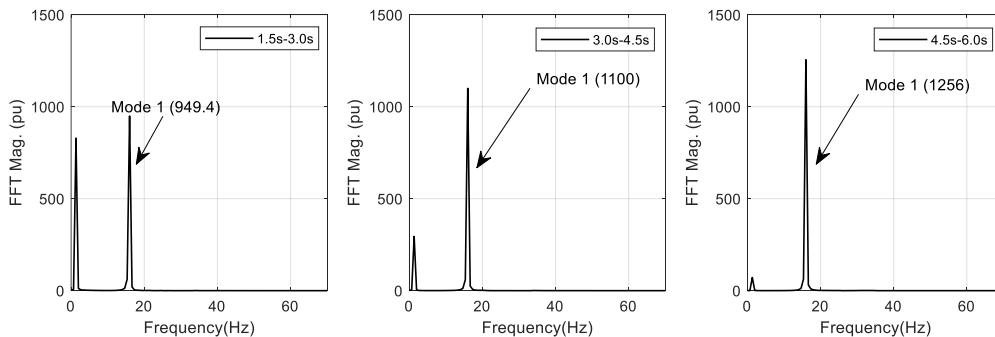


Figure 5-33: Rotor speed deviation's FFT results in case (bb) without compensators

Moreover, Figure 3-34 describes the performance of both the Mode 1 (15.71 Hz) controller and the PSS on the power system's operation when working under the case (bb) conditions. The results show that the SMDC and the proposed PSS have fulfilled their torsional oscillation stabilization purpose. These compensators' addition allowed the torsional oscillation's adverse effect to neutralize from the instant of AC fault occurrence, i.e., from 1.5 s. The reduction of the oscillatory amplitude of Mode 1 (15.71 Hz) in each time interval sufficiently proves these compensators' effectiveness.

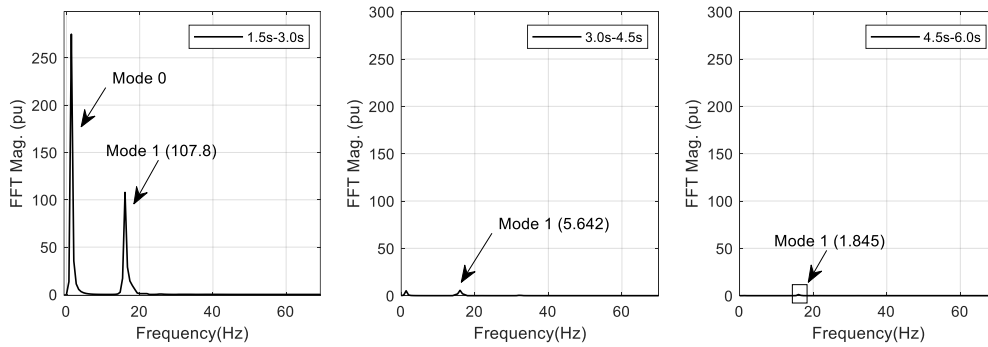


Figure 5-34: FFT analysis of rotor speed deviation for case (bb) with the Multi-Modal Damping Controller and Power System Stabilizer

5.4.2.2 Multimodal Instability HVDC-based Single Mode Damping Controller Performance at a different HVDC power

5.4.2.2.1 Introduction

Figure 5-35 shows the time domain response and FFT analysis of rotor speed deviation when the AC line compensation is set to 41%, as described in case (cc) without and with the addition of HVDC. Under these operating conditions, the generator provides a power of 0.70 pu with a power factor of 0.9. The rectifier current regulator parameters are $K_R=5$, $T_R=0.0109$, $U_{Rmax}=0.1$, and $U_{Rmin}=-0.1$. As in the previous cases, the power system was subjected to an electrical fault at 1.5 s lasting 0.75 ms.

Figure 5-35 reveals that the resonant AC line is exposed to immense Mode 3 (25.25 Hz) instability while the HVDC is out of operation, whereas switching on the HVDC with SMDC offers considerable positive damping to Mode 3 while destabilizing Mode 1 (15.99 Hz) and Mode 4 (32.285 Hz), which previously seemed stable. This demonstrates an HVDC system's ability to induce subsynchronous torsional oscillations due to current and voltage regulators' configuration and parameters. Following the addition of the parallel HVDC tie, instability of three unstable torsional modes, including Mode 0 (1.67 Hz), can be observed, although Mode 4 seems less impacting. The FFT results were captured over the time interval between 4.5 and 6.0 sec.

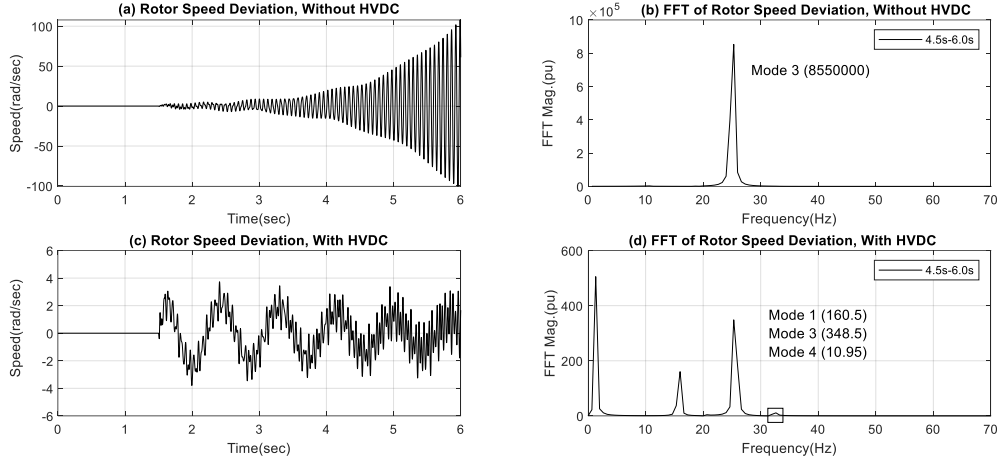


Figure 5-35: Transient response and FFT results of rotor speed deviation in case (cc) with HVDC tie on and off.

5.4.2.2.2 SMDC and PSS Applied to Case (cc)

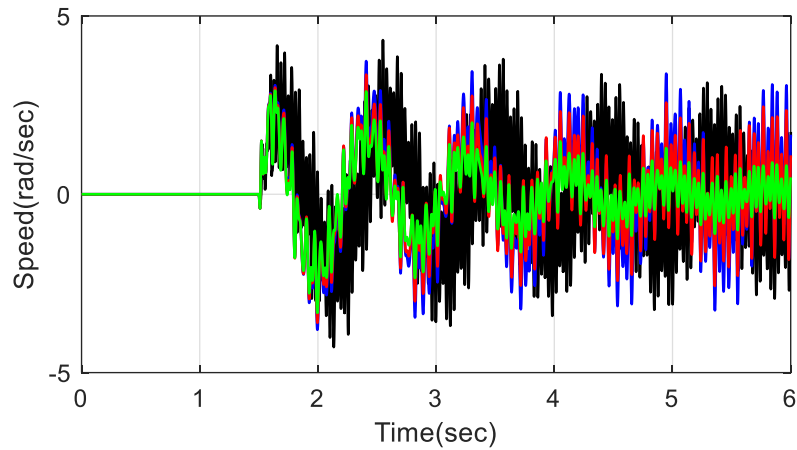
Three single-mode damping controllers developed using the previously discussed method were applied separately with the proposed PSS [97] to the AC-DC parallel system under these operating conditions to assess their ability to stabilize the power system operation. Equations (5-18) to (5-20) describe each controller's transfer function.

$$SMDC(s)_{M1} = 1.1 \left(\frac{1 + 0.00789463s}{1 + 0.01254907s} \right) \quad 5.13$$

$$SMDC(s)_{M3} = 1.5 \left(\frac{1 + 0.041239512s}{1 + 0.000963394s} \right) \quad 5.14$$

$$SMDC(s)_{M4} = 1.8 \left(\frac{1 + 0.015301484s}{1 + 0.001588692s} \right) \times \left(\frac{1 + 0.015301484s}{1 + 0.001588692s} \right) \times \left(\frac{1 + 0.006542929s}{1 + 0.003715361s} \right) \quad 5.15$$

Figure 5-36 displays the rotor speed deviation's time-domain responses demonstrating each SMDC's impact on the damping of SSO. It is worth remembering that this operating point is distinguished by a dominant instability in Mode 3 (20.25 Hz), although Mode 1 (15.71 Hz) and Mode 4 (32.28 Hz) are also unpredictable. It can be noticed that there is no meaningful contribution to the damping of subsynchronous oscillation by the single-mode damping controllers designed for Mode 1 (15.99Hz) and Mode 4 (32.25 Hz). On the contrary, the Mode 1 controller appears to have adversely interacted with the turbogenerator. However, the Mode 4 controller positively impacted the system's dynamics, although it did not stabilize it. Designed for the more extreme oscillatory mode, the Mode 3 controller successfully added considerable positive damping to the TG's torsional dynamics, although the system remains unstable.



— No compensators — Mode 3 controller and PSS
— Mode 1 controller and PSS — Mode 4 controller and PSS

Figure 5-36: System Response for Various SMDC and PSS applied to Case (cc)

It is to be noted that it is impossible to identify unstable torsional modes from the time domain by merely observing its oscillations. This is why the FFT analysis of signals is undertaken to investigate the signal's torsional behavior essentially. Therefore, to evaluate each single-mode damping controller's impact on torsional modes' stability, the investigation was carried out, as in previous cases, utilizing FFT analysis of rotor speed deviation as it is fitted with all the modal characteristics of the turbogenerator shaft. The FFT results of rotor speed deviation when the power system is subject to the operating conditions described in case (cc) without any compensator and with the damping compensators made up with the proposed PSS [97] and a single-mode damping controller are displayed in Figure 5-37 and Figure 5-38, respectively.

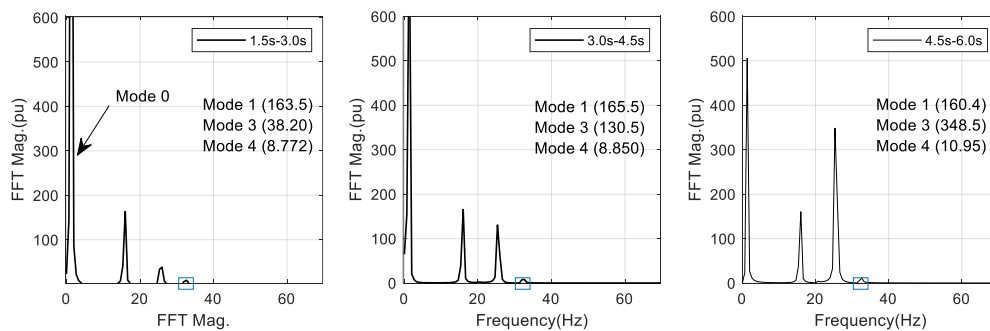


Figure 5-37: Rotor speed deviation's FFT results in case (cc) without compensators

As in the previous cases, this power system's torsional behavior is evaluated over three time periods. Figure 5-37 demonstrates the power system's torsional behavior without considering the damping compensators.

After incorporating the Mode 1 damping controller, designed following the previous section's procedure and PSS, Figure 5- 38(a) displays the resulting system response. From 4.5 sec to 6.0 sec (see Figure 5- 38(a)), it can be seen that inserting the SMDC and PSS has provided positive damping to Mode 1 and Mode 3, while the state of Mode 4 has worsened. Worsening in Mode 4 is due to interactions induced by Mode 1 damping controller. This analysis shows that the single-mode damping controller designed for Mode 1 (15.71 Hz) cannot stabilize the oscillations due to other torsional modes.

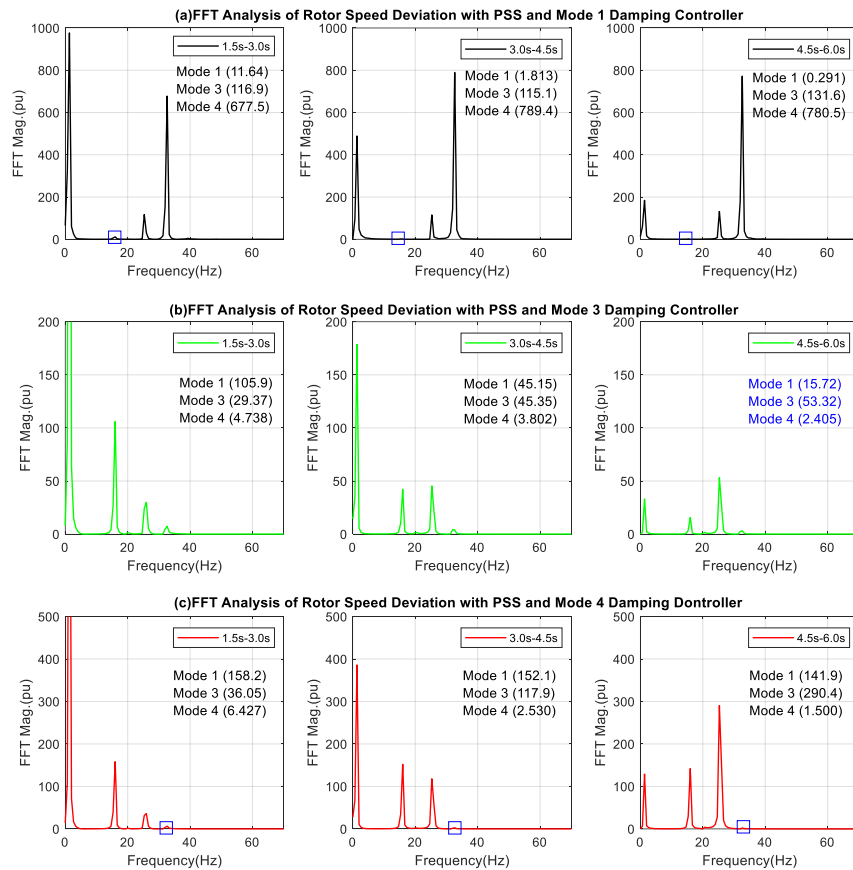


Figure 5-38: Rotor speed deviation's FFT analysis in case (cc) with SMDC and PSS

Figure 5-38(b) illustrates the system behavior after connecting the Mode 3 (25.25 Hz) damping controller (with Mode 1 damping controller out of service). It should be recalled that Mode 3 is the most unstable oscillatory mode under Case (cc) operating conditions. Typically, in power systems with radial operating HVDC, the single-mode damping controller design is based on the severe torsional mode. In this scenario, the Mode 3 damping controller and PSS have provided sufficient positive damping to the system compared to the previous damping compensators' contribution.

Figure 5-38(c) illustrates the system's torsional behavior after applying the Mode 4 damping controller with PSS (the other controllers are disconnected). The figure shows that the SMDC provided positive damping to Mode 4 (32.28 Hz). However, the system is still unstable. Although the oscillatory amplitude of Mode 4 was low before applying compensators, the compensators offered significant damping to this torsional mode.

Furthermore, the damping controller designed for the most severe torsional oscillatory mode was more efficient in all cases, providing considerable damping to the system. However, it did not wholly stabilize the turbogenerator set's torsional dynamics. Hence, in the next section, the impact of the MMDC is investigated at this particular different HVDC power in the study system.

5.4.2.3 Multi-Modal Damping Controller Performance (MMDC) at a different HVDC power

The methodology of multimodal controller design follows the same process as explained in the previous sections. The multimodal damping controller is also incorporated in the block diagram of Figure 5.5 to allow control of unstable torsional oscillations. This section is conducted for the last two case studies in Table 5-5. As previously observed, the study system is subjected to torsional oscillations from both the DC converter controls and the series capacitors following the application of a three-phase-to-ground fault of 75 ms. The first case study investigates the impact of the MMDC in Case (cc) and subsequently in Case (dd). Case (cc) was previously analyzed with single-mode damping controllers.

5.4.2.3.1 MMDC and PSS applied to Case (cc)

In this investigation, each of the single-mode controllers' parameters described in the previous section was modified slightly to prevent harmful interactions between torsional mode channels. Each torsional frequency mode path of MMDC is equipped with a bandpass filter to facilitate the corresponding frequency component's tracking from the rotor speed deviation. Following the MMDC design outlined in Section 5.3.4, step three was taken into account to determine each channel's gains while preventing adverse interactions between controllers. Therefore, Table 5-7 presents the MMDC's parameters obtained with a slight change in controllers gains to stabilize the power system's operation and torsional dynamics under Case (cc)'s operating conditions.

Table 5-5: Parameters of MMDC Designed for Case (cc)

Modes	Lead-Lag compensators	gain
Mode 1 Channel	$\left(\frac{1 + 0.00789463s}{1 + 0.01254907s} \right)$	2.5
Mode 3 Channel	$\left(\frac{1 + 0.041239512s}{1 + 0.000963394s} \right)$	4
Mode 4 Channel	$\left(\frac{1 + 0.015301484s}{1 + 0.001588692s} \right) \times \left(\frac{1 + 0.015301484s}{1 + 0.001588692s} \right) \times \left(\frac{1 + 0.006542929s}{1 + 0.003715361s} \right)$	5

The time-domain response of the different components of the power system, when exposed to the operating conditions described in Case (cc), is shown in Figure 5-39. It can be observed that without SSDC, the power system is unstable. In the different components of the turbogenerator shaft, torsional

oscillation is remarkable, although at low amplitude. These torsional oscillations have created significant fluctuations in the electrical torque and the AC network's active power. Due to the strong fluctuations of the transmission network arising from the instability of the TG shaft's torsional dynamics, the AC line's power transfer under these operating conditions is significantly disturbed. This, therefore, requires the installation of damping devices for both torsional and low-frequency oscillations. By observing the blue-color signal reflecting the influence of the MMDC and the PSS on the TG shaft's torsional dynamic, it can be seen that SSO has been effectively reduced. As in the previous case, the time domain response of the rotor speed deviation (see Figure 5-39 (i)) shows the most significant impact of MMDC on torsional oscillation. The findings obtained in this section show the efficacy of MMDC and PSS in stabilizing both the power system operation and torsional oscillations encountered in the AC-DC grid.

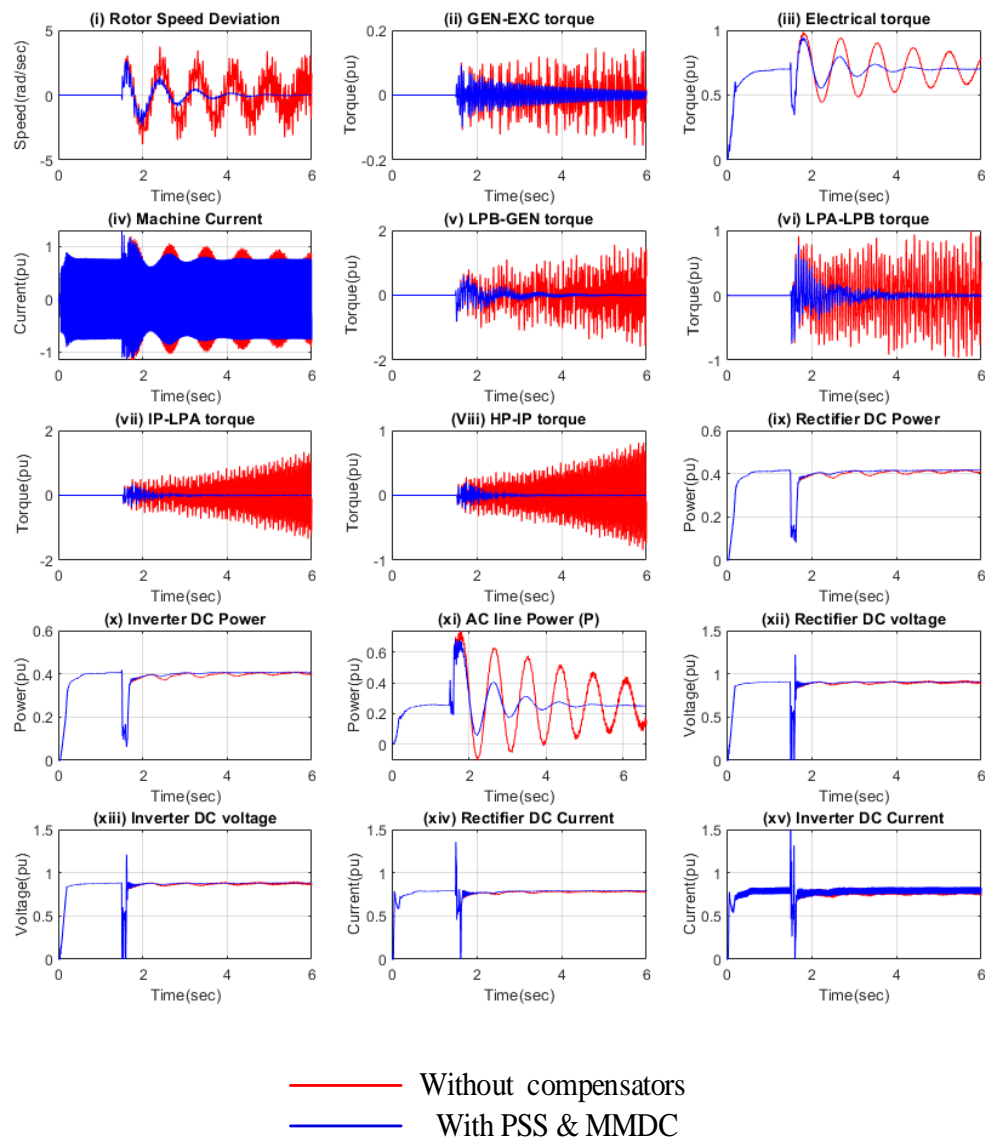


Figure 5-39: System Response in Case (cc) following a 75 ms 3-phase short-circuit on the resonant AC line ($K=0.41$, $P_g=0.7$ pu, $P_d=0.4154$ pu, $PF=0.9$)

Figure 5-40 displays the FFT findings representing the power system's torsional behavior for case (cc) when fitted with PSS and the MMDC. These results first confirm the ability of SSDC to suppress torsional oscillation as shown by the time domain results, and second, they demonstrate the controller efficiency. The MMDC's performance can also be seen within the three-time intervals showing a precise offset of the decrease in oscillatory amplitude compared with the previous analysis, using, in particular, the best SMDC (i.e., Mode 3 damping controller). Specifically, within the time interval of 4.5 s to 6.0 s (see Figure 5-40 and Figure 5- 38(b)), it can be seen that the amplitudes of unstable torsional frequencies have been significantly reduced compared to those of the previous case using Mode 3 damping controller.

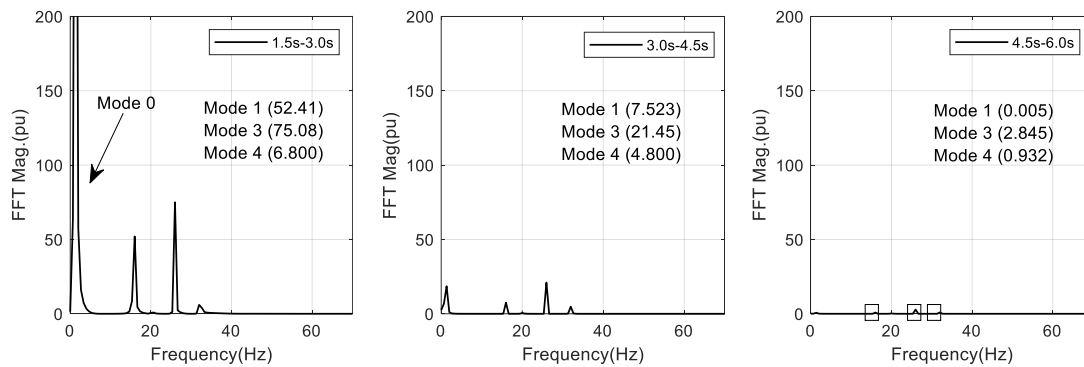


Figure 5-40: Rotor speed deviation's FFT results in case (cc) with MMDC and PSS

5.4.2.3.2 MMDC and PSS Applied to Case (dd)

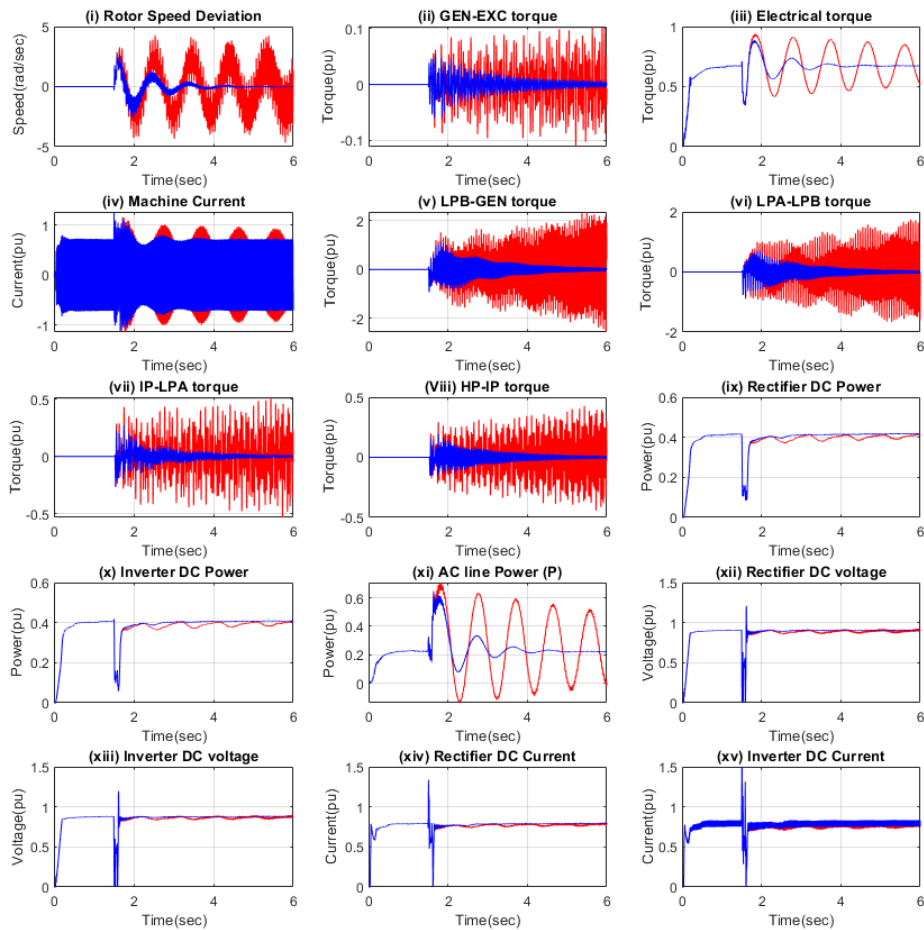
Under operating conditions described in Case (dd), the degree of compensation is 23%, the generator provides a power of 0.67 pu at a power factor of 0.9. The parameters of the rectifier current regulator are the same as in the previous case, i.e. $K_R = 5$, $T_R = 0.0109$, $U_{Rmax} = 0.1$, and $U_{Rmin} = -0.1$. The three unstable oscillatory modes categorize Case (dd)'s operating conditions with a Mode 4 (32.28 Hz) oscillating at very large amplitudes. Following the previous investigation conducted on SSO sources in the AC-DC parallel system, the HVDC system's negative contribution was noted on the TG shaft's torsional dynamics. However, its insertion added positive damping on Mode 4 (32.28 Hz). Therefore, following the phase correction method based on the test signal investigation illustrated in section 5.3.4, Table 5-8 presents the obtained optimal MMDC parameters. As in all cases, the torsional and inertial modes are controlled using the damping controller and PSS.

Figure 5-41 illustrates the Case (dd)'s time-domain results when the damping compensators made up of MMDC and PSS are turned on and off. Before applying the damping compensators, large amplitude oscillations in the TG shaft's torsional dynamics can be observed. The rotor speed deviation goes from -5 rad / s to 5 rad / s up to 6 sec after the occurrence of the fault at 1.5 sec. The transient effect amplification has also affected the generator electrical torque, the AC line power, and other power system parameters. However, with the damping compensators' application, i.e., MMDC and PSS, the torsional oscillation has been damped out, inducing power transfer stabilization improvement. These

two compensators' application has rendered the synchronous machine's electrical torque stable and the power transfer along the AC line feasible.

Table 5-6: Parameters of MMDC used for case (dd)

Modes	Lead-Lag compensators	gains
Mode 1 Controller	$\left(\frac{1 + 0.00789463s}{1 + 0.01254907s} \right)$	5
Mode 3 Controller	$\left(\frac{1 + 0.015301484s}{1 + 0.001588692s} \right) \times \left(\frac{1 + 0.015301484s}{1 + 0.001588692s} \right) \times \left(\frac{1 + 0.006542929s}{1 + 0.003715361s} \right)$	8.5
Mode 4 Controller	$\left(\frac{1 + 0.015301484s}{1 + 0.001588692s} \right) \times \left(\frac{1 + 0.015301484s}{1 + 0.001588692s} \right) \times \left(\frac{1 + 0.006542929s}{1 + 0.003715361s} \right)$	5



— Without compensators
 — With PSS & MMDC

Figure 5-41: System Response in Case (dd) following a 75 ms 3-phase short-circuit on the resonant AC line ($K=0.23$, $P_g=0.67$ pu, $P_d=0.4154$ pu, $PF=0.9$)

Figure 5-42 illustrates the FFT analysis of rotor speed deviation related to the case (dd) before applying the MMDC and the PSS. It can be seen that Mode 1 (15.99 Hz), Mode 3 (25.25 Hz), and Mode 4 (32.28 HZ) are unstable for this operating point. However, Mode 4 is the most serious one, with a fast-growing peak between 1.5 sec to 6 sec. The unpredictable state of the TG shaft's oscillatory modes requires damping compensators to stabilize the power system's torsional behavior.

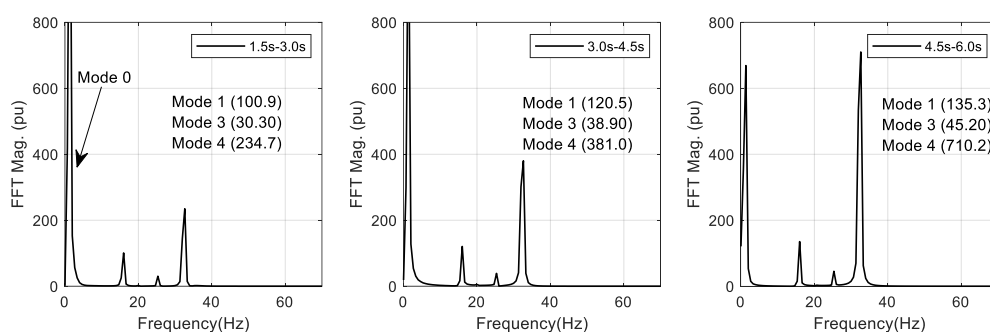


Figure 5-42: Rotor speed deviation's FFT results in case (dd) without compensators

Figure 5-43 displayed the FFT analysis of rotor speed deviation for case (dd), including MMDC and PSS. It can be seen that torsional oscillations have been reduced significantly following the incorporation of controllers. The torsional amplitude of the most unstable frequency mode (32.28 Hz) started from 65 pu between 1.5 s and 3.0 s to 0.167 pu between 4.5 s and 6.0 s. This condition endorses the damping compensators' efficiency shown in Figure 5-41 by the time domain results.

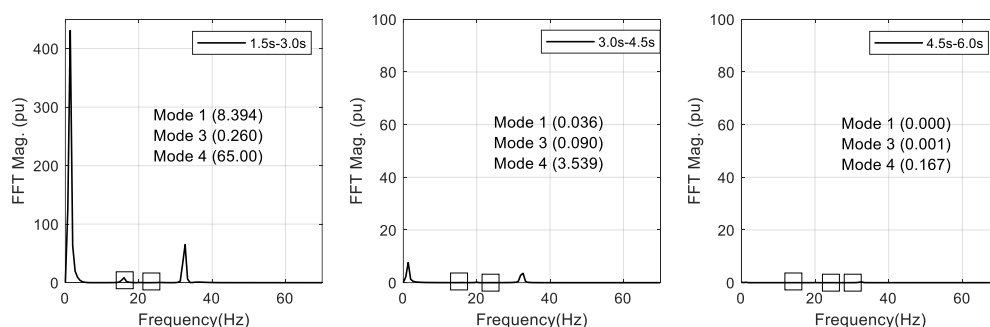


Figure 5-43: Rotor speed deviation's FFT results in case (dd) with MMDC and PSS

5.5 Conclusion

This chapter has investigated the SSR stability in parallel AC-DC systems containing an inverter station connected to an AC bus with moderate stiffness. The essential purpose of this work was to design subsynchronous damping controllers and evaluate their performance. This research used phase correction and test signal methods to design subsynchronous damping controllers. FFT analysis demonstrated the torsional behavior of the power system's operating points and the damping controller performance. Three torsional oscillatory modes, namely Mode 1 (15.99 Hz), Mode 3 (25.25 Hz), and

Mode 4 (32.28 Hz), were found to be unstable in these parallel AC-DC systems as in [97], varying the degree of compensation from 23 percent to 70 percent. Therefore, a compensator consisting of SSDC and PSS was implemented to suppress the power system oscillations. The object of this compensator structure, adopted from [97], was to control both the unstable modes and the electromechanical Mode 0 (i.e., low-frequency oscillations). Two controller configurations, namely the single-mode damping and the multimode damping controllers, were used to control the turbogenerator shaft's torsional dynamics.

The single-mode damping controller effectively suppressed SSO (and SSR) for the operating points exposed to single-mode instability only. The controller's performance was even investigated in the worst-case situation where the generator-inverter electrical coupling was reasonably strong (i.e., higher compensation levels). However, we also performed their performance tests when designed for Mode 1 (15.99 Hz), Mode 3 (25.25 Hz), and Mode 4 (32.28 Hz), including the proposed PSS [97]. We conducted this investigation to observe their ability to damp out torsional oscillations for operating points leading to multimodal instability (i.e., series capacitor and HVDC controls). Thus, the performance of separately implemented single-mode damping controllers revealed that they could not provide the system with adequate positive damping for all the torsional modes. The interaction between the designed controller and the other torsional modes is the risk of using a controller designed for a specific mode (i.e., less dominant mode). In this analysis, the Mode 1 (15.99 HZ) controller provided its corresponding torsional frequency with adequate damping while adversely affecting the Mode 4 (32.28 Hz) condition for the operating point related to 41 % with a DC power of 0.4846 pu. However, in contrast to the less dominant mode controllers, the single-mode damping controller developed for the most unstable mode added more positive damping. However, in some cases, the system was still sustaining torsional oscillations at low amplitude. The most unstable torsional mode is the one oscillating with the highest torsional amplitude. Finally, for operating points with multiple unstable torsional modes, multimodal damping controllers with benefits focused on controlling every single mode by controlling each TG shaft's torsional frequency through a bandpass filter were found more effective than single-mode damping controllers.

In short, this research does not conclude, given the studies carried out, that a single-mode damping controller is incapable of stabilizing torsional oscillations in a power system with HVDC parallel to a resonant AC line. However, it suggests that it is preferable to use a multimodal damping controller or a single-mode damping controller whose target frequency is that of the most degraded torsional mode when the operating point is exposed to many unstable torsional modes. This suggestion is given because the risk of torsional instability in the parallel AC-DC system is of various origins.

CHAPTER SIX: CONCLUSION AND FUTURE WORK

In recent decades, improving power transmission networks is becoming necessary to increase their output and alleviate bottlenecks to satisfy the ever-increasing demand for electric energy. This efficient use of the existing utility grid dramatically reduces the need to build new generating units. As a result of global pressures on energy plants to limit their carbon pollution and the threat of exhausting non-renewable energy resources, the power sector has seen an upward trend in the penetration of solar, wind, and hydroelectric power sources. Therefore, besides making these electric power grids' operation practical and reliable, future production units should be compatible with implementing these power sources and the stability issues. However, the traditional method of increasing energy transmission capability has been fixed series capacitor banks for many decades. These components generally have adverse effects, which can cause severe torsional oscillations of the turbogenerator's shaft and cause failure.

Furthermore, researchers have used several approaches to address the problem posed by series capacitors in transmission lines to uphold the productivity level of power plants, ensure their reliable and practical operation, and extend the life of turbogenerator units. Most of these methods used additional controllers of power system components such as the excitation system, FACTS devices, and HVDC. However, many aspects also lead to adverse torsional interaction between these devices' parameters and the nearby turbogenerator shafts.

This study relied on HVDC links' advantages to solve the SSR problem based on their high controllability. Several researchers have used HVDC controls for stability studies of the various concept of the power system. The HVDC controls in this study also showed their adversity by inducing torsional oscillations. This research conducted the performance assessment of supplementary HVDC controls in the AC-DC parallel system.

6.1 Summary of the Results

The points below outline the findings obtained at the end of this research:

- A. Chapter Three modeled the different power system elements: the synchronous machine, the AC transmission line equipped with series capacitors, the excitation system, and the HVDC link. This section underlined the critical operating points of the IEEE FBM. The analyses carried out in this thesis focused on these critical operating points, which generally depend on the compensating reactance's degree. We have also discussed two types of excitation systems in a very particular way: manual excitation and the IEEE type ST1A. In the PSCAD environment, IEEE FBM contains a manual excitation device to maintain a constant field voltage depending on the generator parameters' reinitialization. However, ST1A allowed the PSS implementation

to control the inertial swing mode while the damping controllers monitored the unstable torsional modes. Finally, this chapter presented the HVDC system's modeling results between two sources, analyzed its transient response, and concluded with the precautions to be considered in case of a significant disturbance. The results have shown that proper HVDC controls from the inverter side must be regarded to avoid commutation failure.

B. Chapter Four investigated the impact of HVDC on SSR damping when added in parallel with the resonant AC line. The studies performed considered the following:

- The IEEE FBM turbogenerator was equipped with its manual excitation system.
- The rectifier was fitted with a standard current regulator (i.e., without SSDC)
- The stiffness of the inverter's AC bus was moderate.

This study proved that the parallel HVDC system's addition could improve the sub-synchronous oscillation damping without fully stabilizing it. However, the HVDC addition also induced some torsional modes' instability due to inappropriate current regulator settings for some operating points. This investigation proved the risk of torsional interaction between HVDC controls and the turbine-generator shaft from the perspective of torsional dynamics

C. Chapter Five investigated two types of damping controllers, an HVDC-based single-mode damping controller and an HVDC-based multimodal damping controller, to stabilize torsional instability in the power system. The subsynchronous oscillation damping system consisted of the PSS and the damping controller. Unlike Chapter Four, Chapter Five's work focused on incorporating PSS via the IEEE-type ST1A excitation system. The two types of damping controllers were used with the ST1A and the PSS to facilitate inertial mode monitoring. We conducted performance testing of these two controllers due to the power system's exposure to various torsional oscillation sources. The chapter suggests a damping controller design method based on a test signal and phase correction between the electromagnetic torque and the converter's reference current deviation. The single-mode damping controller's design is carried out in most cases, considering the frequency of the most unstable oscillatory mode. This damping controller has a configuration achieved through a broad bandpass procedure in the literature. However, the multimodal damping controller takes the design resulting from the narrow bandwidth method. The latter generally has advantages based on effective control of each torsional mode. Chapter Five investigated single-mode controllers' performances when designed from the least unstable modes to the most unstable. In this chapter, the controllers' performance tests included observing the power system's torsional dynamics response when subjected to a multimodal torsional instability at critical operating points. The chapter also tested the performance of multimodal controllers for the same operating points. In addition to

the nominal HVDC power, Chapter Five also investigated the damping controllers' performances when setting the DC power at 0.4154 pu.

The general study aimed to stabilize the turbine-generator shaft's torsional dynamics. The investigation concentrated on the power system's critical operating points destabilizing the torsional oscillatory modes. This research performed four scenarios considering varying the DC power at each compensation level. The findings obtained are the following:

Three oscillatory modes, namely Mode 1 (15.71 Hz), Mode 2 (25.25 Hz), and Mode 3 (32.285 Hz), were unstable when the percentage of compensation varied from 23 percent to 70 percent. Each operating point exhibited a particular torsional instability. Some results showed multiple unstable torsional oscillatory modes, while other results had only one unstable torsional mode. In some cases, adding the parallel HVDC link showed that the latter improved the damping but destabilized some specific oscillatory modes due to the change in the rectifier's current regulator's parameters. In both parallel AC-DC systems, the operating points for which the compensation percentage exceeded 61 were subjected to severe instability in Mode 1 (15.71 Hz). In contrast, the three aforementioned torsional modes were unstable for the operating points, whose compensation was less than 61 percent. The investigation into adding the parallel HVDC link showed that all three oscillatory modes had both AC and DC origins.

Controller performance tests have shown that single-mode damping controllers designed to attenuate the most critical oscillatory mode provided more stability to the system than those designed for the less unstable modes. Single-mode damping controllers proved their positive performance in severe cases where the generator-inverter electrical coupling was high (i.e., for K greater than 61%). The results show that single-mode damping controllers' performance in multimodal instability was limited when designed for the less unstable modes. In contrast, the single-mode controller provided more positive damping when designed for the most severe torsional mode. Beyond the single-mode damping controller's inability when designed for a modal frequency less influential in multimodal instability, this research's results have proven the risk of the controller's harmful interaction with other oscillatory modes destabilizing the torsional dynamics of the power system. This thesis showed that a single-mode damping controller should be designed, considering the most unstable oscillatory mode when the system is under multimodal instability. However, multimodal controllers' performance tests have shown very satisfactory results for the parallel AC-DC system's operating points with multimodal instability. The benefits of multimodal controllers are generally based on individually monitoring each oscillatory torsional mode.

Chapter Five also evaluated the impact on the TG shaft's torsional dynamics when varying the DC power at each compensation level. An evaluation based solely on observing the FFT response of the most influential torsional mode. The results show that torsional oscillations are more harmful to each compensation level in the system with higher DC power. The higher the HVDC power, the lower the inverter's AC bus's stiffness, and the greater the torsional oscillation risk at a specific operating point.

In conclusion, this work does not exclude the fact that the single-mode damping controller may be allowed in parallel AC-DC systems, as reported in the literature. However, since it is based on the broad bandpass approach, its design should target the most influential torsional frequency in multimodal instability. And the design must consider a dynamic optimization procedure to obtain its adequate parameters, ensuring all torsional modes' stability. Preferably, in the case of multimodal instability, we suggest using a multimodal damping controller.

6.2 Possible Future Work Suggestions

For future research on this topic, the following points will be good projects:

- The analysis of the turbine-generator shaft's electromechanical system response was carried out using the FFT algorithm in MATLAB. Further work can be done on an experimental study aiming to set up a sensor of the subsynchronous oscillation's nature to design a damping controller based on the resulting torsional characteristics. The sensor will act as a smart device, thus enabling efficient monitoring of the turbine generator shaft's electromechanical stability.
- Since this work used the test signal method and the phase compensation method to design the damping controllers, the subsequent study may focus on implementing software intended to generate the controllers' optimal parameters from information on the power system's torsional dynamics.
- The literature has highlighted several factors influencing the oscillation of the torsional oscillation due to HVDC parameters. Further research into this work could focus on studying the impact of HVDC control schemes, namely Equidistant Pulse Control and Individual Pulse Control, on the turbine-generator shaft's torsion interaction. This investigation can also relate to the inverter's control mode change, namely the extinction angle control mode or the voltage control mode.

REFERENCES

1. Kundur, P.J.P.s.s. and control, *Power system stability*. 2007. **10**.
2. Bergen, A.R., D.J.J.I.t.o.p.a. Hill, and systems, *A structure preserving model for power system stability analysis*. 1981(1): p. 25-35.
3. Adrees, A., *Risk Based Assessment of Subsynchronous Resonance in AC/DC Systems*. 2014, The University of Manchester (United Kingdom).
4. Kundur, P., N.J. Balu, and M.G. Lauby, *Power system stability and control*. Vol. 7. 1994: McGraw-hill New York.
5. Preece, R., *Improving the stability of meshed power networks: a probabilistic approach using embedded HVDC lines*. 2013: Springer Science & Business Media.
6. Van Cutsem, T. and C. Vournas, *Voltage stability of electric power systems*. 2007: Springer Science & Business Media.
7. Gao, B., G. Morison, and P.J.I.t.o.p.s. Kundur, *Voltage stability evaluation using modal analysis*. 1992. **7**(4): p. 1529-1542.
8. Puri, R.K.J.M.c. and t.s.L.e.k.i.I.S. Asia, *Responses to Medium-term Stability*. 2007. **6**: p. 46.
9. Buser, D., et al., *Long-term stability of contour augmentation with early implant placement following single tooth extraction in the esthetic zone: a prospective, cross-sectional study in 41 patients with a 5-to 9-year follow-up*. 2013. **84**(11): p. 1517-1527.
10. Varaiya, P., F.F. Wu, and R.-L.J.P.o.t.I. Chen, *Direct methods for transient stability analysis of power systems: Recent results*. 1985. **73**(12): p. 1703-1715.
11. apparatus, I.S.w.g.J.I.t.o.p. and systems, *First benchmark model for computer simulation of subsynchronous resonance*. 1977. **96**(5): p. 1565-1572.
12. FANDOM. *Oscillate*. [cited 2020 December, 20, 2020]; Available from: <https://engineering.fandom.com/wiki/Oscillate>.
13. G, R., *Power system oscillations*. Springer Science & Business Media. 2012.
14. Britannica. *Damping*. [cited 2020 December, 5, 2020]; Available from: <https://www.britannica.com/science/damping>.
15. Sharaf, A., et al., *Damping torsional oscillations of nuclear generators by using firing delay angle modulation of HVDC schemes*. 1987. **13**(1): p. 11-20.
16. Zhou, H., et al., *Ultra-high voltage AC/DC power transmission*. 2018: Springer.
17. Liu, P., et al. *Detailed modeling and simulation of+ 500kV HVDC transmission system using PSCAD/EMTDC*. in *2015 IEEE PES Asia-Pacific Power and Energy Engineering Conference (APPEEC)*. 2015. IEEE.
18. Kamakshaiyah, S. and V. Kamaraju, *HVDC transmission*. 2011: TATA McGraw-Hill.
19. Facchin, C. and H.J.A.R. Fässler, Special Report, *60 years of HVDC*. 2014. **9**.
20. Zizliauskas, P., *Subsynchronous torque interaction for HVDC Light B*. 2001, Lund University.
21. Sellick, R. and M. Åkerberg, *Comparison of HVDC Light (VSC) and HVDC Classic (LCC) site aspects, for a 500MW 400kV HVDC transmission scheme*. 2012.
22. Grainger, J.J. and W.D.J.I.E. Stevenson, *Power System Analysis, 1994*. 2019.
23. Fossen, E., *Mitigation of Subsynchronous Resonance with Thyristor Controlled Series Compensation in the Great Britain Power Network*. 2016, NTNU.

24. He, C., et al., *Analysis of Subsynchronous Resonance Characteristics and Influence Factors in a Series Compensated Transmission System*. 2019. **12**(17): p. 3282.
25. Gruenbaum, R., J. Rasmussen, and C. Li. *Series capacitors for increased power transmission capability of a 500 kV grid inertia*. in *2012 IEEE Electrical Power and Energy Conference*. 2012. IEEE.
26. Ballance, J.W., S.J.I.T.o.P.A. Goldberg, and Systems, *Subsynchronous resonance in series compensated transmission lines*. 1973(5): p. 1649-1658.
27. Abdelaziz, A., et al., *Modern approaches for protection of series compensated transmission lines*. 2005. **75**(1): p. 85-98.
28. Padiyar, K., *Analysis of subsynchronous resonance in power systems*. 2012: Springer Science & Business Media.
29. Anderson, P.M., B.L. Agrawal, and J.E. Van Ness, *Subsynchronous resonance in power systems*. Vol. 9. 1999: John Wiley & Sons.
30. Hedin, R.A., et al., *SSR characteristics of alternative types of series compensation schemes*. 1995. **10**(2): p. 845-852.
31. Xie, R. and D. Trudnowski. *Distinguishing features of natural and forced oscillations*. in *2015 IEEE Power & Energy Society General Meeting*. 2015. IEEE.
32. Carpanen, R.P., *Analysis of the impact of a facts-based power flow controller on subsynchronous resonance*. 2012.
33. Khu, K.T., *SUBSYNCHRONOUS RESONANCE IN POWER SYSTEMS: DAMPING OF TORSIONAL OSCILLATIONS*. 1977: Iowa State University.
34. Wang, L., et al., *Mitigation of multimodal subsynchronous resonance via controlled injection of supersynchronous and subsynchronous currents*. 2013. **29**(3): p. 1335-1344.
35. Bengtsson, T., et al. *Case studies and experiences with Sub-synchronous resonance (SSR) detection technique*. in *2016 Power Systems Computation Conference (PSCC)*. 2016. IEEE.
36. Kilgore, L., et al., *Simplified transmission and generation system analysis procedures for subsynchronous resonance problems*. 1977. **96**(6): p. 1840-1846.
37. Brunet-Watson, M., J. Leighfield, and P. America, *Review of series compensation for transmission lines*. 2014.
38. Virulkar, V., G.J.R. Gotmare, and S.E. Reviews, *Sub-synchronous resonance in series compensated wind farm: A review*. 2016. **55**: p. 1010-1029.
39. Damas, R.N., et al., *Subsynchronous oscillation and advanced analysis: A review*. 2020. **8**: p. 224020-224032.
40. Tambwe, C.B. and R.P. Carpanen. *Investigating the Impact of HVDC on the Damping Subsynchronous Resonance*. in *2020 International SAUPEC/RobMech/PRASA Conference*. 2020. IEEE.
41. Himanshu B., B.P., *SUBSYNCHRONOUS RESONANCE ANALYSIS*, in *International Journal of Advanced Engineering Research and Technology (IJAERT)*. 2014.
42. Gotmare, G.V. and V.B.J.J.o.T.I.o.E.S.B. Virulkar, *Assessment of Subsynchronous Resonance in Series Compensated Type-1 Wind Farm*. 2015. **96**(2): p. 111-119.
43. Leon, A.E. and J.A.J.I.T.o.P.S. Solsona, *Sub-synchronous interaction damping control for DFIG wind turbines*. 2014. **30**(1): p. 419-428.
44. Tang, G., *Damping subsynchronous resonance oscillations using a VSC HVDC back-to-back system*. 2006.

45. Kundur, P., et al., *Application of power system stabilizers for enhancement of overall system stability*. 1989. **4**(2): p. 614-626.
46. Lee, D., et al., *Effects of governor characteristics on turbo-generator shaft torsionals*. 1985(6): p. 1254-1261.
47. Rogers, G.J.I.P.E.R., *Effects of Governor Characteristics on Turbo-Generator Shaft Torsionals DC Lee, Member, IEEE, and RE Beaulieu Ontario Hydro Research*. 1985(6): p. 27-28.
48. Padiyar, K., *HVDC power transmission systems: technology and system interactions*. 1990: New Age International.
49. Bahrman, M., et al., *Experience with HVDC-turbine-generator torsional interaction at Square Butte*. 1980(3): p. 966-975.
50. Demarest, D. and M.J.T.D. Bahrman, *Square Butte advances HVDC technology*. 1978. **30**(3).
51. Krishayya, P., R. Adapa, and M.J.C. Holm, France, *IEEE guide for planning DC links terminating at AC locations having low short-circuit capacities, part I: AC/DC system interaction phenomena*. 1997.
52. Jiang-Hafner, Y., et al. *Improvement of subsynchronous torsional damping using VSC HVDC*. in *Proceedings. International Conference on Power System Technology*. 2002. IEEE.
53. Cheng, Y., S.H. Huang, and J.J.I.T.o.P.D. Rose, *A series capacitor based frequency scan method for SSR studies*. 2019. **34**(6): p. 2135-2144.
54. Ordóñez, C.A., A. Gómez-Expósito, and J.M.J.E. Maza-Ortega, *Series compensation of transmission systems: A literature survey*. 2021. **14**(6): p. 1717.
55. Kim, D., H. Nam, and Y.J.I.P.V. Moon, *Eigenvalue Analysis Program of Small-Signal Stability of Power System Including Network Dynamics for the Subsynchronous Resonance Study*. 2003. **36**(20): p. 709-715.
56. Varma, R.K., S. Auddy, and Y.J.I.t.o.p.d. Semsedini, *Mitigation of subsynchronous resonance in a series-compensated wind farm using FACTS controllers*. 2008. **23**(3): p. 1645-1654.
57. Xu, Y. and S.J.I.A. Zhao, *Mitigation of subsynchronous resonance in series-compensated DFIG wind farm using active disturbance rejection control*. 2019. **7**: p. 68812-68822.
58. Baker, D.H., et al. *Subsynchronous resonance studies and mitigation methods for series capacitor applications*. in *2005 IEEE Power Engineering Society Inaugural Conference and Exposition in Africa*. 2005. IEEE.
59. Grünbaum, R., et al. *765 kV series capacitors for increasing power transmission capacity to the Cape Region*. in *IEEE Power and Energy Society Conference and Exposition in Africa: Intelligent Grid Integration of Renewable Energy Resources (PowerAfrica)*. 2012. IEEE.
60. Grunbaum, R. and J. Samuelsson. *Series capacitors facilitate long distance AC power transmission*. in *2005 IEEE Russia Power Tech*. 2005. IEEE.
61. Bhargava, B. and R.G. Haas. *Thyristor protected series capacitors project at Southern California Edison Co*. in *IEEE Power Engineering Society Summer Meeting*. 2002. IEEE.
62. Farmer, R., et al., *Navajo project report on subsynchronous resonance analysis and solutions*. 1977. **96**(4): p. 1226-1232.
63. Cen, H. and X. Wang. *Analysis of self-excitation in turbine-generators induced by static blocking filter*. in *2010 Asia-Pacific Power and Energy Engineering Conference*. 2010. IEEE.
64. Limebeer, D., R. Harley, and M. Lahoud. *Suppressing subsynchronous resonance with static filters*. in *IEE Proceedings C-Generation, Transmission and Distribution*. 1981. IET.

65. Singh, A., N. Verma, and A. Kumar. *Mitigation technique and measurement of subsynchronous resonance*. in *2016 International Conference on Innovation and Challenges in Cyber Security (ICICCS-INBUSH)*. 2016. IEEE.
66. Bowler, C., et al., *Operation and test of the Navajo SSR protective equipment*. 1978(4): p. 1030-1035.
67. Wang, S., Z. Xu, and F.J.E.P.S.R. Xing, *Application of bypass damping filter in suppressing subsynchronous resonance of multi-generator series-compensated systems*. 2019. **168**: p. 117-126.
68. Kilgore, L., D. Ramey, and W. South. *Dynamic filter and other solutions to the subsynchronous resonance problem*. in *Proc. Am. Power Conf.:(United States)*. 1975. Westinghouse Electric Corp., East Pittsburgh, PA.
69. Apparatus, I.S.R.W.G.J.I.T.o.P. and Systems, *Countermeasures to subsynchronous resonance problems*. 1980. **99**(5): p. 1810-1818.
70. Kumar, S., N. Kumar, and V.J.E.P. Jain, *Comparison of various auxiliary signals for damping subsynchronous oscillations using TCR-FC*. 2012. **14**: p. 695-701.
71. Kirschner, L. and G.H. Thumm. *Design and experience with thyristor controlled and thyristor protected series capacitors*. in *Proceedings. International Conference on Power System Technology*. 2002. IEEE.
72. Othman, H.A. and L.J.I.T.o.P.S. Angquist, *Analytical modeling of thyristor-controlled series capacitors for SSR studies*. 1996. **11**(1): p. 119-127.
73. Carpanen, R.P., *Enhancing transient stability of power systems using a thyristor controlled series capacitor*. 2005.
74. TCSC, T.C.S.C.J.A.F., Sweden, *Keeping grids together*.
75. Pilotto, L.A., et al., *Impact of TCSC control methodologies on subsynchronous oscillations*. 2003. **18**(1): p. 243-252.
76. Kakimoto, N. and A.J.I.T.o.P.D. Phongphanphanee, *Subsynchronous resonance damping control of thyristor-controlled series capacitor*. 2003. **18**(3): p. 1051-1059.
77. Varma, R.K., Y. Semsedini, and S. Auddy. *Mitigation of subsynchronous oscillations in a series compensated wind farm with thyristor controlled series capacitor (TCSC)*. in *2007 Power Systems Conference: Advanced Metering, Protection, Control, Communication, and Distributed Resources*. 2007. IEEE.
78. Yingjun, W., T. Yi, and L. Yang. *Analysis of subsynchronous oscillation (SSO) damping characteristic of the AC/HVDC parallel transmission system using TCSC*. in *2009 Asia-Pacific Power and Energy Engineering Conference*. 2009.
79. Zheng, X., Z. Xu, and J. Zhang. *A supplementary damping controller of TCSC for mitigating SSR*. in *2009 IEEE Power & Energy Society General Meeting*. 2009. IEEE.
80. Padayasi, J. and S.M. Kotian. *Design of Supplementary Excitation Damping Controller for Mitigation of Subsynchronous Resonance*. in *TENCON 2019-2019 IEEE Region 10 Conference (TENCON)*. 2019. IEEE.
81. Ghorbani, A., S.J.I.J.o.E.P. Pourmohammad, and E. Systems, *A novel excitation controller to damp subsynchronous oscillations*. 2011. **33**(3): p. 411-419.
82. Wang, L. and Y.-Y.J.I.t.o.e.c. Hsu, *Damping of subsynchronous resonance using excitation controllers and static VAr compensations: A comparative study*. 1988. **3**(1): p. 6-13.
83. Xi, W., et al. *Mitigation of sub-synchronous oscillation caused by TCSC using supplementary excitation damping controller*. in *2011 International Conference on Electrical Machines and Systems*. 2011. IEEE.

84. Dong, X., X. Wang, and Y. Yang. *Suppression of sub-synchronous oscillation caused by HVDC using supplementary excitation damping controller*. in *2014 17th International Conference on Electrical Machines and Systems (ICEMS)*. 2014. IEEE.
85. Zhao, X. and S. Gao. *Damping subsynchronous oscillation by static var compensator*. in *CICED 2010 Proceedings*. 2010. IEEE.
86. Hsu, Y.-Y. and C.-J.I.T.o.E.C. Wu, *Design of PID static VAR controllers for the damping of subsynchronous oscillations*. 1988. **3**(2): p. 210-216.
87. Wasynczuk, O.J.I.T.o.P.A. and Systems, *Damping subsynchronous resonance using reactive power control*. 1981(3): p. 1096-1104.
88. Hammad, A., M.J.I.t.o.p.a. El-Sadek, and systems, *Application of a thyristor controlled var compensator for damping subsynchronous oscillations in power systems*. 1984(1): p. 198-212.
89. Deb, A.K. *Static VAR compensator*. 2020 [cited 2020 December, 07, 2020]; From Wikipedia, the free encyclopedia]. Available from: [https://en.wikipedia.org/wiki/Static VAR compensator#Principle](https://en.wikipedia.org/wiki/Static_VAR_compensator#Principle).
90. Oni, O.E., A.G. Swanson, and R.P. Carpanen. *Small signal stability analysis of a four machine system with strategic placement of monopolar LCC-HVDC link*. in *2019 Southern African Universities Power Engineering Conference/Robotics and Mechatronics/Pattern Recognition Association of South Africa (SAUPEC/RobMech/PRASA)*. 2019. IEEE.
91. Chen, H., et al. *Research of Sub-synchronous Oscillations in HVDC and SSDC Designing*. in *Advanced Materials Research*. 2014. Trans Tech Publ.
92. Rauhala, T., et al. *A PSCAD case study of the main factors influencing the level of subsynchronous torsional interaction caused by HVDC*. in *Proc. International Conference on Power System Transients, IPST*. 2005.
93. Li, W., X. Xiao, and S. Tao. *Design and engineering practice of HVDC SSDC for suppressing sub-synchronous oscillations*. in *2017 IEEE Power & Energy Society General Meeting*. 2017. IEEE.
94. Zhang, D., et al. *Research on SSO caused by HVDC based on eigenvalue analysis*. in *Advanced Materials Research*. 2012. Trans Tech Publ.
95. Chen, Q.L., et al. *Design of HVDC Supplementary Subsynchronous Damping Controller*. in *Advanced Materials Research*. 2014. Trans Tech Publ.
96. Wang, S. and Z.J.E. Xu, *Research on shaft subsynchronous oscillation characteristics of parallel generators and SSDC application in mitigating SSO of multi-generators*. 2015. **8**(3): p. 1644-1662.
97. Hsu, Y.-Y. and L. Wang. *Modal control of an HV DC system for the damping of subsynchronous oscillations*. in *IEE Proceedings C (Generation, Transmission and Distribution)*. 1989. IET.
98. Jiang, Q., S. Cheng, and Y. Cao. *A genetic approach to design a HVDC supplementary subsynchronous damping controller*. in *Proceedings. International Conference on Power System Technology*. 2002. IEEE.
99. Harley, R. and J. Balda. *Subsynchronous resonance damping by specially controlling a parallel HVDC link*. in *IEE Proceedings C (Generation, Transmission and Distribution)*. 1985. IET.
100. Iravani, M., Z. Zhao, and R.J.I.t.o.p.s. Hamouda, *Impact of inverter station on torsional dynamics of parallel HVDC-AC power system*. 1993. **8**(3): p. 997-1003.
101. Hamouda, R., M. Iravani, and R.J.I.T.o.P.S. Hackam, *Torsional oscillations of series capacitor compensated AC/DC systems*. 1989. **4**(3): p. 889-896.

102. Rebled Lluch, J., *Modelling, control and simulation of LCC-HVDC systems for stability studies*. 2017, Universitat Politècnica de Catalunya.
103. Arrillaga, J. and J. Arrillaga, *High voltage direct current transmission*. Vol. 29. 1998: Iet.
104. Jovic, D., *High voltage direct current transmission: converters, systems and DC grids*. 2019: John Wiley & Sons.
105. Eremia, M., C.-C. Liu, and A.-A. Edris, *Advanced solutions in power systems: HVDC, FACTS, and Artificial Intelligence*. 2016: John Wiley & Sons.
106. From Wikipedia, t.f.e. *HVDC converter*. Type of HVDC Converters, Electromechanical converters, Line Commutated Converters, Voltage Source Converters 14 October 2020 [cited 2020 08 December 2020]; From Wikipedia, the free encyclopedia]. Available from: https://en.wikipedia.org/wiki/HVDC_converter.
107. Oni, O.E., *Technical performance and stability analysis of eskom power network using 600kv, 800kv, and 1000kv hvdc*. 2016.
108. Zidi—Mohammed, M.K.S.-A. and K.F.S.H.R.J.J.o.E.E. Amiri, *Performance evaluation of an HVDC link with a capacitor commutated inverter connected to a very weak receiving ac network*. 2009. **60**(4): p. 209-214.
109. Sood, V.K., *HVDC and FACTS controllers: applications of static converters in power systems*. 2006: Springer Science & Business Media.
110. Arrillaga, J., Y.H. Liu, and N.R. Watson, *Flexible power transmission: the HVDC options*. 2007: John Wiley & Sons.
111. Carlson, A.J.A.T.A., *Specific requirements on HVDC converter transformers*. 1996: p. 1-4.
112. Melvold, D.J. and W.F. Long, *Back-to-back HVDC system performance with different smoothing reactors*. 1989.
113. Reactors, B. *BPEG - The Biggest Manufacturer of Air Core Reactors*. [cited 2020 13 October 2020]; Available from: <http://www.bpeg-usa.com/>.
114. Capacitors, P. and H. Filters, *Buyer's Guide*. 2017, Accessed: Dec.
115. Chetty, L., *Design synthesis of LCC HVDC control systems*. 2011.
116. Balda, J.C., *Subsynchronous Resonance of Turbogenerators, with Particular Reference to a Few Selected Countermeasures*. 1986, University of Natal, Durban.
117. Daryabak, M., *Modeling line-commutated converter HVDC transmission systems using dynamic phasors*. 2014.
118. Faruque, M., Y. Zhang, and V.J.I.t.o.p.d. Dinavahi, *Detailed modeling of CIGRE HVDC benchmark system using PSCAD/EMTDC and PSB/SIMULINK*. 2005. **21**(1): p. 378-387.
119. Bhattacharya, S. and H.J.I.t.o.p.s. Dommel, *A new commutation margin control representation for digital simulation of HVDC system transients*. 1988. **3**(3): p. 1127-1132.
120. Funaki, T. and K.J.I.T.o.P.D. Matsuura, *Predictive firing angle calculation for constant effective margin angle control of CCC-HVDC*. 2000. **15**(3): p. 1087-1093.
121. Kim, C.-K., et al., *HVDC transmission: power conversion applications in power systems*. 2009: John Wiley & Sons.
122. Dongyuan, Z., et al. *Harmonic cancellation for HVDC using a novel control scheme*. in *IECEC'02. 2002 37th Intersociety Energy Conversion Engineering Conference, 2002*. 2002. IEEE.
123. Society, I.P.E., *IEEE Guide for Application and Specification of Harmonic Filters*. IEEE Std 1531™-2003 ed. 2003, Inc. 3 Park Avenue, New York, NY 10016-5997, USA: The Institute of Electrical and Electronics Engineers, . 69.

124. Arrillaga, J. and N.R. Watson, *Power system harmonics*. 2004: John Wiley & Sons.
125. PSCAD. *Passive Filter Design*. 2021 [cited 2021 06 January 2021]; Harmonic Filter Design Procedure]. Available from: https://www.pscad.com/webhelp/Master_Library_Models/Passive/Filters/Passive_Filter_Design.htm.
126. Muchtar, A. and W.M. Muttaqin. *Comparison between single tuned filter and c-type filter performance on the electric power distribution network*. in *Journal of Physics: Conference Series*. 2019. IOP Publishing.
127. Zamani, M. and M. Mohseni. *Damped-type double tuned filters design for HVDC systems*. in *2007 9th International Conference on Electrical Power Quality and Utilisation*. 2007. IEEE.
128. HE, Y.-h. and S. Heng. *A new method of designing double-tuned filter*. in *Proceedings of the 2nd International Conference on Computer Science and Electronics Engineering*. 2013. Atlantis Press.
129. Heising, C.J.I.I., New York, *IEEE recommended practice for the design of reliable industrial and commercial power systems*. 2007.
130. Kim, C.-K., et al., *Interactions between AC and DC Systems*. 2009.
131. Van Hertem, D., O. Gomis-Bellmunt, and J. Liang, *HVDC grids: for offshore and supergrid of the future*. 2016: John Wiley & Sons.
132. M, M., *Simulation of HVDC Transmission System in PSCAD/EMTDC and Protection Scheme under Fault Conditions*, in *National Conference On Power System Protection 27-28 Feb 2015*, K.P. Vittal, Editor. 2015: Central Power Research Institute, Bangalore.
133. Andersson, M., R. Cai, and H. Xie. *Novel solutions for LCC-HVDC fault ride through*. in *Proceedings of International High Voltage Direct Current Conference*. 2016.
134. Hajagos, L. and M. Basler. *Changes to IEEE 421.5 recommended practice for excitation system models for power system stability studies*. in *IEEE Power Engineering Society General Meeting, 2005*. 2005. IEEE.
135. Masenkane, M.J., *Damping subsynchronous resonance using supplementary controls around the static synchronous series compensator*. 2018.
136. Upadhyay, K.P.A., *Simulation of IEEE FIRST BENCHMARK Model for SSR Studies*.
137. Dimarogonas, A., N.J.I.t.o.p.a. Aspragathos, and systems, *The Effects of Some System Parameters on the Fatigue Life Reduction of Turbine-Generator Shafts Due to Electrical Transients*. 1984(8): p. 2308-2317.
138. Theja, B.S., et al. *Design of PID controller based power system stabilizer using Modified Philip-Heffron's model: An artificial bee colony approach*. in *2013 IEEE Symposium on Swarm Intelligence (SIS)*. 2013. IEEE.
139. Wenpei, Z., et al. *Design and Implementation of Subsynchronous Damping Controller for HVDC*. in *Journal of Physics: Conference Series*. 2020.
140. Jiang, Q.Y., Y.J. Cao, and S.J.J.I.t.o.p.d. Cheng, *A genetic approach to design a HVDC supplementary subsynchronous damping controller*. 2005. **20**(2): p. 1059-1064.
141. Petrosen, H., P.J.I.t.o.p.a. Krause, and systems, *A direct-and quadrature-axis representation of a parallel ac and dc power system*. 1966(3): p. 210-225.
142. Kim, D.-J., H.-K. Nam, and Y.-H.J.I.T.o.P.S. Moon, *A practical approach to HVDC system control for damping subsynchronous oscillation using the novel eigenvalue analysis program*. 2007. **22**(4): p. 1926-1934.
143. Tang, N., et al., *Phase correction method of HVDC supplementary subsynchronous multiple models damping controller*. 2011. **37**(4): p. 1015-1021.

144. Tambwe, *Damping Subsynchronous Oscillations using an HVDC-based Single-Mode Damping Controller*. 2021 IEEE PES/IAS PowerAfrica, 2021.
145. Choo, Y.C., et al., *Analysis of subsynchronous torsional interaction of HVDC system integrated hydro units with small generator-to-turbine inertia ratios*. 2013. **29**(3): p. 1064-1076.
146. Feng-Wei, H., *Modelling and analysis of inverter-based facts devices for power system dynamic studies*. 2006.
147. Zheng, X. and F. Zhouyan. *A novel unified approach for analysis of small-signal stability of power systems*. in *2000 IEEE Power Engineering Society Winter Meeting. Conference Proceedings (Cat. No. 00CH37077)*. 2000. IEEE.

APPENDIX

APPENDIX A: IEEE FIRST BENCHMARK MODEL

A1. Per Unit Base

Table A1: Per Unit Base Parameters

Parameters	Grid Side	Generator Side
3-phase Base Power	892.4 MVA	892.4 MVA
Base Voltage (Line-to-Line)	539 kV	26 KBV
Base Impedance	325.55 Ω	0.7575 Ω
Base Current	955.8 A	19.82 KA
Base Frequency	60 Hz	60 Hz

A.2 IEEE FBM Parameters

The IEEE FBM generator adopted from the Navajo Project [11] has two damper windings on the q -axis and one on the d -axis. The generator parameters listed in Table A2 are given in the generator per unit base given in Table A1 with a 0.9 lagging power factor. The turbogenerator multi-mass parameters have already been outlined in section 4.3.

Table A2: Generator Parameters

Parameters	Value	Parameters	Value
R_a	0.0	X_{mq}	1.58 pu
X_p	0.19 pu	X'_q	0.228 pu
X_l	0.135 pu	T'_{do}	4.3 s
X_d	1.79 pu	T''_{do}	0.032 s
X'_d	0.169 pu	T'_{qo}	0.85 s
X_q	1.71 pu	T''_{qo}	0.05 s

Table A3: Step-up Transformer Parameters

Parameters	Value	Parameters	Value
Rated Power	892.4 MVA	Rated Frequency	60 Hz
Rated Low Voltage (L-L)	26 kV	Rated High Voltage (L-L)	539 kV
Positive sequence impedance	0.14 pu	Negative sequence impedance	0.14 pu

Table A4: Rotor Circuit parameters in pu (base 892.4 MVA)

Parameters	d-axis (pu)	q-axis (pu)
$\omega_0 R_f$	0.53	5.3
X_f	0.062	0.326
$\omega_0 R_k$	1.54	3.1
X_k	0.0055	0.095
X_a	1.66	1.58
X_L	0.13	0.13

Table A5: Single line transmission network parameters in pu (base 892.4 MVA)

Parameters	Positive Sequence	Zero Sequence
R_L	0.02	0.50
X_L	0.50	1.56
X_S	0.06	0.06

Table A6: IEEE FBM Multi-Mass Parameters (base 892.4 MVA)

Inertia	Inertia Constant(s)	Shaft section	Spring constant (pu torque/ rad)	Torque fraction
HP turbine	0.092897	-	-	0.3
IP turbine	0.155589	HP-IP	7277	0.26
LPA turbine	0.85867	IP-LPA	73168	0.22
LPB turbine	0.884215	LPA-LPB	13618	0.22
G	0.868495	LPB-G	26716	-
Ex	0.034217	G-Ex	1064	-

APPENDIX B: PARALLEL AC/DC SYSTEM

B1. HVDC scheme between two sources

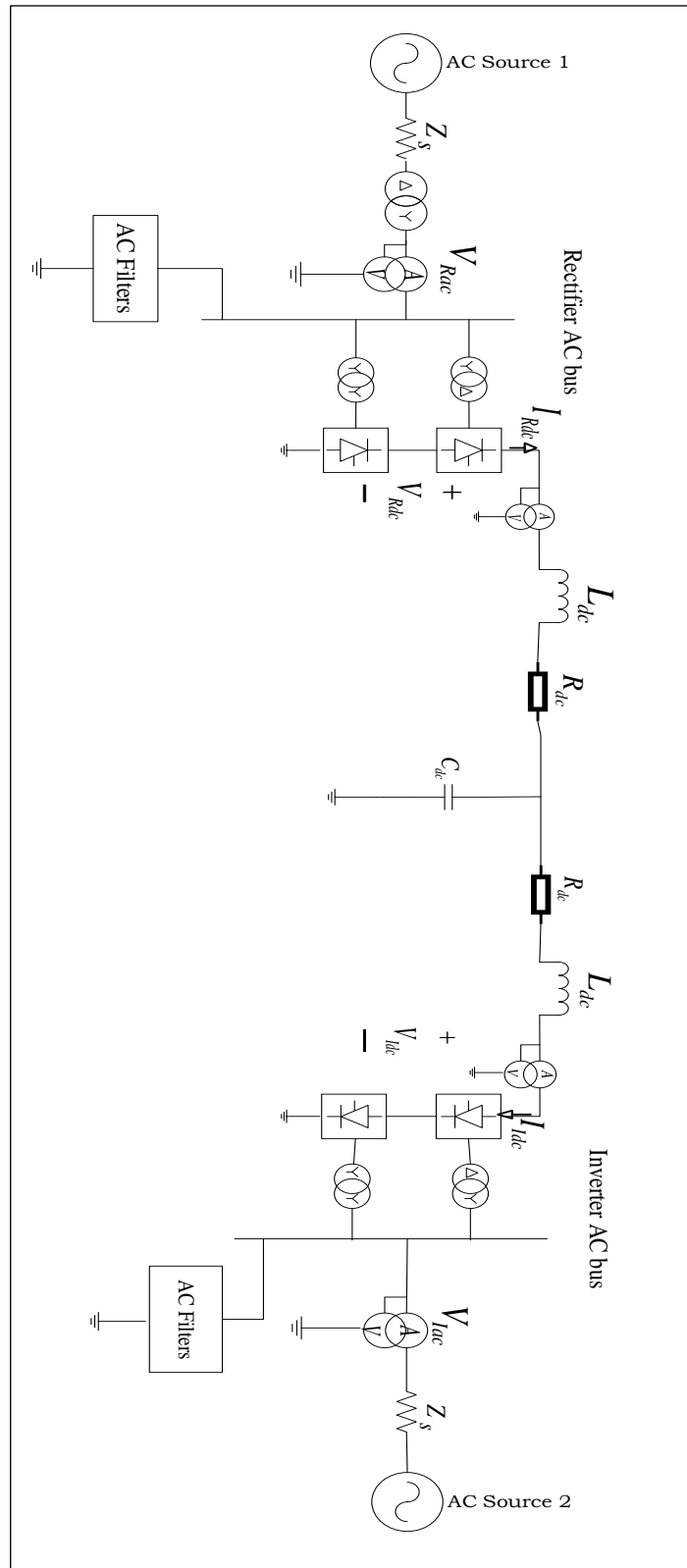


Figure B1: HVDC Link between two sources

B2. Parallel AC-DC Configuration

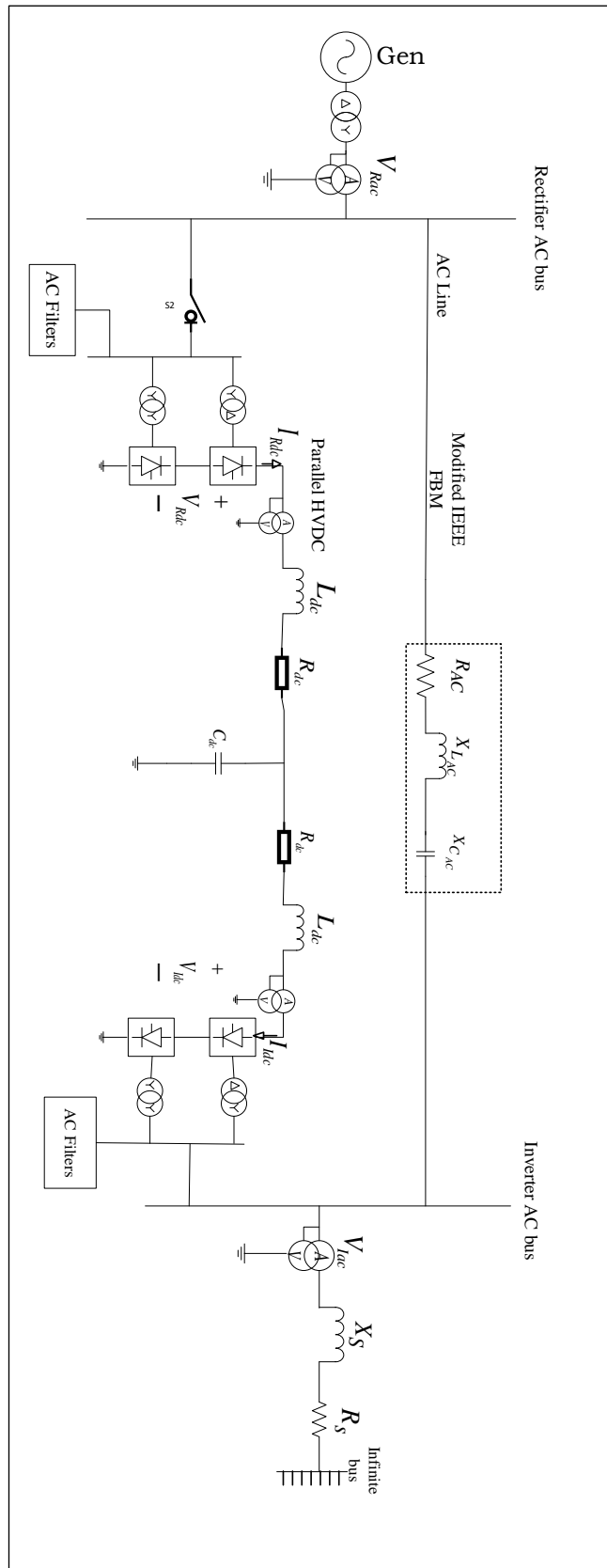


Figure B1: Parallel AC-DC System Configuration

B3. General HVDC Parameters

This research was based on two HVDC operating points (i.e., $P_{dc}=0.4846$ pu and $P_{dc}=0.4154$ pu). The nominal power of the DC line is 0.4846 pu. The parameters presented in *Table B3.1* are similar for all HVDC operating points.

Table B3.1: General HVDC parameters

Parameters	Symbol	Value	Unit
Rectifier side's rated line to line voltage	V_{SR}	539	kV
Inverter side's rated line to line voltage	V_{SI}	477.8	kV
Rated DC Voltage	V_{dc}	500	kV
Rectifier's firing angle	α	18	°
Minimum gamma	γ	15	°
Transmission lines' length	L_{transm}	276	Miles
Positive Sequence Resistance	R_{dc}	0.01	Ohm/Km
Positive Sequence Inductance	L_{dc}	0.0023827	H/Km
Number of bridges per converter	B	2	Bridges
Transformers' commutating reactance	X_{tr}	0.14	pu
Equivalent commutating resistance	R_t	0.01	pu
Filters' equivalent capacitive reactance	X_{CF}	10	pu
Transmission lines'type	Overhead lines		

B4. Detailed HVDC link's parameters when placed between two sources ($P_{dc}=0.4846$ pu)

Table B4.1: HVDC Operating point when placed between two sources (ideal sources)

Parameters	Rectifier	Inverter
α	18°	-
β	-	152.7681
T	0.3673	0.4025
V_{do}	534860 V	524000.0640 V
ΔV_d	18754.7315 V	20112.0629 V
R_C	10.6240 Ω	11.3929 Ω /phase
X_C	11.1060 Ω	10.9306 Ω /phase
$V_{AC,LL}$	198023 V	194006.1200V
V_{dc}	489950.0325 V	486079.0184 V
I_{L1} (A)	505.6767 A	611.6488 A
PF	0.9160	0.9275
ϕ	23.6468°	21.9448°
$P_{AC,HT}$	432.4568 MW	428.9989MW
$Q_{AC,HT}$	189.2567 MVar	172.8450 MVar

B.4.1 Filter Design

The 12-pulse converter typically has AC current characteristic harmonics of order $kp \pm 1$, i.e., the harmonics of orders 11, 13, 23, 25, etc. In this thesis, we applied damped type filters to minimize these characteristic harmonics. Figure B2 shows the harmonics of the AC current entering the rectifier. The figure was reproduced in PSCAD with the FFT component. It can be seen from these results that the AC current distortion involves harmonics of significant amplitude at positions $kp \pm 1$ (i.e., 11, 13, 23, 25, etc.). There are also non-characteristic harmonics, but they have a less adverse effect on the AC current distortion. As a result, a double-tuned filter was applied to reduce both the 11th and 13th harmonics, and a second-order high pass filter tuned to the 24th harmonic was used to minimize the 23rd and 25th harmonics and the other high-frequency harmonics. Both the AC filters and the capacitor bank deliver 61 % of the converter's reactive power demand. The rated reactive power provided by AC filters and the capacitor bank is given in Table B4.2.

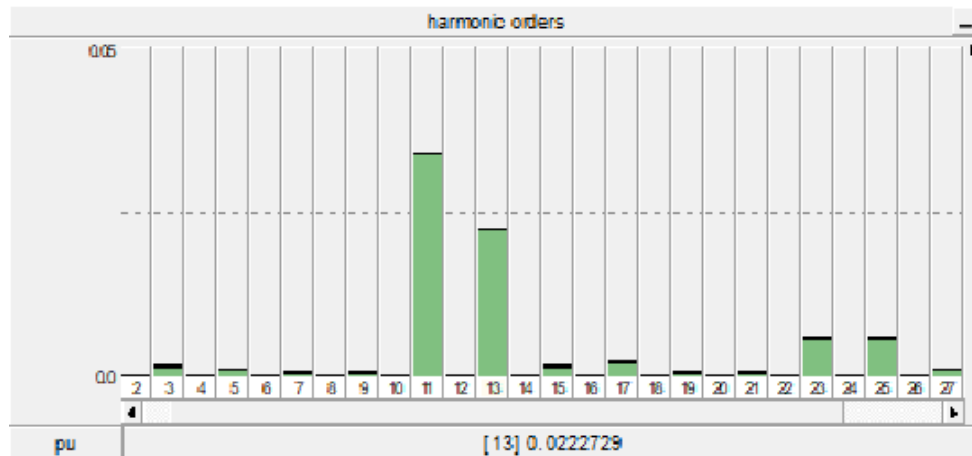


Figure B2: Rectifier's AC current harmonics without AC filters

Table B4.2 Rated Reactive Power Compensation

Parameters	Rated MVAR	Rectifier (Mvar)	Inverter (Mvar)
Q_F	$60\% Q_{AC,HT}$	94.67836973	103.7079741
$Q_{High-Pass}$	$40\% Q_F$	37.87134789	41.48318963
Q_{DT_F}	$40\% Q_F$	37.87134789	41.48318963
$Q_{Cap-bank}$	$20\% Q_F$	18.93567395	20.74159482

Table B4.3: Second-Order High Pass Filter ($kV_{LLR}=0.99pu$, $kV_{LLI}=0.8865pu$, $Q_F=1$, $h=24$)

Parameters	Rectifier	Inverter
$Q_{High-Pass}$ (Mvar)	37.8713479	41.4831896
C (μF)	0.34591013	0.48200188
L (mH)	35.3144139	25.3434973
R (Ω)	319.597289	229.302562

Table B4.4: Double Tuned Filter ($P_{dc}=0.4846 pu$, $kV_{LLR}=0.99pu$, $kV_{LLI}=0.8865pu$, $Q_F=45$)

Parameters	Rectifier	Inverter
Q_{DT_F} (Mvar)	37.8713479	41.4831896
C_1 (uf)	0.69156357	0.94600000
C_2 (uf)	25.2432511	35.1987244
L_1 (mH)	70.1677662	50.3375674
L_2 (mH)	1.97646013	1.41743262
R (Ω)	6.54882939	4.69776422

Table B4.5: Capacitor Bank ($P_{dc}=0.4846 pu$)

Parameters	Rectifier	Inverter
$Q_{Cap-bank}$ (M var)	18.93567395	20.74159482
C(uf)	0.172890489	0.189379289

Figure B3 illustrates the AC current time-domain response before and after applying AC filters. It can be seen that AC filters have significantly reduced harmonics.

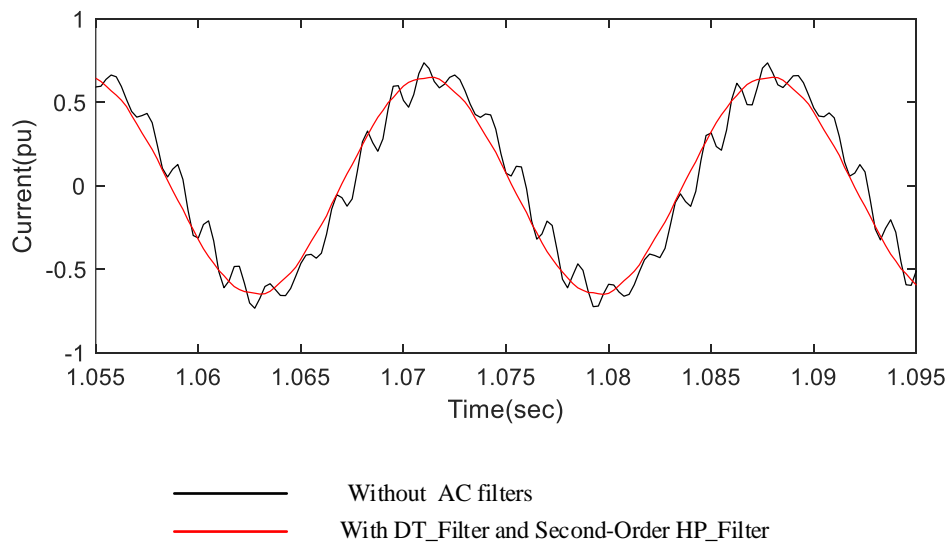


Figure B3: Time domain response of the rectifier bus's single-phase AC current with a double-tuned filter and a second-order High-pass filter

Figure B4 illustrates the performance of harmonics. The results in Figure B4 show the effectiveness of the AC filters proposed. The filters have reduced the harmonic currents considerably.

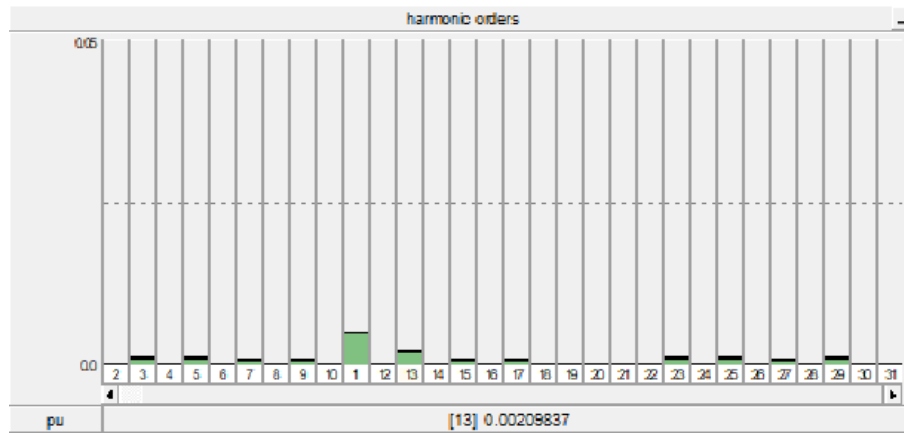


Figure B4: Rectifier bus's AC current harmonics, AC filters included

B5. Detailed parameters of the parallel AC-DC system

Table B5.1: Parameters of the Parallel AC-DC system made up with the Modified IEEE FBM and the Parallel HVDC link

Sections	Parameters
AC Transmission Line (Modified IEEE)	Type= Overhead Lines, Length=276 Miles, $V_{LL}=500$ KV, $R_{AC}=0.04$ pu, $X_{LAC}=1.00$ pu
DC transmission lines	Type= Overhead lines, Length=276 Miles
DC scheme 1	$P_R=0.485$ pu, $V_R=0.909$ pu, $I_{R0}=0.923$ pu, $V_{qR}=0.414$ pu, $V_{qA0}=0.682$ pu, $V_{dA0}=0.712$ pu, $I_{qACR}=0.676$ pu, $I_{dACR}=0.249$ pu, $I_{q(rec)}=0.300$ pu, $I_{d(rec)}=0.655$ pu, $\phi_R=20.208$ deg, $P_I=0.481$ pu, $V_I=0.902$ pu, $I_{I0}=0.923$ pu, $V_{qI}=0.400$ pu, $I_{qACIo}=0.687$ pu, $I_{dACIo}=0.217$ pu, $I_{q(inv)}=0.322$ pu, $I_{d(inv)}=0.644$ pu, $\phi_I=17.5$ deg, $\alpha=18^\circ$, $\gamma=15^\circ$, ($Q_{RMAX}=295.63$ Mvar, $Q_{IMAX}=250$ Mvar, $P_G=0.9$, $K=0.7$, $PF=0.9$).
DC scheme 2	$P_R=0.415$ pu, $V_R=0.909$ pu, $I_{R0}=0.792$ pu, $V_{qR}=0.414$ pu, $I_{qACR}=0.580$ pu, $I_{dACR}=0.211$ pu, $I_{q(rec)}=0.258$ pu, $I_{d(rec)}=0.493$ pu, $\phi_R=20.081$ deg, $P_I=0.413$ pu, $V_I=0.902$ pu, $I_{I0}=0.792$ pu, $V_{qI}=0.404$ pu, $I_{qACIo}=0.589$ pu, $I_{dACIo}=0.184$ pu, $I_{q(inv)}=0.278$ pu, $I_{d(inv)}=0.479$ pu, $\phi_I=17.38$ deg, $\alpha=18^\circ$, $\gamma=15^\circ$, ($Q_{RMAX}=293.63$ Mvar, $Q_{IMAX}=247.59$ Mvar, $P_G=0.9$, $K=0.7$, $PF=0.9$).
Infinite bus	Rated Voltage, $V_{LL}=500$ kV, Rated Frequency, $f=60$ Hz, $X_S=0.5$ pu, $R_S=0.06X_S$

B5.1 Filter Design for $P_{dc}=0.4846$ pu, $K=0.7$

The AC line's compensation percentage variation induces voltages' variations at both ends of the HVDC system. Therefore, filters and capacitor banks have been applied to keep these voltages within +/- 5% of their nominal value. The maximal reactive power demand at both ends of the HVDC links are listed in Table B5.1. [97] proposed a typical value (X_{CF}) of the capacitor bank equals 10 pu. The assumptions given in Table B5.2 and Table B5.6 were applied to design filters and capacitor banks.

Table B5.2 Rated Reactive Power Compensation

Parameters	Rated MVar	Rectifier (Mvar)	Inverter (Mvar)
Q_F	$60\% Q_{AC,HT}$	177.3780	150.0000
$Q_{High-Pass}$	$25\% Q_F$	44.34450	37.50000
Q_{DT_F}	$25\% Q_F$	44.34450	37.50000
$Q_{Cap-bank}$	$50\% Q_F$	88.68900	75.00000

Table B5.3: Second-Order High Pass Filter ($Q_F=2$, $h=24$)

Parameters	Rectifier	Inverter
$Q_{High-Pass}$ (Mvar)	44.34450	37.50000
C (μF)	0.432096	0.373851
L (mH)	28.27059	32.67507
R (Ω)	511.5726	591.2741

Table B5.4: Double-tuned Filter ($Q_F=30$)

Parameters	Rectifier	Inverter
Q_{DT_F} (Mvar)	44.34450	37.50000
C_1 (uf)	0.730806	0.747702
C_2 (uf)	26.67568	27.29243
L_1 (mH)	66.39997	64.89945
L_2 (mH)	1.870330	1.828064
R (Ω)	7.224138	7.060886

Table B5.5: Capacitor Bank ($P_{dc}=0.4846$ pu)

Parameters	Rectifier	Inverter
$Q_{Cap-bank}$ (MVar)	88.68900	75.00000
C (μF)	0.864192	0.747700

B5.2 Filter Design for $P_{dc}=0.4154$ pu, $K=0.7$

Table B5.6 Rated Reactive Power Compensation

Parameters	Rated MVar	Rectifier (Mvar)	Inverter (Mvar)
Q_F	$60\% Q_{AC,HT}$	176.1780	148.5540
$Q_{High-Pass}$	$25\% Q_F$	44.04450	37.13850
Q_{DT_F}	$25\% Q_F$	44.04450	37.13850
$Q_{Cap-bank}$	$50\% Q_F$	88.08900	74.27700

Table B5.7: Second Order High Pass Filter ($h=24$, $Q_F=2$)

Parameters	Rectifier	Inverter
$Q_{High-Pass}$ (Mvar)	44.04450	37.13850
C (μF)	0.429173	0.370247
L (mH)	28.46315	32.99312
R (Ω)	515.0570	597.0295

Table B5.8: Double-Tuned Filter ($Q_F=45$)

Parameters	Rectifier	Inverter
Q_{DT_F} (Mvar)	44.04450	37.13850
C ₁ (uf)	0.858346	0.740494
C ₂ (uf)	31.33111	27.02933
L ₁ (mH)	56.53370	65.53117
L ₂ (mH)	1.592421	1.845858
R (Ω)	5.276348	6.116229

Table B5.9: Capacitor Bank ($P_{dc}=0.4154 pu$)

Parameters	Rectifier	Inverter
$Q_{Cap-bank}$ (MVar)	88.08900	74.27700
C (μF)	0.858346	0.740493

APPENDIX C: EQUIDISTANT SHORT-CIRCUIT RATIO CALCULATIONS

C.1 Equidistant Short Circuit Ratio Calculation

The calculation of the inverter station AC bus's strength (i.e., stiffness) considering the two HVDC operating points was achieved following the procedure outlined in section 2.3.10. The AC filters and capacitor banks on converters' AC buses provide 60 percent of the reactive power demand for each HVDC operating point. An R-L type AC source with an equivalent series impedance of $X_S=0.5$ pu (with $R_S=0.06X_S$) was applied on the inverter side. The Point of Common Coupling (PCC) Voltage was 0.928 pu. The AC Filters and capacitor bank provide 60% of reactive power compensation (See Figure C.1).

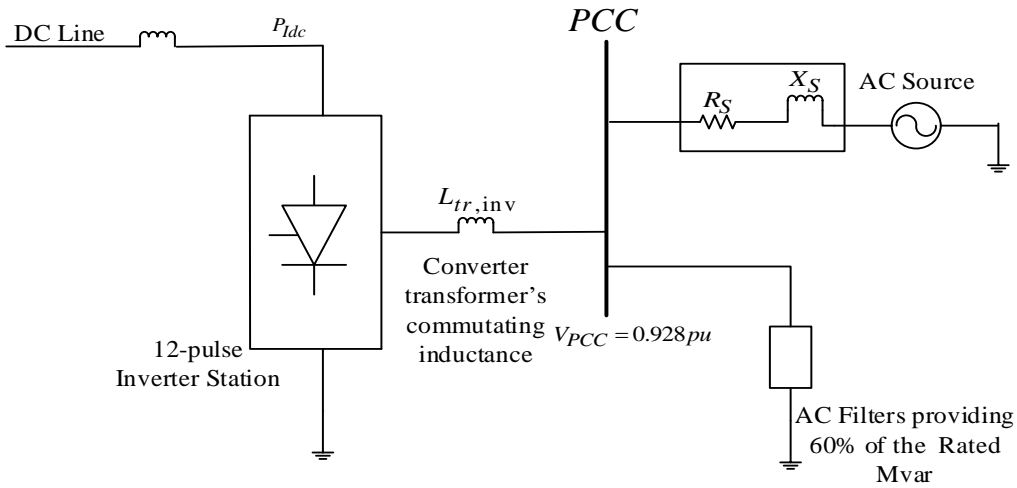


Figure C1: Inverter AC system's Point of Common Coupling Characteristics

The Short-Circuit Level at the inverter AC bus was determined in the following way:

$$SCL = \frac{V_{PCC}^2}{Z_S} = \frac{(500 \times 1000)^2}{163.068} = 1533103000 \approx 1.53 \text{ GVA}$$

Therefore, the Short-Circuit Ratio (SCR) can be calculated as follows:

- For $P_{dc} = 0.4846 \text{ pu}$

$$SCR = \frac{SCL}{P_{dc}} = \frac{1533103000}{432546280} = 3.54$$

- For $P_{dc} = 0.4154 \text{ pu}$

$$SCR = \frac{SCL}{P_{dc}} = \frac{1533103000}{370702960} \approx 4.12$$

By considering the influence of the reactive power Q_{FI} provided by AC filters and the capacitor bank on the inverter side at both HVDC operating points, the Equivalent Short-Circuit Ratio (ESCR) can be calculated as follows:

- For $P_{dc} = 0.4846 pu$

$$ESCR = \frac{SCL - Q_{FI}}{P_{dc}} = \frac{1533103000 - 150000000}{432546280} = 3.20$$

- For $P_{dc} = 0.4154 pu$

$$ESCR = \frac{SCL - Q_{FI}}{P_{dc}} = \frac{1533103000 - 176800000}{370702960} = 3.73 \approx 4.0$$

C.2 DC Power Level Based-Torsional Interaction Response

As pointed out in the review, the DC power level has an enormous impact on torsional interaction [51]. It can alter the inverter bus's stiffness, making the parallel AC-DC system vulnerable to unwanted torsional interactions [101]. In all the reported cases, X_s equals 0.5 pu and $R_s=0.06X_s$. This research focused on an inverter station connected to an AC bus with moderate stiffness. This study investigated the TG shaft's torsional dynamics response when varying the DC power. Table C.1 illustrates the FFT result of the most influential torsional modes of the TG shaft's changing the DC power at each compensation level. Observation-based on operating points with the same level of compensation shows that the reduction in DC power also reduces the adverse impact of torsional oscillation. The higher the DC power, the lower the inverter AC bus's stiffness and the more exposed the parallel AC-DC system is to a significant negative damping torque [51, 101].

Table C.1: DC Power Level Based Torsional Damping Impact

Percentage Level K (%)	Severe Mode	Pdc=0.4874 pu	Pdc=0.4154 pu
70	Mode 1	1139 000 pu	264 800 pu
61	Mode 1	2206 pu	1255 pu
41	Mode 3	2065 pu	348 pu
23	Mode 4	14 278 pu	710 pu

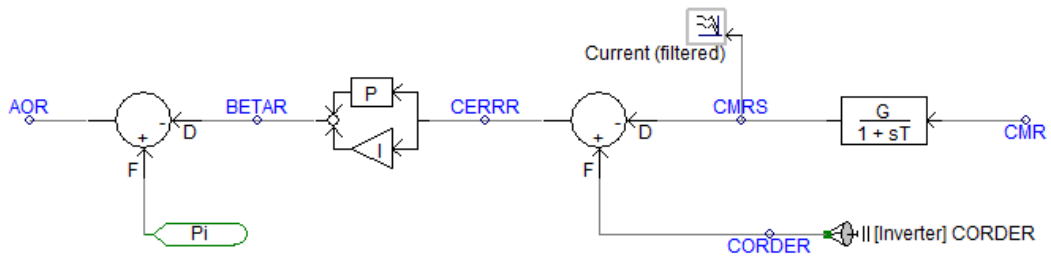


Figure D3: Rectifier Current Regulator PSCAD Model

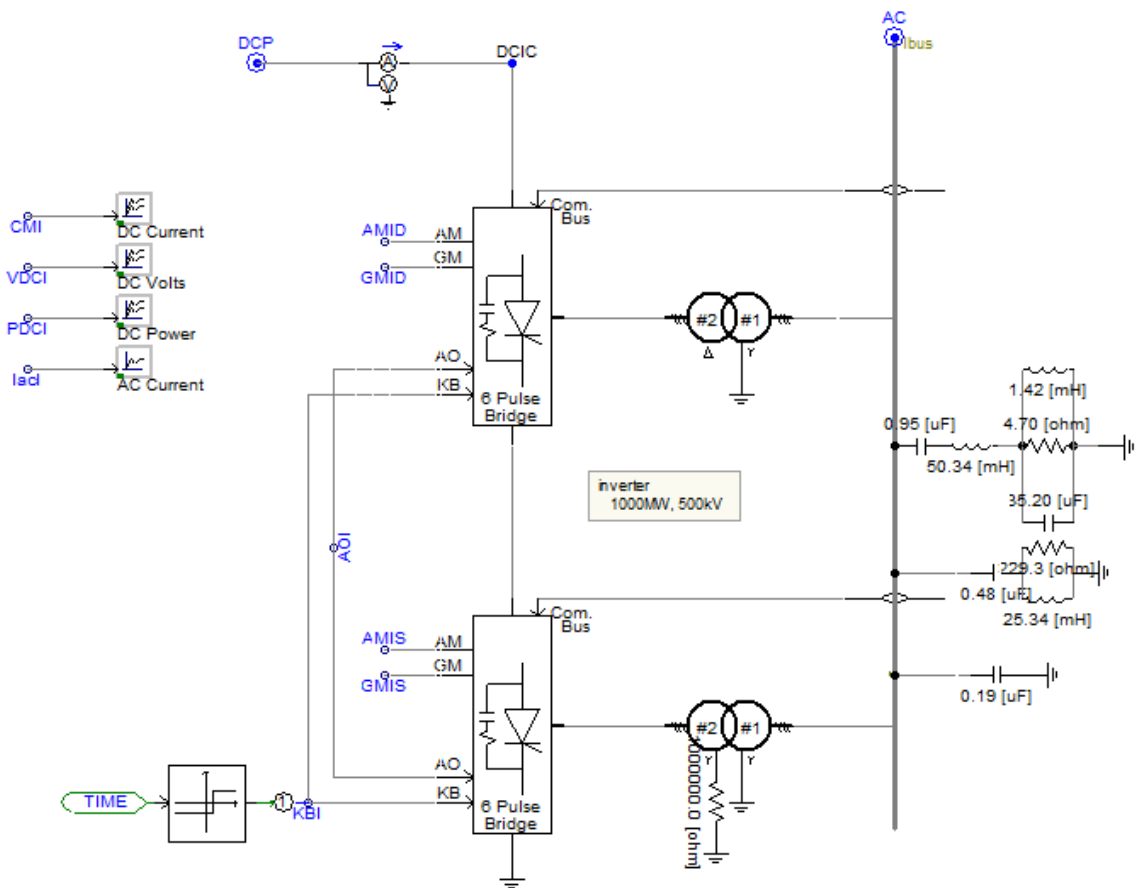


Figure D4: 12-Pulse Converter Configuration on Inverter Side

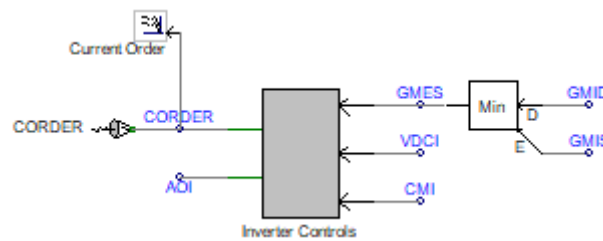


Figure D5: Inverter Control PSCAD Model

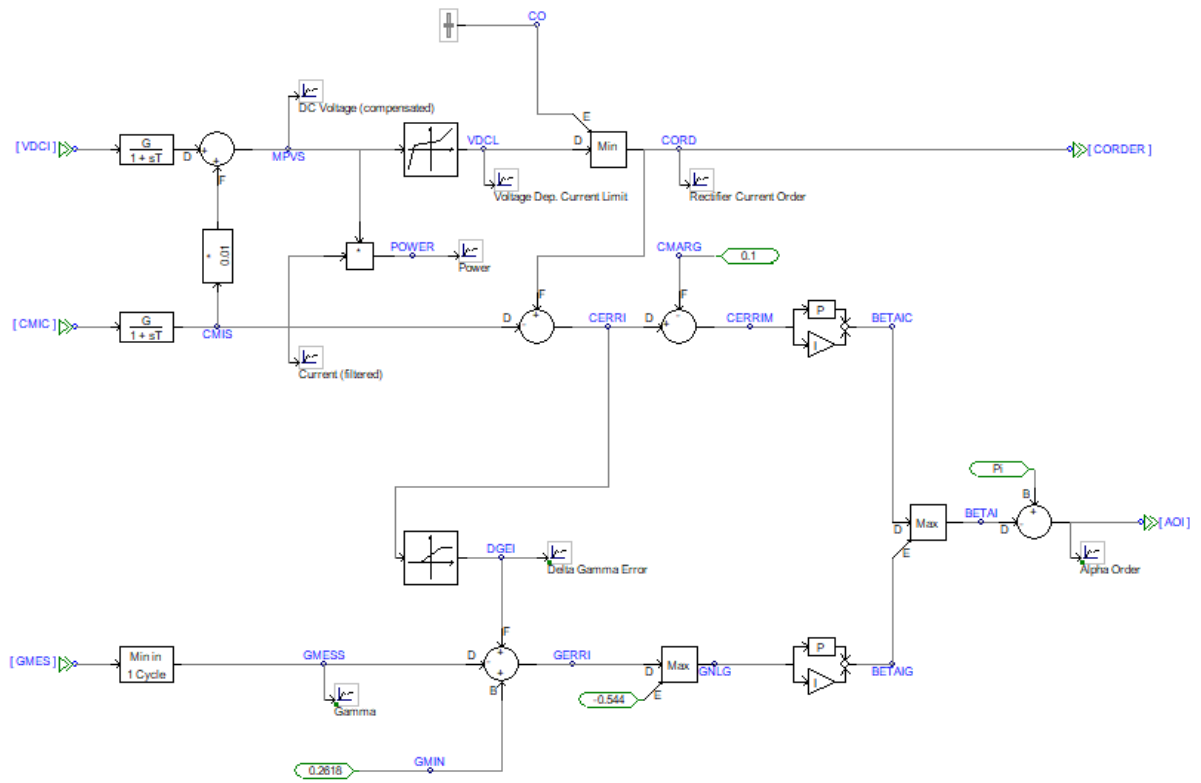


Figure D6: Inverter Voltage Regulator PSCAD Model

APPENDIX E: PSCAD MODELING OF THE MODIFIED IEEE FBM MODEL WITH THE PARALLEL HVDC LINK (USING MANUAL EXCITATION)

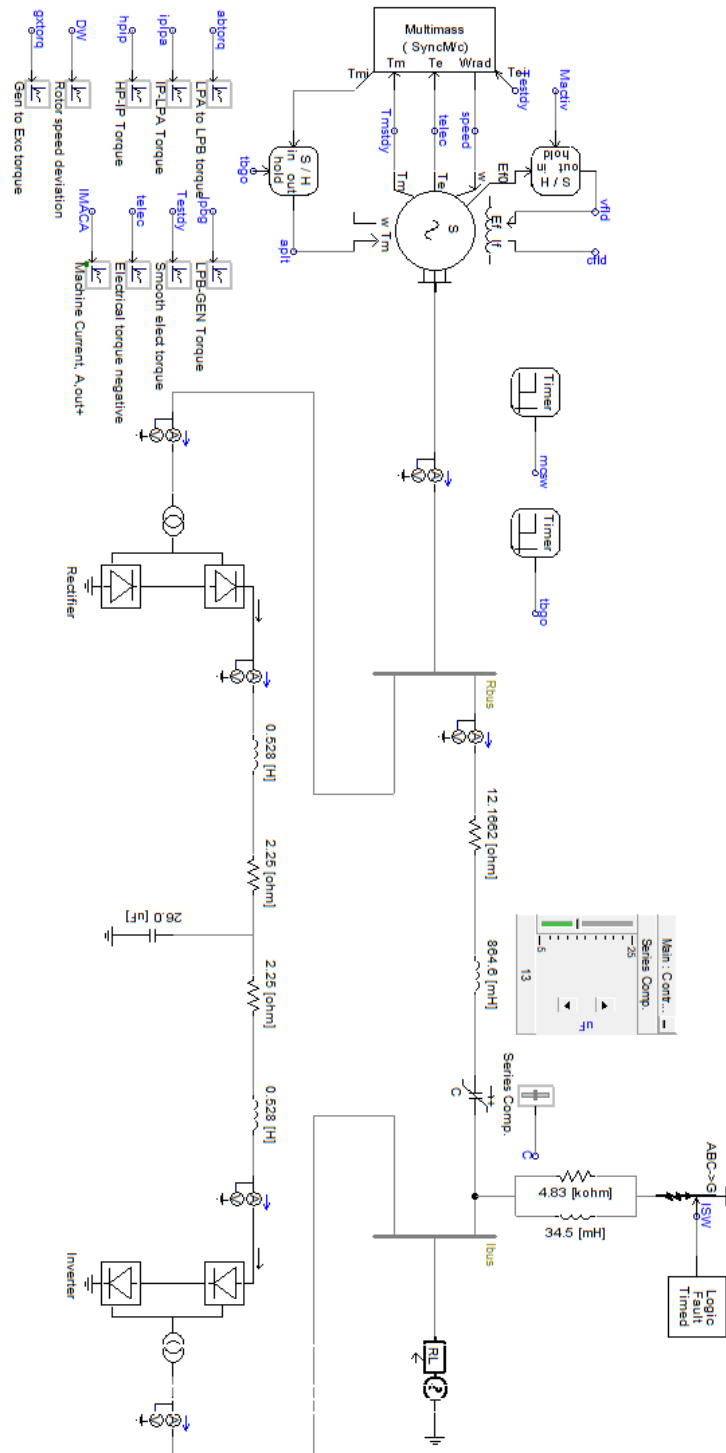


Figure E1: PSCAD Model of the Modified IEEE with the parallel HVDC Link

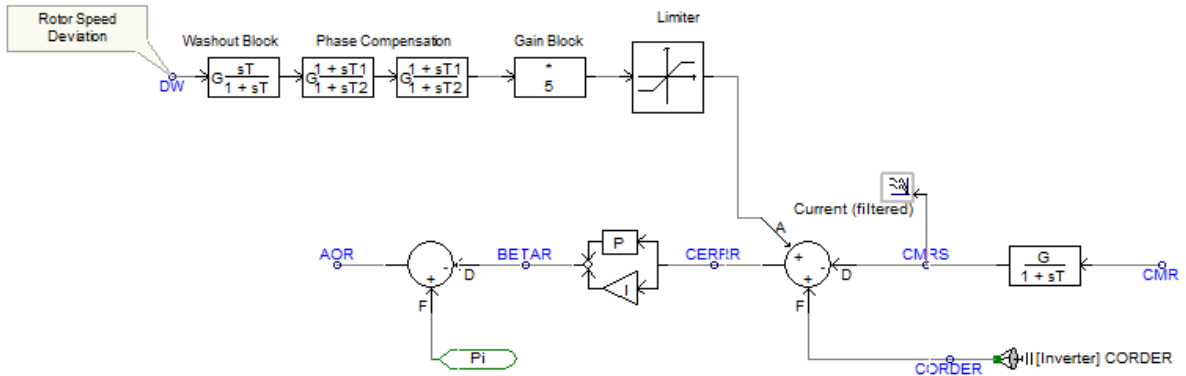


Figure F2: Rectifier Current Regulator Equipped with a Single-Mode Damping Controller

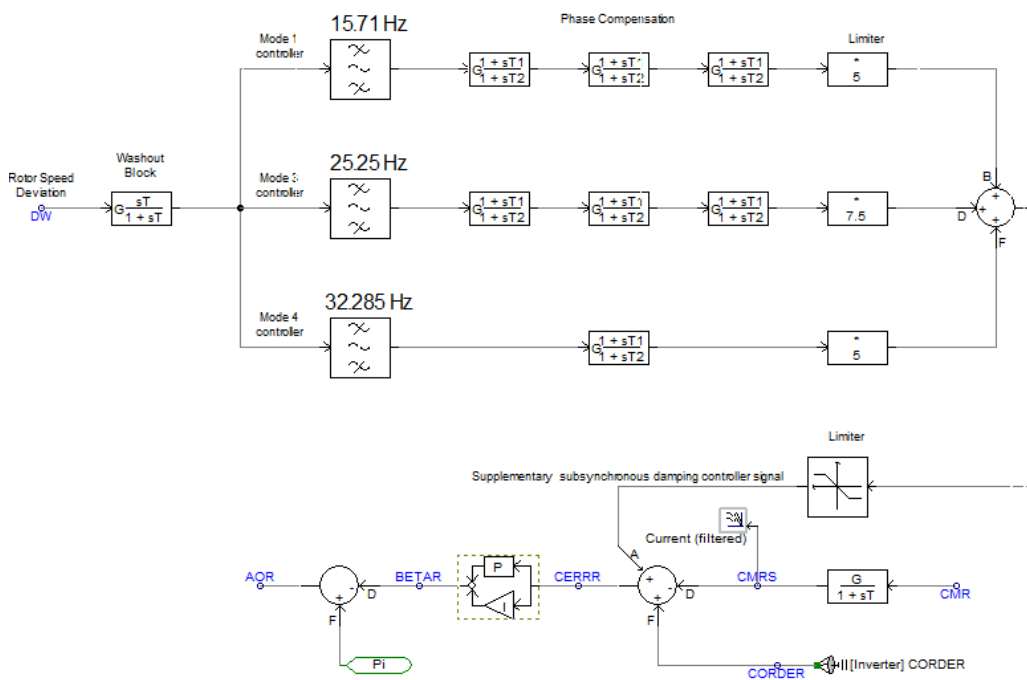


Figure F3: Rectifier Current Regulator Equipped with the Multi-Modal Damping Controller designed for Case (c).

Table F1. IEEE Type ST1A Excitation System Parameters

Parameters	Value	Parameters	Value
K_A	210.0	K_{LR}	4.54
T_A	0	I_{LR}	4.4
T_C	1.0	T_{B1}	0
T_B	1.0	V_{RMAX}	6.43
T_{C1}	0	V_{RMIN}	-6.0
K_F	0	K_C	0.038
T_R	0	X_C, R_C	0

Table F2: Power System Stabilizer Parameters [97]

Parameters	Value	Parameters	Value
K_{PSS}	-0.03,	T_4	0.5
T_1	0.1	T_{S1}	0.03
T_2	0.5	V_{STMAX}	0.09
T_3	0.1	V_{STMIN}	-0.09

APPENDIX G: TEST SIGNAL AND PHASE CORRECTION METHODS, INCLUDING FFT ANALYSIS

G.1 PSCAD based-Sinusoidal Test Signal [96]

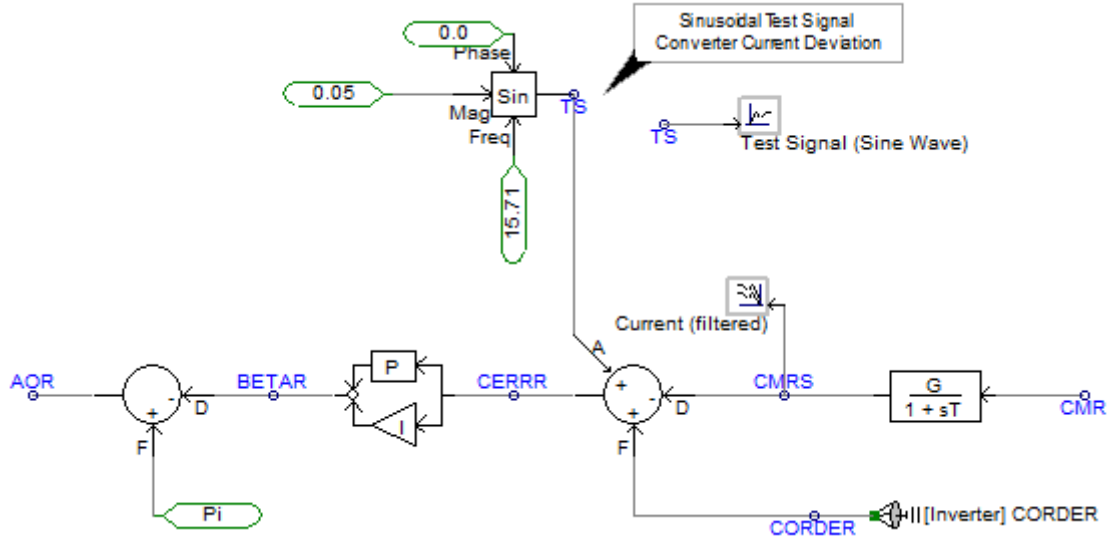


Figure G2: Rectifier Current Regulator with the Sinusoidal Test Signal of 0.05 pu and 15.71 Hz

G.2 Lead-Lag Compensator Design [143]

The phase compensation blocks of damping controllers shown in Figure F2 and Figure F3 can be summarized as follows;

$$\left(\frac{1 + sT_1}{1 + sT_2} \right)^n$$

Where T_1 , T_2 , and n are obtained as follows:

$$\left\{ \begin{array}{l} a = \frac{T_2}{T_1} = \frac{1 - \sin \phi}{1 + \sin \phi} \\ T_1 = \frac{1}{(\omega_x \sqrt{a})} \\ T_2 = aT_1 \end{array} \right.$$

Where ω_x is the angular frequency of the point needed phase compensation, and ϕ is the phase angle.

T_1 and T_2 are the time constant of the phase compensation part. When the compensation phase's angle

is relatively large, small phase compensation links can be adopted in series, making the phase-frequency response of the phase compensation link has a better compensation characteristic.

G.3 MATLAB codes for FFT Analysis

```
clc
clear all
close all
```

% LOADING THE NOTEPAD FILES AND DECLARATION OF VARIABLES

```
load -ascii paper_03.out; % Loading paper_03 for the HVDC with  $P_{dc}=0.4846$  pu
%load -ascii papa_03.out; % Loading paper_03 for the HVDC with  $P_{dc}=0.4154$  pu
t=paper_03(:,1); % Time data
rotsp=paper_03(:,2); % Rotor Speed Deviation for HVDC with  $P_{dc}=0.4846$  pu
%rotsp=papa_03(:,2); % Rotor Speed Deviation for HVDC with  $P_{dc}=0.4154$  pu
Fs=1/0.001; % Sampling Frequency
```

% PLOTTING FFT RESULTS FROM 1.5 SEC TO 3.0 SEC

```
subplot (131)
B=rotsp (1501:3001, :);
nfft= length(B);
x=fft(B,1501);
A1=(abs(x).^2)/nfft;
f= ((0: nfft-1) *(Fs/nfft));
plot (f, A1,'k','LineWidth',1);
grid on
% xlim ([0 70]);
% ylim ([0 500])
ylabel ('FFT Mag. (pu)');
xlabel ('Frequency (Hz)');
```

% PLOTTING FFT RESULTS FROM 3.0 SEC TO 4.5 SEC

```
subplot (132)
B=rotsp (3001:4501, :);
nfft= length(B);
x=fft(B,1501);
A2=(abs(x).^2)/nfft;
f= ((0: nfft-1) *(Fs/nfft));
plot (f, A2,'k','LineWidth',1);
grid on
% xlim ([0 70]);
% ylim ([0 500])
ylabel ('FFT Mag. (pu)');
xlabel ('Frequency (Hz)');
```

% PLOTTING FFT RESULTS FROM 4.5 SEC TO 6.0 SEC

```
subplot (133)
B=rotsp (4501:6001, :);
nfft= length(B);
x=fft(B,1501);
A3=(abs(x).^2)/nfft;
```

```
f= ((0: nfft-1) *(Fs/nfft));
plot (f, A3, 'k', 'LineWidth', 1);
grid on
% xlim ([0 70]);
% ylim ([0 500])
ylabel ('FFT Mag. (pu)');
xlabel ('Frequency (Hz)')
```

G.4 Phase Difference Using MATLAB Program

The MATLAB codes below made it possible to compute the phase difference between the converter current deviation-based test signal and the electromagnetic torque at a frequency of interest (15.71 Hz in the current case).

```
clc
clear all
close all

% LOADING THE NOTEPAD FILES AND DECLARATION OF VARIABLES

load -ascii Phasedi_01.out;
t=Phasedi_01(:,1);
Fs=1/0.001;
t1=t (4501:6001, :);
Telec=Phasedi_01(:,7); % Electrical torque negative
Tsteady=Phasedi_01(:,8); % Steady state electrical torque
TS= Phasedi_01(:,6); % test signal or converter current deviation

% DEFINING THE FREQUENCY OF INTEREST

frequ=15.71; % Defining frequency of interest in HZ

% FFT ANALYSIS OF BOTH SIGNALS
% FFT of the sinusoidal test signal from 4.5 sec to 6.0 sec

B= TS (4501:6001, :);
nfft4= length(B);
x4=fft(B,1501);

% FFT of the Electromagnetic torque from 4.5 sec to 6.0 sec

B=Tsteady (4501:6001, :);
nfft6= length(B);
x6=fft(B,1501);

% Computing the phase difference between  $\Delta I_{ref}$  and  $\Delta T_e$ 

x4_phase=unwrap(angle(x4));
x6_phase=unwrap(angle(x6));
x_phdiff=(180/pi) *(x4_phase-x6_phase);
yy1 = smooth (f, x_phdiff,0.01, 'rloess');
plot (f, yy1, 'r')
xlim ([0 70]);
```

```
ylabel ('Phase (deg)');
xlabel ('Frequency (Hz)');
```

```
% Phase shift at the frequency of interest
```

```
binNum = ((length(B))/Fs) *(frequ);
binNum = round(binNum);
phase_diff =x_phdiff(binNum);
```

```
% Display result in degrees
```

```
sprintf ('Phase difference between signals at %d Hz is %f degrees', frequ, (phase_diff))
```

G.5 Performance Investigation of PSS and Single-mode damping controllers ($P_{dc}=0.4846$ pu)

```
clc
clear all
close all
```

```
%LOADING THE NOTEPAD DATA FILE AND DECLARATION OF VARIABLES
```

```
load -ascii paper_03.out; % System Without damping compensators
load -ascii paperM1_03.out; % Compensator 1 Notepad file
load -ascii paperM3_03.out; % Compensator 3 Notepad file
load -ascii paperM4_03.out; % Compensator 4 Notepad file
```

```
t=paperM1_03(:,1); % Data for column vector “t”: time constant
Fs=1/0.001; % Sampling frequency
rotsp=paper_03(:,2); % Rotor speed deviation without compensators.
rotspM11=paperM1_03(:,2); % Rotor speed deviation with PSS and Mode 1 damping controller
rotspM33=paperM3_03(:,2); % Rotor speed deviation with PSS and Mode 3 damping controller
rotspM44=paperM4_03(:,2); % Rotor speed deviation with PSS and Mode 4 damping controller
```

```
% PLOTTING FFT RESULTS FOR THE THREE CASES
```

```
% RESULTS FOR SYSTEM WITHOUT COMPENSATORS
```

```
subplot (4,3,1)
B=rotsp (1501:3001, :);
nfft= length(B);
x=fft(B,1501);
A1=(abs(x). ^2)/nfft;
f= ((0: nfft-1) *(Fs/nfft));
plot (f, A1,'k','LineWidth',1);
grid on
xlim ([0 70]);
ylim ([0 600])
ylabel ('Magnitude (pu)');
xlabel ('FFT Mag.');
```

```
subplot (4,3,2)
B=rotsp (3001:4501, :);
nfft= length(B);
x=fft(B,1501);
A2=(abs(x). ^2)/nfft;
```

```

f= ((0: nfft-1) *(Fs/nfft));
plot (f, A2,'k','LineWidth',1);
grid on
xlim ([0 70]);
ylim ([0 600])
title ('FFT of Rotor speed deviation 3s-4.5s');
xlabel ('Frequency (Hz)');
ylabel ('FFT Mag.(pu)');

subplot (4,3,3)
B=rotsp (4501:6001, :);
nfft= length(B);
x=fft(B,1501);
A3=(abs(x). ^2)/nfft;
f= ((0: nfft-1) *(Fs/nfft));
plot (f, A3,'k');
grid on
xlim ([0 70]);
ylim ([0 600])
xlabel ('Frequency (Hz)');
ylabel ('FFT Mag.(pu)');
title('(a) FFT analysis of rotor speed deviation without damping controller');

```

% PSS AND MODE 1 DAMPING CONTROLLER FFT RESULTS

```

subplot (4,3,4)
B=rotspM11(1501:3001, :);
nfft= length(B);
x=fft(B,1501);
A1=(abs(x). ^2)/nfft;
f= ((0: nfft-1) *(Fs/nfft));
plot (f, A1,'k','LineWidth',1);
grid on
xlim ([0 70]);
ylim ([0 1000])
ylabel ('FFT Mag.(pu)');
xlabel ('Frequency (Hz)');

subplot (4,3,5)
B=rotspM11(3001:4501, :);
nfft= length(B);
x=fft(B,1501);
A2=(abs(x). ^2)/nfft;
f= ((0: nfft-1) *(Fs/nfft));
plot (f, A2,'k','LineWidth',1);
grid on
xlim ([0 70]);
ylim ([0 1000])
title ('FFT of Rotor speed deviation 3s-4.5s');
ylabel ('FFT Mag.(pu)');
xlabel ('Frequency (Hz)');

subplot (4,3,6)
B=rotspM11(4501:6001, :);
nfft= length(B);

```

```

x=fft(B,1501);
A3=(abs(x). ^2)/nfft;
f= ((0: nfft-1) *(Fs/nfft));
plot (f, A3,'k','LineWidth',1);
grid on
xlim ([0 70]);
ylim ([0 1000])
ylabel ('FFT Mag.(pu)');
xlabel ('Frequency (Hz)')
title('(b) FFT Analysis of Rotor Speed Deviation with PSS and Mode 1 Damping Controller');

```

% PSS AND MODE 3 DAMPING CONTROLLER FFT RESULTS

```

subplot (4,3,7)
B=rotspM33(1501:3001, :);
nfft= length(B);
x=fft(B,1501);
A1=(abs(x). ^2)/nfft;
f= ((0: nfft-1) *(Fs/nfft));
plot (f, A1,'g','LineWidth',1);
grid on
xlim ([0 70]);
ylim ([0 200])
ylabel ('FFT Mag.(pu)');
xlabel ('Frequency (Hz)');

```

```

subplot (4,3,8)
B=rotspM33(3001:4501, :);
nfft= length(B);
x=fft(B,1501);
A2=(abs(x). ^2)/nfft;
f= ((0: nfft-1) *(Fs/nfft));
plot (f, A2,'g','LineWidth',1);
grid on
xlim ([0 70]);
ylim ([0 200])
ylabel ('FFT Mag.(pu)');
xlabel ('Frequency (Hz)');

```

```

subplot (4,3,9)
B=rotspM33(4501:6001, :);
nfft= length(B);
x=fft(B,1501);
A3=(abs(x). ^2)/nfft;
f= ((0: nfft-1) *(Fs/nfft));
plot (f, A3,'g','LineWidth',1);
grid on
xlim ([0 70]);
ylim ([0 200])
ylabel ('FFT Mag.((pu)');
xlabel ('Frequency (Hz)')
title('(c) FFT Analysis of Rotor Speed Deviation with PSS and Mode 3 Damping Controller');

```

% PSS AND MODE 4 DAMPING CONTROLLER FFT RESULTS

```

subplot (4,3,10)
B=rotspM44(1501:3001, :);
nfft= length(B);
x=fft(B,1501);
A1=(abs(x). ^2)/nfft;
f= ((0: nfft-1) *(Fs/nfft));
plot (f, A1,'r','LineWidth',1);
grid on
xlim ([0 70]);
ylim ([0 500])
ylabel ('FFT Mag.(pu)');
xlabel ('Frequency (Hz)');

subplot (4,3,11)
B=rotspM44(3001:4501, :);
nfft= length(B);
x=fft(B,1501);
A2=(abs(x). ^2)/nfft;
f= ((0: nfft-1) *(Fs/nfft));
plot (f, A2,'r','LineWidth',1);
grid on
xlim ([0 70]);
ylim ([0 500])
ylabel ('FFT Mag.(pu)');
xlabel ('Frequency (Hz)');

subplot (4,3,12)
B=rotspM44(4501:6001, :);
nfft= length(B);
x=fft(B,1501);
A3=(abs(x). ^2)/nfft;
f= ((0: nfft-1) *(Fs/nfft));
plot (f, A3,'r','LineWidth',1);
grid on
xlim ([0 70]);
ylim ([0 500])
ylabel ('FFT Mag. ');
xlabel ('Frequency (Hz)')
title('(d) FFT Analysis of Rotor Speed Deviation with PSS and Mode 4 Damping Controller');

```

G.6 Performance Investigation of PSS and Single-mode damping controllers ($P_{dc}=0.4154$ pu)

```

clc
clear all
close all

load -ascii papa_02.out; % Notepad file with no compensators
load -ascii papaM1_02.out; % Compensator 1 Notepad file
load -ascii papaM3_02.out; % Compensator 3 Notepad file
load -ascii papaM4_02.out; % Compensator 4 Notepad file

t=papaM1_02(:,1); % Data for column vector “t”: time constant
Fs=1/0.001; % sampling frequency
rotsp=papa_02(:,7); % Rotor speed deviation without compensators
rotspM1=papaM1_02(:,7); % Rotor speed deviation with PSS and SMDC (1)

```

```

rotspM3=papaM3_02(:,7); % Rotor speed deviation with PSS and SMDC (3)
rotspM4=papaM4_02(:,7); % Rotor speed deviation with PSS and SMDC (4)

```

% RESULTS FOR SYSTEM WITHOUT COMPENSATORS

```

subplot (4,3,1)
subplot (1,3,1)
B=rotsp (1501:3001, :);
nfft= length(B);
x=fft(B,1501);
A1=(abs(x). ^2)/nfft;
f= ((0: nfft-1) *(Fs/nfft));
plot (f, A1,'k','LineWidth',1);
grid on
xlim ([0 70]);
ylim ([0 2100])
ylabel ('FFT Mag(pu)');
xlabel ('Frequency (Hz)');

subplot (4,3,2)
B=rotsp (3001:4501, :);
nfft= length(B);
x=fft(B,1501);
A2=(abs(x). ^2)/nfft;
f= ((0: nfft-1) *(Fs/nfft));
plot (f,A2,'k','LineWidth',1);
grid on
xlim ([0 70]);
ylim ([0 2100])
ylabel ('FFT Mag (pu) ');
xlabel ('Frequency (Hz)');

subplot (4,3,3)
B=rotsp (4501:6001, :);
nfft= length(B);
x=fft(B,1501);
A3=(abs(x). ^2)/nfft;
f= ((0: nfft-1) *(Fs/nfft));
plot (f, A3,'k','LineWidth',1);
grid on
xlim ([0 70]);
ylim ([0 2100])
title('(a) FFT analysis of rotor speed deviation without damping controller');
ylabel ('FFT Mag (pu) ');

```

% PSS and MODE 1 DAMPING CONTROLLER FFT RESULTS

```

subplot (4,3,4)
B=rotspM1(1501:3001, :);
nfft= length(B);
x=fft(B,1501);
A1=(abs(x). ^2)/nfft;
f= ((0: nfft-1) *(Fs/nfft));
plot (f,A1,'k','LineWidth',1);
grid on

```

```

xlim ([0 70]);
ylim ([0 200])
ylabel ('FFT Mag (pu)');
xlabel ('Frequency (Hz)');

```

```

subplot (4,3,5)
B=rotspM1(3001:4501, :);
nfft= length(B);
x=fft(B,1501);
A2=(abs(x). ^2)/nfft;
f= ((0: nfft-1) *(Fs/nfft));
plot (f, A2,'k','LineWidth',1);
grid on
xlim ([0 70]);
ylim ([0 200])
ylabel ('FFT Mag (pu)');
xlabel ('Frequency (Hz)');

```

```

subplot (4,3,6)
B=rotspM1(4501:6001, :);
nfft= length(B);
x=fft(B,1501);
A3=(abs(x). ^2)/nfft;
f= ((0: nfft-1) *(Fs/nfft));
plot (f, A3,'k','LineWidth',1);
grid on
xlim ([0 70]);
ylim ([0 200])
ylabel ('FFT Mag');
xlabel ('Frequency (Hz)')
title('(b) FFT analysis of rotor speed deviation with PSS and Mode 1 damping controller');

```

% PSS and MODE 3 DAMPING CONTROLLER FFT RESULTS

```

subplot (4,3,7)
B=rotspM3(1501:3001, :);
nfft= length(B);
x=fft(B,1501);
A1=(abs(x). ^2)/nfft;
f= ((0: nfft-1) *(Fs/nfft));
plot (f, A1,'g','LineWidth',1);
grid on
xlim ([0 70]);
ylim ([0 200])
ylabel ('FFT Mag (pu)');
xlabel ('Frequency (Hz)');

```

```

subplot (4,3,8)
B=rotspM3(3001:4501, :);
nfft= length(B);
x=fft(B,1501);
A2=(abs(x). ^2)/nfft;
f= ((0: nfft-1) *(Fs/nfft));
plot (f, A2,'g','LineWidth',1);
grid on

```

```

xlim ([0 70]);
ylim ([0 200])
ylabel ('FFT Mag');
xlabel ('Frequency (Hz)');

subplot (4,3,9)
B=rotspM3(4501:6001, :);
nfft= length(B);
x=fft(B,1501);
A3=(abs(x). ^2)/nfft;
f= ((0: nfft-1) *(Fs/nfft));
plot (f, A3,'g','LineWidth',1);
grid on
xlim ([0 70]);
ylim ([0 200])
ylabel ('FFT Mag (pu)');
xlabel ('Frequency (Hz)');
title('(c) FFT analysis of rotor speed deviation with PSS and Mode 3 damping controller');

```

% PSS and MODE 4 DAMPING CONTROLLER FFT RESULTS

```

subplot (4,3,10)
B=rotspM4(1501:3001, :);
nfft= length(B);
x=fft(B,1501);
A1=(abs(x). ^2)/nfft;
f= ((0: nfft-1) *(Fs/nfft));
plot (f, A1,'r','LineWidth',1);
grid on
xlim ([0 70]);
ylim ([0 1500])
ylabel ('FFT Mag(pu)');
xlabel ('Frequency (Hz)');

```

```

subplot (4,3,11)
B=rotspM4(3001:4501, :);
nfft= length(B);
x=fft(B,1501);
A2=(abs(x). ^2)/nfft;
f= ((0: nfft-1) *(Fs/nfft));
plot (f, A2,'r','LineWidth',1);
grid on
xlim ([0 70]);
ylim ([0 1500])
ylabel ('FFT Mag');
xlabel ('Frequency (Hz)');

```

```

subplot (4,3,12)
B=rotspM4(4501:6001, :);
nfft= length(B);
x=fft(B,1501);
A3=(abs(x). ^2)/nfft;
f= ((0: nfft-1) *(Fs/nfft));
plot (f, A3,'r','LineWidth',1);
grid on

```

```
xlim ([0 70]);  
ylim ([0 1500])  
ylabel ('FFT Mag.(pu)');  
xlabel ('Frequency (Hz)')  
title('(d) FFT analysis of rotor speed deviation with PSS and Mode 4 damping controller');
```